

INFORMATION TO USERS

This manuscript has been reproduced from the microfilm master. UMI films the text directly from the original or copy submitted. Thus, some thesis and dissertation copies are in typewriter face, while others may be from any type of computer printer.

The quality of this reproduction is dependent upon the quality of the copy submitted. Broken or indistinct print, colored or poor quality illustrations and photographs, print bleedthrough, substandard margins, and improper alignment can adversely affect reproduction.

In the unlikely event that the author did not send UMI a complete manuscript and there are missing pages, these will be noted. Also, if unauthorized copyright material had to be removed, a note will indicate the deletion.

Oversize materials (e.g., maps, drawings, charts) are reproduced by sectioning the original, beginning at the upper left-hand corner and continuing from left to right in equal sections with small overlaps. Each original is also photographed in one exposure and is included in reduced form at the back of the book.

Photographs included in the original manuscript have been reproduced xerographically in this copy. Higher quality 6" x 9" black and white photographic prints are available for any photographs or illustrations appearing in this copy for an additional charge. Contact UMI directly to order.

UMI

A Bell & Howell Information Company
300 North Zeeb Road, Ann Arbor MI 48106-1346 USA
313/761-4700 800/521-0600

THE EFFECT OF IMPLANTATION CONDITIONS ON
MICROSTRUCTURAL EVOLUTION IN OXYGEN IMPLANTED SILICON

By

RANJU DATTA

A DISSERTATION PRESENTED TO THE GRADUATE SCHOOL OF THE
UNIVERSITY OF FLORIDA IN PARTIAL FULFILLMENT OF THE
REQUIREMENTS FOR THE DEGREE OF DOCTOR OF PHILOSOPHY

UNIVERSITY OF FLORIDA

1998

UMI Number: 9837376

UMI Microform 9837376
Copyright 1998, by UMI Company. All rights reserved.

**This microform edition is protected against unauthorized
copying under Title 17, United States Code.**

UMI
300 North Zeeb Road
Ann Arbor, MI 48103

ACKNOWLEDGMENTS

I would like to extend my gratitude to my advisor Dr. K. S. Jones, for providing encouragement, and allowing me much freedom in this work. The support and encouragement of my committee members, Dr. C. Abernathy, Dr. S. S. Pearton, Dr. R. M. Fox and Dr. R. Singh are greatly appreciated.

I am indebted to Dr. David Venables at North Carolina State University for his invaluable and selfless help with this work. Dr. Venables not only provided much motivation and ideas for this work, but also provided extensive mentoring on scientific writing by editing much of this dissertation. Further, Dr. Venables patiently assisted me with all of the HRTEM and SIMS studies, which constitute a major portion of this study. Without the support of Dr. Venables, who is my husband, this work would not have been possible. I would like to extend my sincerest thanks to Dr. Venables for being my mentor and partner in life.

I extend my thanks to Dr. Lisa P. Allen, at Ibis Technology Corporation, for providing all the samples used in this study and for the tremendous encouragement she has provided. Thanks are due to all the staff at the MAIC facility, and especially to Dr. A. Morrone for his help. I am extremely grateful to Dr. D. Maher at North Carolina State University for allowing me the liberty to work at his laboratory during my stay at Raleigh.

I sincerely appreciate and thank Dr. V. Krishnamoorthy for all the assistance he has provided, especially with HRXRD. To all my friends, Dr. Jinning Liu, Kristie MacDonald, Brent P. Gilla, Sushil Bharatan, Dr. Brad Herner and Dr. V. Krishnamoorthy, I am indebted for making my stay in Gainesville more pleasant.

I wish to thank my parents Rabindra Nath Datta and Sova Datta for their constant encouragement in the pursuit of knowledge, and their invaluable loving support and care, at all times. I extend my sincerest appreciation to my brother Rajen and sister-in-law Sanhita for their constant assistance and support through some very difficult times. Their continued encouragement has always provided me with much strength. Last but by no means the least, I would like to thank my in-laws, Dr. John D. Venables, Kathryn E. Venables, Lee and Jess, for their encouragement, love and support, especially during the final phase of my dissertation.

TABLE OF CONTENTS

ACKNOWLEDGMENTS	ii
ABSTRACT.....	v
CHAPTERS	
1 INTRODUCTION	1
Background	1
Motivation and Objectives	26
2 EXPERIMENTAL PROCEDURES	30
Implantation and Annealing	30
Analytical Techniques.....	31
3 EFFECT OF IMPLANTATION CONDITIONS.....	39
Dose and Energy.....	40
Substrate Temperature	86
Beam Current	107
Discussion and Conclusions.....	115
4 PRECIPITATION PROCESSES IN ION BEAM SYNTHESIS.....	130
Experimental Details	132
Results	133
Models and Discussion.....	159
Conclusions.....	173
5 SUMMARY AND CONCLUSIONS	176
REFERENCES.....	184
BIOGRAPHICAL SKETCH	190

Abstract of Dissertation Presented to the Graduate School of the University
of Florida in Partial Fulfillment of the Requirements for the Degree Doctor
of Philosophy

THE EFFECT OF IMPLANTATION CONDITIONS ON
MICROSTRUCTURAL EVOLUTION IN OXYGEN IMPLANTED SILICON

By

Ranju Datta

May 1998

Chairman: Kevin S. Jones

Major Department: Materials Science and Engineering

Ion implantation is used for the fabrication of SIMOX (separation by implanted oxygen). SIMOX is a silicon on insulator structure used for microelectronic devices, where a buried oxide layer insulates a silicon overlayer from the substrate. High energy, high dose oxygen ions are implanted into a heated single crystalline silicon wafer, followed by high temperature annealing to create a uniform buried oxide and eliminate implantation damage.

The final quality of SIMOX material depends on the properties of the silicon overlayer and the buried oxide. The dominant defects are threading dislocations in the silicon overlayer and silicon inclusions (silicon islands) within the buried oxide, both of which are detrimental. The objectives of this dissertation were to evaluate the effect of implantation conditions on the formation of these defects, and to understand the underlying physical mechanisms which govern microstructural evolution in this system.

The effects of implant dose, energy, substrate temperature and beam current variations on microstructural evolution were investigated, primarily, by transmission electron microscopy and x-ray diffraction. Only specific dose ranges yielded low defect density SIMOX. Threading dislocation densities were low for intermediate doses and were high for very low and very high doses. However, low silicon island densities in the buried oxide were obtained at only one specific low dose and at high doses. These dose windows were affected to different extents by the other implantation parameters.

The physical mechanisms for these effects were established. Threading dislocations in the annealed state evolved from dislocation half loops present in the as-implanted state at high doses. The presence of dislocation half loops was a result of strain relief processes in the near surface region during implantation. Threading dislocations at low doses were the result of defect pinning by a bilayer oxide structure.

The precipitate distribution in the as-implanted state controlled the coarsening process during annealing, and thus determined the final morphology of the buried oxide. Severe inhomogeneities in precipitate sizes after implantation led to the formation of silicon islands during annealing. A roadmap for manipulating the implantation parameters to improve SIMOX has been developed based on this mechanistic understanding.

CHAPTER 1 INTRODUCTION

The main objective of ion implantation is to incorporate a desired atomic species into a target material. Even though this process has been used most frequently for introducing dopants in a semiconductor, compound synthesis using this method has also proved to be efficient. Separation by implanted oxygen (SIMOX) uses a high energy and high dose of oxygen ion implantation process at an elevated temperature to create a buried oxide layer under a single crystalline silicon overlayer. Presently SIMOX is one of the leading technologies to create a silicon on insulator (SOI) structure [1].

In this study the evolution of the microstructure in single implant SIMOX has been studied using independent control of the implantation parameters. The effects of implant dose, implant energy, substrate temperature and beam current variation on the structural features in SIMOX have been studied using transmission electron microscopy (TEM), high resolution x-ray diffraction (HRXRD), secondary ion mass spectrometry (SIMS) and atomic force microscopy (AFM).

Background

In this section the fundamentals of ion implantation are outlined followed by the application of this process to SIMOX fabrication. An extensive review of the existing literature is presented emphasizing the

process of silicon dioxide precipitation, defect microstructures and the effect of implantation conditions on the evolution of the SIMOX structure.

Ion Implantation

Ion implantation is the process by which foreign atoms are introduced directly into a material by bombarding it with energetic ions. It allows very precise control over the number and distribution of atoms that are injected. The two main processes which occur [2] when energetic ions strike an elemental solid are

1. implantation
2. damage production.

The incoming ion loses energy in a series of collision with the lattice atoms (nuclear stopping), and electrons (electronic stopping) of the target material, before coming to rest. The distribution of the implanted ions is nearly Gaussian in nature--i.e. they are distributed about a mean depth [3]. The ion mass, kinetic energy, and the mass of the target species all determine the mean range/depth of penetration. Hence, lighter and/or more energetic ions have a greater penetration depth than heavier and/or less energetic ions.

The transfer of energy by elastic collisions between the incoming moving ions and stationary target atoms results in damage production [2]. Since the displacement energy of an Si atom is about 15 eV, an incoming single ion with keV energy is capable of displacing many lattice atoms before coming to rest. Multiple collision cascades occur because many of the displaced target atoms have sufficient kinetic energy to displace additional atoms. Amorphization of a crystalline target often occurs when there is severe damage production. However, light ions suffer

predominantly electronic losses while heavy ions lose most of their energy by nuclear collisions.

In the case of heavy ions, amorphization in Si occurs over a critical dose, when the discrete amorphous zones created by the incoming ions overlap. The total dose and energy determine the depth at which this amorphous layer is created. Light ions usually create small discrete defect clusters and amorphization by overlap and accumulation of these regions is a less efficient process. So a lower dose of heavy ions is more efficient in inducing amorphization than light ions [4].

The temperature of the target is a vital parameter that determines the degree of amorphization. The competition between the damage production rate and dynamic or self-anneal effects determines the final defect type and density in the target material.

SIMOX Fabrication

Implantation of a high dose of energetic oxygen ions into Si is used to create a buried insulation layer under a single crystalline silicon overlayer. This silicon on insulator (SOI) technology is known as SIMOX (Separation by Implanted Oxygen) [1].

There are a myriad of advantages in terms of device performance obtained by isolating the active layer from the substrate, with an insulating layer, especially in CMOS technology [5]. Some of these advantages are prevention of latch-up, reduction in junction capacitance, and improved radiation hardness. SOI technologies are particularly promising candidates for low power and low voltage applications [6-8].

Amongst all the other existing SOI technologies such as silicon-on-sapphire (SOS), zone-melting recrystallization (ZMR) and wafer bonding (BSOI), SIMOX has appeared to be the most promising candidate [9].

Typically, the SIMOX process consists of two main steps. (1.) Oxygen is implanted at a high energy (~ 150 keV) to a high dose of up to $2 \times 10^{18} \text{ cm}^{-2}$ at an elevated temperature. Beneath a damaged but monocrystalline Si overlayer an amorphous stoichiometric SiO_2 layer is formed. (2.) Post-implantation annealing at an elevated temperature ($\sim 1300^\circ\text{C}$) is necessary to remove the damage in the single crystalline Si overlayer and create a uniform buried oxide underneath.

Unfortunately, the post-implantation annealing does not effectively remove all the crystallographic defects formed in the Si overlayer during ion implantation. These defects affect the performance of minority carrier devices by reducing carrier lifetime and acting as leakage paths [10-12]. Hence, it is of technological importance to determine the mechanism by which they form and monitor the implantation process to reduce them. Even though there has been a large volume of research to explain the evolution of single implant SIMOX, no unanimous theory has been accepted as yet. Innovative processing schemes [13,14] have been found to produce low threading dislocation densities but no clear understanding exists behind the success of these methods. Hence to make this technology commercially viable it is necessary that an in-depth understanding of the effect of the processing conditions on the evolution of the microstructure be obtained.

High dose implantation is associated with two main categories of problems [15]: those caused as a result of damage to the target and those caused from variation in the temperature of the target. Hence it is apparent that the implantation conditions dictate the final microstructure of the material. It is therefore essential to understand the effect of each of the implant conditions individually on the microstructure. The lack of

agreement existing in the literature today is due to the complex nature of the structures formed by ion beam synthesis using high dose, energy, beam current and temperature and the intricate way by which implantation and annealing parameters influence the evolution of the structural features. Moreover, until very recently, the energy, beam current and substrate temperature could not be controlled independently of each other, and thereby the individual effect of these implant conditions on the SIMOX microstructure could not be assessed.

Previous studies on the evolution of the microstructure used coupled implantation conditions. Effectively, none of the implantation parameters could be varied independently except for the implant angle and dose. Thus, these studies failed to achieve a clear understanding of the effect of implantation conditions on the SIMOX microstructure.

Recently, using the new Ibis 1000 implanter it has become possible to control all implantation conditions independently. Hence, for the first time, it has become possible in this study to investigate the individual effects of these implantation conditions on the SIMOX microstructure.

Oxygen Precipitation in Silicon

High dose SIMOX ensures that the oxygen implanted exceeds the solid solubility limit. Oxygen normally occupies an interstitial site [16] in solid solution and the maximum solubility is about $2 \times 10^{18} \text{ cm}^{-3}$ at 1410°C , the melting point of silicon [17]. However, the primary precipitation path depends on the temperature range used, as observed in single stage annealing experiments [18,19]. Rod-like defects, similar to $\{113\}$ defects, occur in the temperature range of 485°C to 750°C . Plate-like precipitates occur on $\{100\}$ planes at temperatures of 650°C to 1050°C . These precipitates consist of mainly square shaped amorphous SiO_x with $x \sim 2$. However, at

higher temperatures precipitation only occurs if nuclei have already been formed at an annealing stage at lower temperatures, since the oxygen supersaturation is low. Large, octahedral precipitates of amorphous SiO_x form in these two stage anneals. These precipitates are faceted along $\{111\}$ and $\{100\}$ planes and no strain field is associated with them.

Extrinsic defects accompany the precipitation of SiO_x [18, 19]. These defects have been characterized as distorted Frank loops on $\{111\}$ planes (also called loopites) at a temperature of 600°C and higher. For temperatures up to 950°C , faulted Frank loops with $b=1/3\langle 111 \rangle$ nucleate in association with precipitates. Small, prismatic loops have also been observed to be punched out at temperatures higher than 900°C .

A strain accommodation mechanism for the SiO_2 precipitate growth is the basic reason for the presence of extrinsic defects. The precipitation of SiO_2 involves a large change in volume and hence a large strain energy since the molecular volume of SiO_2 is 2.25 times the atomic volume of silicon. It has been proposed [20, 21] that the ejection of excess silicon atoms as interstitials could relieve the excess strain. The equation which describes this situation is



where Si_I is the silicon self interstitial ejected.

Experimental verification of this mechanism was obtained by quantifying the number of interstitials bound by extrinsic loopites and the number of molecules of SiO_2 formed [22]. Thus, for strain free precipitation it is required that $x=2.2$, which results in excess Si interstitials in the matrix [23]. It has been reported [24, 25] that Si_I has a high formation energy but a low migration energy, and the sum of these two activation energies is ~ 5 eV. In SIMOX, oxidation of Si to SiO_2 leads to the emission of

Si interstitials by the process described above. The energy necessary to break silicon bonds is provided by the ion implantation process. During implantation, both vacancies and interstitials are created. Excess vacancies encourage SiO₂ precipitation. Stoemenos et al. [23] show that a flux of $0.63F_0 \text{ cm}^{-2}\text{s}^{-1}$ of Si interstitials from the buried oxide is necessary for strain-free oxidation (where F_0 is the flux of implanted oxygen). The surface is a natural sink for Si interstitials. If Si interstitial migration to the surface is inhibited, supersaturation of Si interstitials will take place. This supersaturation of Si interstitials would cause a chemical potential to build up which consequently would inhibit SiO₂ precipitation. They showed that the Si_I supersaturation C_I/C_I^* is related to the incident oxygen flux by

$$C_I/C_I^* = 1 + .63F_0 w^2 / 8D_S C_S$$

where, w is the distance from free surface, D_S is the Si interstitial diffusivity, C_S is the Si concentration $\sim 5.5 \times 10^{22} \text{ atoms cm}^{-3}$, and C_I^* is the equilibrium Si interstitial concentration.

In SIMOX, D_S is strongly dependent on the density of SiO₂ precipitates. Hence, the formation of SiO₂ precipitates is often associated with extrinsic defects in silicon.

Structural Features in SIMOX

Ion implantation damage during the high dose and high energy implant of oxygen in silicon leads to a number of unique structural features in SIMOX. The most prominent ones are discussed here. The major structural defects in as-implanted SIMOX are cavities and dislocation half loops near the surface. Stacking faults and silicon dioxide precipitates occur beneath the surface. Upon annealing, the primary defects are threading dislocations in the SI overlayer and Si islands in the buried oxide. Further, the quality of the top Si surface and Si/buried oxide interface is of

importance. The fundamental structure of each of these features and the possible effects of the implant conditions on their evolution is discussed in the following sections. A schematic diagram illustrating the dominant defects which may be present in the as-implanted state and annealed state are shown in Figure 1.1 and Figure 1.2, respectively.

Cavities

Cavities form in the as-implanted SIMOX structure due to the agglomeration of vacancies which are stabilized by the incoming oxygen [26]. They appear at and in the near surface region of the Si overlayer. Cavities have been reported to discourage near surface precipitation, thereby eliminating the possibility for precipitation induced defects to be pinned and evolve into threading dislocations [27]. Some studies report that highly defective regions are not found near the surface, when cavities are present [28, 29]. Other reports indicate the presence of high densities of half loops in association with cavities [27]. These cavities are largest at the surface and decrease in size with depth. Also, a high density of cavities have been reported to show a columnar structure, while at lower densities the cavities seem to be randomly distributed at the surface [30]. The direction of the columns are parallel to the oxygen-ion beam and not to any particular crystallographic direction. The shape of the cavities in general is oblate spheroidal in nature. Previous studies show that the nucleation of cavities occurs in the early stage of the implantation process, usually within the first 30% or so of the dose deposited [31]. It has been found that heterogeneous nucleation is not the cause for cavity formation [31].

It has been established that only very specific conditions encourage the growth and stabilization of cavities. The cavities are stabilized in the presence of a rapid supply of oxygen. Vacancy clusters are formed by the

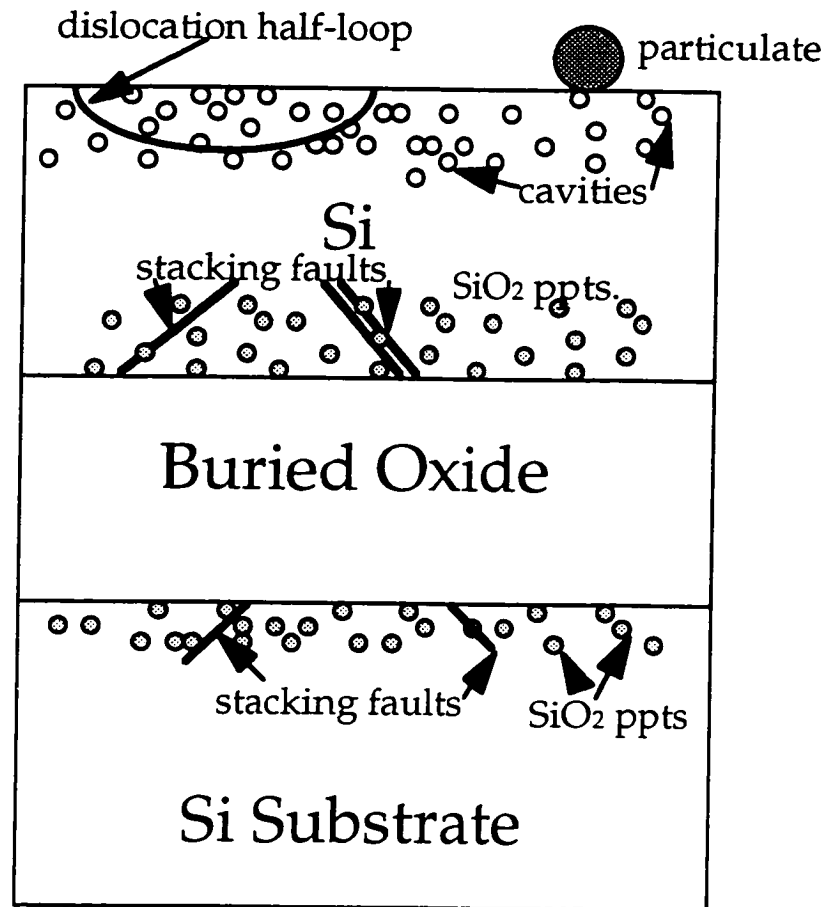


Figure 1.1. Schematic of microstructural features in as-implanted SIMOX.

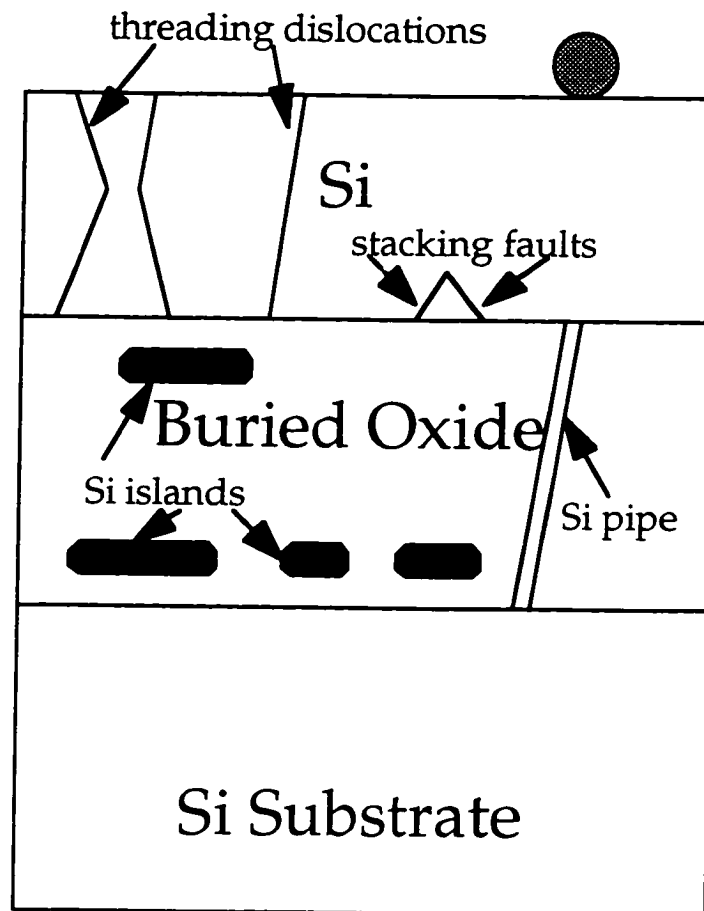


Figure 1.2. Schematic of microstructural features in annealed SIMOX.

instantaneous overlap of the local disorder regions caused by the individual projectiles [26]. Higher dose rates provide a greater availability of fast moving oxygen atoms. Interstitial supersaturation in the areas near the bare silicon surface may suppress nucleation of vacancy clusters.

The implantation conditions affect the morphology and distribution of the cavities. The diameter and depth of the cavities grow as the dose increases while the density of the cavities does not change significantly [32]. Maszara [26] found that lower doses seemed to produce deeper cavity layers while higher doses produced shallower ones. He attributed this to extensive sputtering at the higher doses. However, a possible cause could have been the temperature variation, dose and dose rate effects which could not be investigated. Other reports indicate no evidence that the size or density of the cavities varies with dose [31].

An attempt to explain the mechanism for cavity/void formation during ion implantation at high doses and high temperature was presented recently [33]. Two models were suggested after studying the effect of ion chemistry on the as-implanted morphology and the evolution of the damage structure.

The first explanation involves cavity formation as a classical nucleation and growth process, as a consequence of vacancy supersaturation [13, 34]. Clustering of vacancies, to reduce free energy can cause nucleation. However, the stability of these clusters is dictated by the competition between the reduction in free energy by formation of a second phase volume and the increase in energy due to interfacial stress at the phase boundary. Experimental results indicate that the implanted species may bind to the walls of cavities in Si and thereby stabilize the cavities.

The second explanation suggests the induction of an internal electric field due to the presence of ionized impurities in Si. This electric field may attract negatively charged vacancies thereby enhancing the vacancy concentration in the region. So, in addition to diffusion, this mechanism would add a drift component to the vacancy flux. Hence, cavity/void formation will be encouraged.

Dislocations and stacking faults

The main defects found in the as-implanted state are stacking faults and dislocation half loops. Dislocation half loops have been found to be extrinsic in character with a Burgers vector of $1/2\langle 110 \rangle$ perpendicular to the plane of the loop [27,35]. Dislocation half loops are located at the surface, in association with cavities [27]. Stacking faults have been found in the silicon overlayer and their locations, as reported in studies, seem to vary. This may be due to the difference in implantation conditions used. After annealing, threading dislocations are the dominant defects in the silicon overlayer and they span from the buried oxide to the surface of the silicon overlayer.

A large number of interstitials form during the ion implantation process. Moreover, stress is generated due to the precipitation of SiO_2 which occupies a larger volume than silicon (2.25 times that of Si). It has been suggested that, if the surface reconstruction rate is less than the rate of arrival of silicon interstitials, then the interstitials can agglomerate to form defects [36].

Dislocation half loops have been found to be predominant in the as-implanted state, and they may evolve into threading dislocations on post implantation annealing [27]. Recent work on dislocation evolution suggests that the density of dislocation half loops after implantation is directly

proportional to the threading dislocation density after annealing [35], for high dose implantation. Other studies [37] claim that no dislocation half loops are present below a dose of $1.0 \times 10^{18} \text{ cm}^{-2}$, which implies threading dislocations in the low dose regime evidently do not evolve from dislocation half loops [37]. The main sources of threading dislocation evolution have been attributed to either defects created during annealing and/or to the growth of defects during annealing from the as-implanted state. Precipitation induced stresses during ramping and annealing have also been suggested to lead to dislocations [27].

For low temperature and low dose rate implantation there are two existing models for dislocation evolution. One study [29] suggests that near surface precipitates generate stacking faults extending to the surface, some of which grow downward to the buried oxide during annealing giving rise to unpaired threading dislocations. Stacking faults may unfault during expansion and leave behind dislocations [29]. No cavities were reported to have been present under these conditions.

The other model [38] describes near-surface defects on {111} habit planes existing during intermediate temperature annealing at 1000°C - 1100°C as precursors of threading dislocations, which are not paired.

The report closest to this study at high dose rate and high substrate temperature implantation conditions suggests that dislocation half loops begin to form by stress assisted climb due to implantation damage [27, 35]. These dislocation half loops evolve into threading dislocation pairs by expansion during annealing. Cavities, dislocation half loops and multiply faulted defects/stacking faults are usually present in the as-implanted state under these implantation conditions.

Silicon dioxide precipitates

The ion implantation of oxygen in silicon to concentrations far above the solubility limit [36, 38] causes precipitation. A continuous buried oxide layer is formed in regions where the concentration is equal to the stoichiometric one in SiO_2 [39, 40]. On either side of the continuous layer, the concentration is insufficient to form a continuous layer and SiO_2 precipitates are formed. Depending on the energy of implantation, the profile evolves from a Gaussian one and then broadens out as the dose increases. Since the volume occupied by SiO_2 is 2.25 times that of the original Si, accommodation volume is necessary to avoid the development of stress in the Si matrix.

Silicon dioxide precipitates are present in the as-implanted state, increasing in size toward the buried oxide [41]. On post-implantation annealing, the smaller precipitates dissolve while the larger ones increase in size until finally they dissolve into the buried oxide which grows in width, preferentially toward the surface [42]. This precipitation process is described as Ostwald ripening. It is important to allow stress free precipitation of these silicon dioxide precipitates to reduce the growth of dislocations [43]. The coarsening mechanism of these oxide precipitates during annealing has been studied [44]. The driving force for their evolution has been attributed to the combined effect of Ostwald ripening and the self organization of SiO_2 precipitates. Near surface precipitation, which takes place under certain implantation conditions, has been found to be detrimental to the quality of the Si overlayer. The near surface precipitates seem to encourage the growth and movement of defects which could later stabilize into threading dislocations [27, 29]. The effect of implantation conditions on the distribution of precipitates in the as-implanted state and

their subsequent evolution during the post-implantation annealing step would reveal the mechanism by which they dissolve as well as the way they effect the growth of dislocation half loops into final threading dislocations. It is necessary to study the growth, nucleation, precipitation and coalescence process of the SiO_2 precipitates as it should be influenced by each of the implantation conditions.

Silicon islands

These features are silicon inclusions present in the buried oxide. For very high doses these islands are confined to the back buried oxide/silicon substrate interface. These Si islands are usually polyhedral in shape and single crystalline in nature and are oriented in the direction of the original silicon substrate [45]. Depending on the dose implanted, it has been found that their location within the buried oxide may vary [46]. Their presence within the buried oxide is undesirable since they reduce the dielectric strength of the buried oxide and thereby cause subsequent device degradation [47]. It has been observed [46] that at low doses, from $0.45 \times 10^{18} \text{ cm}^{-2}$ to $0.675 \times 10^{18} \text{ cm}^{-2}$, there is an increase in the Si island density with the increase in oxygen dose. There is, at present, no understanding of this behavior. An important microstructural feature which has been observed in some studies is "leaf-like" defects in the buried oxide in the as-implanted state, which have been suggested to give rise to silicon islands after annealing [32]. It has been proposed [45] that Si inclusions can be trapped in the buried oxide because of the low diffusivity of Si in SiO_2 , even at high temperatures. The diffusivity of Si in SiO_2 [17] is $(3.4 \times 10^{-17} \text{ cm}^2/\text{s})$ at 1320°C , which is eight orders of magnitude lower than that of oxygen in SiO_2 . This does not explain the behavior reported at lower doses [46]. During high temperature, post-implantation annealing, the SiO_2 precipitates coalesce

and can trap unoxidized Si. This unoxidized Si develops a characteristic faceted morphology to minimize the surface tension and interface energy.

Effect Of Implantation Parameters

The implantation parameters which have a direct consequence on the evolution of the microstructure are implant energy, angle of implantation, dose, substrate temperature and beam current. A detailed discussion of the effects of each of these parameters from existing literature is given in the following sections.

Implant energy

The implantation energy determines the depth to which the oxygen penetrates into the Si, thereby determining the thickness of the Si overlayer. Moreover, the depth at which the buried oxide is created [48 - 51] and the radiation damage associated with the high dose implants are also influenced by the energy. The energy of implantation determines the optimal dose necessary for a completely stoichiometric buried oxide layer. If the implant energy is reduced by an order of magnitude, the thickness of the silicon and buried oxide layers also reduce by an order of magnitude. In addition, the dose for SOI fabrication reduces by an order of magnitude. There are a number of advantages as well as disadvantages of low energy implantation. Lower energy implants allow lower doses and hence the implantation time is greatly reduced. The crystalline quality of the top Si layer is maintained since the number of ions traversing the top Si layer is decreased. Si/SiO₂ interfaces become sharp due to the decrease in the width of the oxygen distribution. Unfortunately, low energy ion implantation has a high sputtering rate. Implanting O₂⁺ instead of O⁺ for low energy implants results in higher sputtering. At low doses, the oxygen depth profile is nearly Gaussian [52]. As the dose is increased, the oxygen profile

saturates once a continuous buried oxide layer is formed. On further increasing the dose, the width of the implanted profile increases and for very high doses, oxide layers extending to the surface can be formed. The implant energy thus determines the depth and thickness of the buried layer. It has been shown [53] that once a surface oxide is formed the thickness of the layer decreases with increasing the dose. This decrease has been suggested [53] to be a result of sputtering, along with an increase in the stopping power once SiO_2 is formed. This effect is independent of the energy of implant.

A critical oxygen dose exists for each implant energy to form a continuous buried SiO_2 layer. When the dose is lower than the critical value the distribution is a skewed Gaussian. Thus there are more oxygen atoms in the upper half of the distribution, i.e., the peak of the distribution (the depth of maximum oxygen concentration) is deeper than the mean range. The peak of the as-implanted oxygen distribution moves deeper into the Si with increase in dose for all energies [54, 55]. The reason behind this peak shift has been explained [54] as a consequence of the volume expansion which is large in SIMOX. It has been suggested [23] that a multi-energy single implant can significantly reduce the dislocation density. This is because if the implant energy is ramped down steadily the blocking of silicon interstitials by SiO_2 precipitates is reduced, since the initial SiO_2 precipitates will be formed deeper in the silicon matrix. Even though a ramped up implant energy would have the same oxygen depth distribution as the ramped down energy implant, the silicon interstitial migration to the surface would be hampered and would not yield low dislocation densities.

Implant angle

Studies on the effect of implant angle [56, 57] show that the layer thickness and composition of the buried oxide strongly depend upon the amount of channeling allowed by the implant. There is a trend toward a thicker superficial silicon layer and a thicker buried oxide when the orientation of the wafer with respect to the ion beam allows more channeling. The implant angle and the initial profile of oxygen affect the integrity of the buried oxide. Pinhole alignment with the major crystallographic directions [58] in the silicon crystal have been observed. Thus, the properties of the buried oxide may depend upon the amount of channeling allowed by the angular relationship between the oxygen beam and silicon crystal. No physical basis for this behavior has yet been suggested.

Implant dose

A critical dose is required to form a completely stoichiometric buried oxide, which is dependent on the implant energy. A stoichiometric dose corresponds to the peak of the oxygen profile reaching 67 at% (the composition of SiO_2). The width of the implanted profile increases with the increase in dose. For doses higher than the stoichiometric dose at energies greater than 100 keV a buried oxide layer is formed. The silicon overlayer is single crystalline in nature but usually defective. Upon annealing the surface silicon is denuded of oxygen and both the buried oxide and surface silicon undergo drastic changes in microstructure. The nature of the final microstructure has been found to be extremely sensitive to the initial implantation conditions.

Studies on the effect of dose on cavities [43 - 44] have revealed that they may appear near the surface of the silicon layer at a dose of $3 \times 10^{17} \text{ cm}^{-2}$. It has been observed that they increase in size as the dose increases. Substantial surface roughness is seen when cavities are present, but upon annealing at 1300°C the surface becomes planar [44].

Strain measurements performed [35] on dose variation samples show that the near surface strain increases with the increase in dose. This study indicates that at high doses the precursors to threading dislocations, which are formed in the annealed state, are dislocation half loops in the as-implanted state. The final threading dislocations occur in pairs. However, all the dislocation half loops do not develop into threading dislocations. The threading dislocations which survive have Burgers vectors parallel or perpendicular to the wafer surface. The reason behind this observation is that in the as-implanted state dislocation half loops with all possible burgers vectors of type $1/2\langle 110 \rangle$ are present. Of these two types $1/2[110]$ and $1/2[-\bar{1}10]$ have Burgers vectors parallel to the surface and hence the dislocation half loops are perpendicular to the surface. All the others are inclined to the surface at 45° . Thus the number of dislocations with Burgers vectors at an angle to the surface compared to those with Burgers vectors parallel to the surface is 2:1, which was confirmed experimentally. After annealing it was found that dislocation half loops with Burgers vectors at an angle to the surface were completely eliminated. Further only $\sim 1\%$ of those with Burgers vectors parallel to the surface formed threading dislocation pairs. The evolution mechanism has been explained as a consequence of dislocation loops moving to the surface along their glide cylinders if the attractive interaction force can overcome the lattice frictional force [59]. Hence, removal of the dislocation half loops with

Burgers vectors at an angle to the surface occurs when their mobility and the attractive image force are high. However, for the elimination of dislocation half loops with Burgers vectors parallel to the surface, climb is the necessary mechanism. These dislocation half loops are extrinsic in nature and their removal can be caused as a result of emitting interstitials or absorbing vacancies. Upon annealing near surface precipitates dissolve introducing an enrichment of vacancies and causes the elimination of some of these dislocation half loops. For doses higher than $1.3 \times 10^{18} \text{ cm}^{-2}$ at 180 keV, Nakashima and Izumi [32] report that an extremely high threading dislocation density $\sim 10^7\text{-}10^9 \text{ cm}^{-2}$ exists in the top silicon layer after annealing at 1300°C .

For high doses the buried oxide grows by the Ostwald ripening process. Silicon islands for these doses are present mainly near the buried oxide/silicon substrate interface, i.e. at the bottom of the buried oxide layer.

For low doses it has been observed [35, 37] that dislocation half loops do not form in the as-implanted state. However at extremely low doses of $0.2 \times 10^{18} \text{ cm}^{-2}$, for conventional energies, a high number of defects are present after annealing [37]. Moreover at this low dose a connected buried oxide does not form. It has been reported recently that a well formed buried oxide appears at a dose of $0.3 \sim 0.45 \times 10^{18} \text{ cm}^{-2}$ [32, 37]. Unfortunately, the quality of the buried oxide deteriorates with increase in dose between $0.5 \times 10^{18} \text{ cm}^{-2}$ and $0.7 \times 10^{18} \text{ cm}^{-2}$. No fundamental understanding exists as yet to explain this process. Studies [32] reveal that multi-layered oxide striations present in the as-implanted buried oxide layer may grow into a multiple buried oxide layer after annealing at 1150°C . This causes a discontinuous buried oxide with numerous Si 'micropaths' between the

surface silicon and silicon substrate. These 'micropaths' deteriorate the electric breakdown strength of the buried oxide.

Substrate temperature

The substrate or implant temperature has been found to affect the evolution of the microstructure in the as-implanted state most significantly. To avoid amorphization of the surface silicon, the substrate is maintained at a high temperature. Most of the previous studies used coupled implant conditions, i.e., the beam current and energy were used to control the implant temperature. Thus, the independent effect of this parameter, especially under high beam current conditions, is not well understood.

Depending on the implant temperature the as-implanted morphology has been reported [60 - 64] to be as follows.

- (1.) For temperatures below 450°C, amorphous silicon sandwiched between defective single crystal silicon and buried oxide forms a multi-layered structure.
- (2.) For temperatures between 450 and 550°C a randomly distributed network of amorphous precipitates extending through a defective though single crystalline silicon surface layer is predominant.
- (3.) For temperature of 550°C and higher the near surface region may be decorated with cavities.

For temperatures lower than 450°C, where amorphization of silicon occurs, studies were done [60] at a dose of $3 \times 10^{18} \text{ cm}^{-2}$, with a 200 keV implant energy. An amorphous silicon layer formed for temperatures of 400°C or lower, which consumed the entire surface silicon at a temperature of 25°C. However, as the implant temperature was increased the thickness of the amorphous layer grew thinner and it formed a buried layer. A 600°C

anneal allowed limited regrowth of the amorphous layer. However, microtwins were formed where the oxygen concentration was highest. On further annealing these samples at 1400°C, the microtwins remained at the edges of the buried oxide, a continuous buried oxide layer with sharp interfaces was formed and no islands were present in the buried oxide. Buried oxide layers with rough interfaces and silicon islands were found in samples with higher implant temperatures where there was no microtwin layer. It was also found [60 - 63] that for very high initial anneal temperatures of 1050°C and higher, the amorphous layer recrystallizes to polycrystalline silicon, and no microtwin layer is formed. For stoichiometric doses, it has been observed [62] that a temperature above 450°C to 475°C is effective in suppressing amorphization.

Extensive studies have been performed using stoichiometric dose implants on a substrate temperature between 450°C and 550°C. In the as-implanted microstructure, a continuous buried oxide is formed at the projected range while numerous oxide precipitates increasing in size and density towards the buried oxide are present in the surface Si layer. Increasing oxygen concentration with depth in the Si layer explains the increase in size of these precipitates. The gradual increase in size and density is explained to be a result of both nucleation and growth rates of homogeneously precipitated oxide being strongly dependent on the oxygen concentration [64].

The as-implanted surface silicon layer has dislocation half loops [65] and stacking faults in association with SiO₂ precipitates [66, 67] which grow with higher implant temperatures. Intermediate annealing at ~1050°C showed that the stacking faults extended to the surface from oxide precipitates in the surface silicon layer [66]. It has been suggested [67] that

the presence of a free surface near the oxide precipitates helps in stabilizing these defects.

Significant rearrangement of this structure is apparent on post-implantation annealing due to the rearrangement of the oxygen profile [64, 68]. The buried oxide thickness increases and the small oxide precipitates in the surface silicon layer dissolve. Intermediate anneals performed [64, 68] at $\sim 1150^{\circ}\text{C}$ show large oxide precipitates adjacent to the surface silicon/buried oxide interface. These precipitates are connected by dislocations. Dislocations also thread to the surface of the silicon from the buried oxide layer. Higher annealing temperatures result in a sharp silicon/buried oxide interface, while all precipitates dissolve. The reported threading dislocation density is $\sim 10^9 \text{ cm}^{-2}$ [34]. Si islands have also been observed in the buried oxide .

This redistribution of oxygen (a coarsening process) has been explained in terms of classical nucleation theory [64, 69]. According to this theory a critical precipitate size r_c exists at a particular temperature as a result of the balance between the chemical driving force for precipitation and the opposing strain energy and surface energy terms. Hence at the intermediate anneal temperature, the smaller precipitates near the surface are below the critical size and dissolve while the larger precipitates near the buried oxide grow at their expense. At even higher temperatures all precipitates dissolve and are incorporated into the buried oxide which is the precipitate of infinite radius.

Another more detailed approach to explain this process [70] accounts for the effect of vacancy and interstitial concentrations on the critical radius. The strain accommodation mechanism is critically affected by the point defect concentrations at low anneal temperatures. The precipitation

process is suppressed by a high interstitial supersaturation while vacancy supersaturation promotes precipitation. At very high anneal temperatures ($\sim 1400^{\circ}\text{C}$), the point defect concentrations reach their equilibrium value. Hence the growth of oxide precipitates initially is accompanied by a high Si interstitial emission rate which may be a cause for the formation of extended defects.

In cases where the implantation temperature was 550°C or higher oxygen containing cavities were observed in the surface silicon layer [13, 26, 31, 34, 66, 71, 72]. This microstructure has been explained in terms of void formation for irradiated metals [71]. One of the most important observations upon annealing these structures is that a very low threading dislocation density is obtained and the cavities dissolve. It has been suggested [66] that the lack of near surface precipitation due to presence of these cavities could be the cause of the low final threading dislocation density. However, others [13] believe that the strain free nature of cavities and their dislocation blocking effect is the reason for low dislocation densities. At the surface silicon and buried oxide interface in the as-implanted state are planar defects on $\{111\}$ planes [72,73], which consist of a series of discontinuous stacking faults both intrinsic and extrinsic in nature. They have been reported to be caused by stresses generated by the growing buried oxide.

Recent improvements in ion implanters have allowed some studies to be performed using high beam currents and high implant temperatures. These studies report [35] that as the substrate temperature is increased the near surface stress as well as the dislocation half loop density decreases with increase in implant temperature. However, above 600°C there is no further reduction in the final threading dislocation density.

Beam current

Most of the work in this field has mainly been in two areas : using low/medium beam currents and high beam currents. For high beam currents, the ion beam was used to heat the substrate and thereby the substrate temperature was intrinsically coupled to the beam current. Thus limiting the wafer temperature lead to a decrease in dose rate and subsequently prolonged the implantation times needed [74]. In the low beam current regime the substrate temperature was maintained independent of the beam current. Using low beam currents, it has been reported [75] that at $18 \mu\text{A}/\text{cm}^2$ polycrystalline silicon was present near the buried oxide interface, and the final defect density was very high after annealing. Samples implanted with $25 \mu\text{A}/\text{cm}^2$ had no polycrystalline silicon in the top silicon layer and resulted in lower defect densities. Different techniques have been used to control the substrate temperatures. Some experiments were performed using external heating [74], while others [30] used resistively heated substrates to start the implantation initially, and then relied upon ion beam heating during the rest of the implantation process. They found that the silicon crystalline quality was improved in comparison to wafers that were not heated. Using low or medium beam current implanters requires the implanted zone to be restricted to a small area in order to reach the necessary temperature [76]. Hence, steep temperature gradients result across the sample which may cause them to break. The use of high beam currents is more favorable commercially since it reduces the implantation time which makes it more economical. More recent studies [29] used high beam currents and the implants were partially controlled by external heating. They found that there was no change in the microstructure on changing the beam current

from 1 mA/cm² to 10 mA/cm². The dose rate influences the damage production rate and thereby the defect growth process. High substrate temperatures on the other hand enhance the self/dynamic annealing process. The competition between damage production rate and dynamic annealing influences the final microstructure significantly [15]. Thus it is imperative to study the effect of the dose rate independent of the substrate temperature.

Motivation and Objectives

Motivation

Reviewing the existing literature it is apparent that even though extensive studies have been done to understand the physical mechanisms of defect growth and buried oxide evolution in SIMOX, no consolidated theory exists as yet. The aspect of defect growth has been widely studied. It has been established that dislocation half loops which occur in the as-implanted state are precursors to threading dislocations in the annealed state [35]. Moreover, it has been observed [35], that the density of dislocation half loops is dependent on the dose of implantation. Recent reports [37] indicate that dislocation half loops are not observed at doses lower than $1.0 \times 10^{18} \text{ cm}^{-2}$ implanted at an energy of 200 keV. Under certain implantation conditions cavities occur in the near surface region. Cavities in the near surface region prohibit near surface precipitation [27]. It has been found [29] that near surface precipitates are detrimental to the quality of the Si overlayer since they pin defects and enhance defect stabilization. However, it is speculated that near surface cavities which result in strain in the near surface region encourage the nucleation and growth of dislocation half loops [27]. Hence it is of importance to understand the correlation between

the near surface strain induced by cavities and the evolution of dislocation half loops.

Recently, there has been more interest in studying the development of the buried oxide at substoichiometric doses. The long times needed to implant wafers at stoichiometric or higher doses is not economical. It has been reported [77] that Si islands are trapped within the buried oxide at most of these substoichiometric doses. These Si islands degrade the quality of the buried oxide and it is essential to eliminate them to produce device quality SIMOX. Most of the studies have been performed on annealed SIMOX whereby the actual precipitation stage in the as-implanted state has been completely ignored. It is known that during post implantation annealing, Ostwald ripening is the major driving force which determines the structure of the final buried oxide. In this process, larger precipitates grow at the expense of smaller ones to reduce the free energy of the system. Hence, it is obvious that the precipitate distribution after implantation, but prior to annealing is the most critical stage which will determine the oxygen redistribution and buried oxide formation. Thus, to understand the buried oxide growth it is vital to obtain an extensive knowledge of the precipitate distribution in the as-implanted state. Until now the precipitate distribution in the as-implanted state has not been studied. Another important issue which has not been studied is the quality (i.e. roughness) of the Si surface and Si overlayer/buried oxide interface as a function of implantation conditions.

Previously, the energy, beam current and substrate temperature could not be varied independently. Inability to control the implantation conditions independently has hindered attempts to correlate variations in implantation conditions to microstructural evolution. Optimization of

implantation conditions is guided by low final threading dislocation densities in the Si overlayer and a continuous buried oxide with few Si islands. These structures are influenced by the implantation conditions and hence it is necessary to study the effect of independent implantation parameters on them. This would provide the road map to produce device quality SIMOX. Using the new Ibis 1000 implanter, it has become possible to control the implant energy, beam current and substrate temperature independently. Hence in this study it has been possible to analyze the effect of each of these conditions on the evolution of the microstructure.

Objectives and Approach

The primary objective behind the first part of this dissertation was to improve the existing level of understanding on defect and buried oxide evolution in SIMOX by studying the independent effect of implantation conditions on these features. Specifically, the near surface strain evolution and its effect on defects were evaluated. Buried oxide growth, especially for substoichiometric doses, was analyzed. For this purpose the following approach was taken. The oxygen dose was varied keeping all other implantation parameters constant. Both substoichiometric and stoichiometric doses were studied. Then, the same dose range was analyzed for a different energy. The results of these experiments showed that a high quality continuous buried oxide formed only at two doses for a particular energy. These two doses were then chosen to study the effect of substrate temperature and beam current variations (keeping all other implantation conditions constant) on the development of the microstructure.

From the first part of the experiment it was apparent that a more intensive analysis of the precipitation process for substoichiometric doses

was critical to understand buried oxide growth. This was the objective for the second part of the dissertation. In this section an extensive evaluation of the precipitate distribution in the as-implanted state was performed. The results of this study greatly enhanced our understanding of the fundamental physical processes involved in buried oxide growth. It was found that the as-implanted precipitate distribution controls the quality of the final buried oxide. Significant inhomogeneity in precipitate sizes at the vicinity of the projected range led to poor quality buried oxides with large Si inclusions. Based on this evaluation, critical processing parameters have been identified which could be manipulated to yield device quality buried oxides. Finally, a theoretical model was developed to enable control of the quality of materials and determine process parameters for reliably forming continuous buried oxide layers.

CHAPTER 2 EXPERIMENTAL PROCEDURES

Implantation and Annealing

P type single crystal silicon, having a resistivity of 10-20 Ohm-cm, with <100> orientation were implanted with $^{16}\text{O}^+$. No screen oxide was used (i.e., the wafers were bare) before implantation. All the wafers were implanted using the new Ibis 1000 implanter which is capable of controlling all implantation parameters independently. All the implants were nonchanneled. Both as-implanted and annealed samples were studied. All anneals were done at 1310°C for 5 hours in an Ar+0.5%O₂ ambient.

To study the effect of dose and energy on the microstructure, samples were implanted at 175 keV and 200 keV, at a substrate temperature of 590°C, with a beam current density of 3.0 mA/cm² for doses of 0.2, 0.4, 0.5, 0.6, 0.8, 1.0, 1.2, and $1.4 \times 10^{18} \text{ cm}^{-2}$.

The effect of substrate temperature was studied using high and low dose implants. At the high dose of $1.4 \times 10^{18} \text{ cm}^{-2}$, samples were implanted at 540°C, 590°C, and 640°C, at an energy of 175 keV, and a beam current density of 3.7 mA/cm².

For the low dose implantations, samples were implanted at substrate temperatures of 490°C, 520°C, 550°C and 580°C for a dose of $0.4 \times 10^{18} \text{ cm}^{-2}$ at 175 keV at 3.0 mA/cm².

To investigate the effect of beam current density, samples were implanted at a dose of $1.4 \times 10^{18} \text{ cm}^{-2}$ at an energy of 175 keV at 590°C at

beam current densities of 3.0, 3.7, and 4.3 mA/cm². It should be noted that these values represent the instantaneous dose rate. The time averaged dose rates are approximately two orders of magnitude lower.

Analytical Techniques

Transmission Electron Microscopy (TEM)

This analytical technique is one of the most versatile methods to determine the atomic structure and the microstructural features of solid materials. A high energy beam of electrons is focused on a thin solid sample (thickness < 200 nm) in vacuum. The transmitted electron signal is then magnified by a series of electromagnetic lenses. A diffraction pattern is obtained beneath the specimen which can be used to determine the crystal structure of the material. Interactions between the electrons and the atomic constituents of the specimen lead to several scattering mechanisms which yield transmitted electrons from regions of the sample containing structural features yielding contrast in the final image. Information on defects and atomic structure can be obtained from the analysis of the transmitted electron images.

A JEOL 200CX transmission electron microscope was used to analyze the defect microstructure in the samples. High resolution lattice images were obtained on a Topcon 002B transmission electron microscope. The diffraction conditions used are described in the respective sections in the following chapters.

Cross sectional TEM (XTEM) samples were prepared by dicing wafers into 0.25 mm wide strips using a Micro Automation Model 1006 high speed saw operating at 70,000 rpm. A polymer adhesive (M-line Accessories M bond 600) was used to glue the strips together such that the surfaces of interest formed a doublet being in contact with each other. The

adhesive was then cured at 80°C for 3 hours. The samples were then polished flat on both cross sectional sides using 400, 600 and 2400 grit sandpaper in succession until the sample was 50 to 100 μm thick. A VCR Group model d500i dimpler was used to dimple the XTEM samples using 6 μm and 1 μm diamond paste (Buehler Inc. MetadiII) until the dimpled area was ~ 10 to 15 μm thick. The specimen was then attached to a copper ring (Ted Pella Inc. 1x2 mm oval) using M bond 600 adhesive. Finally, the samples were ion milled using an Ar^+ ion beam in a Gatan model 600 dual ion mill at 1 mA current and 4 keV gun voltage, until a hole was obtained near the area of interest.

The plan view TEM (PTEM) samples were made by cutting 2.7 mm diameter discs of the wafer with a Gatan model 601 ultrasonic disc cutter using SiC cutting grit. These discs were polished down to ~ 100 μm thickness using 15 μm and 5 μm Al_2O_3 grit on a glass sheet. The front side of the sample (region of interest) was protected against chemical attack with paraffin wax. These samples were then drip etched from the back side with an acid solution (25% HF: 75% HNO_3) until light was visible but no hole was formed. The wax was removed by dipping the samples into a heptane solution. Finally, the samples were ion milled from the back side until a hole appeared. During ion milling the front side was protected from contamination using a sheet of teflon.

PTEM specimens of annealed samples with doses higher than $1.0 \times 10^{18} \text{ cm}^{-2}$ were made by the lift/float off method. In this method, samples 3 mm x 3 mm were scribed from the annealed wafers. These samples were then immersed in a bath of concentrated HF (49%) for a few hours. The HF preferentially etches the buried oxide. When the buried

oxide was completely etched, the surface silicon layer floated off and was caught on a copper grid.

Conventional two beam bright field imaging was used for an overview of the defect microstructure and verifying the Burgers vectors of defects. When only two beams are excited, i.e., the transmitted beam and one diffracted beam, contrast from the dislocations and stacking faults can be explained by the dynamical theory [78].

Defects are invisible under the condition when $\mathbf{g} \cdot \mathbf{R} = 0$, where \mathbf{g} is the reciprocal lattice vector of the operative reflection and \mathbf{R} is the displacement vector of the defect. For dislocations, \mathbf{R} is the Burgers vector (i.e., $\mathbf{R} = \mathbf{b}$) and the contrast consists of a thick dark line. For stacking faults, \mathbf{R} is the fault displacement vector and the contrast consists of alternating bright and dark fringes bounded by partial dislocations.

For maximum transmitted intensity, images are taken with a slight deviation from the Bragg condition, i.e., $s < 1/\xi_g$, where s is the deviation parameter and ξ_g is the extinction distance. For $\langle 110 \rangle$ oriented cross sectional TEM samples, the defect microstructure was imaged with either \mathbf{g}_{220} or \mathbf{g}_{400} , while \mathbf{g}_{220} was used in the $\langle 100 \rangle$ oriented plan view samples.

Threading dislocation densities were obtained from plan view specimens using a \mathbf{g}_{220} reflection. The lower limit of the measurable dislocation density is about 10^5 cm^{-2} . For dislocation densities lower than this value, etch pit counts using Secco etching were done.

Weak beam dark field imaging provides a high contrast for dislocations with greatly improved spatial resolution compared to bright field imaging. When the third order diffracted beam is excited the first order beam is used for centered dark field imaging, producing a $\mathbf{g}-3\mathbf{g}$ weak

beam image. This method yields narrower images than that in the bright field, and allows closely spaced defects to be imaged.

To image the cavities, the rules of Ruhle and Wilkens [79] were followed. In a focused conventional bright field image, cavities are invisible. But, by under focusing or over focusing a kinematical image (i.e., $s \gg 0$) the cavities show either bright or dark contrast at the edges. This method has been used to obtain the best cavity contrast in the samples.

Secco Etching

PTEM analysis on some of the annealed samples showed no defects. This indicated that the density of defects in these samples was less than 10^5 cm^{-2} . In these cases, samples were analyzed over large areas using the Secco etch. The Secco etch preferentially etches defects, giving rise to etch pits at the surface. It was made by dissolving 44g of $\text{K}_2\text{Cr}_2\text{O}_7$ in 1000 ml of water. Then, it was mixed 1:2 with 48% HF. Ultrasonic agitation was used to avoid bubble formation. The etch rate is slow and good delineation of defects on {100} surfaces was possible. These etched pits were then analyzed using a scanning electron microscope (SEM).

Atomic Force Microscopy (AFM)

To obtain information regarding surface topography, atomic force microscopy is one of the most efficient analytical tools. It uses a sharp tip located within a few Å of the surface to scan the specimen. The microfabricated cantilever is deflected by the interatomic forces between the atoms on the specimen surface and those on the tip. Surface topography is mapped out with high resolution using the magnitude of the cantilever deflection, which strongly depends upon the separation between the tip and surface atoms. AFM is especially useful to obtain information about the

quality of the surface in non conductors. This method is also known as scanning force microscopy (SFM).

To analyze the silicon surface and top silicon/buried oxide interface, atomic force microscopy was used. The Si surface was first analyzed in the annealed samples, after which a KOH etch was used to remove this Si overlayer to examine the top silicon/buried oxide interface.

All samples were cleaned using an ultrasound bath of methanol for 5 minutes prior to mounting. A Digital Instruments Nanoscope III was used to analyze the surface and interface roughness. Measurements were performed using the tapping mode with a silicon tip. Cantilever tuning was done according to the Digital Instruments software. The root mean square roughness was estimated from the amplitude variations.

Secondary Ion Mass Spectrometry (SIMS)

In this technique, a solid sample is placed in a vacuum chamber and is bombarded with a beam of ions (primary ions) having sufficient energy to cause the ejection/sputtering of atoms and ions (secondary ions) from the specimen surface. Primary ions which are commonly used are Cs^+ , O_2^+ , O^+ , and Ar^+ in the energy range of 2 to 20 keV, at angles of incidence between 45° and 90° . The sputtered species from the sample surface may have a positive or negative charge. The ejected secondary ions are analyzed according to their mass-to-charge ratio in a mass spectrometer. Concentrations are obtained by using standards for comparison with the relative quantities of the secondary ions. Hence information about the composition as a function of depth (obtained from the sputtering time) of the sample can be evaluated. SIMS can be used to obtain a depth concentration profile of the near surface region to a resolution of 2 ~ 30 nm at a detection

limit of $\sim 10^{16} \text{ cm}^{-3}$. This is a destructive technique used mainly for depth profiling trace level impurities with materials.

Oxygen concentration depth profiles for the SIMOX samples were obtained using a Perkin-Elmer 6300 secondary ion mass spectrometer (SIMS). A 3 keV Cs^+ beam at an incident angle of 60° was rastered over a $500 \mu\text{m} \times 500 \mu\text{m}$ area. The secondary ions detected from the central $200 \mu\text{m} \times 200 \mu\text{m}$ area of the sputter crater were $^{16}\text{O}^-$, $^{30}\text{Si}^-$, $^{32}\text{O}_2^-$, $^{44}\text{SiO}^-$ and $^{56}\text{Si}_2^-$. The $^{44}\text{SiO}^-$ signal was normalized to the $^{30}\text{Si}^-$ signal. A relative sensitivity factor for converting this ratio to oxygen atomic concentration was obtained from an implantation standard of oxygen in silicon. The depth scale was determined from stylus profilometer measurements of the sputtered crater depths.

High Resolution X-Ray Diffraction (HRXRD)

X-ray diffraction is a nondestructive analytical technique which is used for obtaining information about crystalline phases, strain, orientation and size of crystallites and atomic arrangements. A collimated beam of x-rays is made incident on the sample. Diffraction by the crystalline planes of the specimen occurs according to Bragg's law. The structural properties, strain, and other information are obtained from the intensity of the diffracted x-rays as a function of the diffraction angle and the specimen orientation.

In this study, high resolution x-ray diffraction was used solely to determine the magnitude and sign of the strain in the specimens. A plot of the diffracted x-ray intensity around the Bragg angle of a particular crystallographic plane of a single crystal material is known as a rocking curve (RC). Hence, if within a material, a thin surface layer having a slightly different lattice parameter exists, diffraction maxima from both the

substrate and the layer will occur. Using Bragg's Law, the lattice parameter difference can be obtained from the angular separation of these peaks. However, closely spaced peaks are difficult to resolve due to the spectral divergence (natural spread in wavelength) and the size of a normal x-ray source. To avoid this problem, more than one beam conditioning crystal is used to collimate and/or monochromate the x-ray beam. A five crystal diffractometer can yield RC for any reflection at any angle of any single crystal material with a resolution of about 5 arc-sec. Dumond transparency diagrams [80] can be used to understand the effectiveness of this technique. Even though the four crystal monochromator/collimator allows any reflection of a sample to be analyzed with high resolution the intensity is much reduced.

The rocking curves in this study were obtained from a Philips high resolution x-ray diffractometer which uses two U-shaped $\langle 110 \rangle$ oriented Ge blocks for the monochromation/collimation in an arrangement developed by Bartels [81, 82]. The intensity loss is minimized due to the high intrinsic reflectivity of Ge, while the $\langle 110 \rangle$ orientation enables the diffractometer to operate in two different modes. For obtaining high resolution (about 5 arc-sec) the $\{440\}$ reflecting planes are used although the intensity is sacrificed. For the 'low' resolution mode (12 arc-sec), the $\{220\}$ reflecting planes of the Ge crystals are used and a factor of twenty gain is obtained in the integrated intensity.

Samples were cleaved from the implanted wafers and cleaned using a buffered oxide etch to remove any surface oxide film. These were then affixed with double sided scotch tape to glass slides and mounted on the diffractometer stage. This method eliminated any accidental straining of the specimen during mounting which could give spurious strain

measurements. Rocking curves were obtained by accurately aligning the specimen and optimizing the rotation and tilt angles.

Determination of the appropriate value of the rotation angle is required to eliminate the possibility of a misorientation or miscut between the sample surface and (004) plane. Optimization of the tilt angle is necessary to ensure that the diffracted beam is centered on the detector window. A detailed analysis of the alignment procedures can be obtained from a previous study [83]. The step size used in this study was 0.0005° using 10 sec counting time for each step.

Using the symmetric (004) reflection, the perpendicular component of the strain, ϵ_{per} , was evaluated from the following equation:

$$\epsilon_{\text{per}} = -\cot\omega \Delta\omega$$

where ω is the substrate peak location and $\Delta\omega$ is the angular difference between the layer peak and the substrate peak. This gives the “x-ray strain” in the layer. The appropriate sign convention for $\Delta\omega$ requires that the difference between the strain layer peak and substrate layer peak be taken. The “x-ray strain” gives the fractional change in lattice parameter of the epitaxial layer with respect to the substrate and not with respect to the bulk lattice parameter of the layer. Hence, this yields the perpendicular component of lattice mismatch and not the actual strain in the layer.

CHAPTER 3

EFFECT OF IMPLANTATION CONDITIONS

In this chapter, the effect of varying the implantation conditions independently on the evolution of the SIMOX microstructure is presented. First, an overview of the SIMOX microstructure as a function of oxygen dose variation was obtained keeping all other implant parameters constant. To study the effect of implant energy these same doses were evaluated for a different implant energy. Based on the results of these experiments it was evident that the quality of the buried oxide was a strong function of implant dose and energy. The effect of variation of substrate temperature was performed at doses which yielded superior quality buried oxides. Finally the effect of variation of the beam current was analyzed.

As is evident from Chapter 1, extensive studies have been done to understand the effect of varying the implantation conditions on the SIMOX microstructure. Yet, no clear understanding exists on a number of issues. The effect of near surface strain on the defect growth process is still unclear. The effect of near surface strain as a function of the change in implant energy has not been studied. The increase in Si island density within the buried oxide with increase in dose for substoichiometric doses is not understood. No studies have been performed to evaluate the quality of the Si surface and upper Si/buried oxide interface. All these outstanding issues motivated a series of experiments to be performed to obtain a

comprehensive picture of the actual physical mechanisms underlying the SIMOX process as a function of implantation conditions.

Dose and Energy

To investigate the effect of oxygen dose and energy on the evolution of the SIMOX microstructure a series of implants were done at 590°C, with a beam current density of 3.0 mA/cm² at energies of 175 keV and 200 keV, for doses of 0.2, 0.4, 0.5, 0.6, 0.8, 1.0, 1.2, and 1.4x10¹⁸ cm⁻². In this section a detailed analysis of the evolution of the microstructure is presented for the as-implanted and annealed states. All the anneals were performed at 1310°C for 5 hours in an Ar + 0.5% O₂ ambient.

As-implanted Microstructure

The main microstructural features in the as-implanted state are cavities near the surface, dislocation half loops, stacking faults and SiO₂ precipitates. These features are discussed separately below.

Cavities and near surface strain

175 keV. XTEM micrographs of the as-implanted samples are shown in Figure 3.1. As discussed in the previous chapter, the cavities, when present in the as-implanted state, occur in the near surface region. The XTEM images show that cavities are resolvable for doses of 0.4x10¹⁸ cm⁻² and higher. Measurements performed on XTEM images indicated that the cavity layer thickness increased with dose, from a value of 32 nm for a dose of 0.4x10¹⁸ cm⁻² to a value of 120 nm for a dose of 1.4x10¹⁸ cm⁻², as shown in Figure 3.2. As mentioned earlier, it has been established [27] that these cavities induce strain in the near surface region. The presence of these cavities motivated HRXRD analysis to estimate the near surface strain variation with dose.

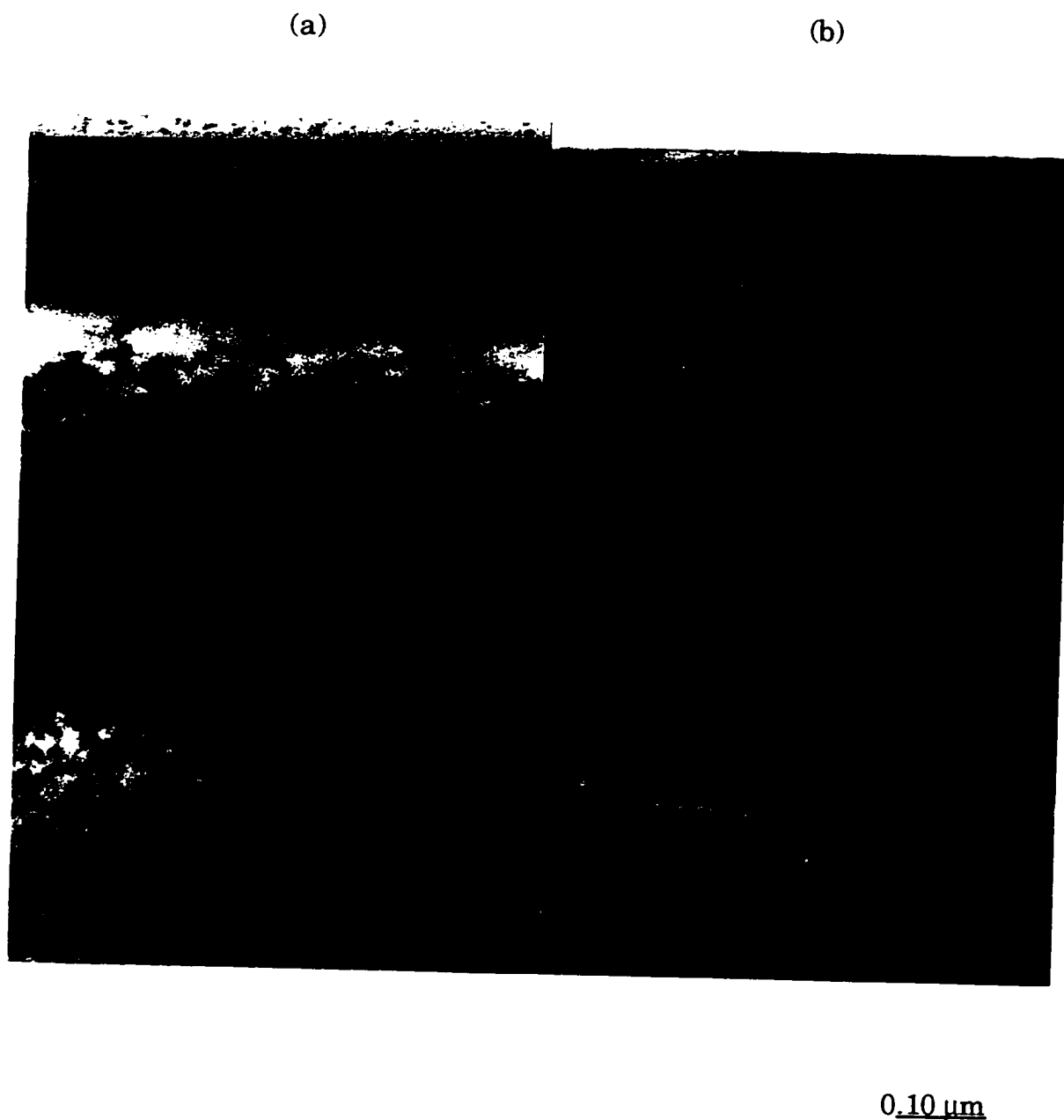


Figure 3.1. XTEM micrographs of samples in as-implanted condition after implantation at 175 keV, showing effect of dose variation.
a) $0.2 \times 10^{18} \text{ cm}^{-2}$; b) $0.4 \times 10^{18} \text{ cm}^{-2}$;

(c)

(d)

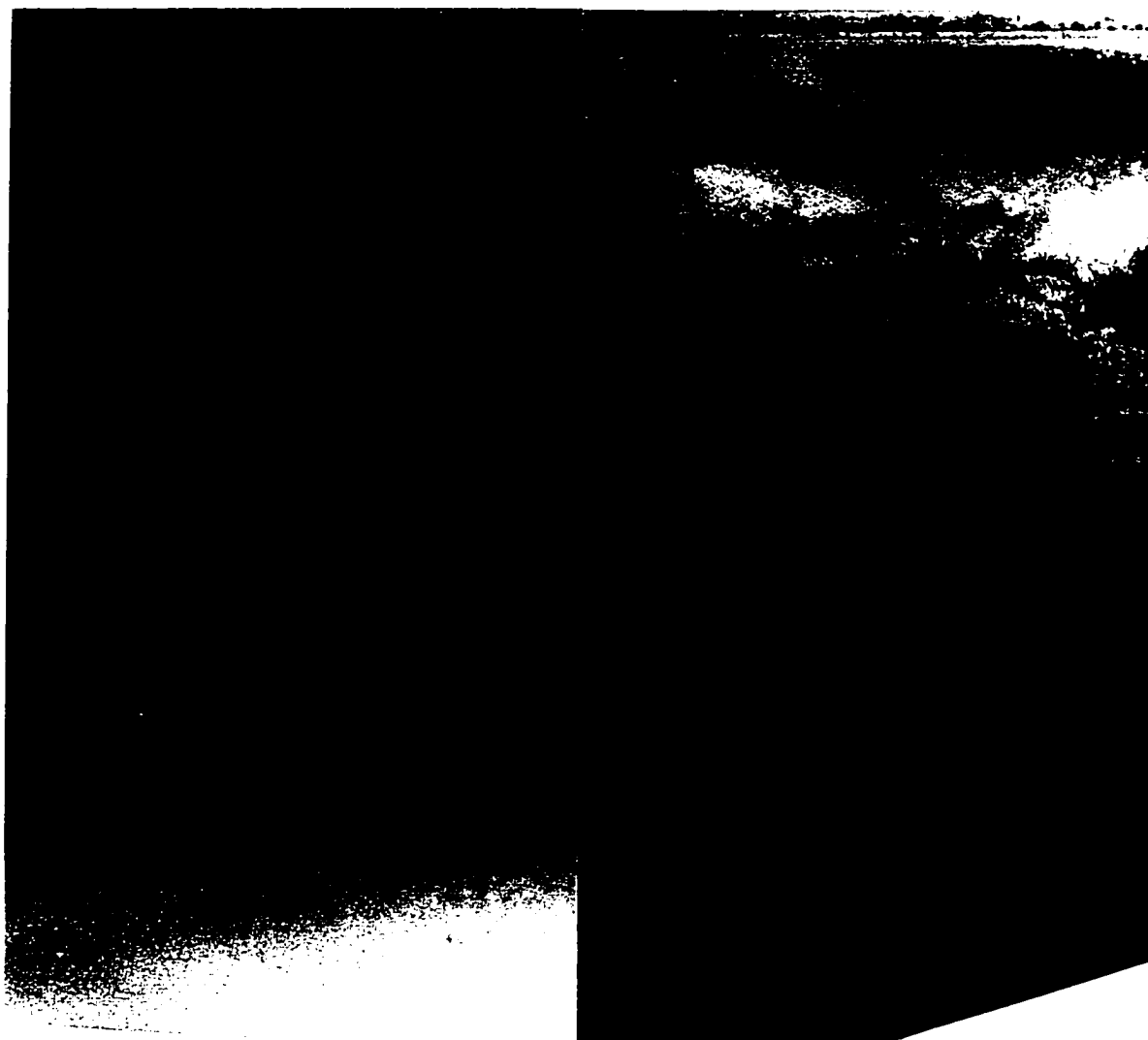
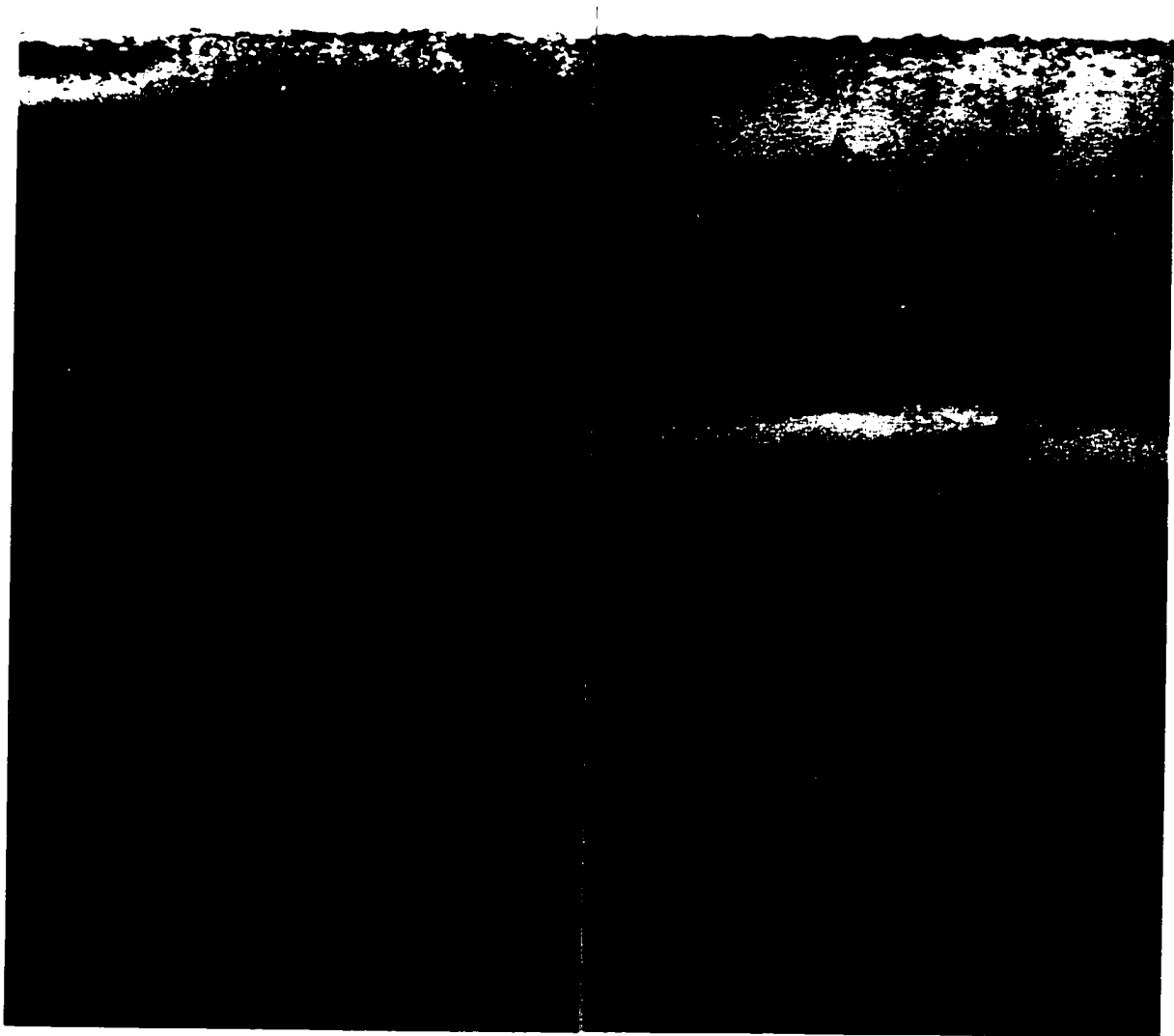
0.10 μm

Figure 3.1 -- continued

c) $0.5 \times 10^{18} \text{ cm}^{-2}$; d) $0.6 \times 10^{18} \text{ cm}^{-2}$;

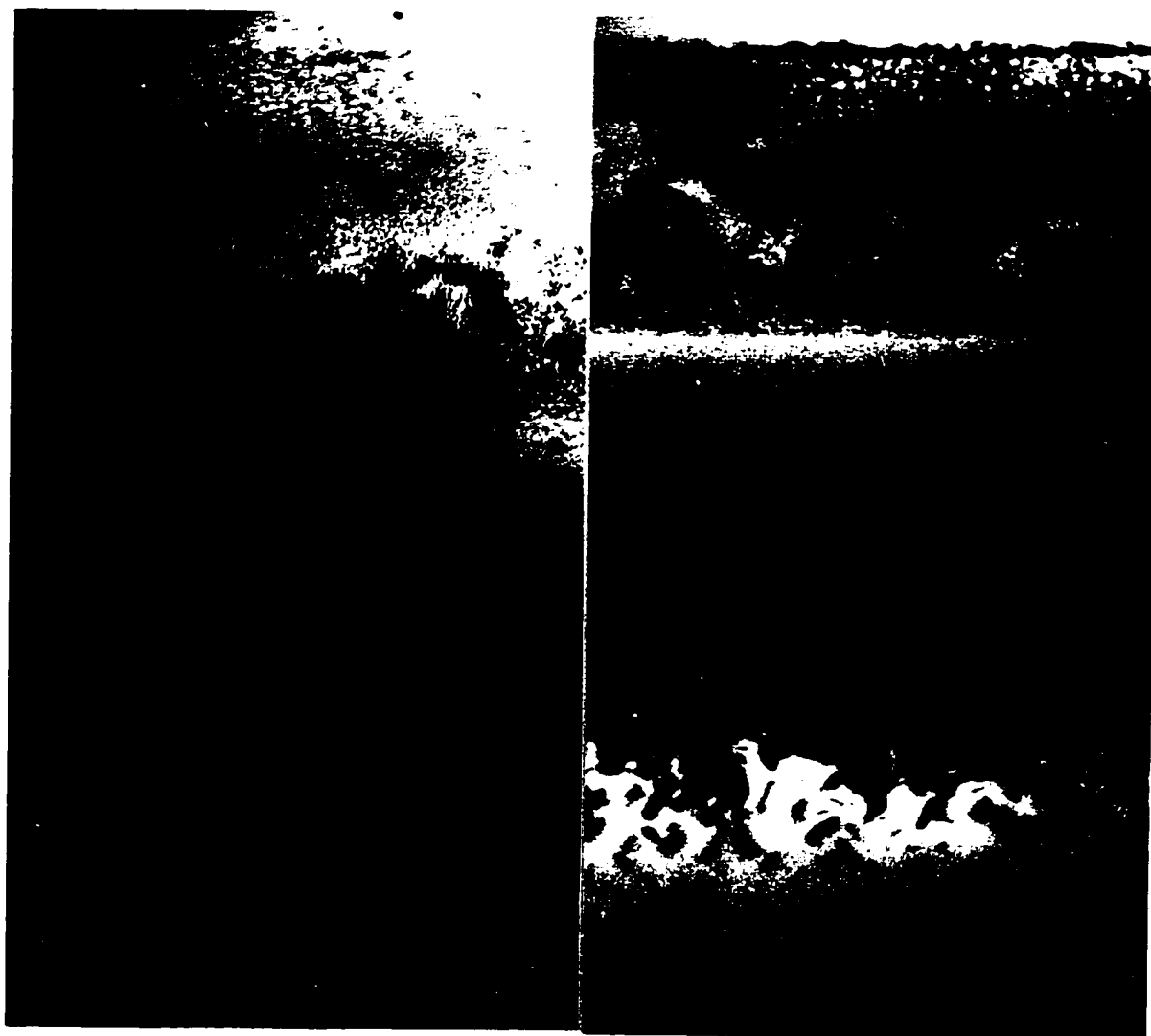
(e)

(f)

0.10 μm Figure 3.1 -- continuede) $0.8 \times 10^{18} \text{ cm}^{-2}$; f) $1.0 \times 10^{18} \text{ cm}^{-2}$;

(g)

(h)

0.10 μm Figure 3.1 -- continuedg) $1.2 \times 10^{18} \text{ cm}^{-2}$; h) $1.4 \times 10^{18} \text{ cm}^{-2}$.

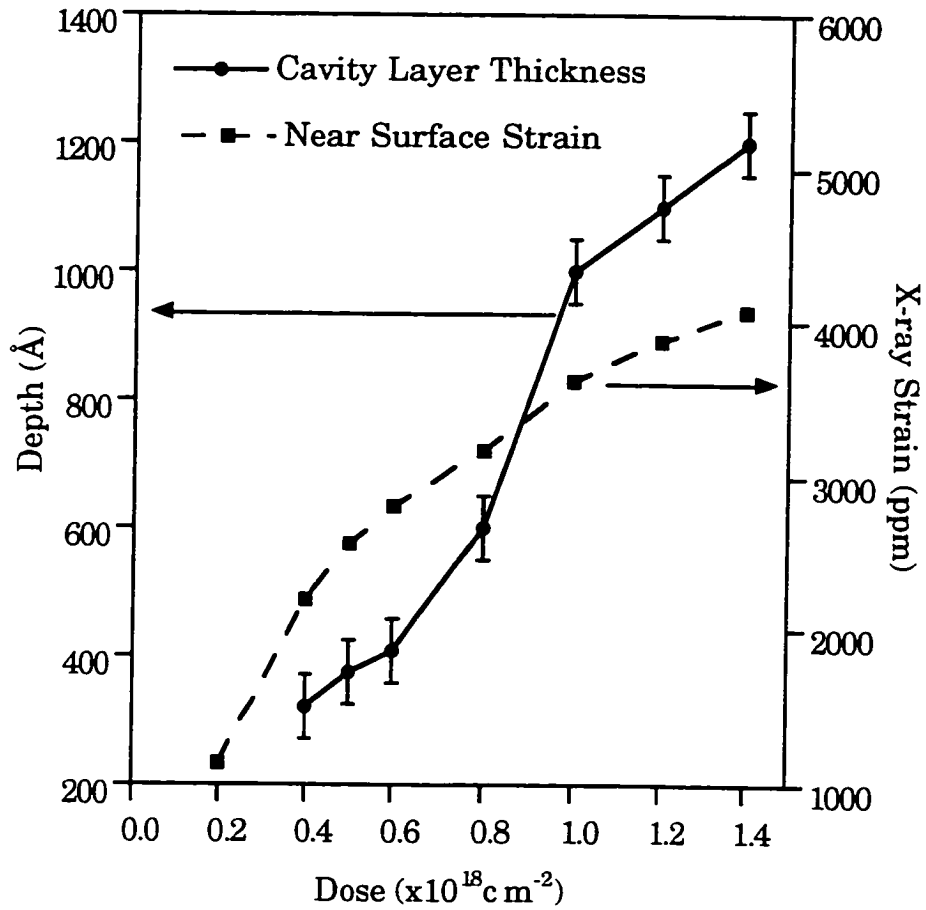


Figure 3.2. Variation of cavity layer thickness and x-ray strain with dose for samples in as-implanted condition after implantation at 175 keV.

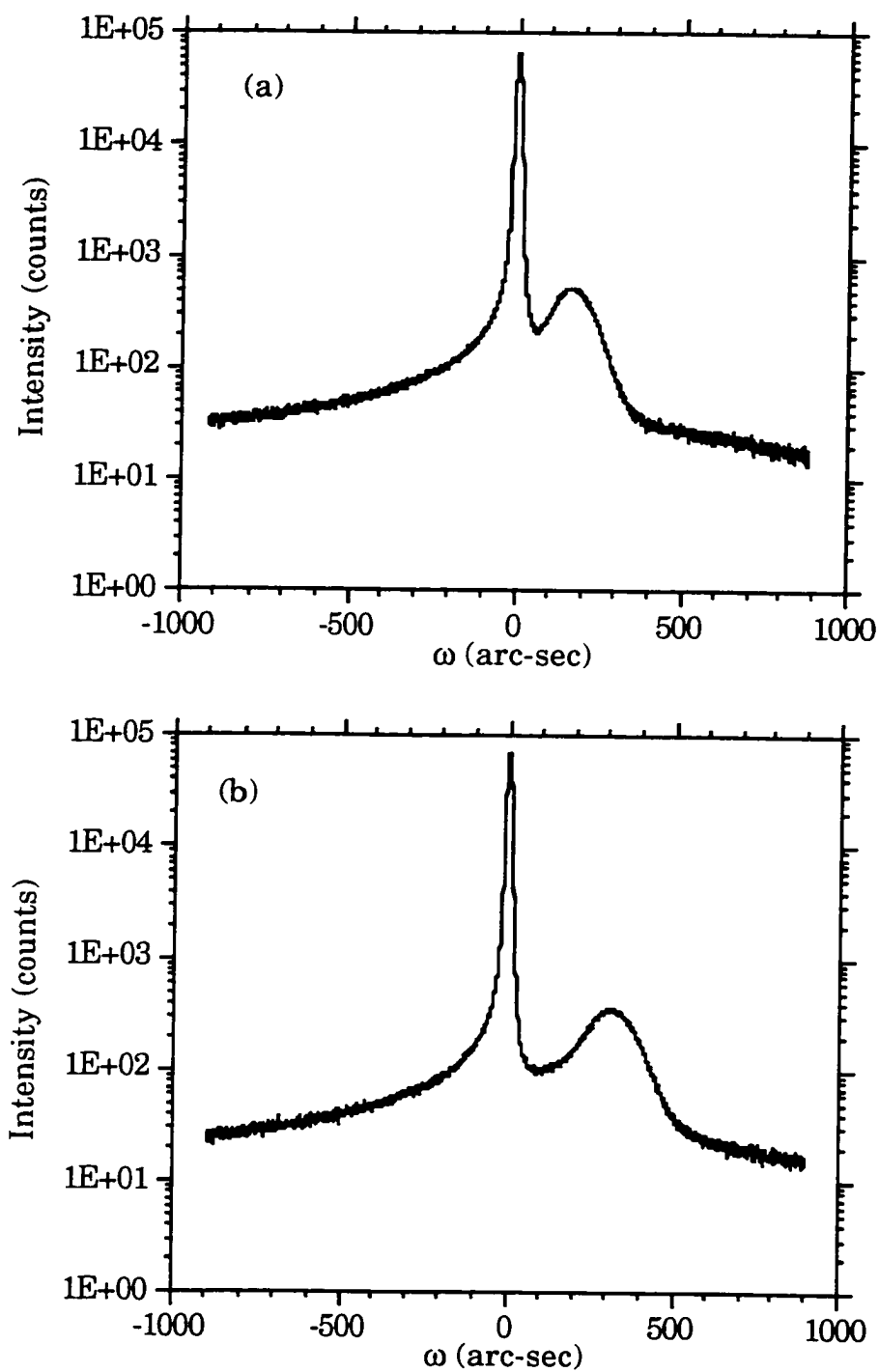


Figure 3.3. X-ray rocking curves about the (004) reflection for samples in as-implanted condition after implantation at 175 keV for various doses.
a) $0.2 \times 10^{18} \text{ cm}^{-2}$; b) $0.4 \times 10^{18} \text{ cm}^{-2}$;

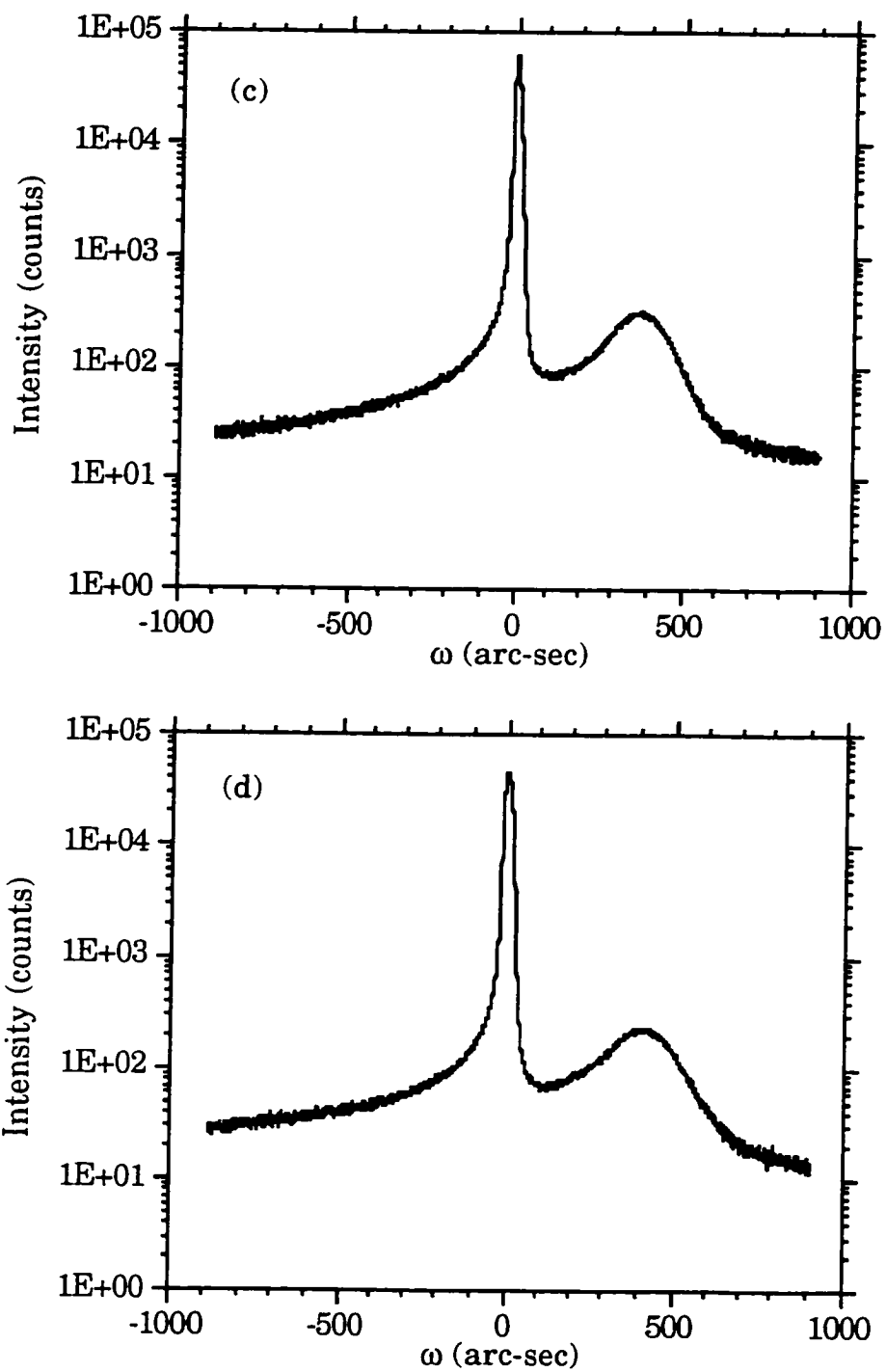


Figure 3.3 -- continued

c) $0.5 \times 10^{18} \text{ cm}^{-2}$; d) $0.6 \times 10^{18} \text{ cm}^{-2}$;

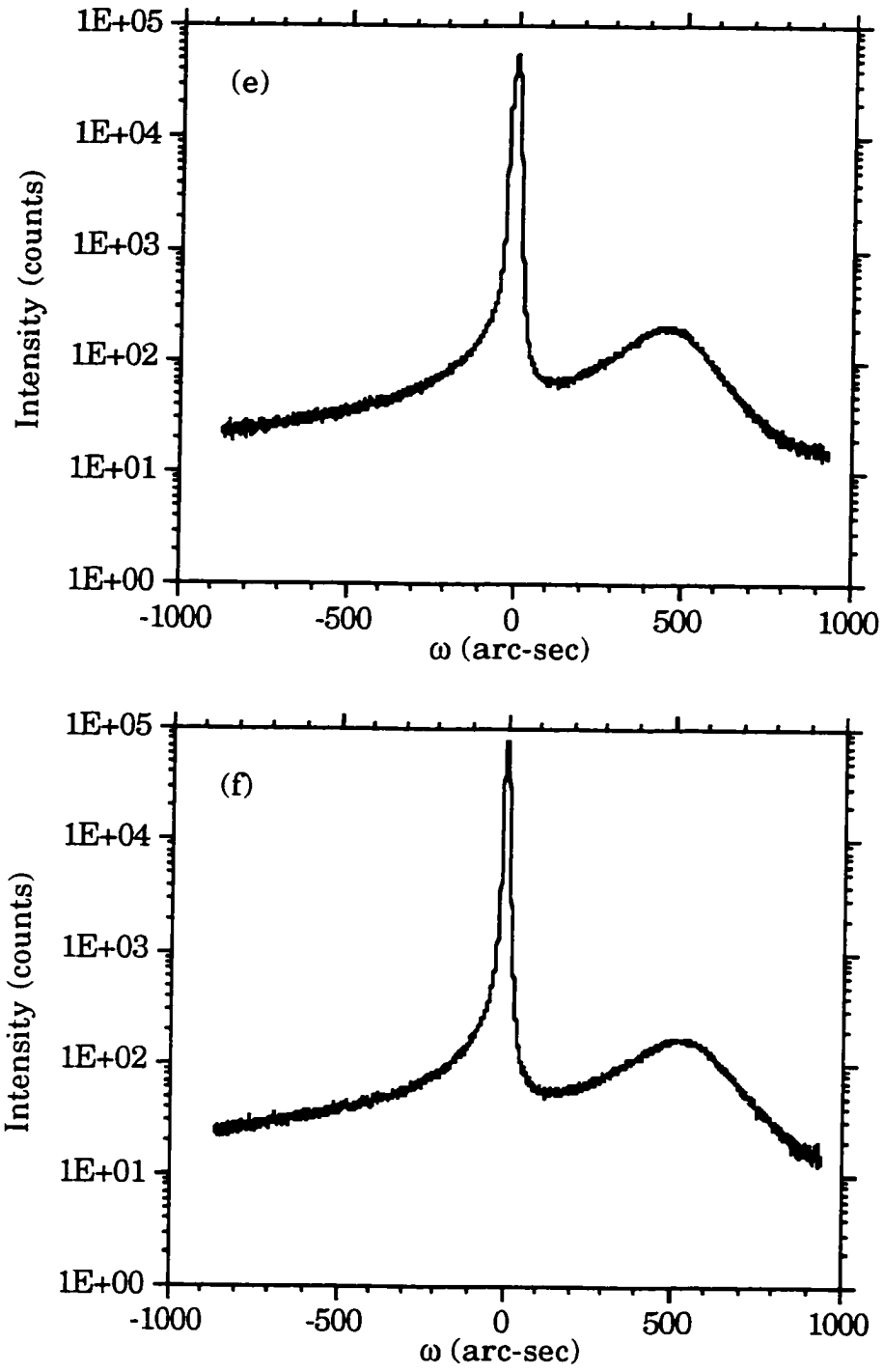


Figure 3.3 -- continued

e) $0.8 \times 10^{18} \text{ cm}^{-2}$; f) $1.0 \times 10^{18} \text{ cm}^{-2}$;

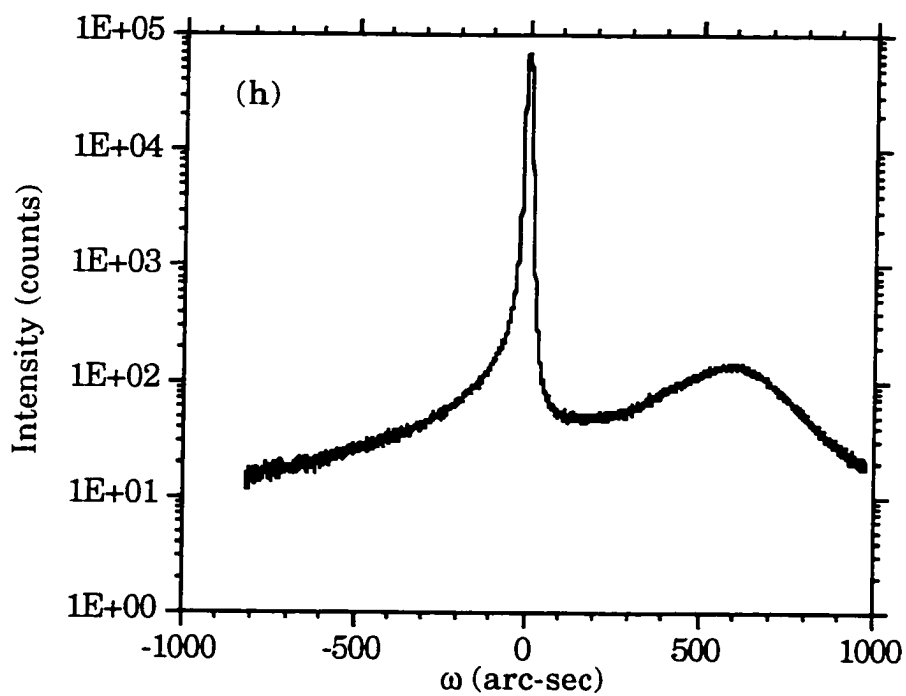
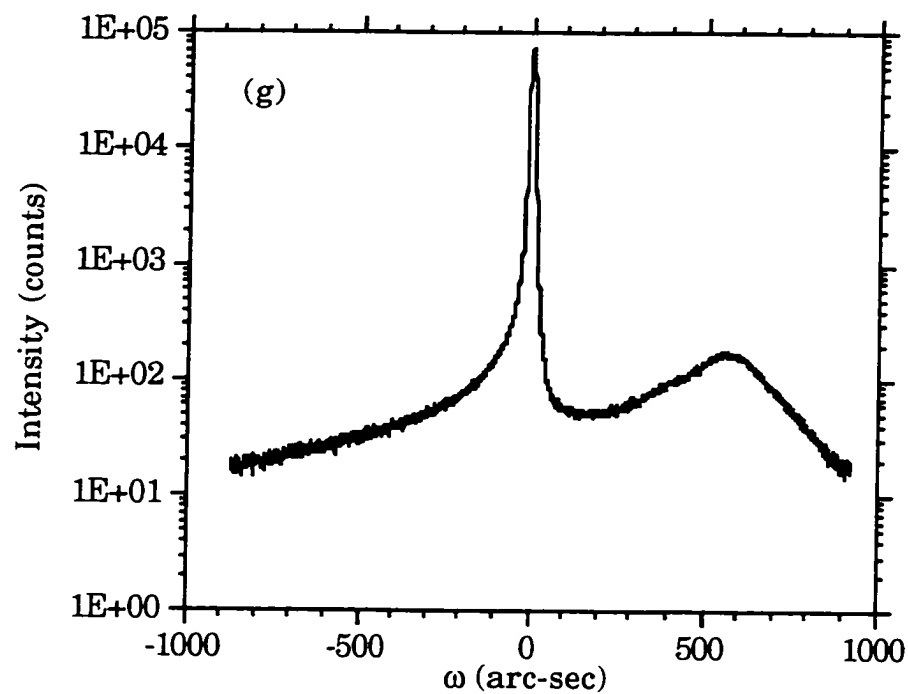


Figure 3.3 -- continued

g) $1.2 \times 10^{18} \text{ cm}^{-2}$; h) $1.4 \times 10^{18} \text{ cm}^{-2}$.

The (004) rocking curves for all the doses are shown in Figure 3.3. The rocking curves show the following similarities. Each rocking curve has a prominent Bragg peak at an angle higher than the substrate peak, indicating the presence of a strained layer which has undergone a lattice contraction. No thickness fringes are evident in the rocking curves, indicating that the strain layers are at or near the surface of the samples. The strain layer peaks are asymmetric indicating the nonuniform nature of the strain.

The maximum strain was estimated from the angular separation of the substrate and strain layer peaks. These results are plotted in Figure 3.2 as a function of the implant dose. The maximum strain increased with the increase in dose from a value of -1134 ppm at a dose of $0.2 \times 10^{18} \text{ cm}^{-2}$ to a value of -4073 ppm at a dose of $1.4 \times 10^{18} \text{ cm}^{-2}$.

200 keV. The XTEM micrographs (Figure 3.4), of the samples implanted at an energy of 200 keV showed the presence of near surface cavities. The analysis of the cavity layer depth distribution showed that, similar to the results obtained for the doses implanted at 175 keV, there was an increase in the cavity depth with the increase in dose, as represented in Figure 3.5. However, in comparison to the 175 keV implants, the cavities in the 200 keV implant did not appear to be densely packed for each dose. To evaluate the strain in this region, HRXRD analysis were performed on five of these samples (doses of 0.2, 0.4, 0.8, 1.0, and $1.4 \times 10^{18} \text{ cm}^{-2}$). The (004) rocking curves had the same general features as discussed above, and are shown in Figure 3.6. The maximum strain increased from a value of -812 ppm for a dose of $0.2 \times 10^{18} \text{ cm}^{-2}$ to a value of -3663 ppm at the dose of $1.4 \times 10^{18} \text{ cm}^{-2}$. This increase in maximum strain with dose is shown in the graph of

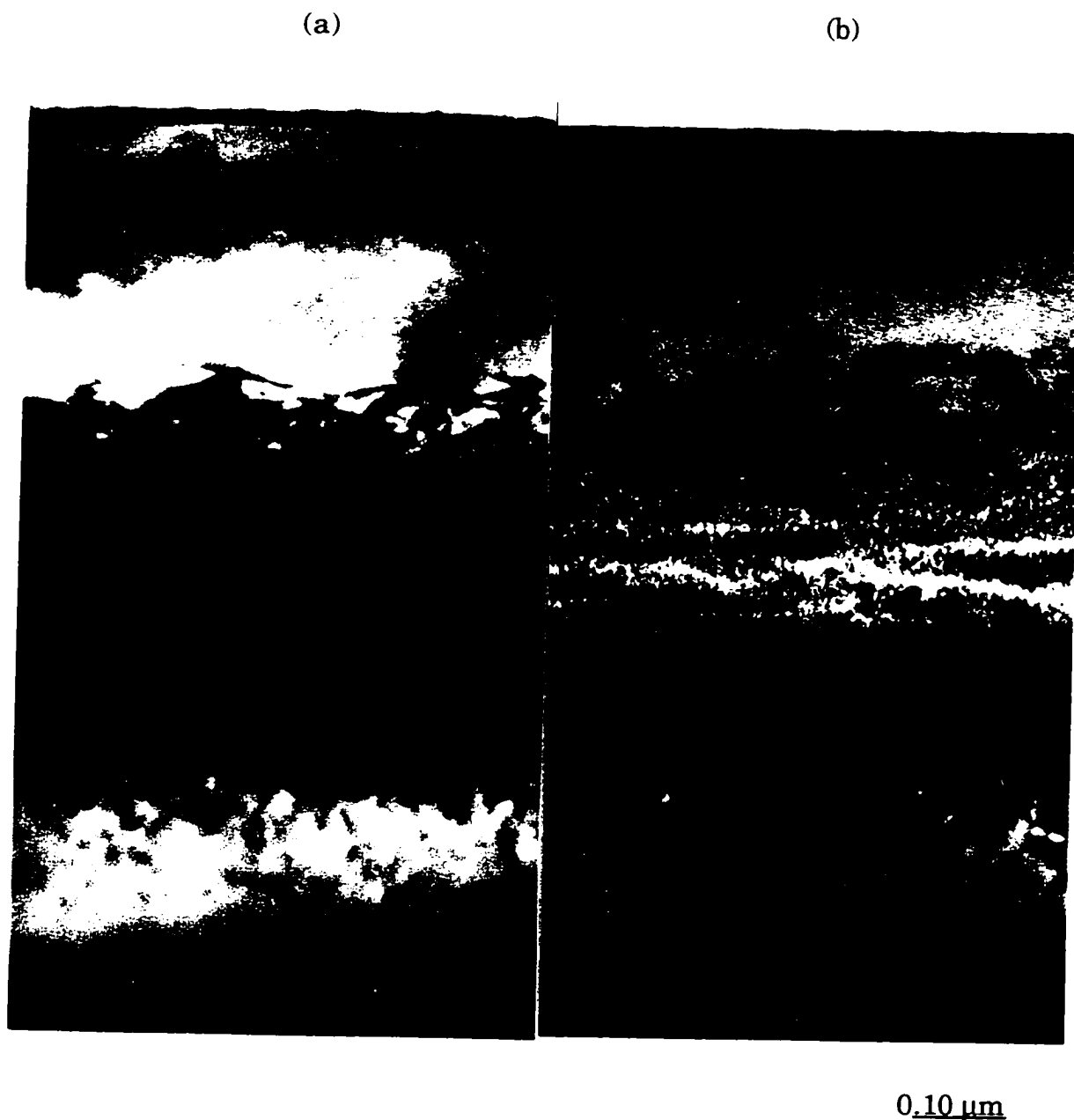
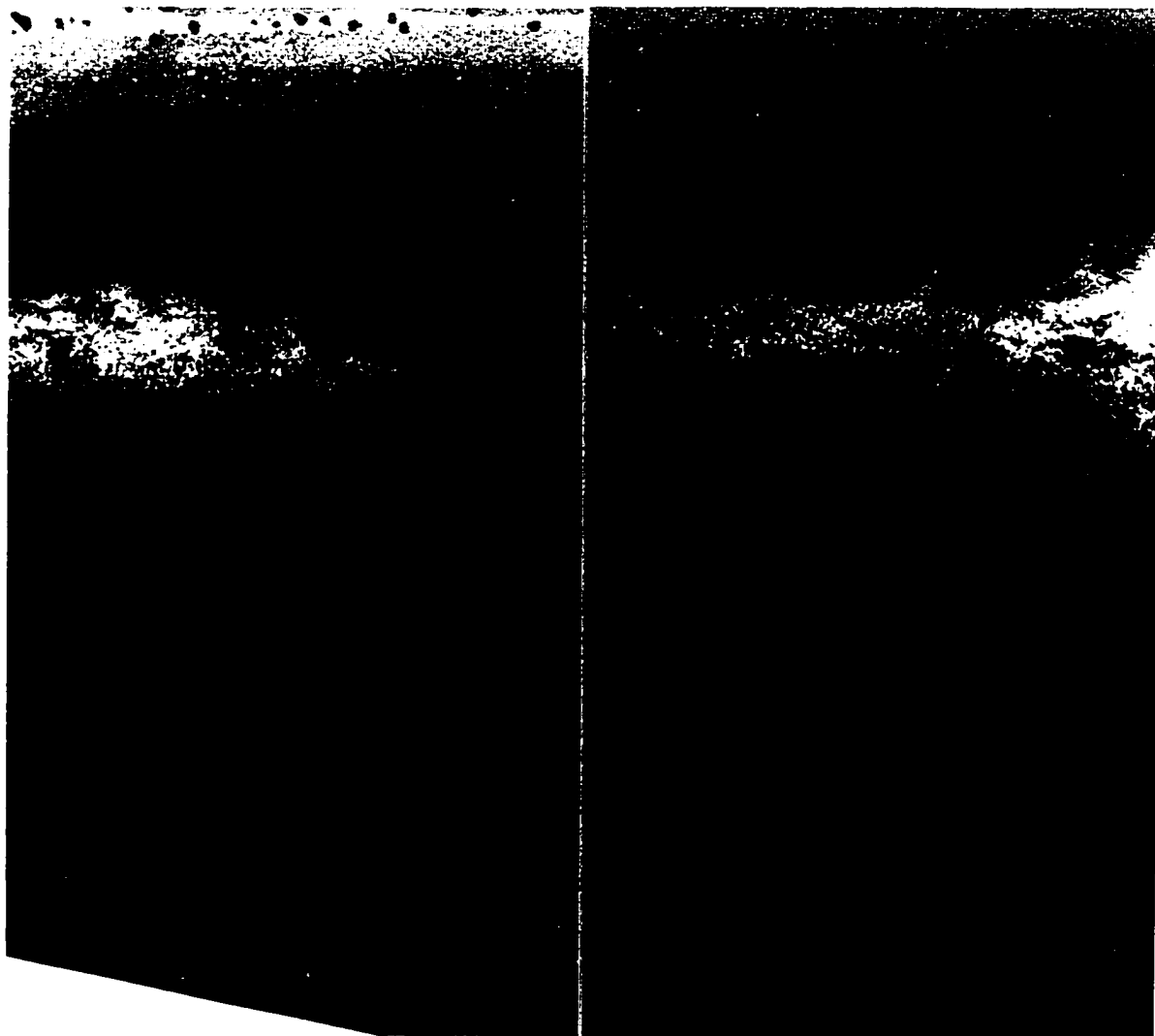


Figure 3.4. XTEM micrographs of samples in as-implanted condition after implantation at 200 keV, showing effect of dose variation.
a) $0.2 \times 10^{18} \text{ cm}^{-2}$; b) $0.6 \times 10^{18} \text{ cm}^{-2}$;

(c)

(d)

0.10 μm Figure 3.4 -- continuedc) $0.8 \times 10^{18} \text{ cm}^{-2}$; d) $1.0 \times 10^{18} \text{ cm}^{-2}$;

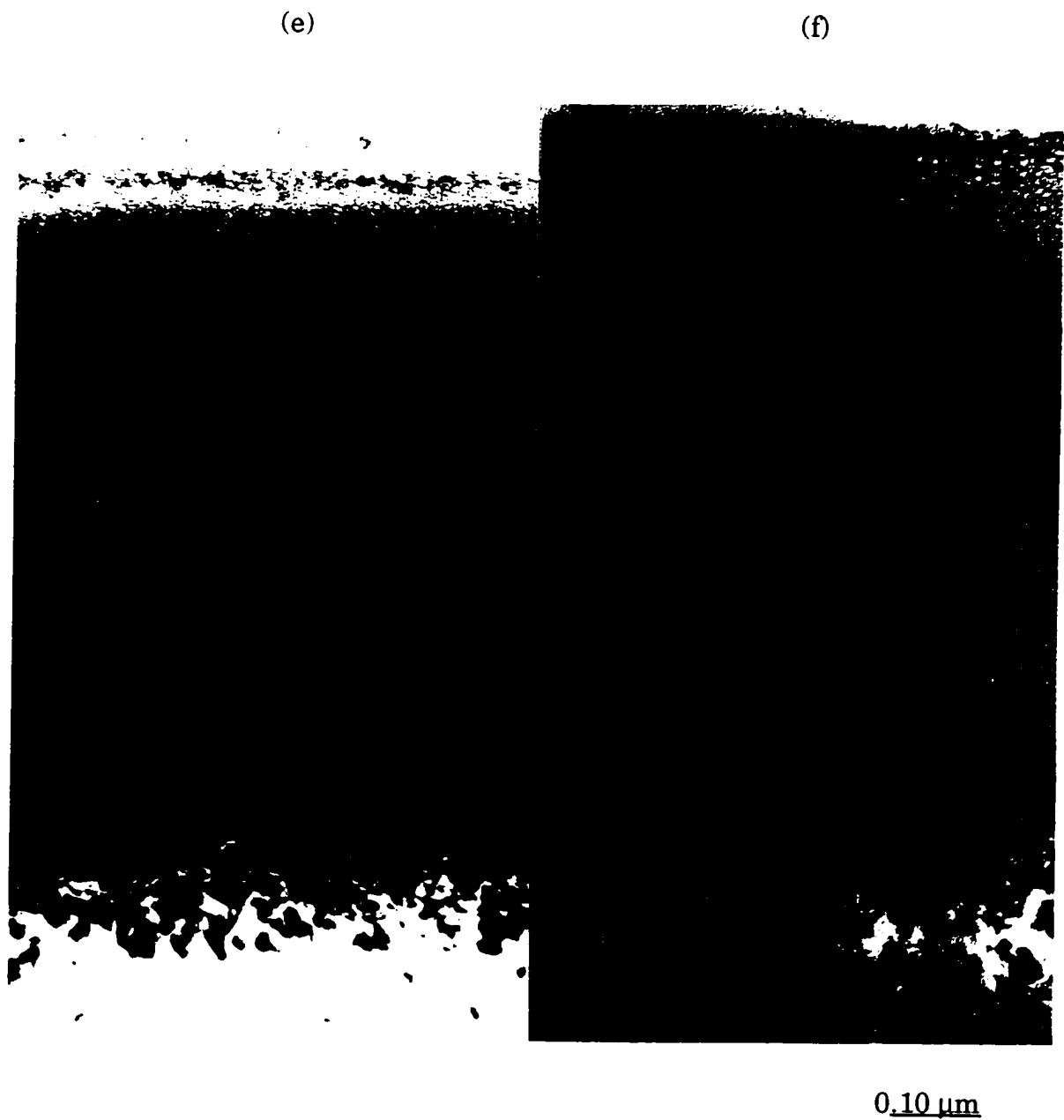


Figure 3.4 -- continued

e) $1.2 \times 10^{18} \text{ cm}^{-2}$; f) $1.4 \times 10^{18} \text{ cm}^{-2}$;

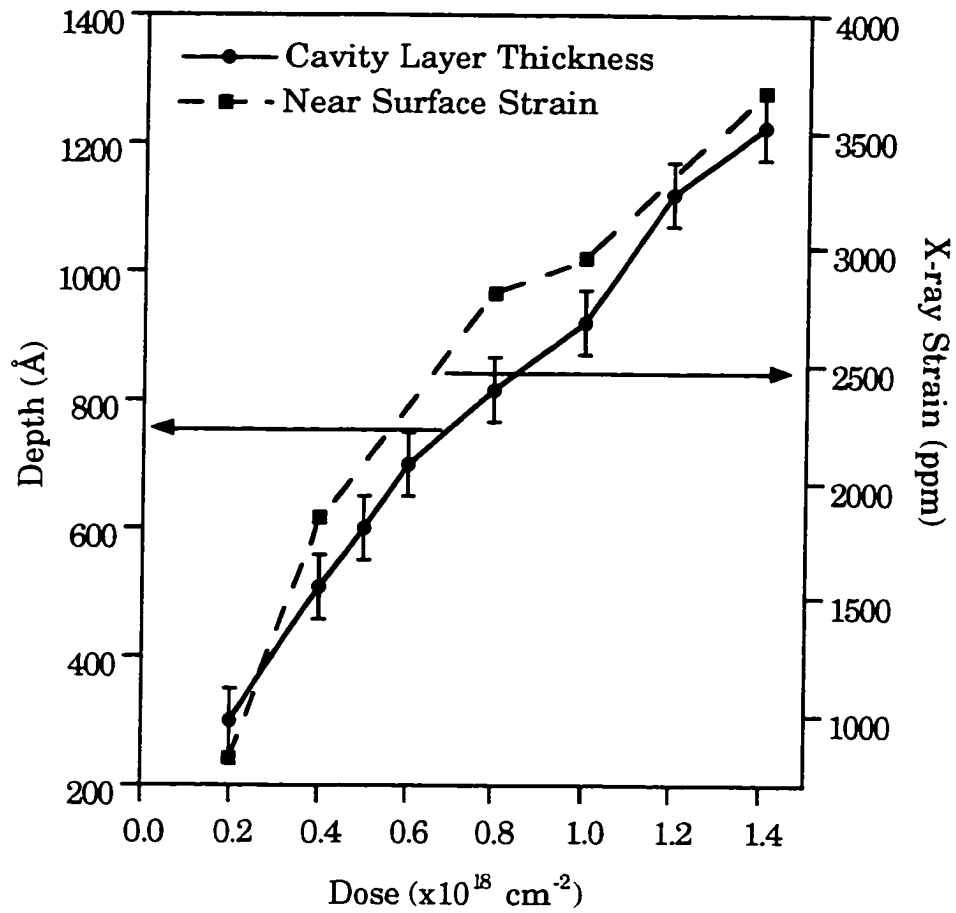


Figure 3.5. Variation of cavity layer thickness and x-ray strain with dose for samples in as-implanted condition after implantation at 200 keV.

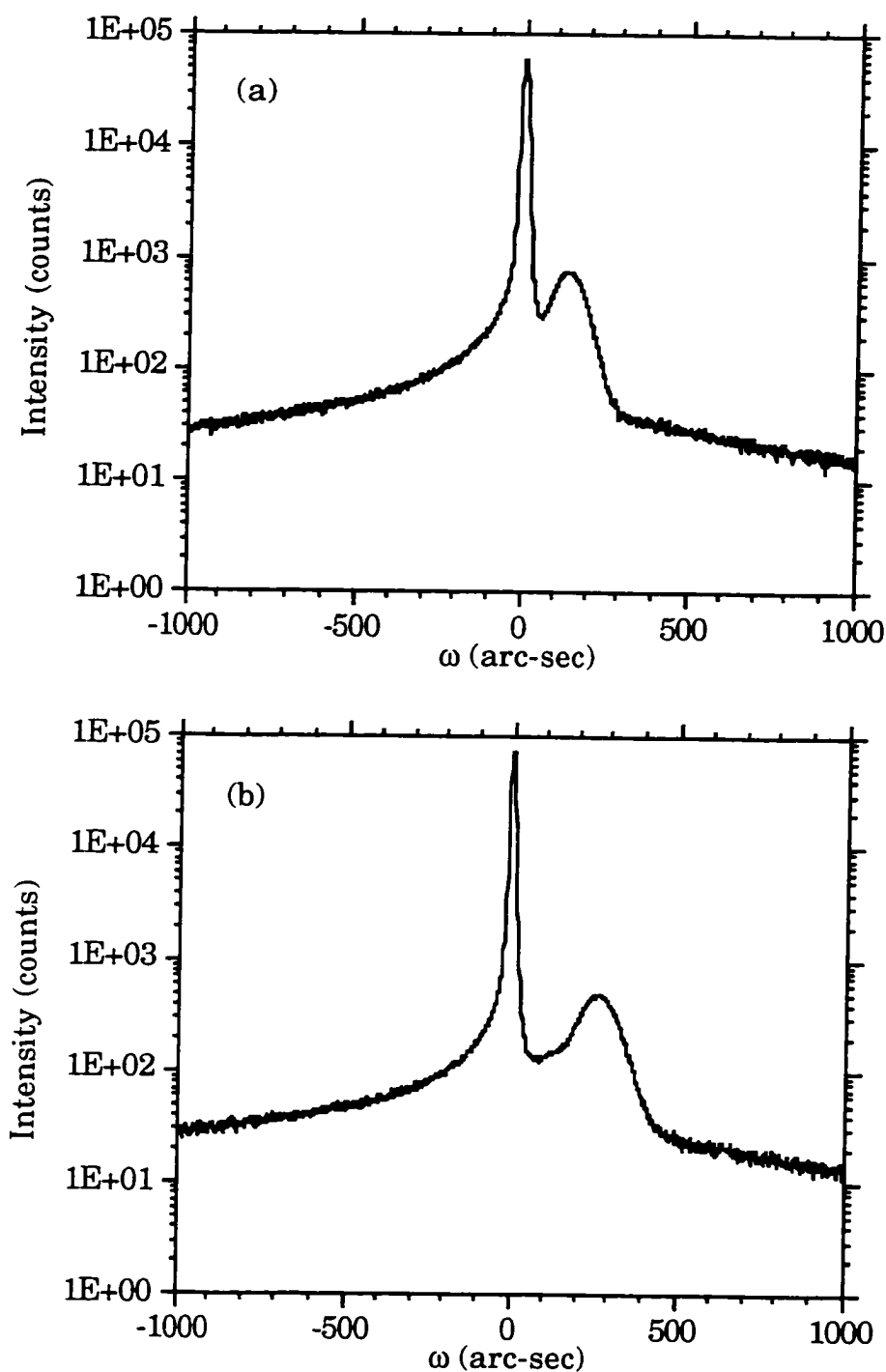


Figure 3.6. X-ray rocking curves about the (004) reflection for samples in as-implanted condition after implantation at 200 keV for various doses.
a) $0.2 \times 10^{18} \text{ cm}^{-2}$; b) $0.4 \times 10^{18} \text{ cm}^{-2}$;

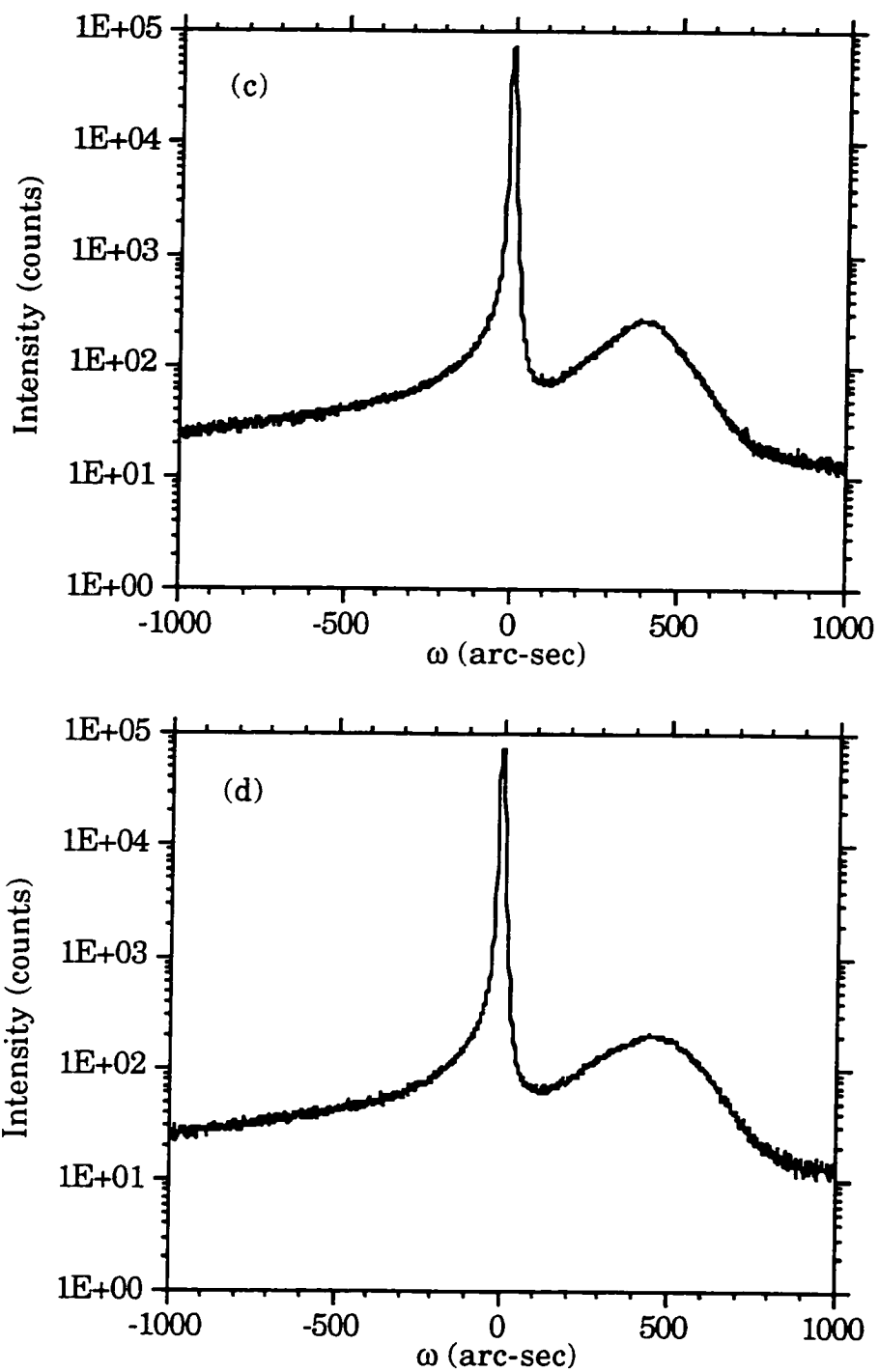


Figure 3.6 -- continued

c) $0.8 \times 10^{18} \text{ cm}^{-2}$; d) $1.0 \times 10^{18} \text{ cm}^{-2}$;

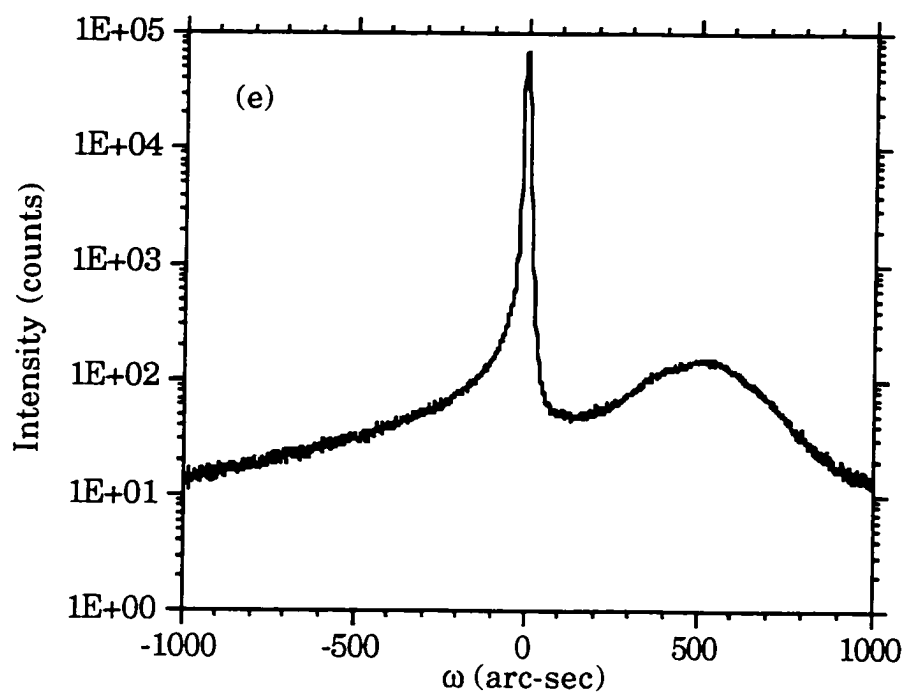


Figure 3.6 -- continued
e) $1.4 \times 10^{18} \text{ cm}^{-2}$.

Figure 3.5. These strain values are consistently ~1.2 times lower than those at 175 keV at each dose.

Near surface defects

175 keV. XTEM and PTEM analysis revealed that for doses lower than $1.0 \times 10^{18} \text{ cm}^{-2}$, stacking faults (also known as multiply faulted defects) were the dominant defects in the as-implanted state. However, for doses higher than $1.0 \times 10^{18} \text{ cm}^{-2}$, both stacking faults and dislocation half loops were present. Representative PTEM images of these defects are shown in Figure 3.7. The XTEM images shown in Figure 3.1 show that the stacking faults are present near top Si overlayer/buried oxide interface in the as-implanted state. PTEM analysis revealed that the density of stacking faults reduced from a value of $9 \times 10^9 \text{ cm}^{-2}$ for a dose of $0.2 \times 10^{18} \text{ cm}^{-2}$ to a value of $5 \times 10^8 \text{ cm}^{-2}$ for a dose of $1.4 \times 10^{18} \text{ cm}^{-2}$. This variation in defect density with dose is shown in Figure 3.8. The apparent decrease in stacking fault density may be a consequence of these defects being consumed by the growth of the buried oxide with increased dose.

For the doses of $1.0 \times 10^{18} \text{ cm}^{-2}$ and higher, dislocation half loops were found near the surface. PTEM analysis showed that these defects increased from a density of $1 \times 10^7 \text{ cm}^{-2}$ for the dose of $1.0 \times 10^{18} \text{ cm}^{-2}$ to a value of $1.7 \times 10^8 \text{ cm}^{-2}$ for the dose of $1.4 \times 10^{18} \text{ cm}^{-2}$, as shown in Figure 3.8. In-depth analysis of the half loops for doses higher than $1.0 \times 10^{18} \text{ cm}^{-2}$ indicated that they occurred on all of the 6 {110} planes. These prismatic half loops are perfect dislocations, pure edge type with $1/2 \langle 110 \rangle$ Burgers vectors, lying on {110} planes. Hence, they involve the insertion of an extra plane of atoms whereby they are extrinsic in nature. Previously, it was suggested that nucleation of half loops was possibly due to shear stress [27]. This means that no half loops should be present on planes which are perpendicular to

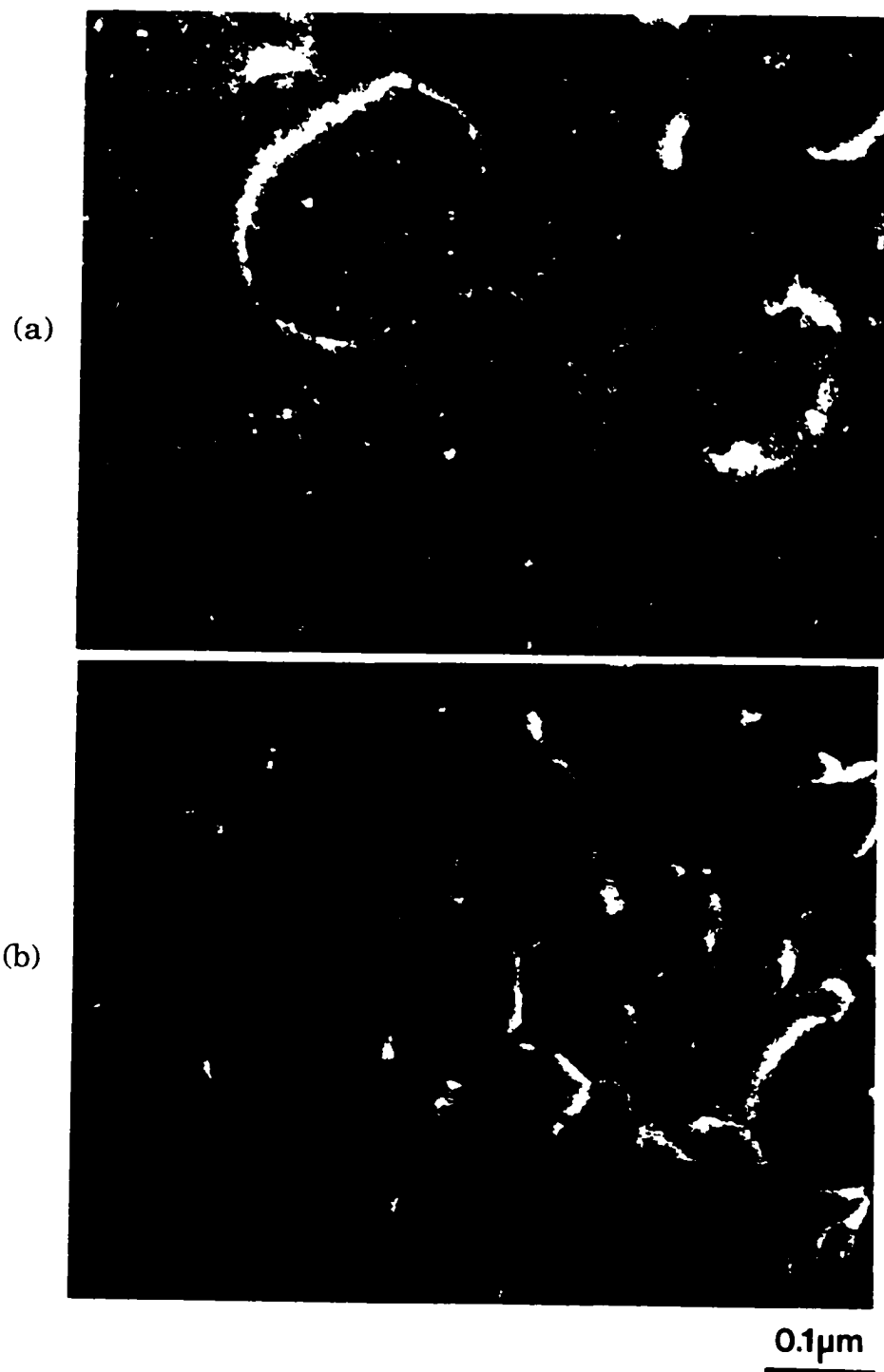


Figure 3.7. Plan view TEM micrographs showing defects in the silicon overlayer in the as-implanted state.
a) dislocation half loops; b) stacking faults.

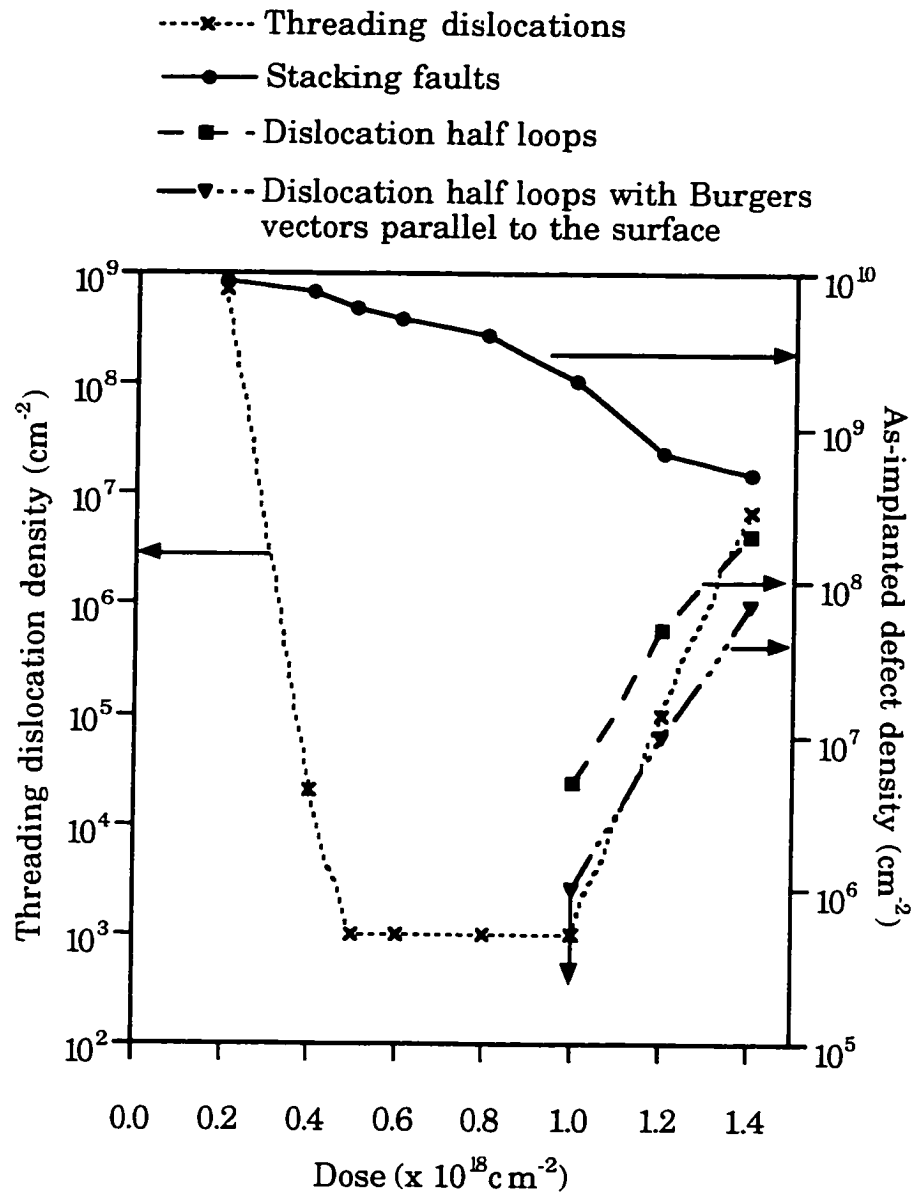


Figure 3.8. Defect densities as a function of dose for samples implanted at 175 keV, in as-implanted and annealed conditions.

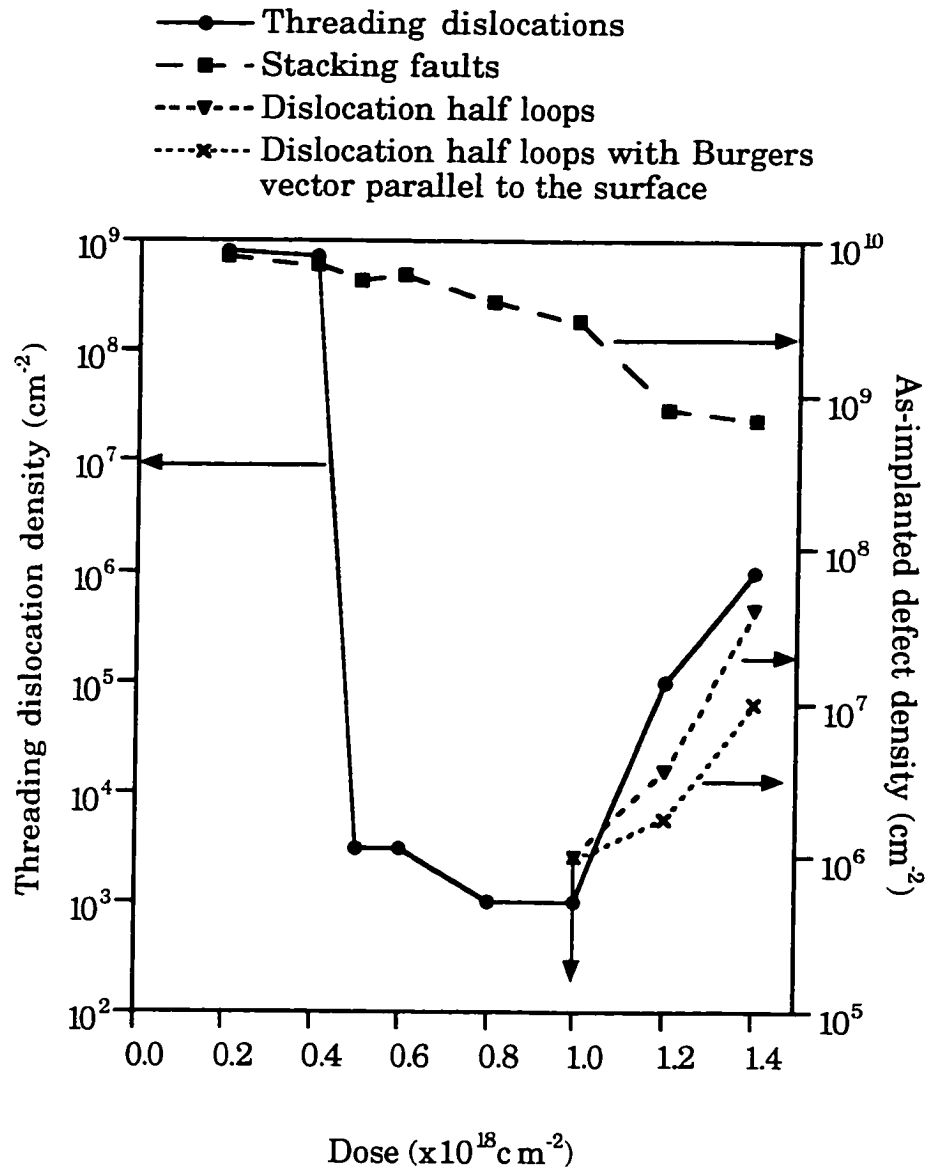


Figure 3.9. Defect densities as a function of dose for samples implanted at 200 keV, in as-implanted and annealed conditions.

the surface. However, shear stress must not be the only criterion for half-loop nucleation since dislocation half loops were found to exist on all of the {110} planes in this study. Lee et al. [35] reported that half loops with Burgers vectors angled to the surface occur at twice the frequency to those with Burgers vector parallel to the surface. In contrast, no such fixed ratio of occurrence was found in this study.

200 keV. The defect density analysis for the 200 keV implants is shown in Figure 3.9. The trends in the data are similar to those observed at 175 keV. Again, stacking faults were the dominant defects for doses of $1.0 \times 10^{18} \text{ cm}^{-2}$ and lower while dislocation half loops were present only at doses between $1.0 \times 10^{18} \text{ cm}^{-2}$ to $1.4 \times 10^{18} \text{ cm}^{-2}$. At each dose, the stacking fault densities are approximately the same for the two energies. However, the half loop densities are slightly higher at 175 keV.

Buried oxide

175 keV. A continuous buried oxide starts to form above a dose of $1.2 \times 10^{18} \text{ cm}^{-2}$ for the 175 keV implant in the as-implanted state. From the XTEM images shown in Figure 3.1 a distinct striated structure appears within the buried oxide for doses between $0.5 \times 10^{18} \text{ cm}^{-2}$ and $1.0 \times 10^{18} \text{ cm}^{-2}$. However, no such striations are evident in the XTEM images for doses of $0.2 \times 10^{18} \text{ cm}^{-2}$ and $0.4 \times 10^{18} \text{ cm}^{-2}$. This striated region grows in thickness with increase in dose and this trend is shown graphically in Figure 3.10. This graph also shows that the distance of the top of the striated region from the Si surface decreases with the increase in dose. Even though these features were observed in some earlier studies [42, 84] no physical understanding for the existence of these structures was presented.

The depth distribution of oxygen, as determined by SIMS analysis, is shown in Figure 3.11. The oxygen concentration increases in a regular

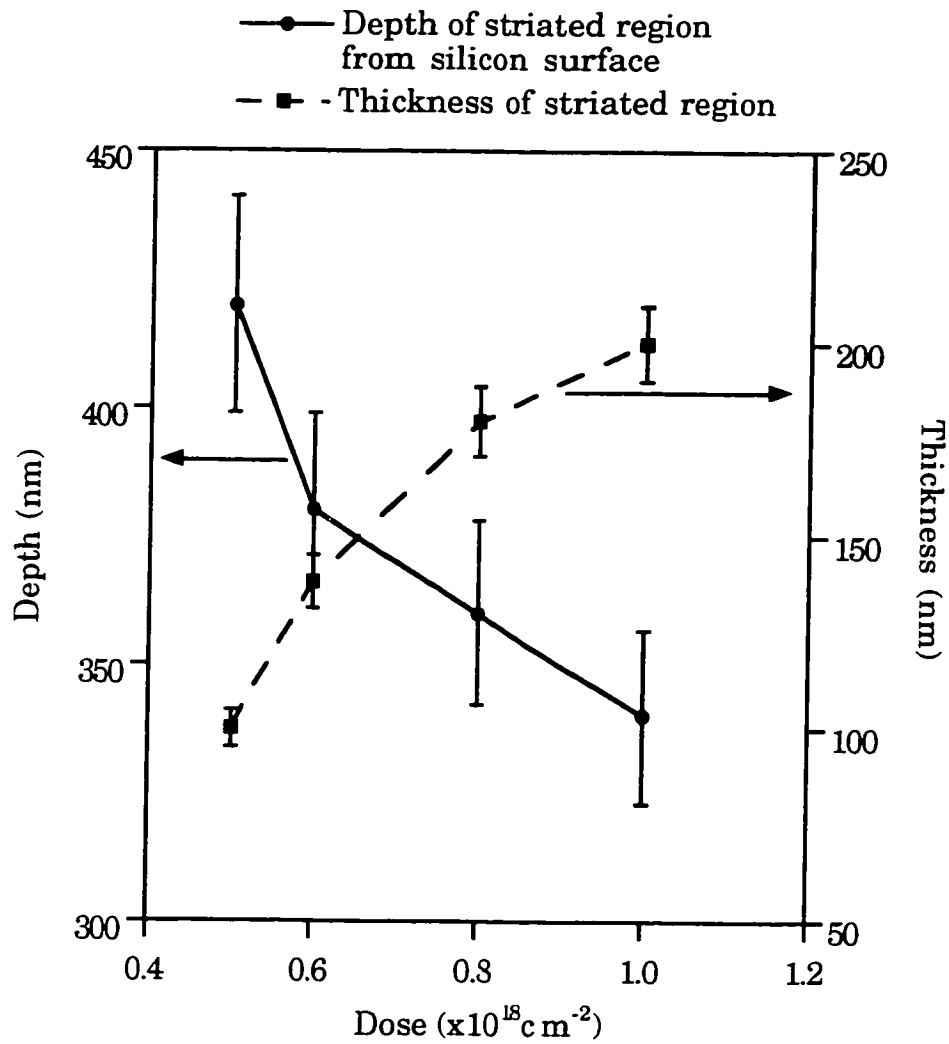


Figure 3.10. Variation of thickness and depth of striated SiO₂ region with dose, for samples in as-implanted condition after implantation at 175 keV.

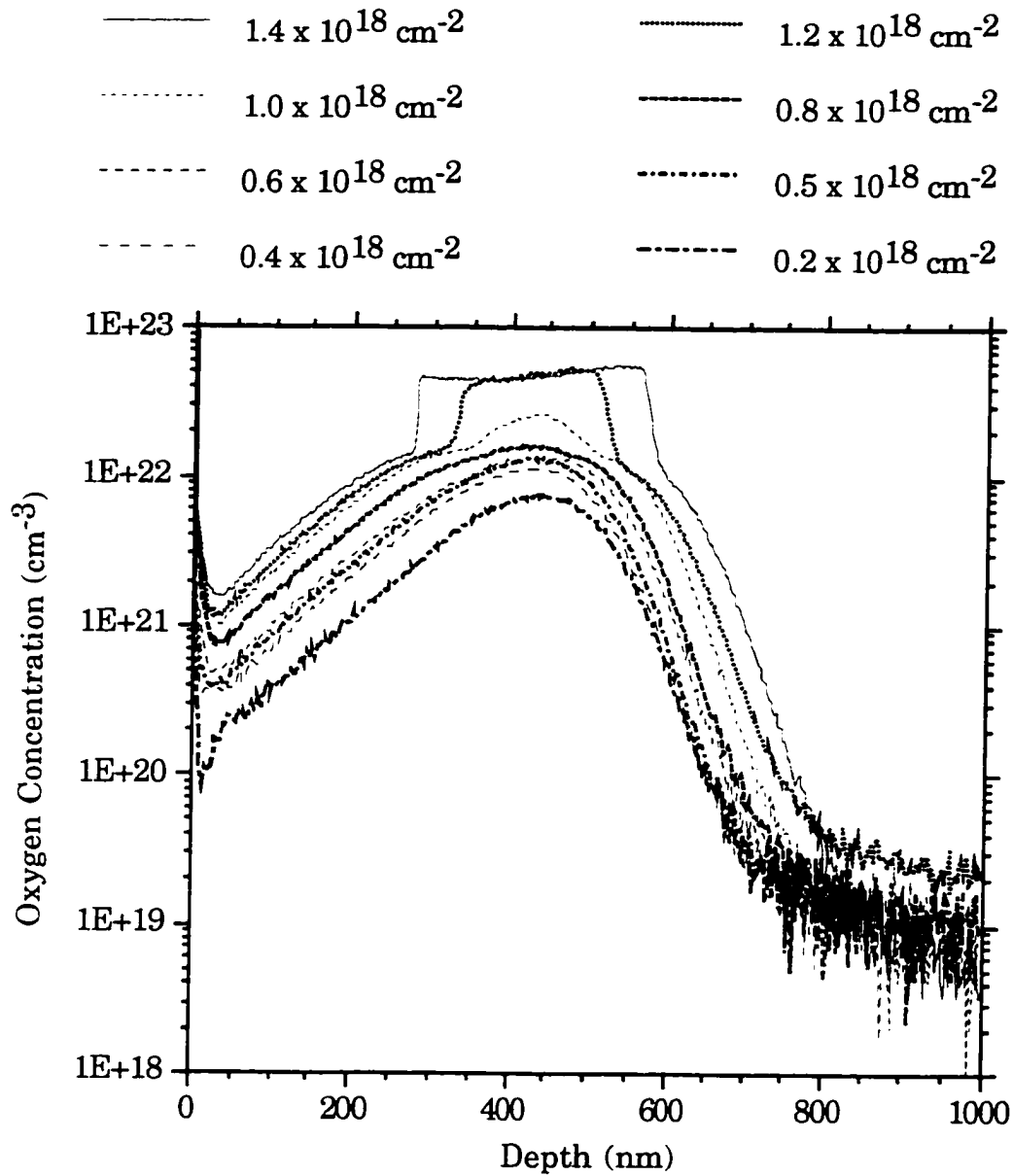


Figure 3.11. SIMS depth profiles of oxygen concentration for samples in as-implanted condition after implantation at 175 keV for various doses.

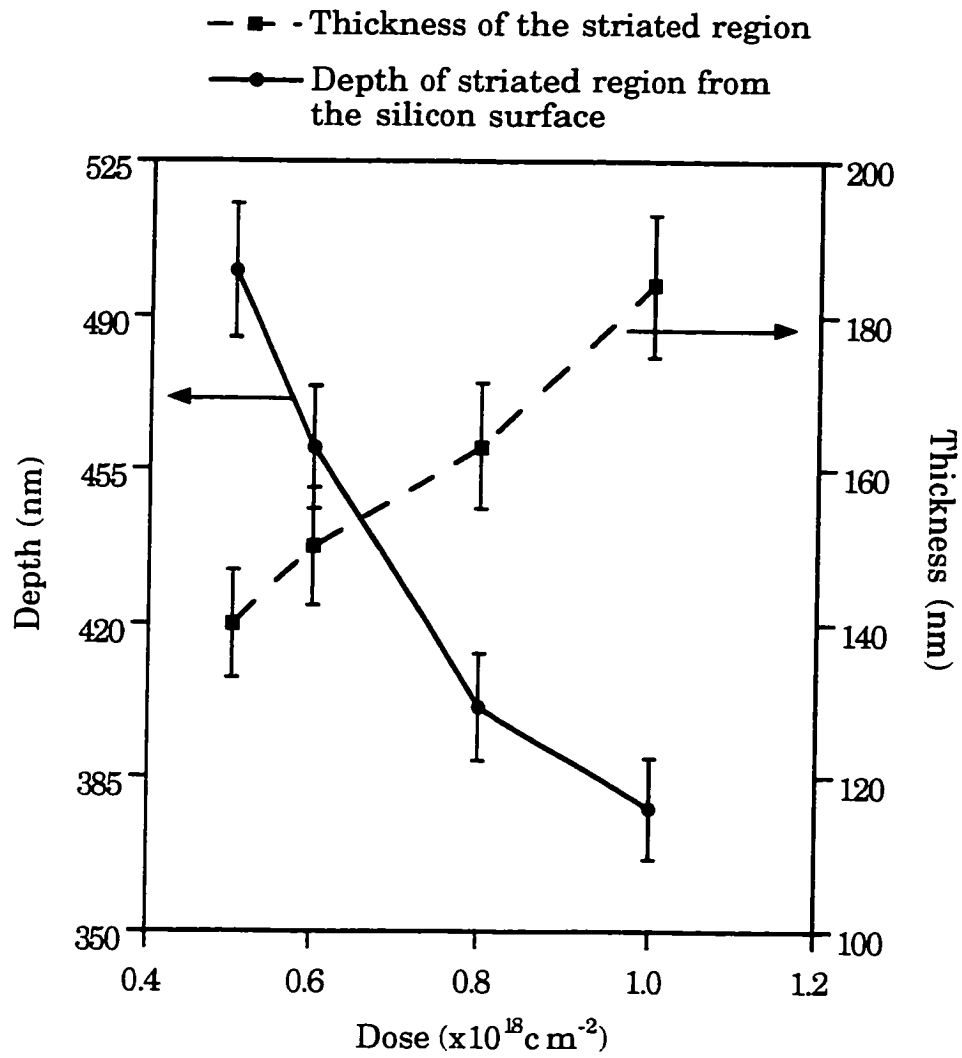


Figure 3.12. Variation of thickness and depth of striated SiO_2 region with dose, for samples in as-implanted condition after implantation at 200 keV.

manner with dose until a continuous buried oxide forms at doses greater than $1.0 \times 10^{18} \text{ cm}^{-2}$. There is no perceptible change in the oxygen concentration profiles to indicate the presence of the striated region in the buried oxide for doses of $0.5 \times 10^{18} \text{ cm}^{-2}$ to $1.0 \times 10^{18} \text{ cm}^{-2}$. Thus, the striations are not a result of large scale variations in oxygen content.

200 keV. From the XTEM images in Figure 3.4 it is evident that a continuous buried oxide does not exist in the as-implanted state for doses lower than $1.2 \times 10^{18} \text{ cm}^{-2}$. Similar to the microstructure observed at 175 keV, striations appear in the region of SiO_2 precipitates for doses between $0.5 \times 10^{18} \text{ cm}^{-2}$ and $1.0 \times 10^{18} \text{ cm}^{-2}$. The depth of these striations from the surface decrease with the increase in dose as is shown in Figure 3.12. Further the width of the striated region increases with the increase in dose, (Figure 3.12). From the XTEM images it is evident that with increase in dose the striations become more continuous and occur at higher densities. At the dose of $1.2 \times 10^{18} \text{ cm}^{-2}$ where a continuous buried oxide forms, a few striations are observable near the top and bottom interfaces of the buried oxide. No striations are observable for the dose of $1.4 \times 10^{18} \text{ cm}^{-2}$.

Annealed Microstructure

XTEM and PTEM analysis were performed on all the doses after annealing at 1310°C for 5 hours in an $\text{Ar}+0.5\%\text{O}_2$ ambient. In the silicon overlayer threading dislocations were the only defects observed. In cases where a continuous buried oxide formed, Si islands were observed for most of the doses. These structures and their dependence on the dose and implant energy are discussed in the following sections.

Defects in the silicon overlayer

175 keV. Threading dislocations were the only defects seen in the surface silicon layer after annealing. PTEM and Secco Etch studies showed

that after annealing the threading dislocation density is a minimum ($\sim 10^4$ to 10^3 cm^{-2}) within a dose range between $0.4 \times 10^{18} \text{ cm}^{-2}$ to $1.0 \times 10^{18} \text{ cm}^{-2}$. The variation of the threading dislocation density with dose is shown in Figure 3.8. XTEM images of the annealed samples are shown in Figure 3.13. At the lowest dose of $0.2 \times 10^{18} \text{ cm}^{-2}$, defects are pinned by SiO_2 precipitates after annealing. Thus, a very high threading dislocation density of $7 \times 10^8 \text{ cm}^{-2}$ is seen at this dose. However, at the next dose of $0.4 \times 10^{18} \text{ cm}^{-2}$, the dislocation density drops dramatically and a low final threading dislocation density of $2 \times 10^4 \text{ cm}^{-2}$ is observed. The final threading dislocation density remains extremely low until a dose of $1.0 \times 10^{18} \text{ cm}^{-2}$. Above this dose, the threading dislocation density increases with increase in dose. PTEM studies showed that the threading dislocations occurred in pairs. It has been experimentally established [35] that these paired threading dislocations evolve from half loops present in the as-implanted state.

200 keV. The variation in the final threading dislocation density as a function of dose for this implant energy is given in Figure 3.9. At this energy, the XTEM images in Figure 3.14a and 3.14b show that at doses of $0.2 \times 10^{18} \text{ cm}^{-2}$ and $0.4 \times 10^{18} \text{ cm}^{-2}$ SiO_2 precipitates are present at a distance of 240 nm from the surface. These precipitates pin defects thereby increasing the defect density. The dislocation density is a minimum within a dose range of $0.5 \times 10^{18} \text{ cm}^{-2}$ and $1.0 \times 10^{18} \text{ cm}^{-2}$. At a dose of $1.2 \times 10^{18} \text{ cm}^{-2}$ and $1.4 \times 10^{18} \text{ cm}^{-2}$ the threading dislocations were found to occur in pairs which implies that they have grown from dislocation half loops. This variation in defect density is strikingly similar to that observed for the 175 keV implant, discussed above.

(a)

(b)

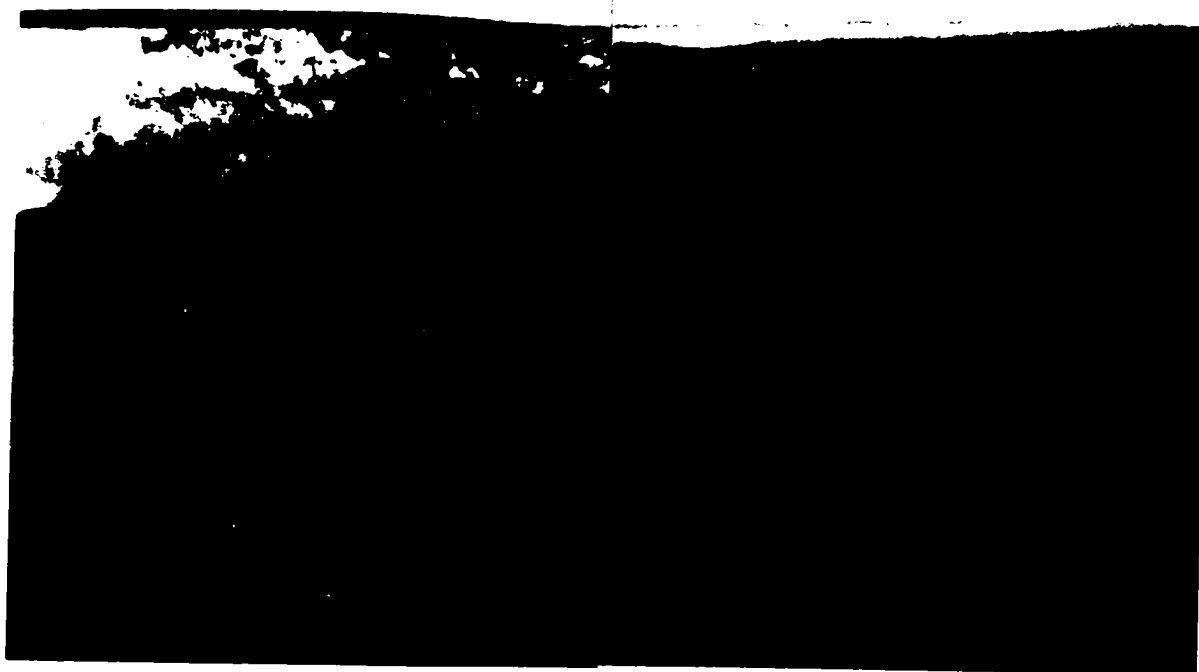
0.10 μm

Figure 3.13. XTEM micrographs of samples in annealed condition after implantation at 175 keV, showing effect of dose variation.
a) $0.2 \times 10^{18} \text{ cm}^{-2}$; b) $0.4 \times 10^{18} \text{ cm}^{-2}$;

(c)

(d)

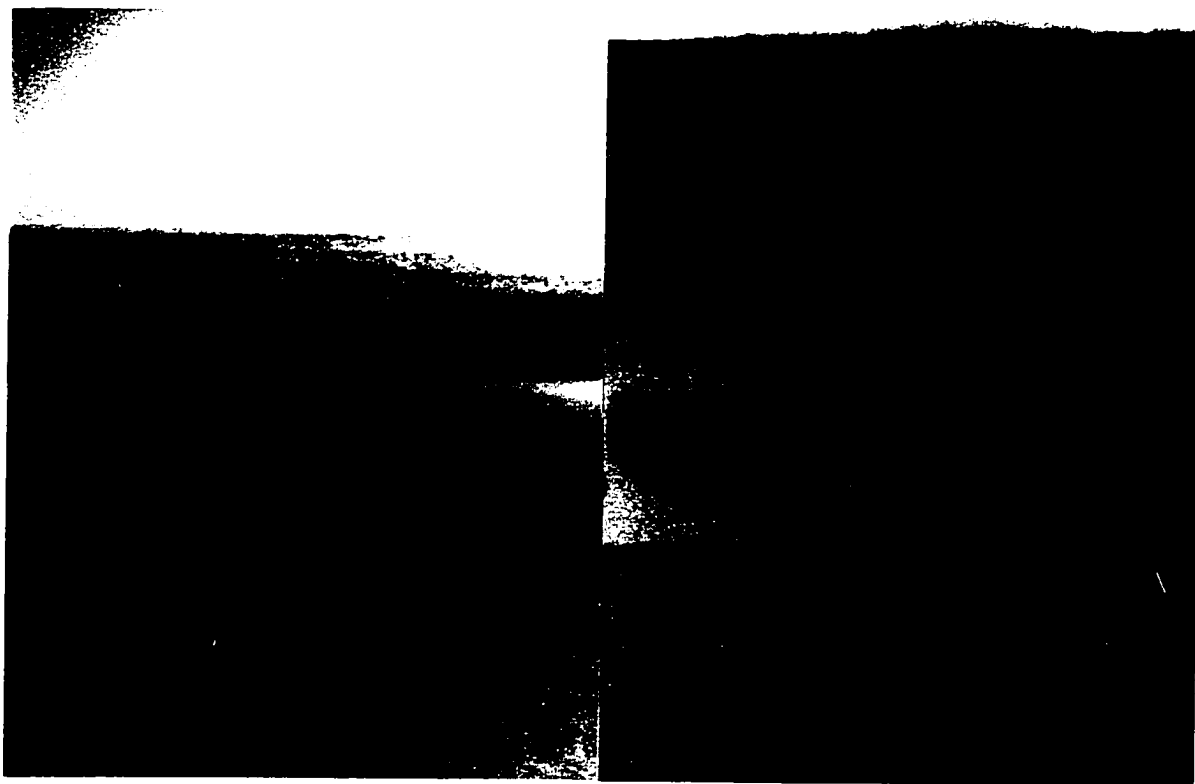
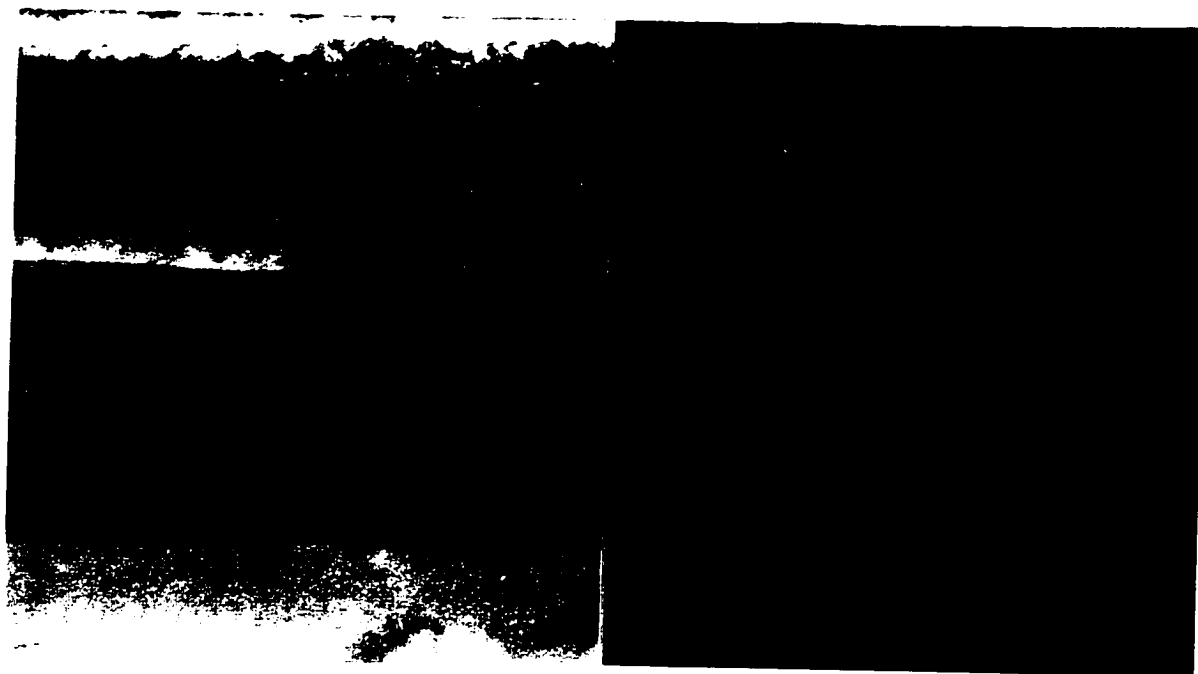
0.10 μm

Figure 3.13 -- continued

c) $0.5 \times 10^{18} \text{ cm}^{-2}$; d) $0.6 \times 10^{18} \text{ cm}^{-2}$;

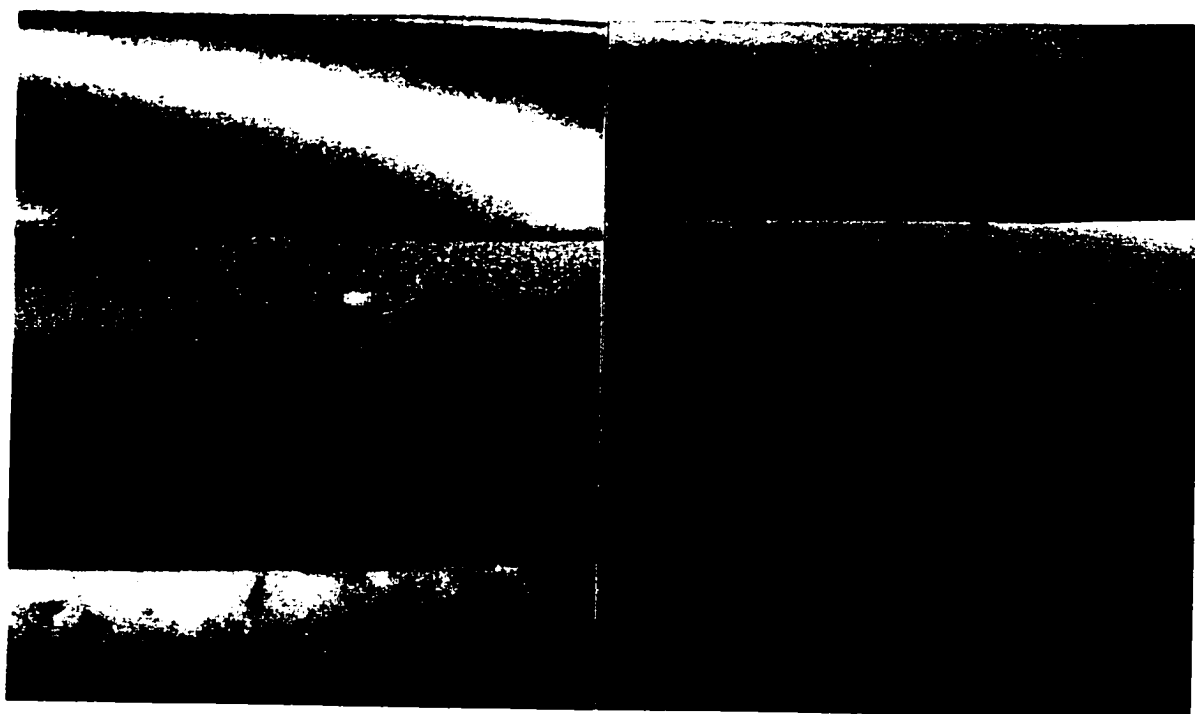
(e)

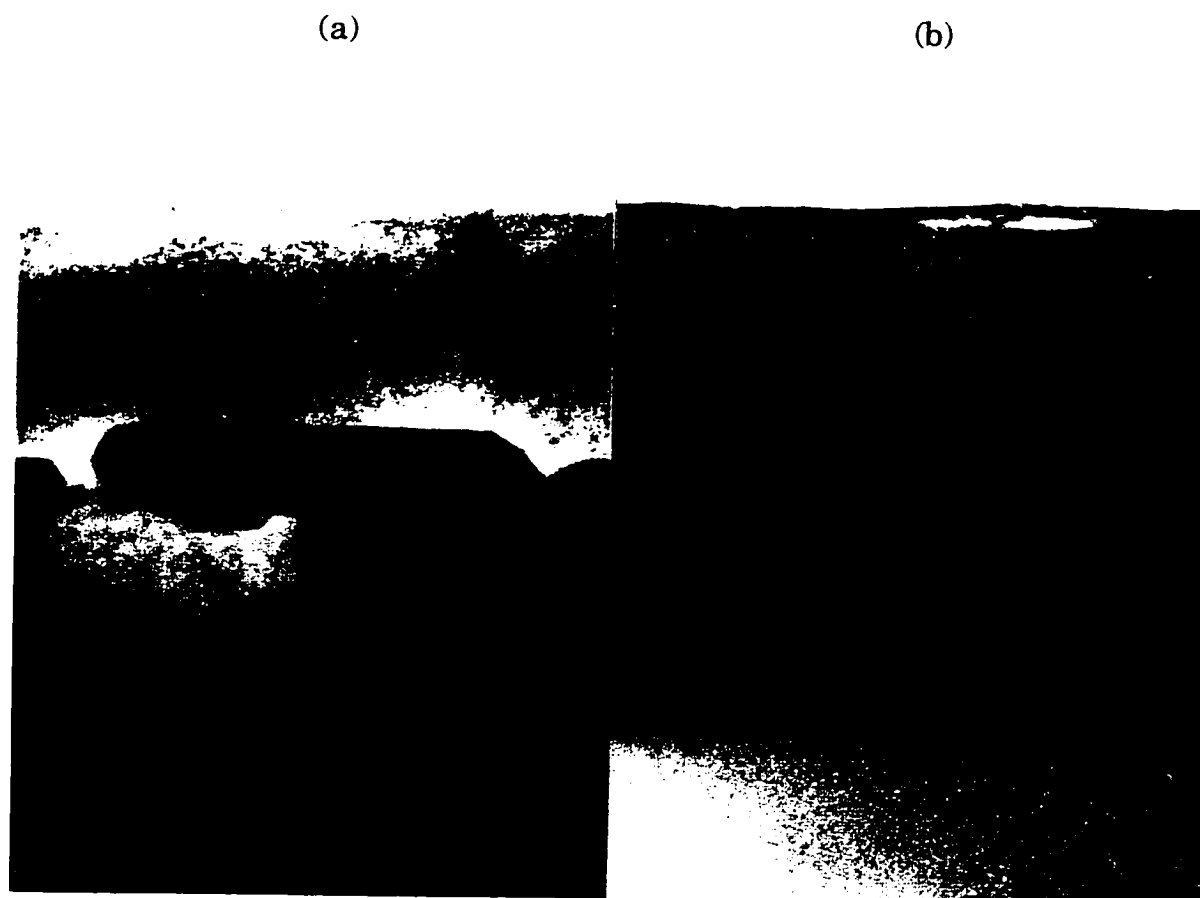
(f)

0.10 μm Figure 3.13 -- continuede) $0.8 \times 10^{18} \text{ cm}^{-2}$; f) $1.0 \times 10^{18} \text{ cm}^{-2}$;

(g)

(h)

0.10 μmFigure 3.13 -- continuedg) $1.2 \times 10^{18} \text{ cm}^{-2}$; h) $1.4 \times 10^{18} \text{ cm}^{-2}$.



0.10 μm

Figure 3.14. XTEM micrographs of samples in annealed condition after implantation at 200 keV, showing effect of dose variation.
a) $0.2 \times 10^{18} \text{ cm}^{-2}$; b) $0.4 \times 10^{18} \text{ cm}^{-2}$;

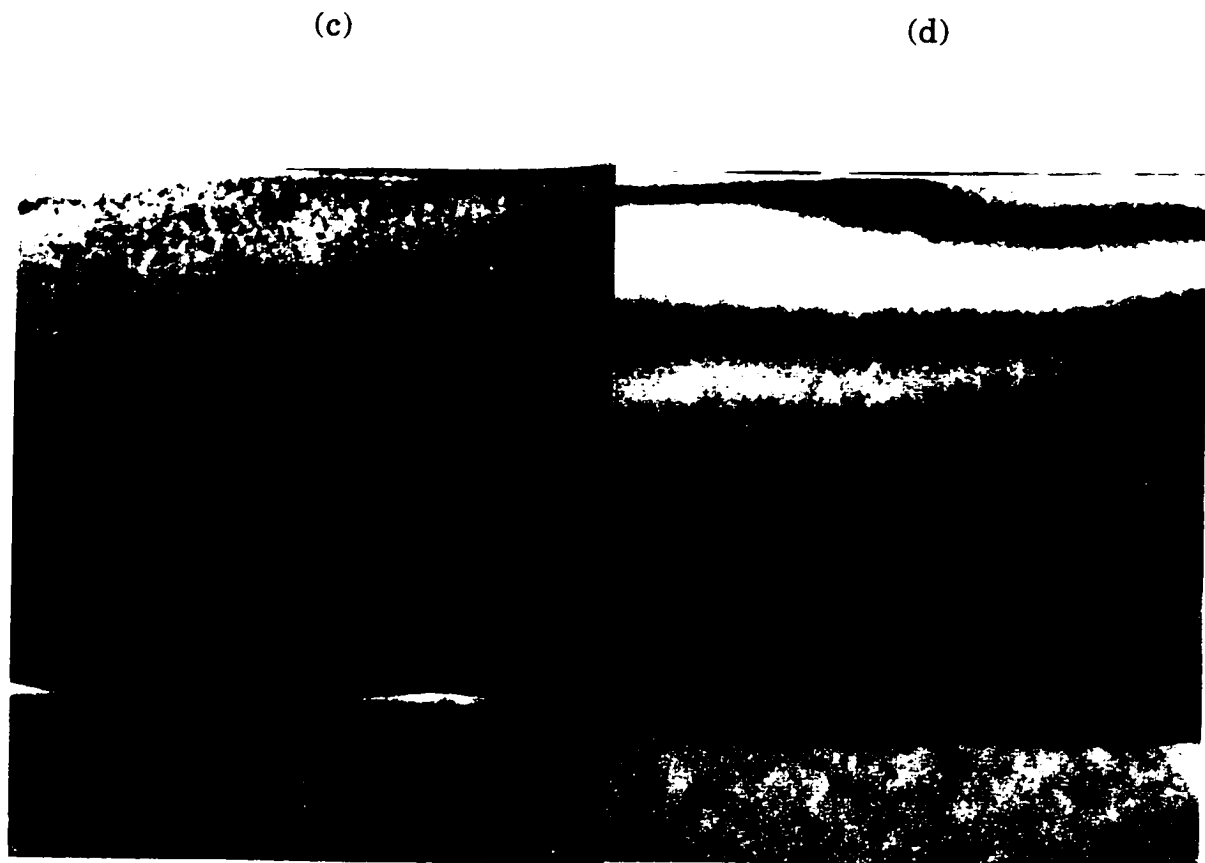
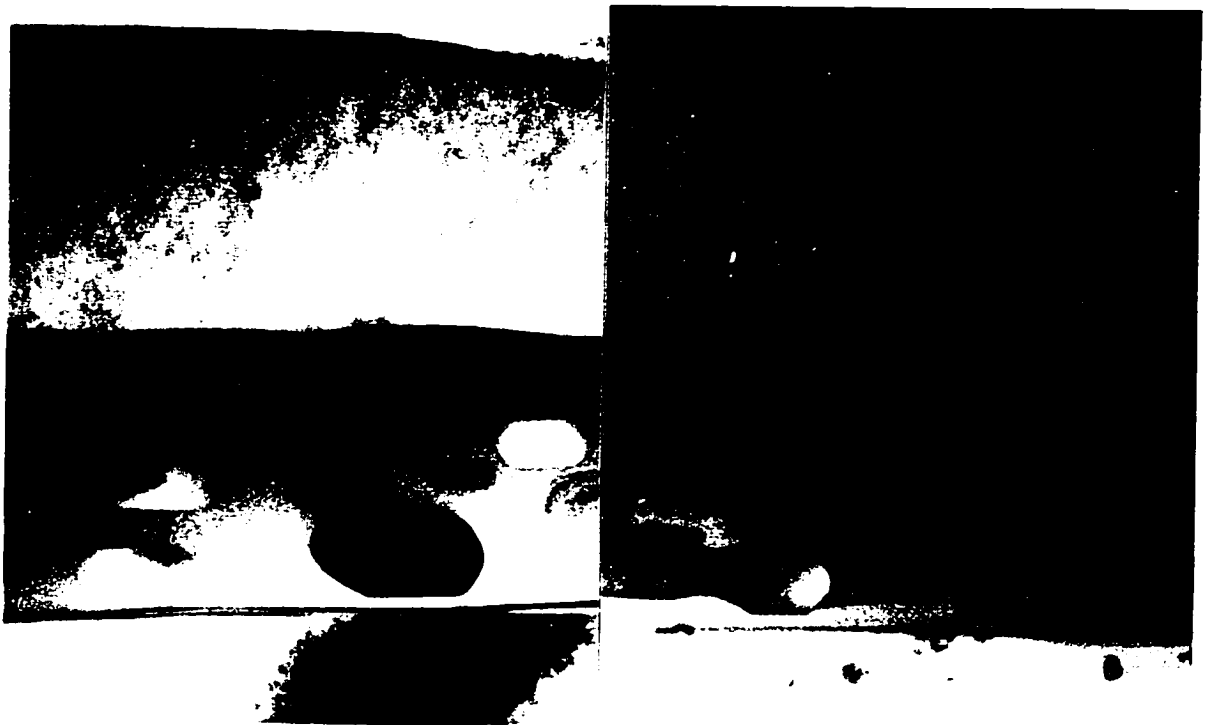


Figure 3.14 -- continued

c) $0.5 \times 10^{18} \text{ cm}^{-2}$; d) $0.6 \times 10^{18} \text{ cm}^{-2}$;

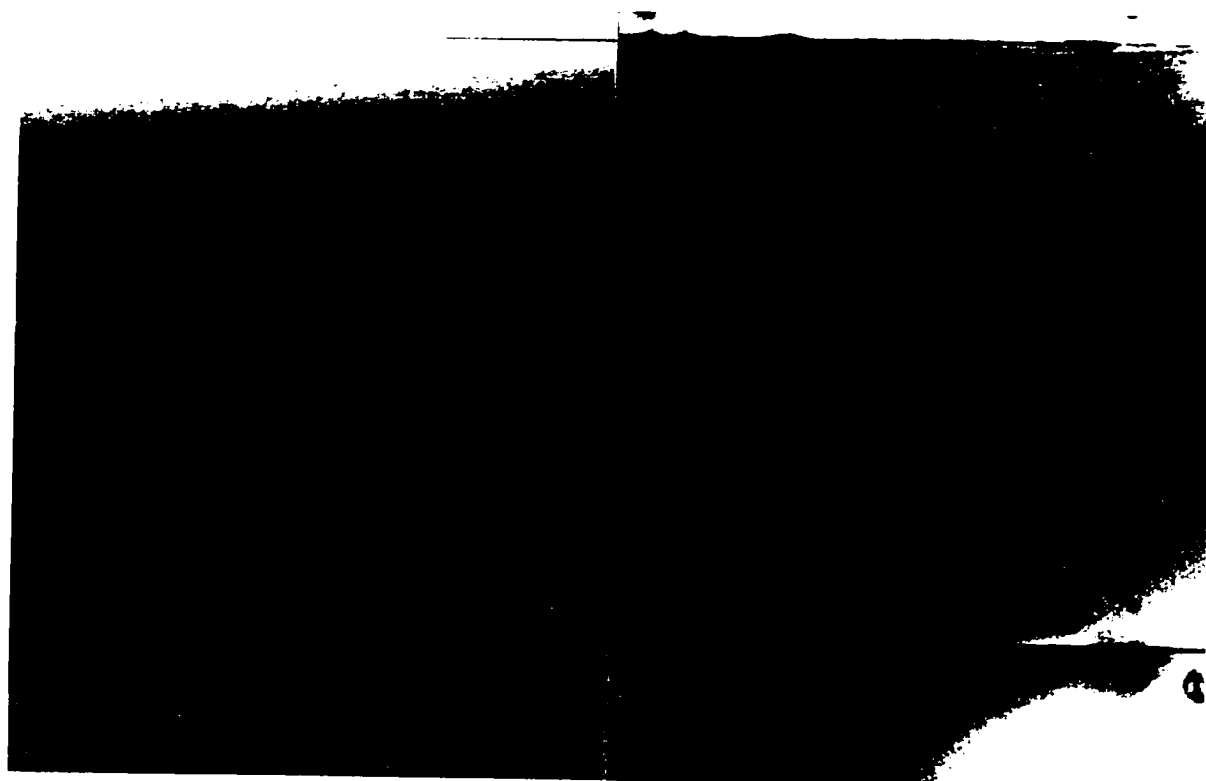
(e)

(f)

0.10 μmFigure 3.14 -- continuede) $0.8 \times 10^{18} \text{ cm}^{-2}$; f) $1.0 \times 10^{18} \text{ cm}^{-2}$;

(g)

(h)

0.10 μmFigure 3.14 -- continuedg) $1.2 \times 10^{18} \text{ cm}^{-2}$; h) $1.4 \times 10^{18} \text{ cm}^{-2}$.

Buried oxide

175 keV. The evolution of the buried oxide after annealing as a function of dose is apparent in the XTEM images shown in Figure 3.13. For the dose of $0.2 \times 10^{18} \text{ cm}^{-2}$, no continuous buried oxide forms. There are two discrete bands of SiO_2 precipitates at depths of 230 nm and 440 nm from the surface. The mean size of the precipitates on the upper layer are smaller than those on the lower layer. This bimodal distribution of precipitates is also seen as two oxygen peaks at a distance of 250 nm and 400 nm from the surface, shown in the SIMS profile in Figure 3.15.

For the doses of $0.4 \times 10^{18} \text{ cm}^{-2}$ and higher, a continuous buried oxide forms as is evident from the XTEM images shown in Figure 3.13. It was found that the Si island density within the buried oxide for a dose of $0.4 \times 10^{18} \text{ cm}^{-2}$ was less than 10^5 cm^{-2} , which indicates the superior quality of the oxide formed at this dose. However, Si islands decorate the buried oxide for doses higher than $0.4 \times 10^{18} \text{ cm}^{-2}$ and hence deteriorate the quality of the oxide for the higher doses. Further, it is apparent from Figure 3.13, that there is a tendency for these Si islands to occur in bands. At the dose of $1.2 \times 10^{18} \text{ cm}^{-2}$ Si islands are present only in two bands, i.e., one close to the top Si/buried oxide interface and one close to the lower Si/buried oxide interface. However, as the dose increases to $1.4 \times 10^{18} \text{ cm}^{-2}$, Si islands are only restricted to the lower buried oxide/silicon substrate interface. The presence of these islands can also be inferred from the regions of lower average oxygen concentration within the buried oxide that appear in the SIMS profiles shown in Figure 3.15.

Even though the XTEM images show an increase in the number of Si islands within the buried oxide with increase in dose, the fraction of the buried oxide occupied by these islands steadily decreases with the increase

in dose. This trend is shown in Figure 3.16. The top Si overlayer/buried oxide interface steadily moves closer towards the surface with increasing dose, as the thickness of the buried oxide increases with dose, and these results are shown in Figure 3.17.

200 keV. Figure 3.14 shows the microstructure of the buried oxide at this energy. There are some notable differences and similarities in the microstructure from those observed at the implant of 175 keV.

For all the doses, the relative position of the buried oxide with respect to the surface is deeper than the 175 keV implant. This is a direct consequence of the higher energy of implant. Moreover, unlike the 175 keV implant, no continuous buried oxide forms at a dose of $0.4 \times 10^{18} \text{ cm}^{-2}$. Two bands of precipitates centered at distances of 275 nm and 450 nm from the surface can be observed (Figure 3.14b).

Similar to the behavior observed at the 175 keV implant, for doses of $0.5 \times 10^{18} \text{ cm}^{-2}$ and higher, the buried oxide is decorated with Si islands. The tendency for the Si islands to occur in bands is also observed at this energy for doses of $0.5 \times 10^{18} \text{ cm}^{-2}$ and higher. In keeping with the trends observed at the 175 keV implant, the density of the Si islands increases, though the fraction of the buried oxide occupied by these islands decreases with increase in dose (see Figure 3.16). Further, the distance of the top Si overlayer/buried oxide interface decreases while the thickness of the buried oxide increases with the increase in dose (Figure 3.17).

Silicon surface and top silicon/buried oxide interface

175 keV. AFM analysis was performed to evaluate the quality of the Si surface and top Si overlayer/buried oxide interface after annealing. From Figure 3.18 it can be seen that the Si surface roughness does not follow any particular dependence on the dose. However, within the dose of

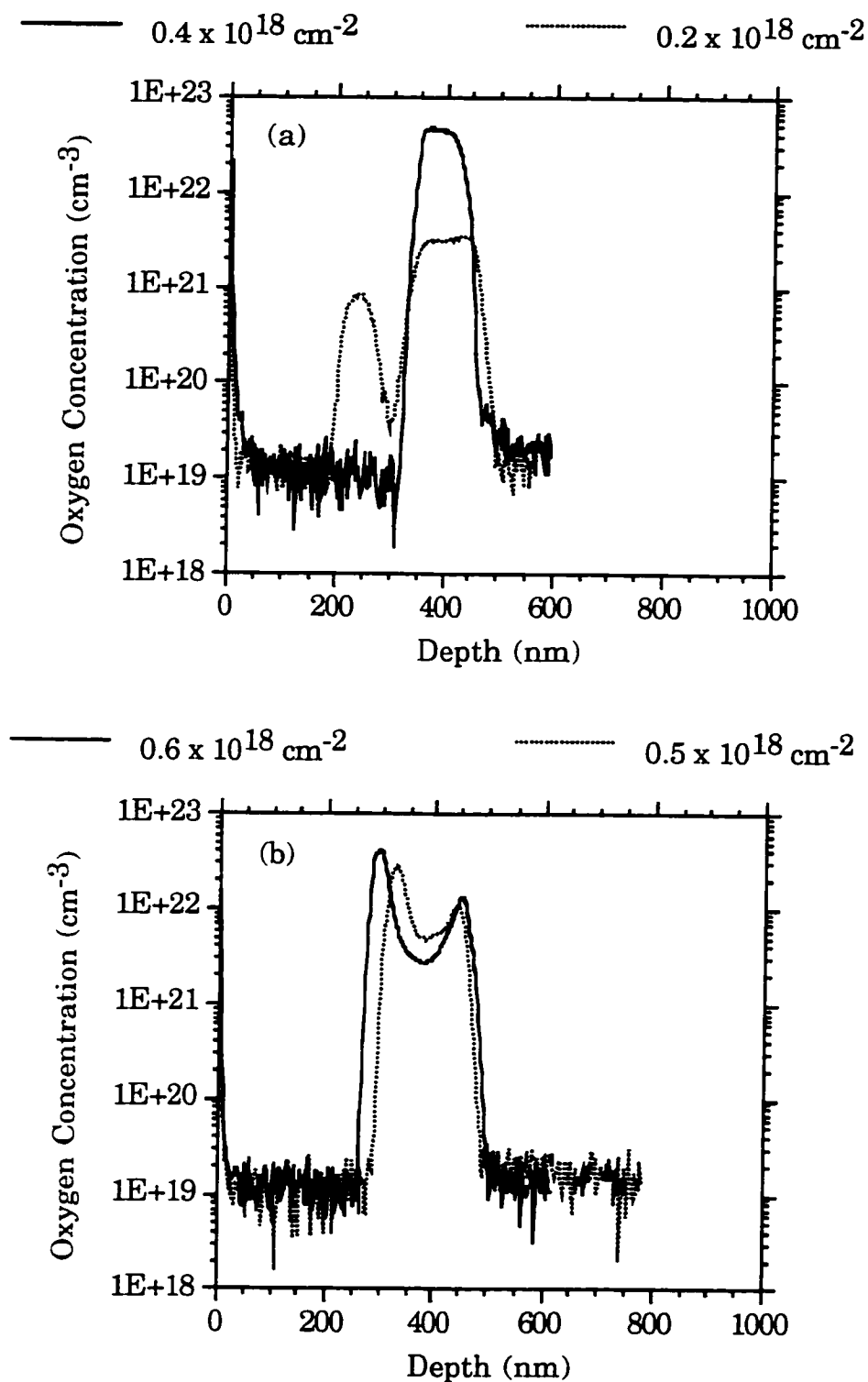


Figure 3.15. SIMS depth profiles of oxygen concentration for samples in annealed condition after implantation at 175 keV for various doses.

a) 0.2 and $0.4 \times 10^{18} \text{ cm}^{-2}$; b) 0.5 and $0.6 \times 10^{18} \text{ cm}^{-2}$;

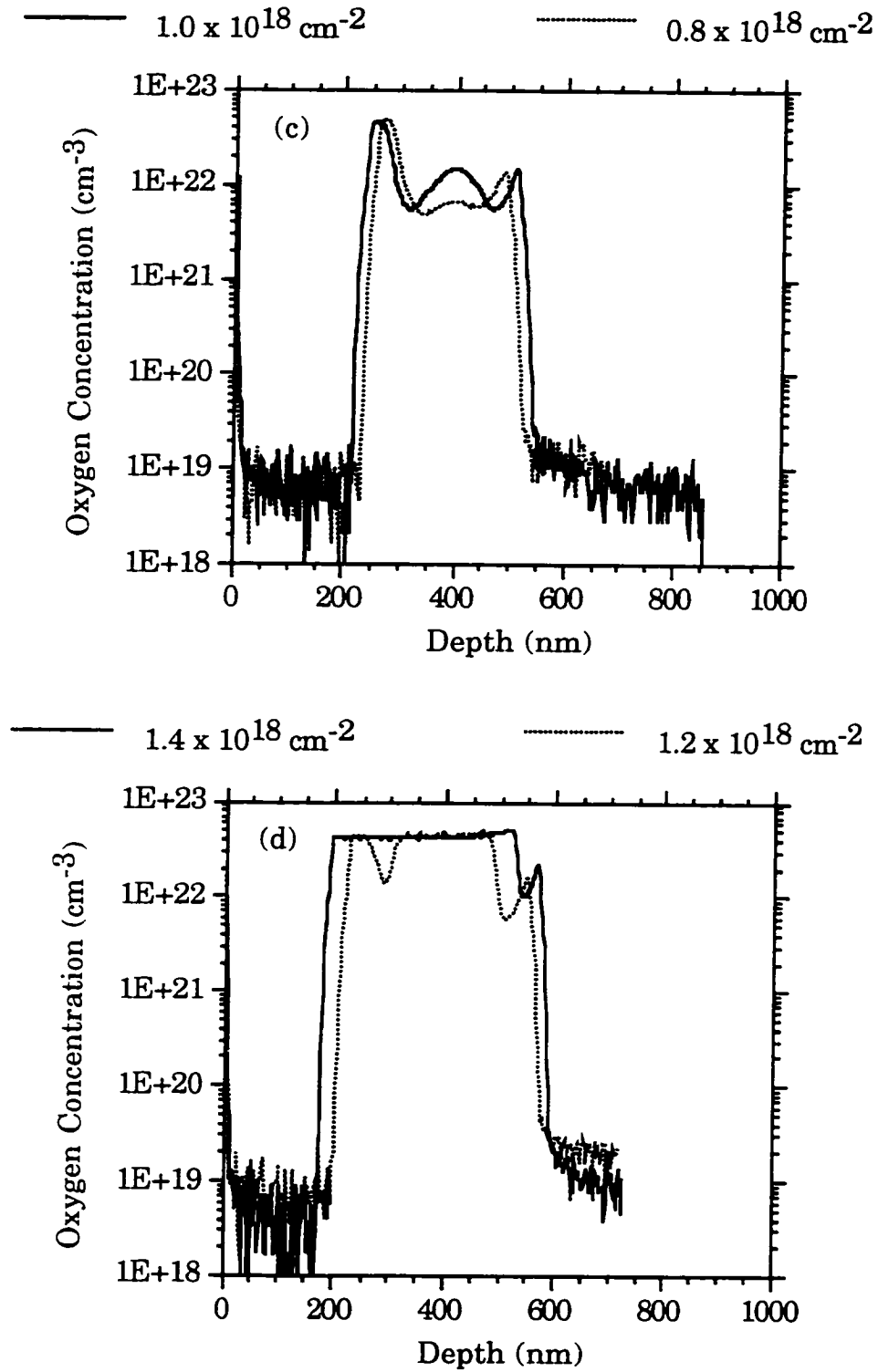


Figure 3.15 -- continued

c) 0.8 and $1.0 \times 10^{18} \text{ cm}^{-2}$; d) 1.2 and $1.4 \times 10^{18} \text{ cm}^{-2}$.

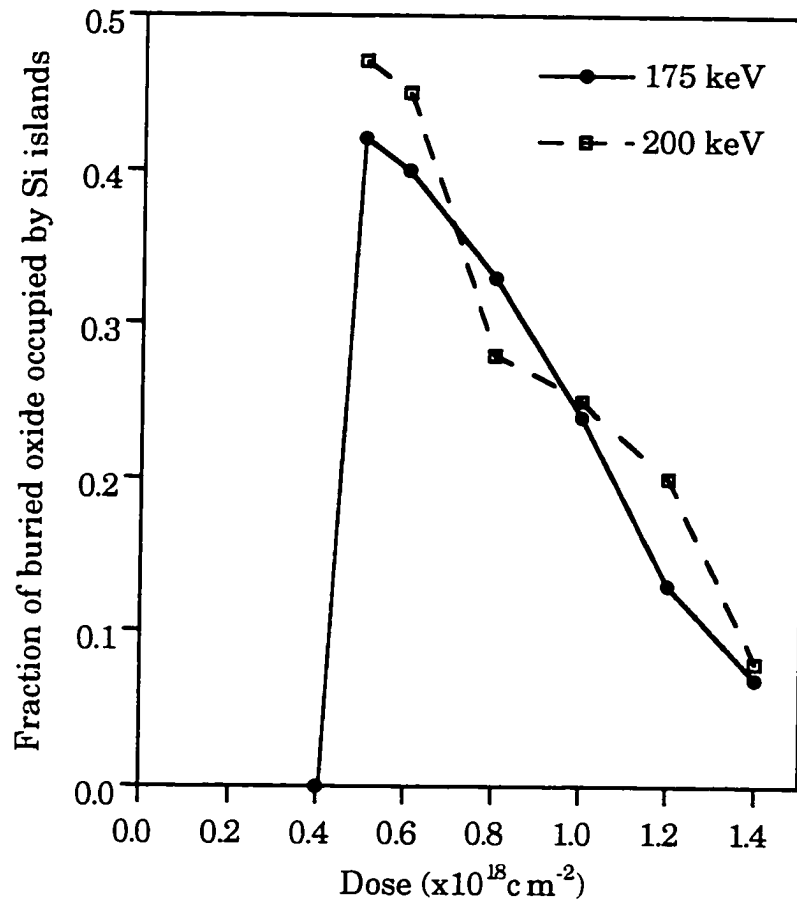


Figure 3.16. Fraction of the buried oxide occupied by Si islands as a function of dose and energy for annealed samples.

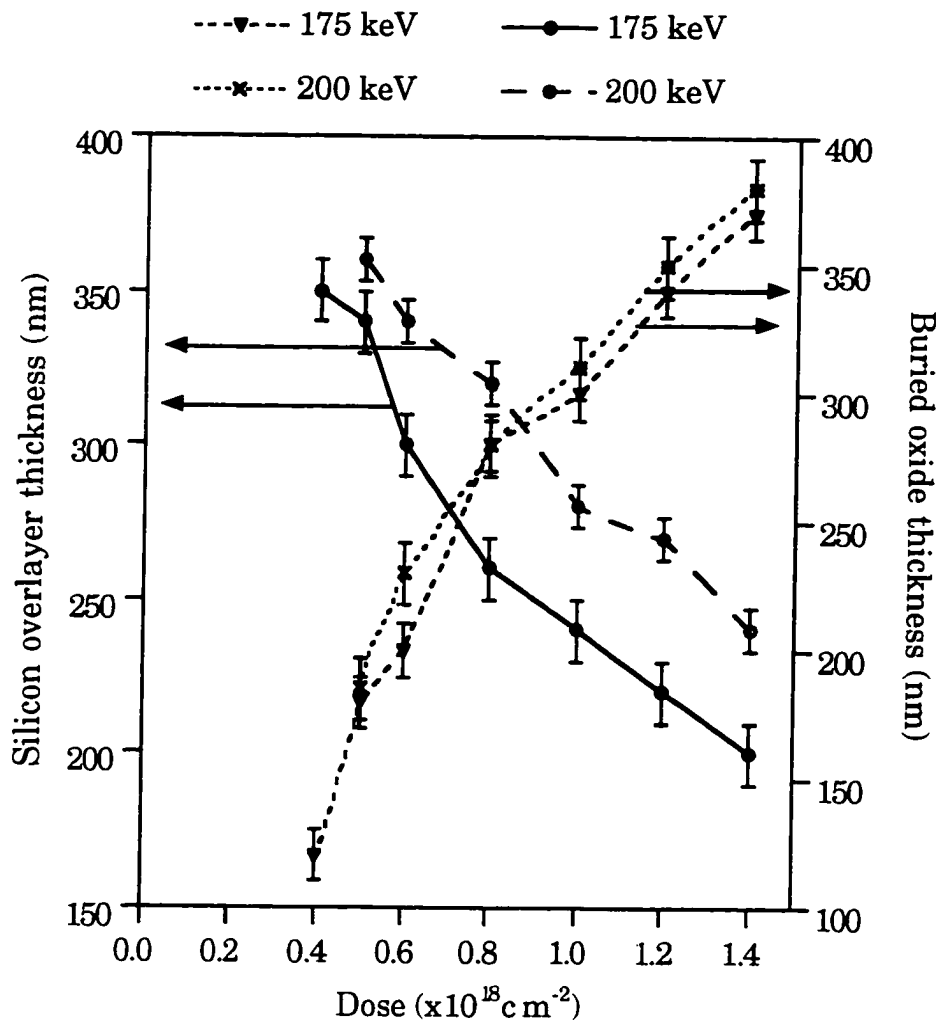


Figure 3.17. Silicon overlayer and buried oxide thickness as a function of dose and energy for annealed samples.

$0.2 \times 10^{18} \text{ cm}^{-2}$ and $0.5 \times 10^{18} \text{ cm}^{-2}$ the quality of the surface is much superior in comparison to the higher doses. This could be due to the extensive sputtering at the surface for the higher doses. The roughness of the interface shows a distinctive variation with the dose. At the lowest dose of $0.2 \times 10^{18} \text{ cm}^{-2}$, it was seen from the XTEM image that no continuous buried oxide layer had formed. The high interface roughness value is a result of this microstructure. At the dose of $0.4 \times 10^{18} \text{ cm}^{-2}$ the quality of the interface improves in comparison to the $0.2 \times 10^{18} \text{ cm}^{-2}$ due to the presence of a continuous buried oxide. However, it was apparent from the XTEM image that the buried oxide for the dose of $0.4 \times 10^{18} \text{ cm}^{-2}$ was not uniform. For doses higher than $0.5 \times 10^{18} \text{ cm}^{-2}$ the roughness values improve considerably, indicating the presence of sharp interfaces at these doses. It is to be noted that from comparing the scales for the surface and interface roughness graphs, it is evident that the variation in the surface quality is insignificant in comparison to the variation of the interface roughness.

200 keV. Si surface and top Si overlayer/buried oxide interface roughness for all the doses were evaluated using AFM for this implant energy. From the graph in Figure 3.18 it is seen that the Si surface roughness varies negligibly with dose.

The interface roughness value for the $0.2 \times 10^{18} \text{ cm}^{-2}$ dose again shows a high value of 2.7 nm which is due to the incomplete buried oxide structure. At $0.4 \times 10^{18} \text{ cm}^{-2}$, the roughness value improves slightly due to the presence of a more continuous buried oxide structure as evident from the XTEM image. There is a significant improvement in the interface quality with dose for doses higher than $0.4 \times 10^{18} \text{ cm}^{-2}$, and no significant variations in the interface quality are apparent.

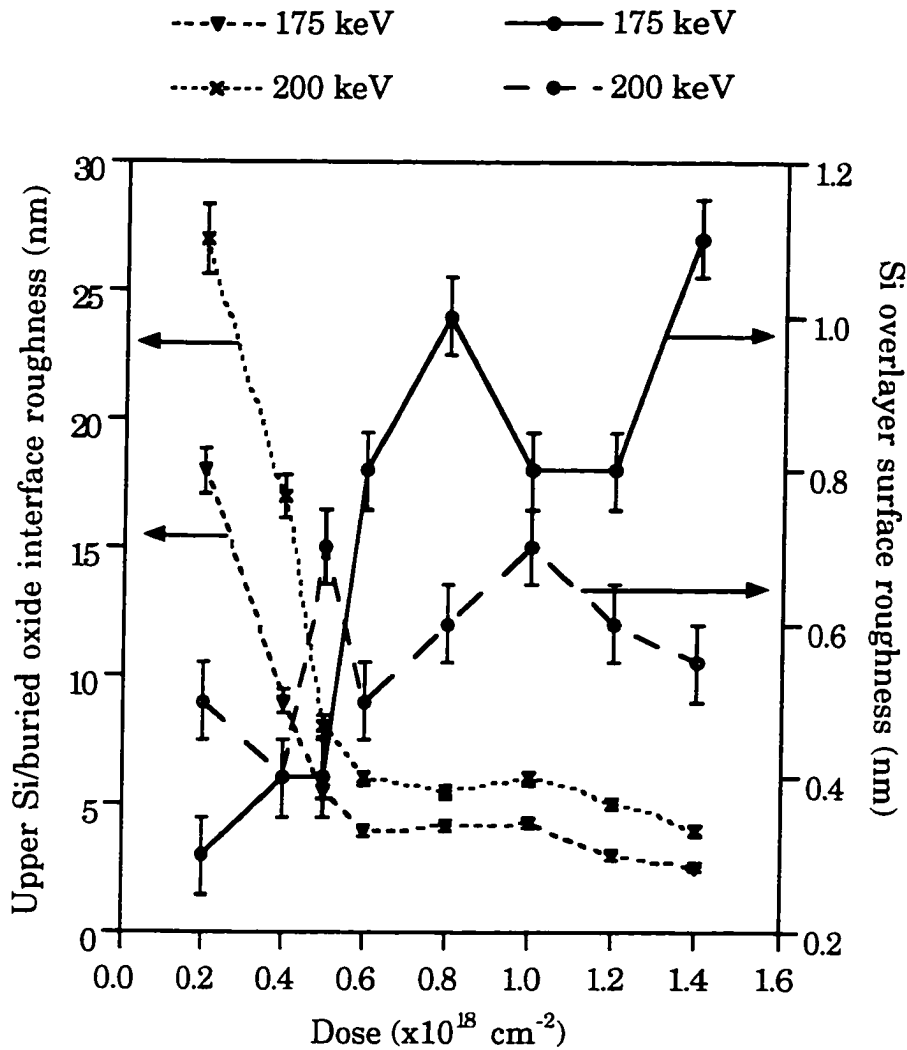


Figure 3.18. Silicon overlayer surface roughness and upper silicon/buried oxide interface roughness as a function of dose and energy for annealed samples.

Summary of Results

Detailed characterization of the effect of variation of dose and energy on single implant SIMOX microstructure yielded the following important results.

As-implanted microstructure

In the near surface region XTEM analysis showed that the depth of the cavity layer increases with increase in dose. HRXRD analysis showed that a prominent Bragg peak was present at an angle higher than the substrate peak. This indicates that the lattice near the surface has undergone a tetragonal distortion and the stress state is one of in plane biaxial tension. The maximum estimated perpendicular strain was found to increase with the increase in dose. SIMS analysis for all doses at 175 keV showed that there is an increase in oxygen concentration with increase in dose in the near surface region, although there is no significant oxygen build up in this region. It was also shown that the x-ray strain values for each dose were ~1.2 times higher for the lower energy (175 keV) implant in comparison to the higher energy (200 keV) implant. XTEM and PTEM analysis of the defects showed that stacking faults were the dominant defects present for doses below $1.0 \times 10^{18} \text{ cm}^{-2}$ while dislocation half loops and stacking faults were present for doses of $1.0 \times 10^{18} \text{ cm}^{-2}$ and higher for both implant energies of 175 keV and 200 keV.

No continuous buried oxide formed in the as-implanted state at either energy, until a dose of $1.2 \times 10^{18} \text{ cm}^{-2}$. The SIMS results for the 175 keV implant showed a plateau in the oxygen concentration for the dose of $1.2 \times 10^{18} \text{ cm}^{-2}$ indicating the presence of a continuous buried oxide in the as-implanted state. XTEM images showed striations within the buried oxide for doses between $0.5 \times 10^{18} \text{ cm}^{-2}$ and $1.0 \times 10^{18} \text{ cm}^{-2}$ for both implant

energies. XTEM analysis showed that the thickness of the striated region increased with dose and their depth from the surface decreased with increase in dose. Moreover, these striations appeared to become continuous with increase in dose.

Annealed microstructure

Threading dislocations were the only extended defects present in the annealed state in the Si overlayer. PTEM and Secco etch results indicated that within a dose range of $0.4 \times 10^{18} \text{ cm}^{-2}$ and $1.0 \times 10^{18} \text{ cm}^{-2}$ the final threading dislocation density was a minimum. Moreover, the threading dislocations for doses of $1.2 \times 10^{18} \text{ cm}^{-2}$ and $1.4 \times 10^{18} \text{ cm}^{-2}$ occurred in pairs, which indicated that they might have developed from dislocation half loops present in the as-implanted state. No continuous buried oxide formed at the dose of $0.2 \times 10^{18} \text{ cm}^{-2}$ and two spatially separated bands of SiO_2 precipitates were present for both implant energies. Even though a continuous buried oxide with very low Si island density formed at a dose of $0.4 \times 10^{18} \text{ cm}^{-2}$ for the 175 keV implant, two spatially separated bands of precipitates were present at this dose for the implant energy of 200 keV. For doses between $0.5 \times 10^{18} \text{ cm}^{-2}$ and $1.4 \times 10^{18} \text{ cm}^{-2}$, Si islands were present within the buried oxide layer. From the XTEM images, it was apparent that the number of Si islands increased with the increase in dose from $0.5 \times 10^{18} \text{ cm}^{-2}$ to $1.0 \times 10^{18} \text{ cm}^{-2}$, though the fraction of the buried oxide occupied by them decreased with increase in dose. AFM analysis of the upper Si overlayer/buried oxide interface showed that there was an improvement in its quality with the increase in dose. However, the Si surface quality showed an inferior roughness above a dose of $0.5 \times 10^{18} \text{ cm}^{-2}$ compared to the lower doses, for the implant energy of 175 keV. No such behavior was evident at 200 keV.

Choice of Dose and Energy

From the above experiments it became obvious that for the implant energy of 175 keV the two doses of $0.4 \times 10^{18} \text{ cm}^{-2}$ (substoichiometric) and $1.4 \times 10^{18} \text{ cm}^{-2}$, (stoichiometric) yield device quality buried oxides. Even though the final defect densities were higher for the dose of $1.4 \times 10^{18} \text{ cm}^{-2}$ the quality of the buried oxide was superior to the other stoichiometric doses. Hence, the effect of substrate temperature variation and beam current were analyzed using these two implant doses at an energy of 175 keV.

Substrate Temperature

From the existing literature it is apparent that it has not been possible to investigate the independent effect of substrate temperature using high beam currents and energies on the evolution of the SIMOX microstructure. A recent report [35] using partial control of the substrate temperature shows that the near surface stress, the half loop density and the threading dislocation density do not change when the implant temperature is raised above 600°C. Moreover, Lee et al. [35] show that threading dislocations are a result of the half loops which have Burgers vectors parallel to the surface.

Inability to control the substrate temperature independent of the beam current and energy have severely limited our understanding of the individual effects of these parameters on the microstructure. Using the new Ibis 1000 implanter it has become possible to control the substrate temperature and beam current independent of the other implant parameters. In this section the experimental results of varying the substrate temperature, independent of beam current and other parameters, on the evolution of the SIMOX microstructure are reported.

Analysis of the effect of dose and energy on the microstructure led to the choice for doses of $0.4 \times 10^{18} \text{ cm}^{-2}$ and $1.4 \times 10^{18} \text{ cm}^{-2}$. Implants were performed at these two doses for different implant temperatures, keeping the implant energy at 175 keV. The specific experimental conditions used will be discussed in the respective sections.

Stoichiometric Dose Implants

Samples were implanted at 175 keV, with a beam current density of 3.2 mA/cm^2 at a dose of $1.4 \times 10^{18} \text{ cm}^{-2}$ for substrate temperatures of 540°C , 590°C , and 640°C . Both as-implanted and annealed microstructures were evaluated. All the anneals were performed at 1310°C for 5 hours in an Ar + 0.5% O_2 ambient.

As-implanted microstructure

The major microstructural features in the as-implanted state were the cavities, dislocation half loops and stacking faults. These structures are discussed in the following sections.

Cavities and near surface strain. XTEM images of the as-implanted samples are shown in Figure 3.19. It is apparent that no cavity layer exists for the sample implanted at a substrate temperature of 540°C . The entire Si overlayer is decorated with a high density of defects. For the implant at 590°C , it is apparent that a thick cavity layer exists near the surface extending to a depth of about 80 nm. The cavities are arranged in columns in the direction of the implantation. At the highest implant temperature of 640°C cavities occur in the near surface region, although no distinct columnar arrangement is apparent. The depth of the cavity layer at this temperature is 50 nm from the surface. It is to be noted that the cavity layer thickness reaches a maximum at a temperature of 590°C , after which it shrinks at the higher substrate temperature of 640°C . The cavities appear

to be large near the surface and decrease in size toward the bulk. The variation of the cavity layer thickness as a function of substrate temperature is shown in Figure 3.20. To analyze the strain induced by cavities HRXRD studies were performed.

The (004) rocking curves for each sample are shown in Figure 3.21. For the sample implanted at 540°C, no identifiable strain layer diffraction peak exists. The elevated background intensity is caused by Huang scattering from the extended defects in this region, which are apparent from the XTEM analysis. Hence, it is likely that a strain layer may still exist, but it is not possible to measure the strain using HRXRD because of its incoherent nature. Similar observations have been made by Venables [83].

The (004) rocking curves for the implants performed at substrate temperatures of 590°C and 640°C show that a prominent Bragg peak is present at an angle higher than the substrate peak. This indicates that the lattice in this region has undergone a contraction in the near surface region. The absence of thickness fringes imply that the strained layer is at the surface. The maximum estimated strain was found to be temperature dependent and decreased with the increase in substrate temperature. The maximum estimated strain values were found to be -4958 ppm and -4809 ppm for the substrate temperatures of 590°C and 640°C respectively, as shown in Figure 3.20.

Near surface defects. The XTEM image of the sample implanted at 540°C (Figure 3.19a) shows that the entire Si overlayer of thickness 300 nm is decorated with defects. The majority of these defects were stacking faults and PTEM analysis showed that no dislocation half loops were present. The defect density analyzed from PTEM images was $2 \times 10^{10} \text{ cm}^{-2}$.

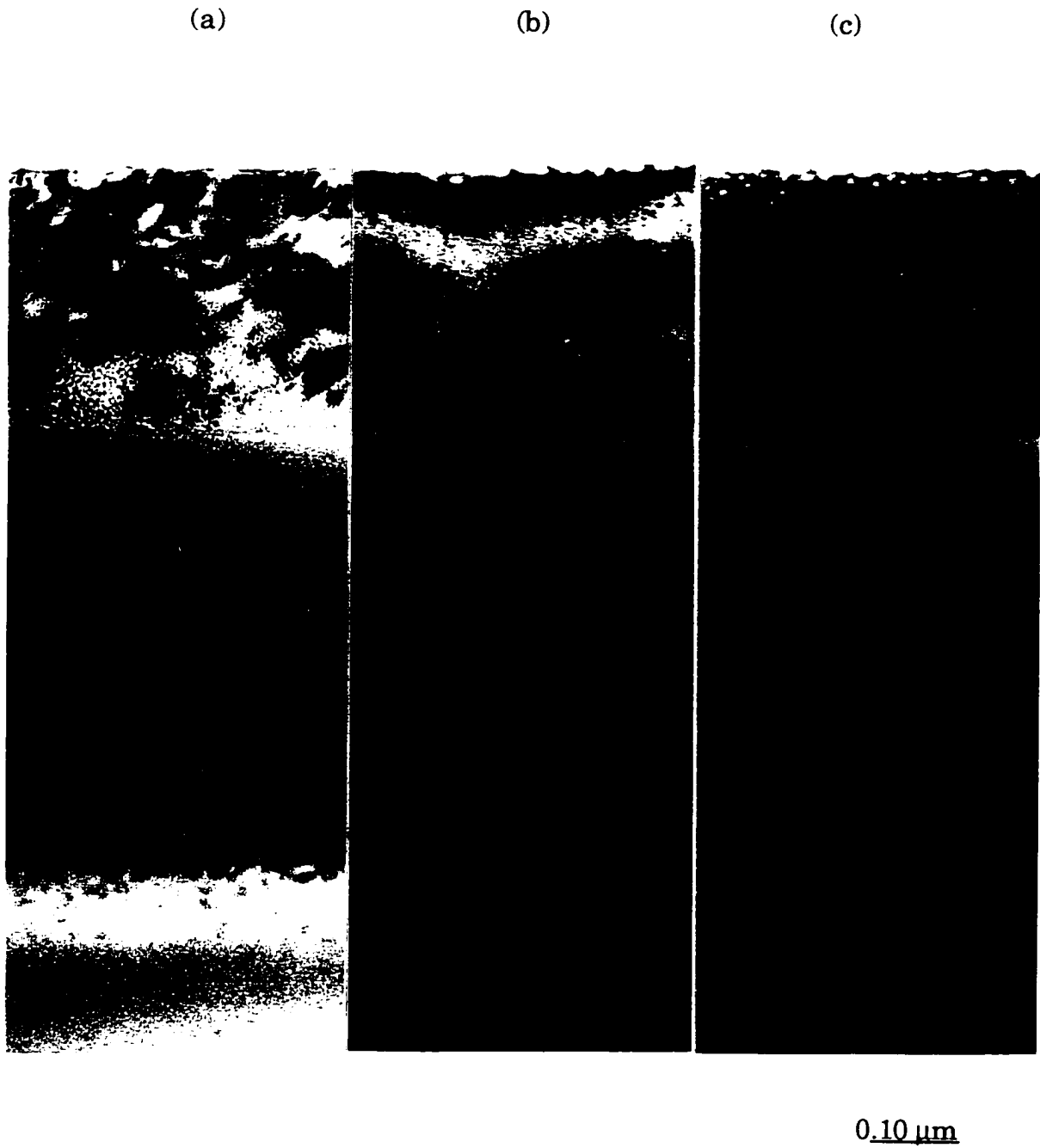


Figure 3.19. XTEM micrographs of samples in as-implanted condition after implantation at 175 keV to a dose of $1.4 \times 10^{18} \text{ cm}^{-2}$ showing effect of substrate temperature variation.
a) 540°C; b) 590°C; c) 640°C.

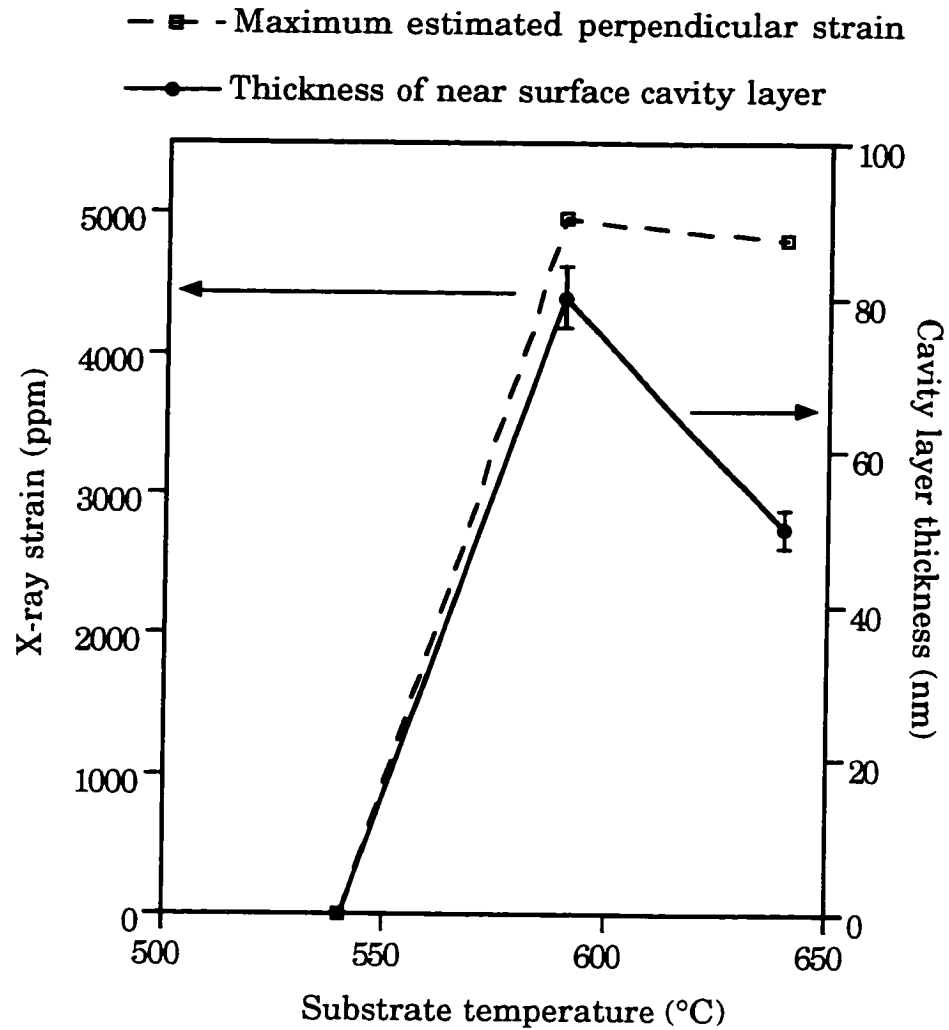


Figure 3.20. Cavity layer thickness and x-ray strain variation as a function of substrate temperature, for as-implanted samples after implantation at 175 keV to a dose of $1.4 \times 10^{18} \text{ cm}^{-2}$.

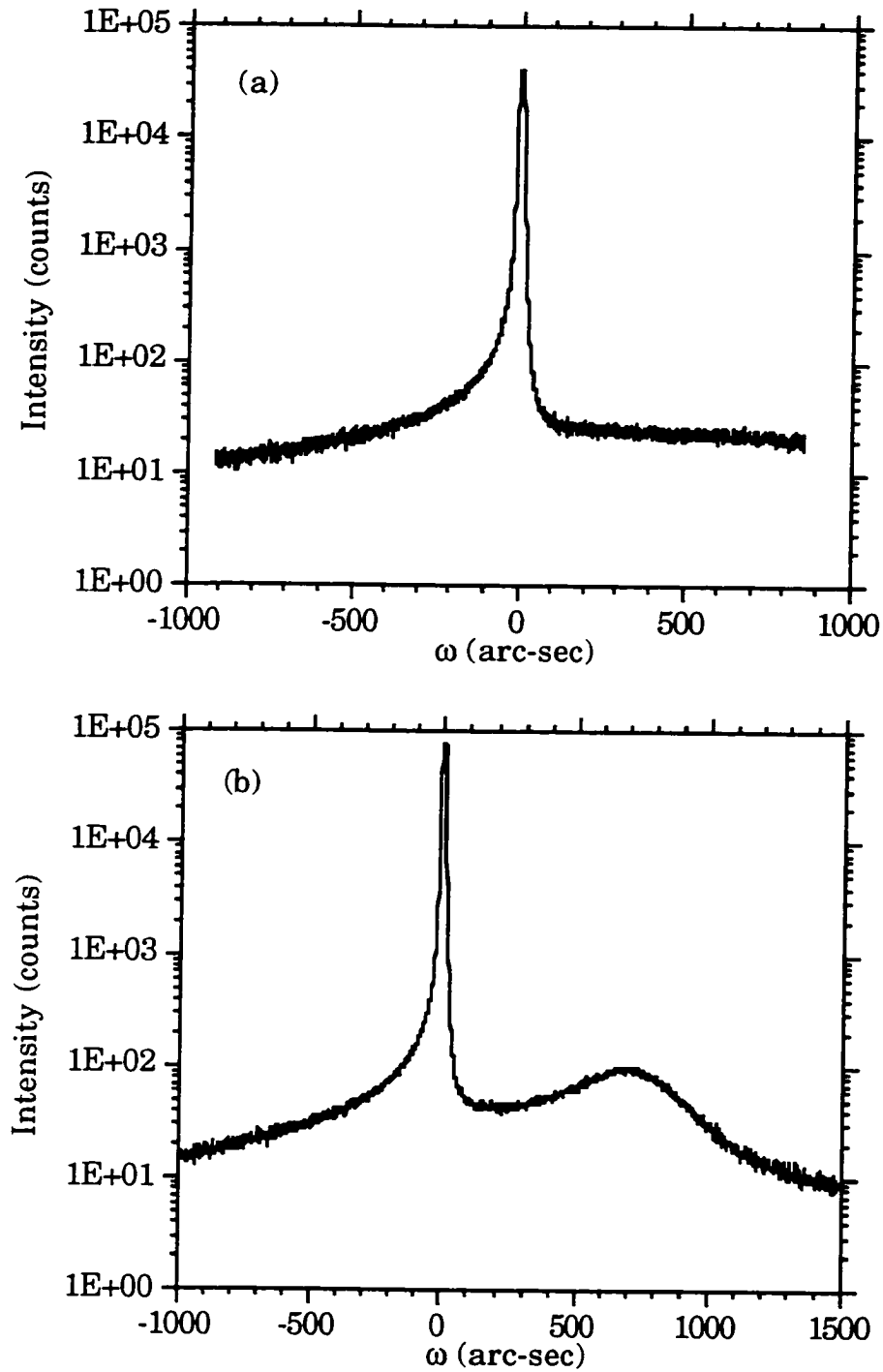


Figure 3.21. X-ray rocking curves about the (004) reflection for samples in as-implanted condition after implantation at 175 keV at a dose of $1.4 \times 10^{18} \text{ cm}^{-2}$ for different substrate temperatures. a) 540°C; b) 590°C;

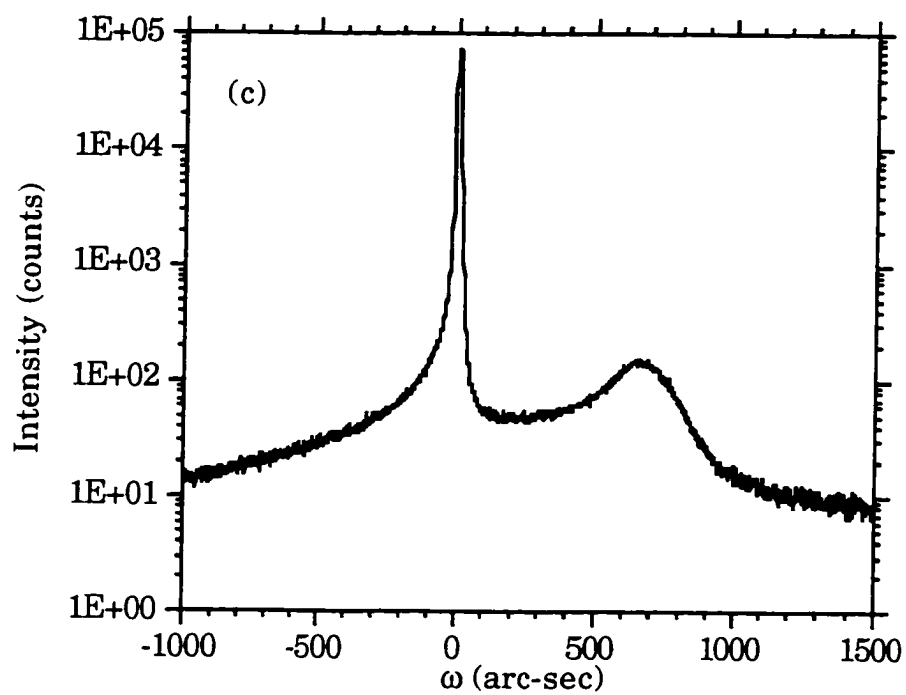


Figure 3.21 -- continued
c) 640°C.

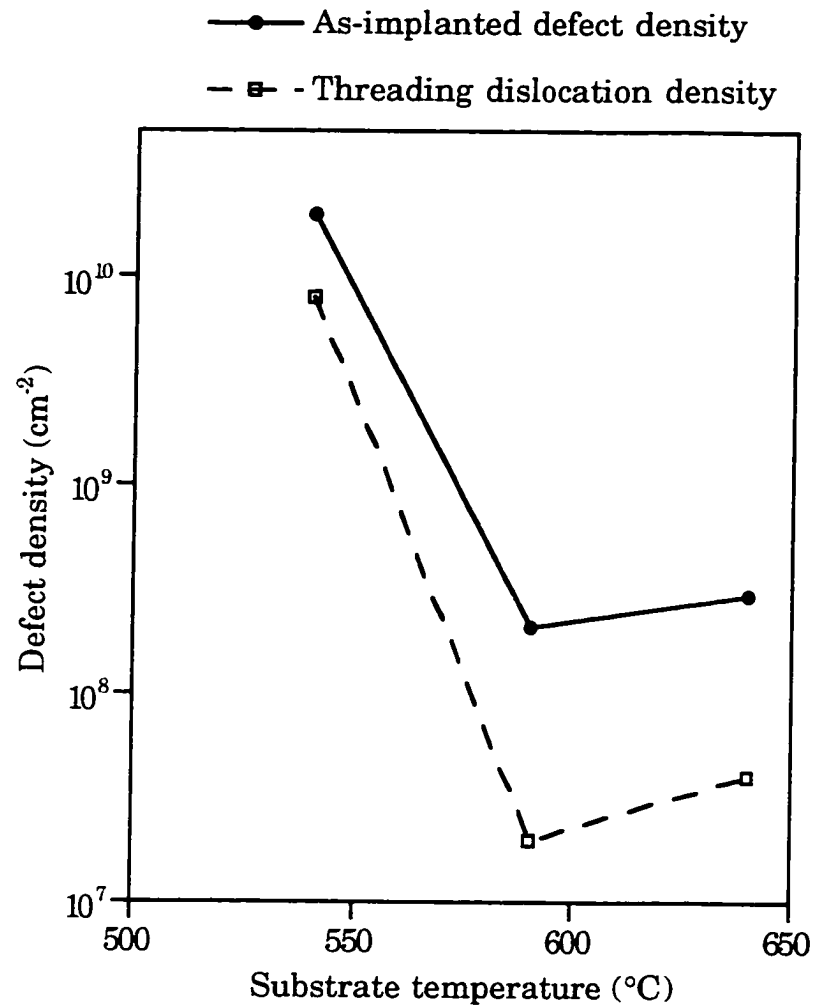


Figure 3.22. Defect density in the silicon overlayer in as-implanted and annealed samples as a function of substrate temperature. Note that the as-implanted defects are stacking faults at 540°C, and dislocation half loops at 590°C and 640°C.

Large stacking faults on {111} planes, of lengths of 180 nm, are also present near the Si overlayer/buried oxide interface. For the 590°C implant the majority of the stacking faults (multiply faulted defects) occur within a depth of 170 nm and 300 nm from the surface. Dislocation half loops occur in the near surface region and their density from PTEM analysis was found to be $2.1 \times 10^8 \text{ cm}^{-2}$. Burgers vector analysis showed that these dislocation half loops were present on all 6 {110} planes. Extensive tilting experiments were performed to ascertain the density of the half loops with Burgers vectors at an angle to the surface to those with Burgers vectors parallel to the surface, and it was found to be $1.1 \times 10^8 \text{ cm}^{-2}$ and $1 \times 10^8 \text{ cm}^{-2}$, respectively.

For the 640°C implant, stacking faults appeared at a distance of 120 nm from the surface and extended to a depth of 300 nm from the surface. PTEM studies revealed that the dislocation half loop density was $2.9 \times 10^8 \text{ cm}^{-2}$. Tilting experiments revealed that the density of half loops with Burgers vectors at an angle to the surface to those with Burgers vectors parallel to the surface was $1.4 \times 10^8 \text{ cm}^{-2}$ and $1.5 \times 10^8 \text{ cm}^{-2}$, respectively.

From the rocking curves (Figure 3.21) it is apparent that the peak for the 590°C implant is broader than that for the 640°C implant. This could be due either to more extended defects being present in the strained layer or because of the increased depth of the strained layer in the 590°C implant. PTEM results, (Figure 3.22), show that there is only a small difference in defect densities for the 590°C implant in comparison to the 640°C implant. Moreover, the depth of the stacking faults from the surface in the 590°C implant sample is deeper than for the 640°C implant. Further, the cavity layer is deeper for the 590°C implant than for the 640°C. This implies that the broadening of the Bragg peak is possibly a consequence of the thicker

strained layer and higher strain value near the surface due to the presence of cavities.

Buried oxide. A continuous stoichiometric buried oxide layer forms at this dose having a thickness of 240 nm. Near the top buried oxide and Si overlayer interface there are an enormous number of SiO₂ precipitates and stacking faults, while near the lower buried oxide/Si substrate interface SiO₂ precipitates are present. At a distance of about 200 nm from this back interface a large number of {113} defects are present within a width of 160 nm to 200 nm. There is no apparent variation of the buried oxide thickness with change in substrate temperature.

Annealed microstructure

Defects in the silicon overlayer. PTEM analysis showed that threading dislocations were the only defects present in the annealed state. The final defect density for the sample implanted at 540°C was $8 \times 10^9 \text{ cm}^{-2}$. The threading dislocations did not occur in pairs. For the 590°C implant the final threading dislocation density was $3 \times 10^7 \text{ cm}^{-2}$ while for the 640°C implant the final threading dislocation density was $4 \times 10^7 \text{ cm}^{-2}$. These defect densities are summarized in Figure 3.22. Threading dislocations for the implants at 590°C and 640°C were paired and Burgers vector analysis showed that they had evolved from half loops with Burgers vectors parallel to the surface. From this analysis it was apparent that an optimum temperature of implant exists for which there is a minimum threading dislocation density in the final annealed state.

Buried oxide. XTEM images of the annealed samples are shown in Figure 3.23. The buried oxide thickness or the silicon overlayer thickness did not vary significantly with the change in implant temperature. Si islands were present near the back interface of the buried oxide. It is



Figure 3.23. XTEM micrographs of samples in annealed condition after implantation at 175 keV to a dose of $1.4 \times 10^{18} \text{ cm}^{-2}$ showing effect of substrate temperature variation. a) 540°C; b) 590°C; c) 640°C.

apparent that the size of the Si islands vary. It was found that the size of the Si islands increased with the decrease in substrate temperature.

Substoichiometric Dose Implants

The effect of varying the substrate temperature at a dose of $0.4 \times 10^{18} \text{ cm}^{-2}$ was investigated. In this experiment implants were performed at 175 keV, at a beam current density of 3.0 mA/cm^2 for substrate temperatures of 490°C , 520°C , 550°C , and 580°C . Both as-implanted and annealed microstructures were studied. The anneals were performed at 1310°C for 5 hours in an $\text{Ar}+0.5\%\text{O}_2$ ambient.

As-implanted microstructure

Cavities and near surface strain. XTEM images, Figure 3.24, showed that cavities were present in the near surface region for all the temperatures. There was a decrease in the cavity layer thickness with the increase in substrate temperature, Figure 3.25. No distinct variation in the cavity diameter was observable with the changes in temperature. Moreover, no prominent variation of the size of cavities with depth was perceptible. Since cavities in the near surface region have been shown [27] to induce strain, HRXRD studies were performed to analyze the variation in strain with changes in substrate temperature.

The (004) rocking curves for all the implants are shown in Figure 3.26. They show the following similarities. A prominent Bragg peak was present at an angle higher than the substrate peak indicating the presence of a near surface strained layer. The existence of this peak at an angle higher than the substrate peak shows that the lattice in this region is contracted with respect to the substrate. The strained peak was asymmetric indicating that the strain was non uniform. It was found that the maximum strain decreased with the increase in substrate temperature

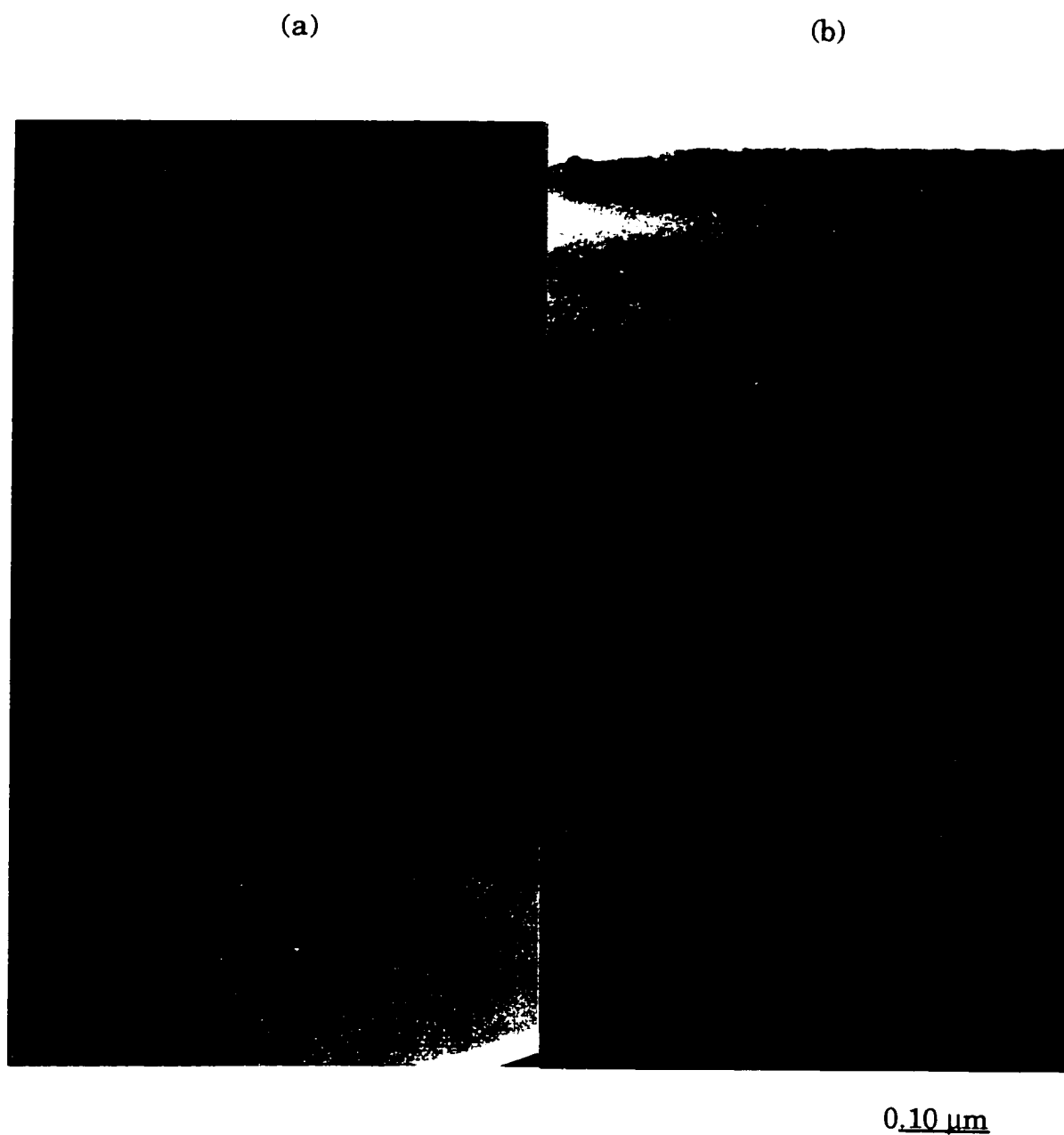


Figure 3.24. XTEM micrographs of samples in as-implanted condition after implantation at 175 keV to a dose of $0.4 \times 10^{18} \text{ cm}^{-2}$ showing effect of substrate temperature variation.
a) 490°C; b) 520°C;

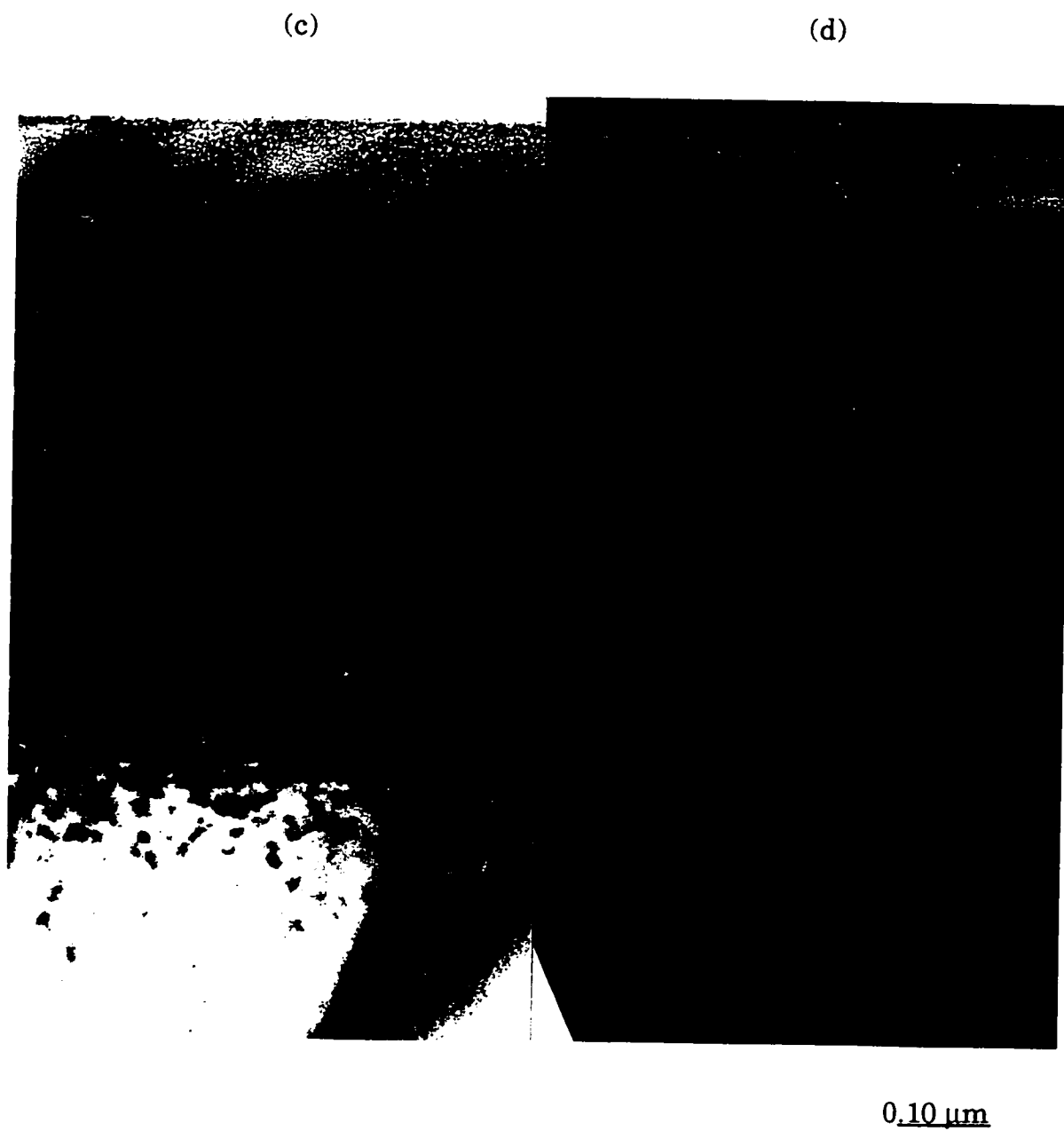


Figure 3.24. -- continued
c) 550°C; d) 580°C;

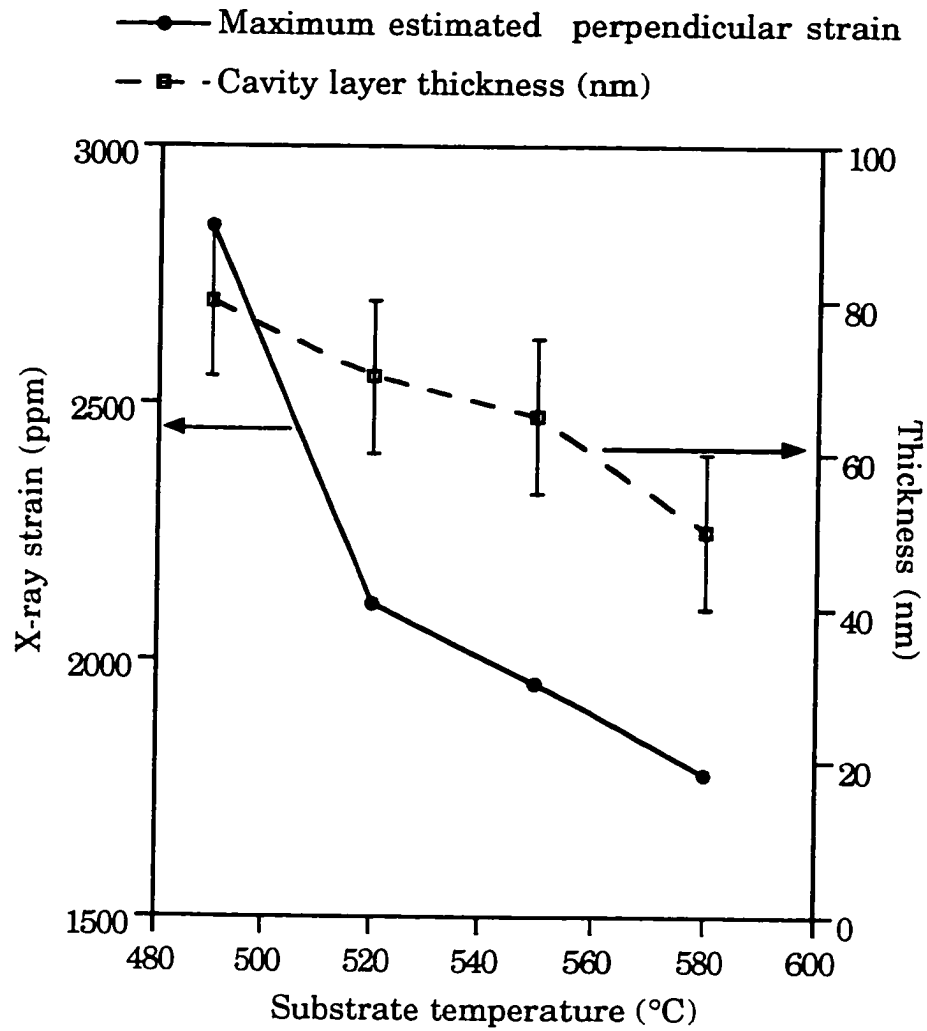


Figure 3.25. Cavity layer thickness and x-ray strain variation as a function of substrate temperature for as-implanted samples after implantation at 175 keV to a dose of $0.4 \times 10^{18} \text{ cm}^{-2}$.

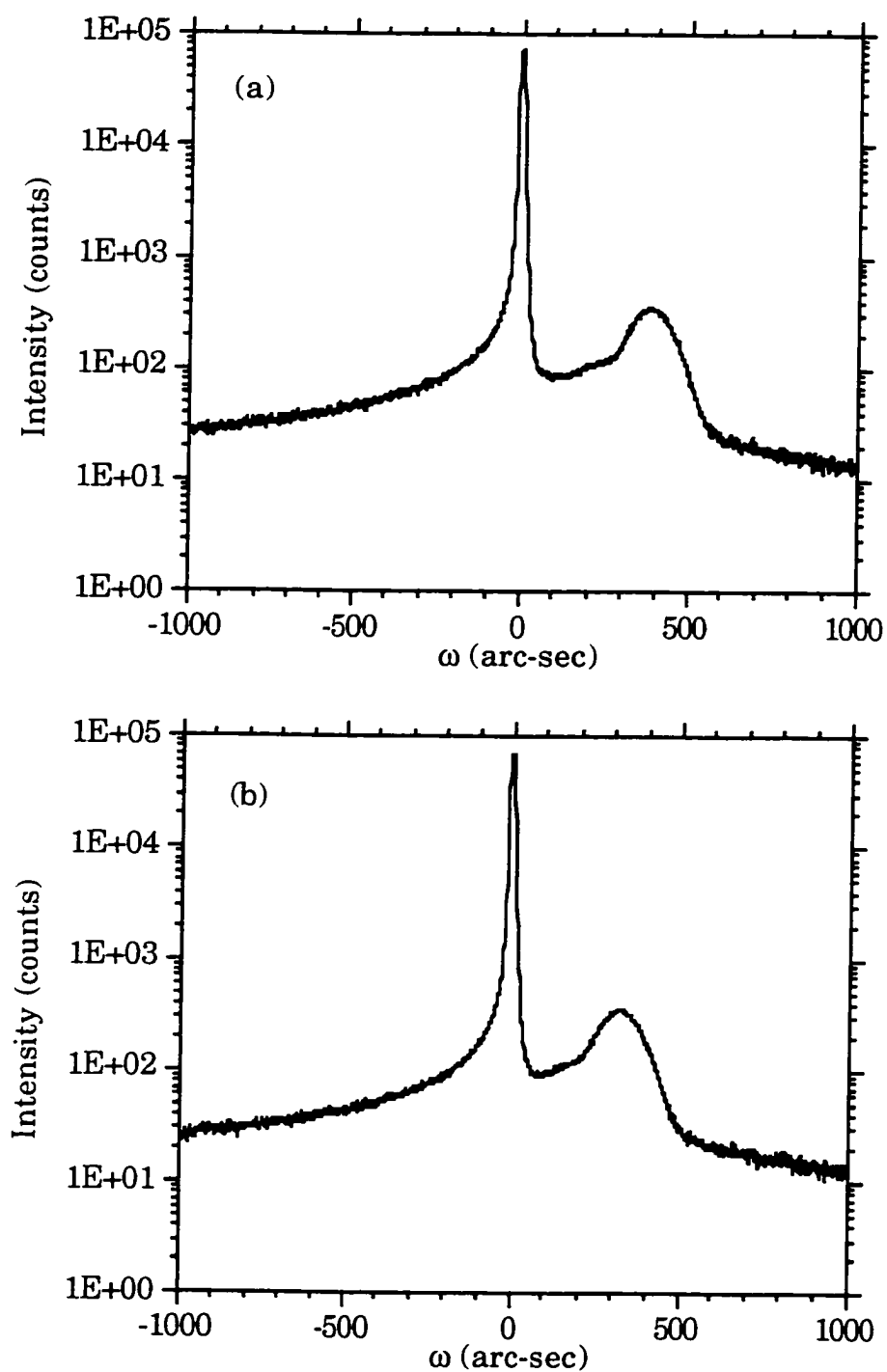


Figure 3.26. X-ray rocking curves about the (004) reflection for samples in as-implanted condition after implantation at 175 keV at a dose of $0.4 \times 10^{18} \text{ cm}^{-2}$ for different substrate temperatures. a) 490°C ; b) 520°C ;

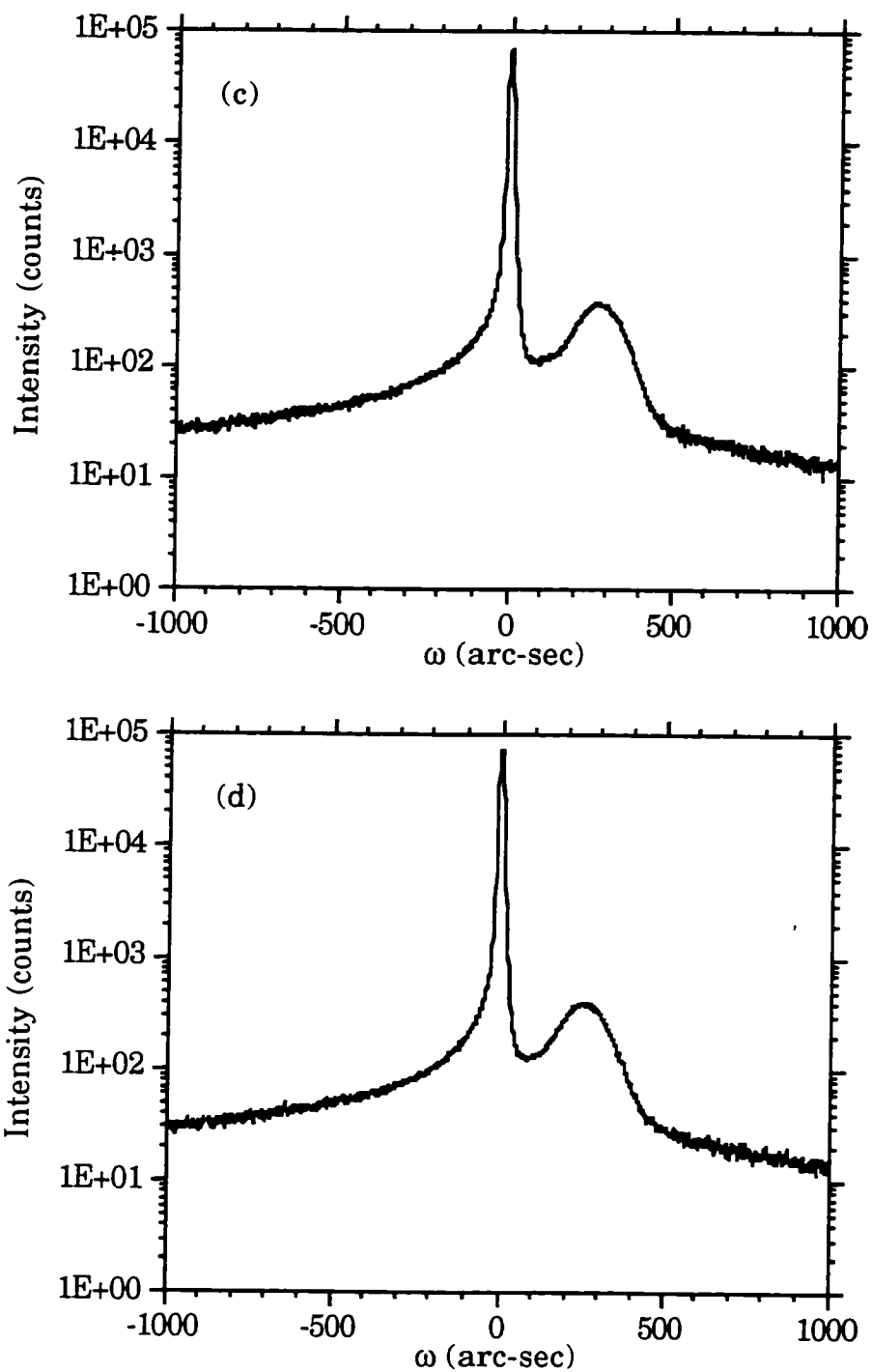


Figure 3.26 -- continued
c) 550°C; d) 580°C;

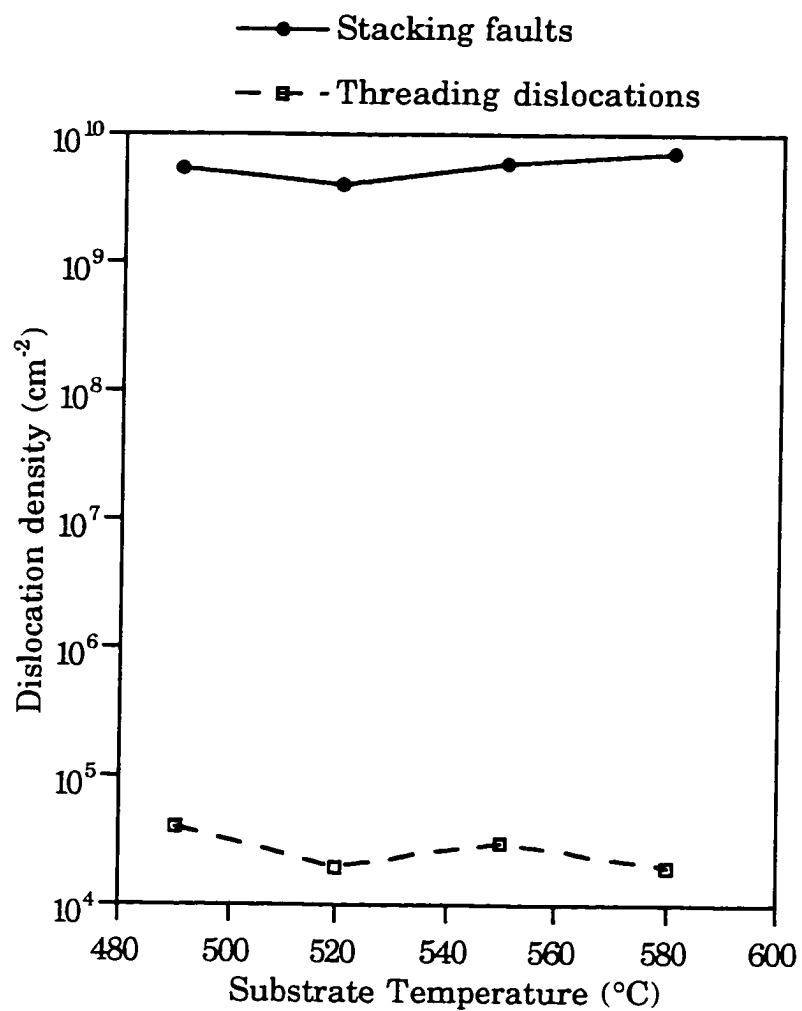


Figure 3.27. Defect densities in the silicon overlayer for as-implanted and annealed samples as a function of substrate temperature after implantation at 175 keV to a dose of $0.4 \times 10^{18} \text{ cm}^{-2}$.

from a value of -2842 ppm for the implant at 490°C to a value of -1776 ppm for the implant at 580°C. These results are shown in Figure 3.25.

Near surface defects. PTEM analysis showed that the dominant defects, for all the implants were stacking faults and no dislocation half loops were detected. From the XTEM images it was found that these defects were situated at a depth of 200 nm from the surface. The average size of these stacking faults ranged from 40 nm to 120 nm and they were situated on {111} planes.

The defect density with change in implant temperature is shown in Figure 3.27. There was no significant variation with the substrate temperature.

Buried oxide. Analysis of the XTEM images for all the samples showed that there was no apparent difference in the buried oxide microstructure. No continuous buried oxide was formed at this dose and temperatures.

Annealed microstructure

Defects in the silicon overlayer. Secco etch results for all the four temperatures showed that the defect densities were of the order of 10^4 cm^{-2} . There was no significant variation in these defect densities as a function of substrate temperature.

Buried oxide. XTEM images of the annealed structure are shown in Figure 3.28. Except for slight variations at the interfaces the buried oxides appeared to be the same. No Si islands were evident in any of the buried oxide structures. The average thickness of the buried oxide was about 110 nm. However, the buried oxide at the 490°C implant appeared to have a varying thickness in comparison to the buried oxide thickness observed at the higher temperatures.

(a)

(b)

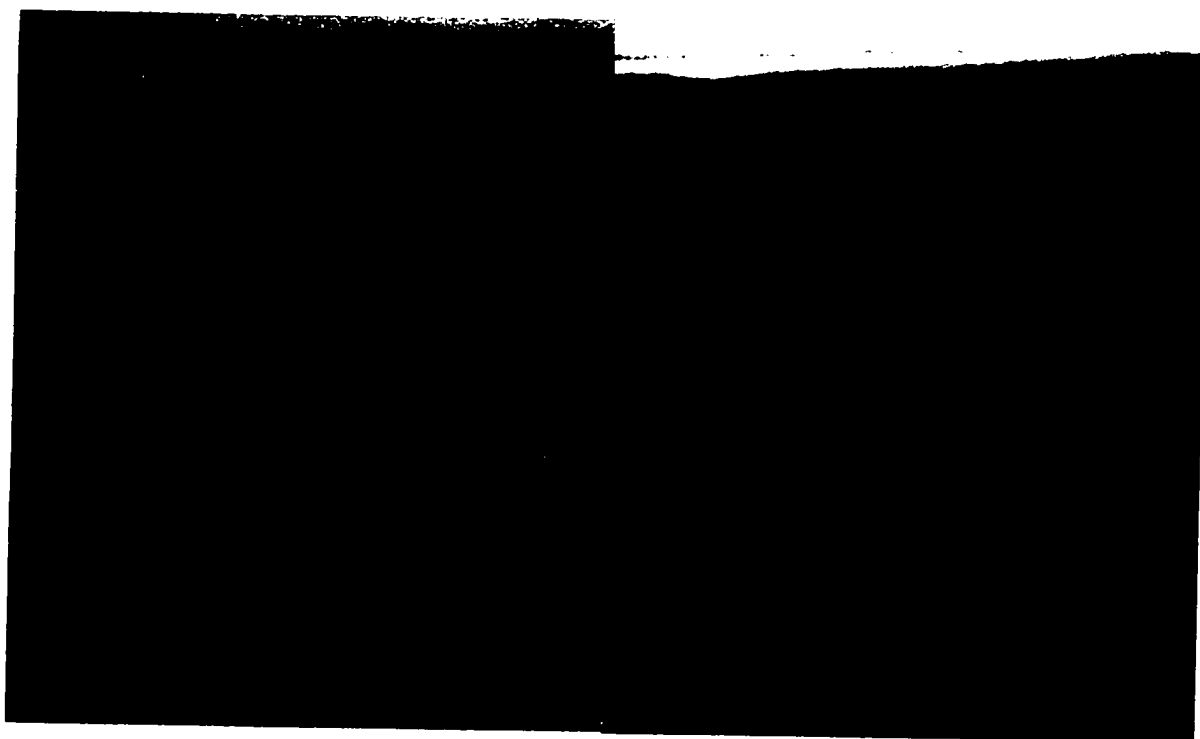
0.10 μm

Figure 3.28. XTEM micrographs of samples in annealed condition after implantation at 175 keV to a dose of $0.4 \times 10^{18} \text{ cm}^{-2}$ showing effect of substrate temperature variation.
a) 490°C; b) 520°C;

(c)

(d)

0.10 μm

Figure 3.28. -- continued
c) 550°C; d) 580°C;

Summary of Results

Variation of substrate temperature for stoichiometric doses showed, that implants performed at low substrate temperatures resulted in a high density of defects ($\sim 2 \times 10^{10} \text{ cm}^{-2}$) in the as-implanted state, with no near surface strained layer. Post implantation annealing was not efficient in removing these defects, leaving behind a high final threading dislocation density of ($\sim 8 \times 10^9 \text{ cm}^{-2}$) in the silicon overlayer. However, higher temperature implants resulted in lower density of defects and a near surface strain layer. Consequently, the final threading dislocation densities were lower for these temperatures. The substrate temperatures did not affect the buried oxide microstructure significantly.

For substoichiometric doses, variation of the substrate temperature did not significantly affect the defect microstructure, though the near surface strain decreased with the increase in substrate temperature. Post implantation annealing showed that there was no apparent difference in the silicon overlayer or the buried oxide microstructures.

Beam Current

Previous efforts to study the effect of varying the beam current on the evolution of the SIMOX microstructure were not performed efficiently since no means of controlling the beam current independent of the other implant parameters was possible. Using high beam currents a study done previously [29] shows that no change in the SIMOX microstructure is perceptible even when the beam current was varied by an order of magnitude. Again this could have been a result of the inability to control the beam control without altering other implant parameters.

To investigate the effect of beam current variation, keeping all other implant conditions constant, the following experiment was performed. The

implant energy used was 175 keV, at a substrate temperature of 590°C, at a dose of $1.4 \times 10^{18} \text{ cm}^{-2}$ for beam currents of 3.0, 3.7 and 4.3 mA/cm². All the anneals were performed at 1310°C for 5 hours in an Ar + 0.5% O₂ ambient. A detailed analysis of the microstructure is given in the next few sections.

As-Implanted Microstructure

Cavities and near surface strain

The XTEM images in Figure 3.29 show that cavities are present in the Si overlayer near the surface for all three beam currents. The cavity layer thickness decreases with the increase in beam current and this trend is shown in the graph in Figure 3.30. To estimate the maximum strain induced in the near surface region HRXRD analysis was performed.

All the three (004) rocking curves shown in Figure 3.31 showed a prominent Bragg peak at an angle higher than the substrate peak indicating that the lattice in this region had contracted. The strain was non uniform since the strain layer peak was asymmetric. The maximum estimated strain was found to decrease with increase in beam current (Figure 3.30).

Near surface defects

PTEM analysis showed that in the near surface region dislocation half loops occurred in association with the cavities. For the sample implanted with a beam current of 3.0 mA/cm², the half loop density was found to be $1.74 \times 10^8 \text{ cm}^{-2}$. Burgers vector analysis showed that the density of half loops which had Burgers vectors at angle to the surface to those with Burgers vectors parallel to the surface were $1.1 \times 10^8 \text{ cm}^{-2}$ and $6.4 \times 10^7 \text{ cm}^{-2}$, respectively.

The half loop density for the sample implanted with a beam current of 3.7 mA/cm² was found from PTEM studies to be $2.1 \times 10^8 \text{ cm}^{-2}$. Tilting

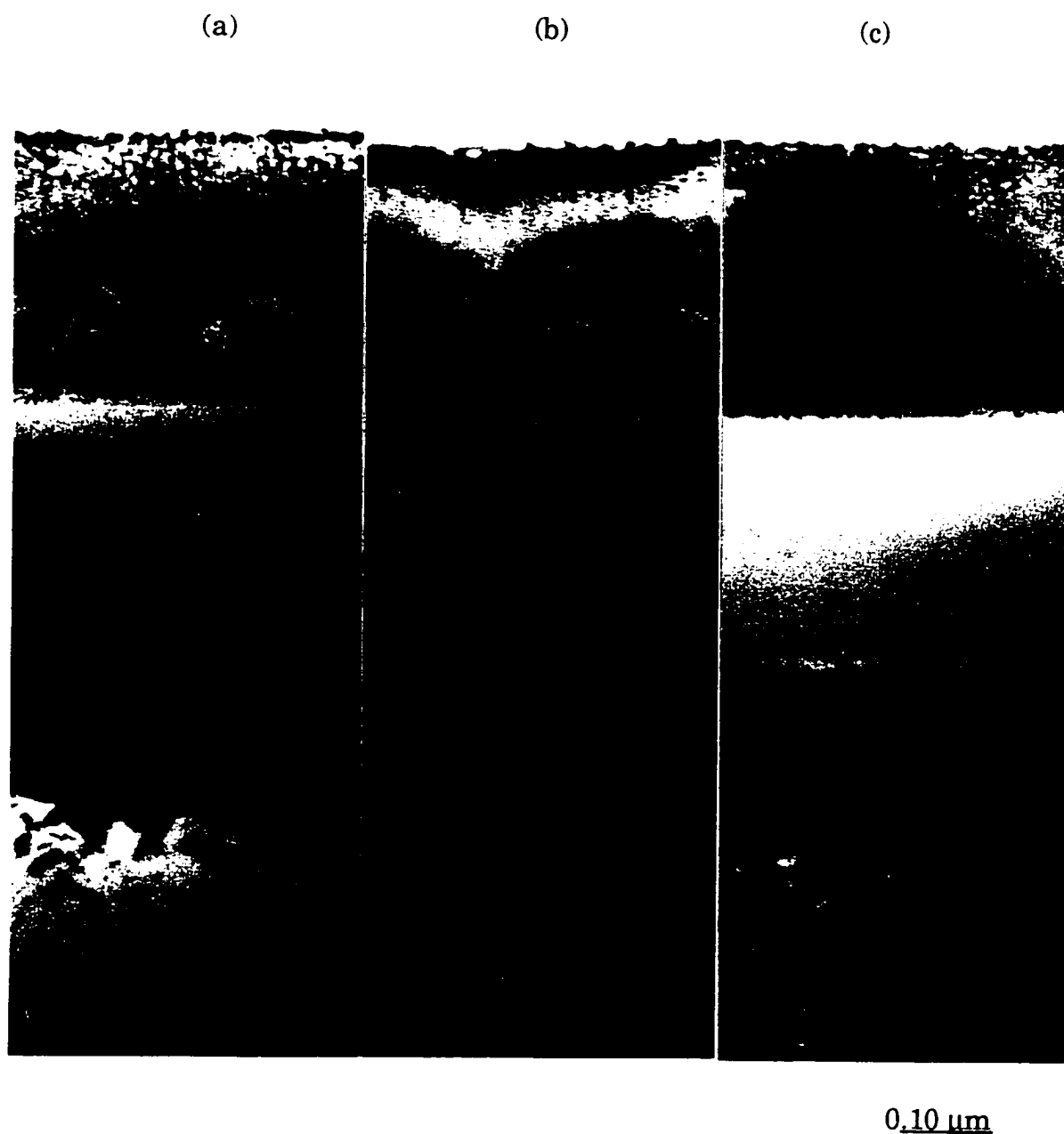


Figure 3.29. XTEM micrographs of samples in as-implanted condition after implantation at 175 keV to a dose of $1.4 \times 10^{18} \text{ cm}^{-2}$ showing effect of beam current variation.
a) 3.0 mA/cm^2 ; b) 3.7 mA/cm^2 ; c) 4.3 mA/cm^2 .

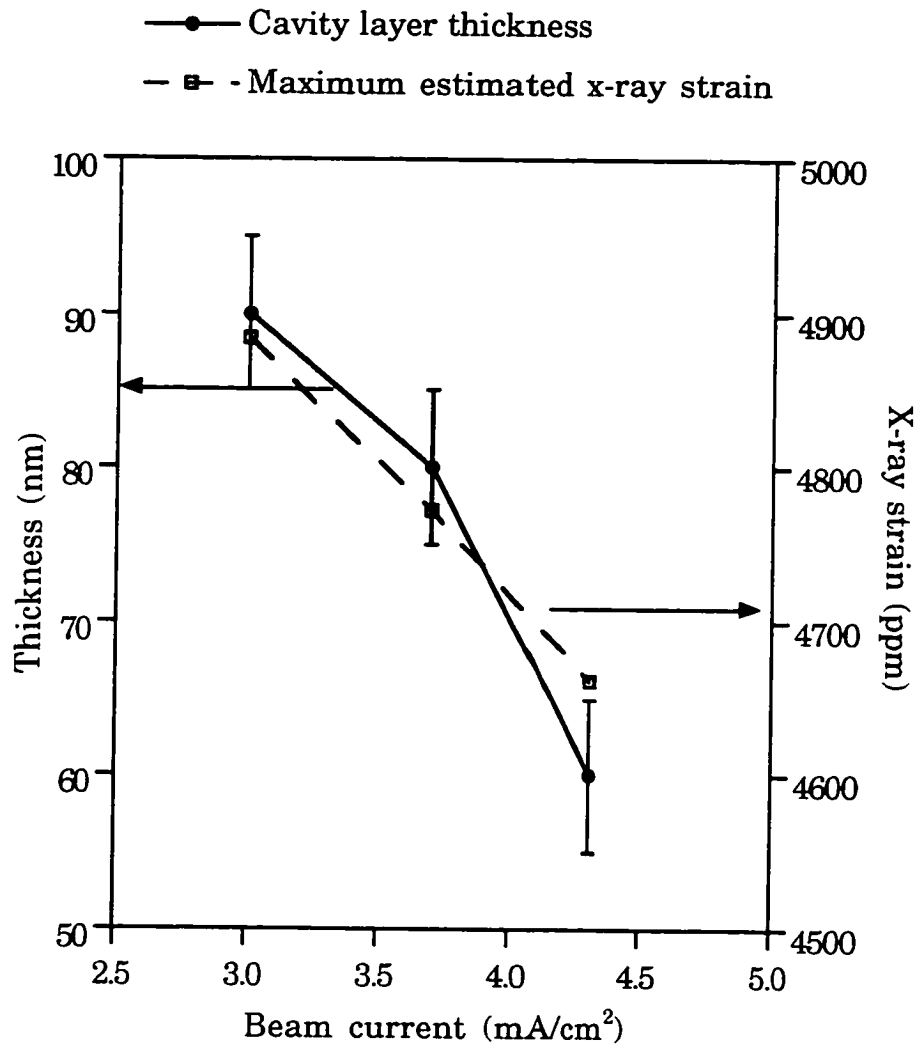


Figure 3.30. Cavity layer thickness and x-ray strain variation as a function of beam current for as-implanted samples after implantation at 175 keV to a dose of $1.4 \times 10^{18} \text{ cm}^{-2}$.

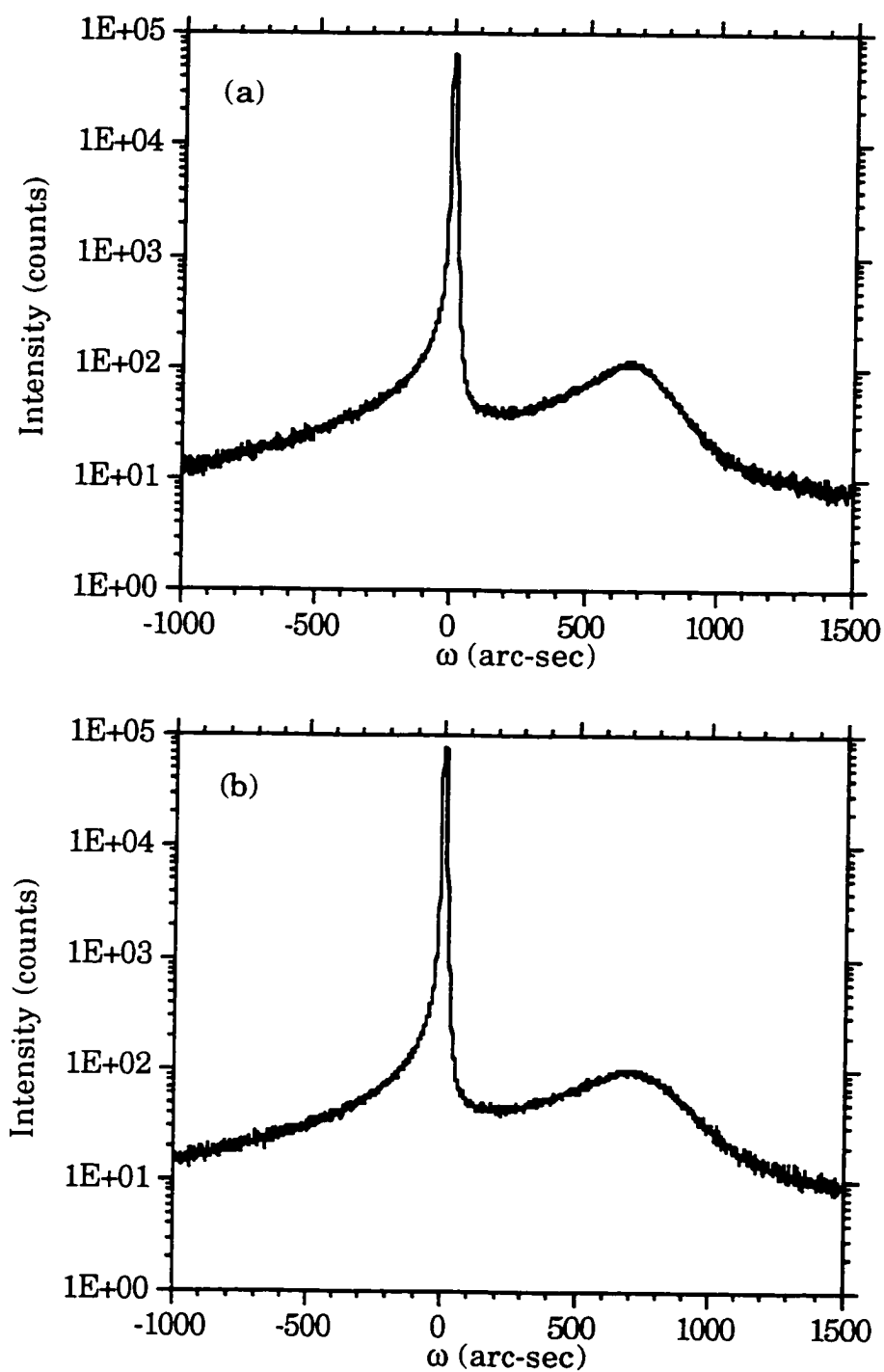


Figure 3.31. X-ray rocking curves about the (004) reflection for samples in as-implanted condition after implantation at 175 keV at a dose of $1.4 \times 10^{18} \text{ cm}^{-2}$ for different beam currents. a) 3.0 mA/cm^2 ; b) 3.7 mA/cm^2 ;

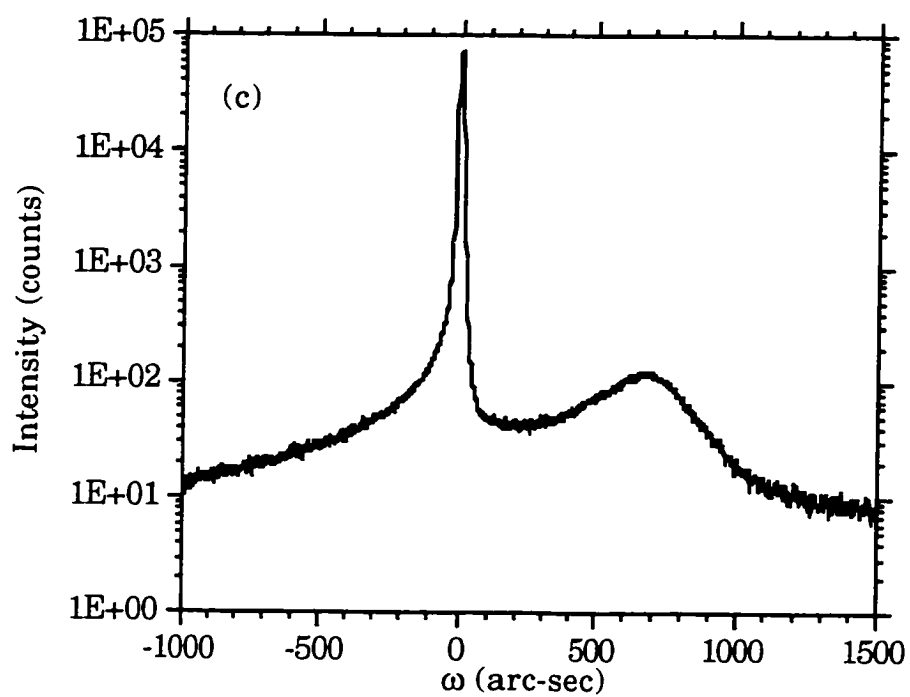


Figure 3.31 -- continued
c) 4.3 mA/cm^2 .

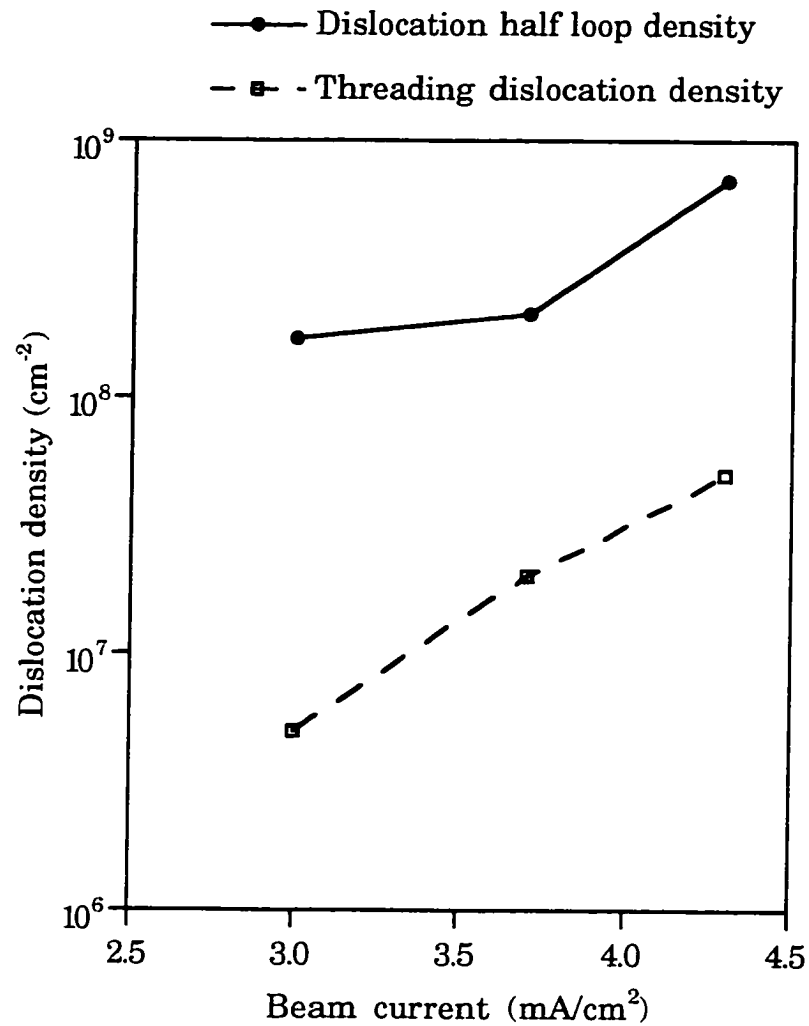


Figure 3.32. Defect densities in the silicon overlayer in the as-implanted and annealed states as a function of beam current after implantation at 175 keV at a dose of $1.4 \times 10^{18} \text{ cm}^{-2}$.

experiments were performed to evaluate the Burgers vectors of these half loops and it was found that the density of dislocation half loops with Burgers vectors at an angle to the surface to those with Burgers vectors parallel to the surface was $1.1 \times 10^8 \text{ cm}^{-2}$ and $1.0 \times 10^8 \text{ cm}^{-2}$, respectively.

The sample implanted with a beam current of 4.3 mA/cm^2 showed a dislocation half loop density of $7 \times 10^8 \text{ cm}^{-2}$, from PTEM analysis. The density of half loops with Burgers vectors angled to the surface and those with Burgers vectors parallel to the surface was found to be $3 \times 10^8 \text{ cm}^{-2}$ and $4 \times 10^8 \text{ cm}^{-2}$, respectively. These defect densities are shown in Figure 3.32.

Multiply faulted defects were present at the vicinity of the Si overlayer and buried oxide layer interface. XTEM images showed that these defects were situated at a distance of about 140 nm from the surface. There was no significant variation in the depth of this layer from the surface with change in the beam current.

Buried oxide

A continuous buried oxide formed at a depth of 300 nm from the silicon surface. The width of the buried oxide layer was found to be 280 nm. No significant change in the buried oxide was evident with the variation of beam current.

Annealed Microstructure

Defects in the silicon overlayer

The defects found in the annealed state were found to be threading dislocations and they occurred in pairs. The defect densities are shown in Figure 3.32. It was found that the sample implanted with the lowest beam current of 3.0 mA/cm^2 had the lowest threading dislocation density of $7 \times 10^6 \text{ cm}^{-2}$. For the samples implanted at beam currents of 3.7 mA/cm^2 and 4.3 mA/cm^2 the threading dislocation density was found to be $3 \times 10^7 \text{ cm}^{-2}$ and

$6 \times 10^7 \text{ cm}^{-2}$ respectively. Extensive tilting experiments were performed and it was found that these defects had Burgers vectors resembling dislocation half loops with Burgers vectors parallel to the surface.

Buried oxide

A continuous buried oxide formed after annealing at a distance of 200 nm from the surface. The thickness of the buried oxide was 360 nm. Si islands were present near the bottom of the buried oxide, 310 nm from the top of the buried oxide layer. No distinct variation in the buried oxide thickness or Si island density or morphology was evident with the change in beam current.

Summary of Results

In the as-implanted state, the defect density increased while the near surface strain decreased with increase in beam current. Consequently, higher threading dislocation densities resulted from samples implanted at higher beam currents. However, no affect of beam current variation on the buried oxide microstructure was apparent.

Discussion and Conclusions

Independent variation of implantation parameters extended our understanding of the effects these parameters have on the evolution of the microstructure in single implant SIMOX. In this section these results have been used to suggest possible mechanisms which control the development of the microstructure. Since the final quality of the SIMOX structure is determined by the silicon overlayer and the buried oxide microstructures, both of these have been treated below.

From the experimental results, it can be concluded that a window exists within the dose range of $0.4 \times 10^{18} \text{ cm}^{-2}$ and $1.0 \times 10^{18} \text{ cm}^{-2}$ for an implant energy of 175 keV, in which the final threading dislocation density

is extremely low ($\sim 10^4 \text{ cm}^{-2}$ to 10^3 cm^{-2}). However, for a higher implant energy of 200 keV, this window for low final threading dislocation density shifts to a higher dose, and lies between $0.5 \times 10^{18} \text{ cm}^{-2}$ and $1.0 \times 10^{18} \text{ cm}^{-2}$.

Coupling the excellent silicon overlayer microstructure to the buried oxide microstructure shrinks this dose window severely. For an implant energy of 175 keV, device quality buried oxide is obtained only for doses of $0.4 \times 10^{18} \text{ cm}^{-2}$ and $1.4 \times 10^{18} \text{ cm}^{-2}$. On the other hand, within the doses studied, only a dose of $1.4 \times 10^{18} \text{ cm}^{-2}$ resulted in device quality buried oxide at an implant energy of 200 keV. However, at doses of $1.4 \times 10^{18} \text{ cm}^{-2}$, the final threading dislocation density in the silicon overlayer is high for both implant energies ($\sim 10^6 \text{ cm}^{-2}$). It is evident that to widen the processing window, it is critical to improve the quality of the buried oxide. For this purpose a better understanding of the buried oxide microstructure is needed.

Substrate temperature and beam current play an important role in determining the quality of the silicon overlayer at stoichiometric doses i.e. $1.4 \times 10^{18} \text{ cm}^{-2}$. Improved quality SIMOX was obtained using an optimum temperature of 590°C and low beam currents. Thus for stoichiometric doses the processing window is rather restricted by parameters which control the quality of the silicon overlayer. A slight improvement in the silicon overlayer quality was obtained by using higher implant energies. Larger variations in implant energy have been observed [85] to affect the final defect density significantly. It has been found [85] that decreasing the energy increases the final threading dislocation density. This was not the effect of increased energy produced for the substoichiometric dose of $0.4 \times 10^{18} \text{ cm}^{-2}$, which resulted in a banded precipitate structure instead of a continuous buried oxide.

Substrate temperature variation at the substoichiometric dose of $0.4 \times 10^{18} \text{ cm}^{-2}$ did not induce Si islands within the buried oxide or increase the final threading dislocation density in the silicon overlayer. However, the interface quality appeared to deteriorate slightly with decrease in substrate temperature. On the other hand, increasing the implant energy to 200 keV resulted in a banded structure for this dose. This implied that, even though the window allowed for the variation of substrate temperature is larger than the stoichiometric case, variation of the implant energy is rather restricted.

Thus, based on the experimental observations, a response surface of the microstructural behavior of the silicon overlayer and buried oxide, with implantation parameters can be developed. These are shown schematically in Figure 3.33. Examining the behaviors with respect to the implant dose it is apparent from this figure that variation of implantation conditions affect stoichiometric and substoichiometric doses quite differently.

For substoichiometric doses i.e. doses lower than $1.0 \times 10^{18} \text{ cm}^{-2}$, an increase in energy would result in poorer quality of the silicon overlayer, at the lowest doses, if a continuous buried oxide does not form. Substrate temperature however, does not have a significant effect on the defect microstructure. In cases where a continuous buried oxide is formed, formation of Si islands is a strong function of dose. The quality of the interface is slightly affected by changes in the substrate temperature.

For stoichiometric doses, i.e., doses higher than $1.0 \times 10^{18} \text{ cm}^{-2}$ (which is dependent on the implant energy), the silicon overlayer quality is affected strongly by changes in substrate temperature, beam current, dose and only slightly by energy. High substrate temperatures of $\sim 600^\circ\text{C}$, low beam currents, and higher energies yield an improved quality silicon overlayer

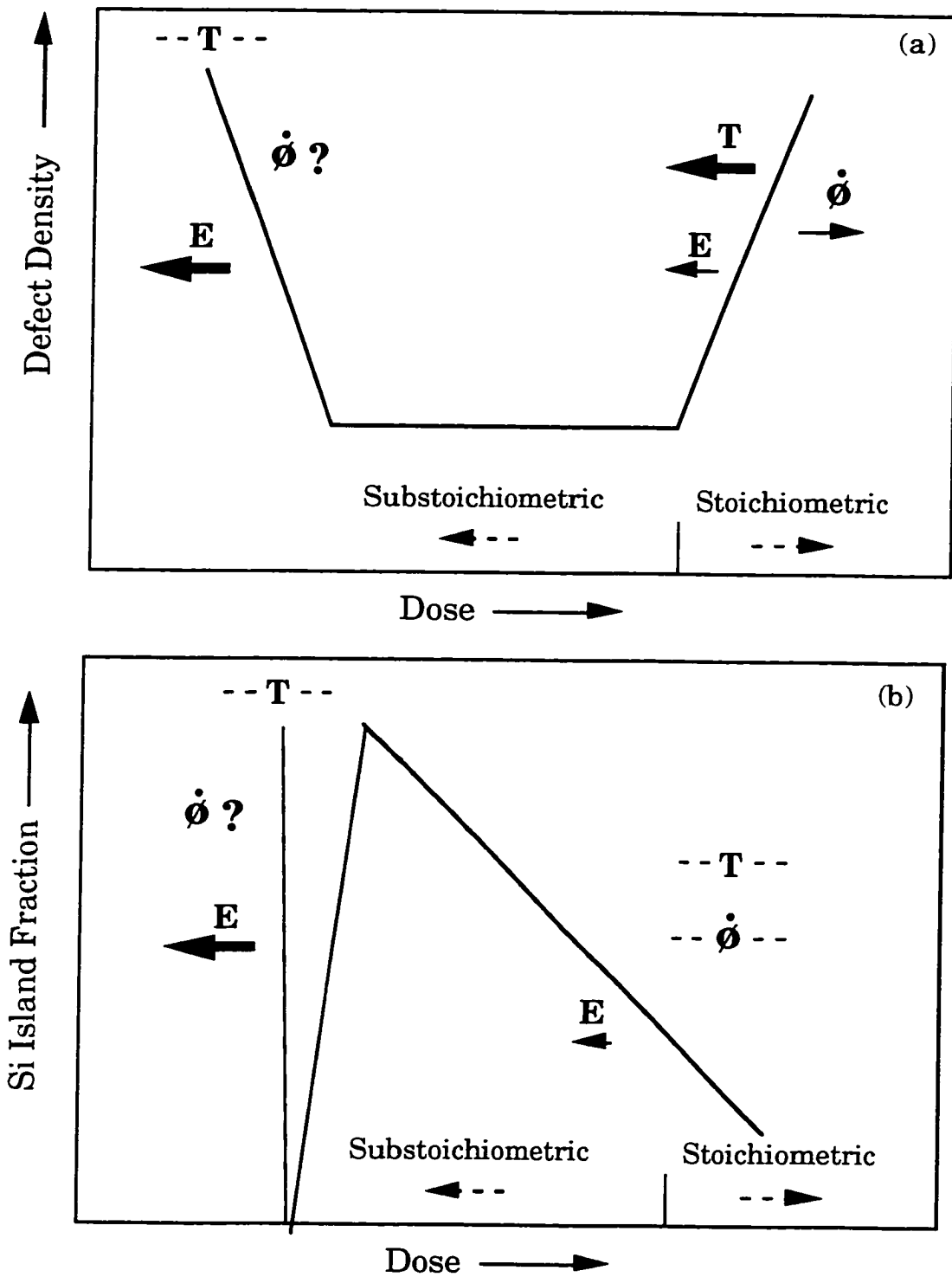


Figure 3.33. Schematic representation of the effect of implantation parameters (E =energy, T =substrate temperature, ϕ =dose rate) on microstructural evolution. The arrows indicate the effect of decreasing the indicated parameters.
 a) silicon overlayer quality; b) buried oxide quality

structure. However, increased dose deteriorates the silicon overlayer quality.

In order to understand the causes behind these processing condition effects, it is necessary to improve our present understanding about the physical mechanisms governing the quality of the silicon overlayer and buried oxide microstructures. This is the aim of the next part of the discussion.

Defect Evolution

It was discussed earlier [27], that the cavity layer near the surface induces a biaxial tensile stress. A shear stress and a component of the normal stress act on the 4 planes which are at an angle of 45° to the surface. However, no shear stress, but only a normal stress, act on the 2 planes perpendicular to the surface.

Implantations performed at low implant temperature ($\sim 500^\circ\text{C}$), low beam currents ($16 \mu\text{A}/\text{cm}^2$), and low doses ($0.3 \times 10^{18} \text{ cm}^{-2}$), showed [27, 83] that dislocation half loops occurred only on planes at 45° to the surface. Under these conditions since no dislocation half loops with Burgers vectors parallel to the surface were observed, it was suggested that a shear stress was possibly necessary for their nucleation.

Two of the objectives of the present study, were to determine the effect of strain on the nucleation and growth of dislocation half loops, and to determine whether dislocation half loops evolve into threading dislocations. The large amount of experimental data collected in the present study and from the existing literature, using many different implantation conditions, should allow for an improved understanding of these aspects.

Experimental results from the present study indicated that the strain induced in the near surface region due to the cavities, increased with

increase in dose, but decreased with increase in energy, and showed marginal effects due to changes in temperature and beam current. Thickness of the cavity layer showed similar trends except in the case of implant energy variation. Increase in energy caused an increase in the cavity layer thickness, but a decrease in strain. The total dislocation half loop density in the as-implanted state showed similar trends as the strain, except for the case of beam current variation. Increase in beam current for stoichiometric doses resulted in an increase in half loop density but a decrease in strain.

To understand if any correlation exists between the near surface strain and dislocation half loops all of the data from this study, and from the literature, have been plotted in Figure 3.34. From this figure, it can be deduced that no apparent correlation exists between dislocation half loops and near surface strain. Based on these results, it is clear that a unique critical strain value necessary for half loop nucleation probably does not exist. However, strain relief processes in thin films are known to be dependent on both the thickness of the film and the strain [86 - 89]. Therefore, to investigate half loop formation as a strain relief process requires consideration of factors beyond just the magnitude of the strain.

It has been established that the strain is confined to a thin near surface region, and that it is accommodated by a tetragonal distortion of the lattice [83]. This situation is analogous to a lattice-mismatched heteroepitaxial thin film. Under this assumption, the energetics of half loop formation have been considered on the basis of existing literature [86 - 89]. The total energy, E_{tot} , of the system can be expressed as the difference between the energy associated with the loop ($E_{1/2\text{loop}}$) and the strain energy released by the presence of the loop (E_{rel}).

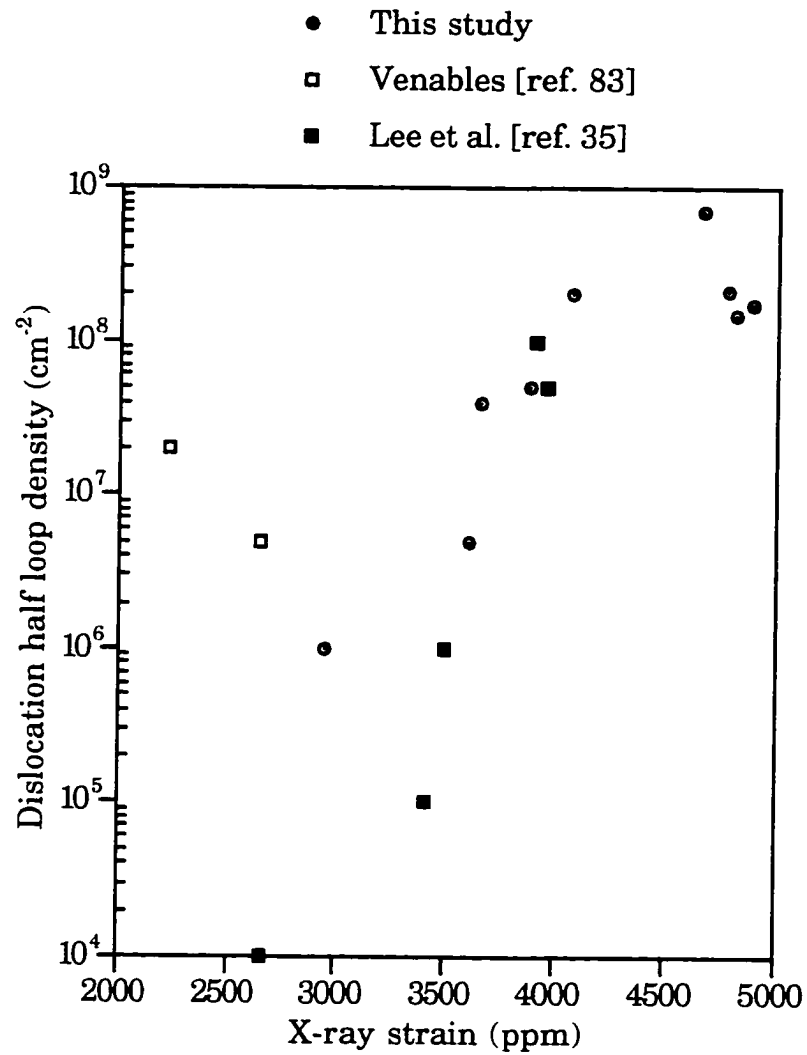


Figure 3.34. Dislocation half loop density as a function of x-ray strain in as-implanted samples from this study and literature.

$$E_{\text{tot}} = E_{1/2\text{loop}} - E_{\text{rel}}$$

When the partial derivative of E_{tot} with respect to R (radius of the loop) is set equal to zero, the critical value of the radius R_c , above which a loop will be stable can be calculated. Using the expressions for $E_{1/2\text{loop}}$ and E_{rel} from Hirth and Loethe [88], it was found that the critical radius R_c and strain ε_p are related by the equation

$$\varepsilon_p = \frac{b}{8\pi R_c \beta (1 + \nu)} \ln\left(\frac{32R_c}{b}\right) \quad (3.1)$$

where b is the Burgers vector, ν is Poisson's ratio and β is a geometrical factor equal to 1/2 for loops at angles to the surface and equal to 1 for loops perpendicular to the surface.

The theoretical value of the critical radius R_c , for half loops at an angle and perpendicular to the surface, is plotted as a function of the strain ε_p in the graph shown in Figure 3.35. To compare these theoretical calculations to experimental results, the thickness of the cavity layer found from XTEM were plotted in Figure 3.35 with respect to the estimated maximum strain from HRXRD measurements. The thickness of the cavity layer gives a good estimate of the maximum radius of the half loops. In this plot, the solid symbols represent samples which contained observable half loops, while the open symbols represent samples in which no half loops were observed.

The theoretical curves for the nucleation of half loops in Figure 3.35 partition the critical radius and strain space into two regions. In the region above the curves, the presence of half loops will lower the strain energy of the system and thus half loops may be present. In the region below the curves half loop formation is precluded. There is a large discrepancy

between theoretical and experimental results for formation of half loops perpendicular to the surface. However, there is remarkable agreement between theory and experiment for formation of half loops at an angle to the surface.

Despite this apparent agreement, it must be noted that the activation energy for such a process to occur homogeneously is unrealistically high. The activation energy required for the nucleation of stable half loops of critical radius R_c can be found by substituting R_c into equation (3.1). The activation energy necessary for the homogeneous nucleation of a 25 nm loop is ~ 375 eV, an enormously large and unrealizable number.

Therefore, homogeneous nucleation of dislocation half loops due to a near surface strained layer is not feasible. However, some form of heterogeneous nucleation could operate to reduce this activation energy. Such a heterogeneous process apparently does operate, since angled half loops only occur in the region predicted by theory. Apparently the nucleation barrier for half loops perpendicular to the surface, even by heterogeneous mechanisms, is higher, since they do not occur throughout the region defined by theory. This result is consistent with the suggestion of Venables and Jones [27] that a shear stress may be necessary for half loop nucleation. Since no component of shear stress is present on planes perpendicular to the surface, nucleation on these planes may be discouraged.

In summary, this analysis is consistent with the hypothesis that half loops are a consequence of a strain relief process. However, this strain relief process must occur by heterogeneous means that reduce the substantial barriers for nucleation. These heterogeneous processes apparently occur to unequal extents for the two types of loop habit planes.

As a result, nucleation of loops perpendicular to the surface is a more difficult, but still operative process.

The next objective was to determine whether all dislocation half loops evolve into threading dislocations.

Dislocation half loops lie on $1/2\{110\}$ planes and can have Burgers vectors of the type $1/2\langle 110 \rangle$. There are 6 such planes, of which 4 are at an angle of 45° to the surface, and 2 perpendicular to the surface. A recent study [35], showed that at high implant temperatures (550°C and higher) dislocation half loops occurred in all the $6\{110\}$ planes. This study [35] also reports that the dislocation half loops with Burgers vectors at angles to the surface occurred with twice the frequency to the dislocation half loops with Burgers vectors parallel to the surface. Lee et al. [35] showed that the dislocation half loops with Burgers vectors parallel to the surface evolved into threading dislocations. The reason behind this was [35] that half loops at angles to the surface have glide cylinders that intersect the surface and can easily escape. On the other hand, dislocation half loops on planes perpendicular to the surface, have glide cylinders parallel to the surface and can escape from the crystal, by glide, only by traveling to the edge of the wafer. However, all half loops can climb to the surface and be eliminated.

Experimentally, it was established from the present study that dislocation half loops, which were only present in the as-implanted state for doses higher than $1.0 \times 10^{18} \text{ cm}^{-2}$, occurred in all of the $6\{110\}$ planes. From PTEM analysis it was found that these dislocation half loops either had Burgers vectors at an angle to the surface or had Burgers vectors parallel to the surface. Extensive analysis performed on all the dislocation half loops indicated that there was no preferred plane on which they existed i.e. there was no fixed ratio in which they occurred. For example, at a dose of

$1.0 \times 10^{18} \text{ cm}^{-2}$, only angled half loops were present. This result contradicts the observations reported earlier [35]. PTEM analysis on the annealed samples showed that threading dislocations had Burgers vectors parallel to the surface and they always occurred in pairs for doses higher than $1.0 \times 10^{18} \text{ cm}^{-2}$. This means that only the dislocation half loops lying on planes perpendicular to the surface evolved into threading dislocations. It was also observed that the final threading dislocation density was a small fraction of the initial dislocation half loop density. These results are consistent with those reported earlier [35].

The dependence of the final threading dislocation density on the density of dislocation half loops perpendicular to the surface in the as-implanted samples is shown in Figure 3.36. Data from this study, and from the work of Lee et al. [35] have been included. This graph explicitly shows that the density of threading dislocation varies proportionately with the density of dislocation half loops which exist on planes perpendicular to the surface. The best fit line through the data indicates that the final threading dislocation density is about one order of magnitude lower than the density of dislocation half loops perpendicular to the surface, over a wide range of densities.

For doses lower than $1.0 \times 10^{18} \text{ cm}^{-2}$ it was experimentally established that stacking faults were present in the as-implanted state and only very few of them developed subsequently into threading dislocations (density $\sim 10^4$ to 10^3 cm^{-2}) upon annealing. However, an explosive increase in the final threading dislocation density was observed for cases where a bilayered structure of precipitates appeared instead of a continuous buried oxide. These precipitates pin defects and contribute to increasing the final dislocation density after annealing. This bilayer precipitate structure is

essentially connected to the formation of the buried oxide, which is discussed below.

Buried Oxide Evolution

The other objective of this study was to understand the basic physical mechanisms governing buried oxide growth and silicon island formation within the buried oxide. In this section the possible parameters and processes that affect these structures are discussed.

Implantation at an energy of 175 keV, and dose of $0.2 \times 10^{18} \text{ cm}^{-2}$, resulted in a double layer of SiO_2 precipitates, instead of a continuous buried oxide, after annealing. However, for the implantation at 200 keV, this bilayer of precipitates was evident for doses of $0.2 \times 10^{18} \text{ cm}^{-2}$ and $0.4 \times 10^{18} \text{ cm}^{-2}$. Therefore, the formation of bilayers is directly dependent on the energy and dose, i.e. to obtain a continuous buried oxide the implant energy and dose are coupled. Higher implant energy necessitates a higher dose for forming a continuous buried oxide, at substoichiometric doses. This is possibly a consequence of the larger straggle associated with higher energy implants. Consequently, it can be concluded that the microstructure of the buried oxide at substoichiometric doses is dominantly dependent on the dose and energy of implant. Substrate temperature and beam current apparently played a lesser role.

The other important microstructural feature which degrades the quality of the buried oxide are silicon inclusions. Experimental results showed that with increase in dose (for substoichiometric doses of $1.0 \times 10^{18} \text{ cm}^{-2}$ and lower), the density of Si islands within the buried oxide increased, although the fraction of the buried oxide occupied by these islands decreased, irrespective of implant energy. This observation led to the conclusion that Si island formation is probably predominantly dependent on

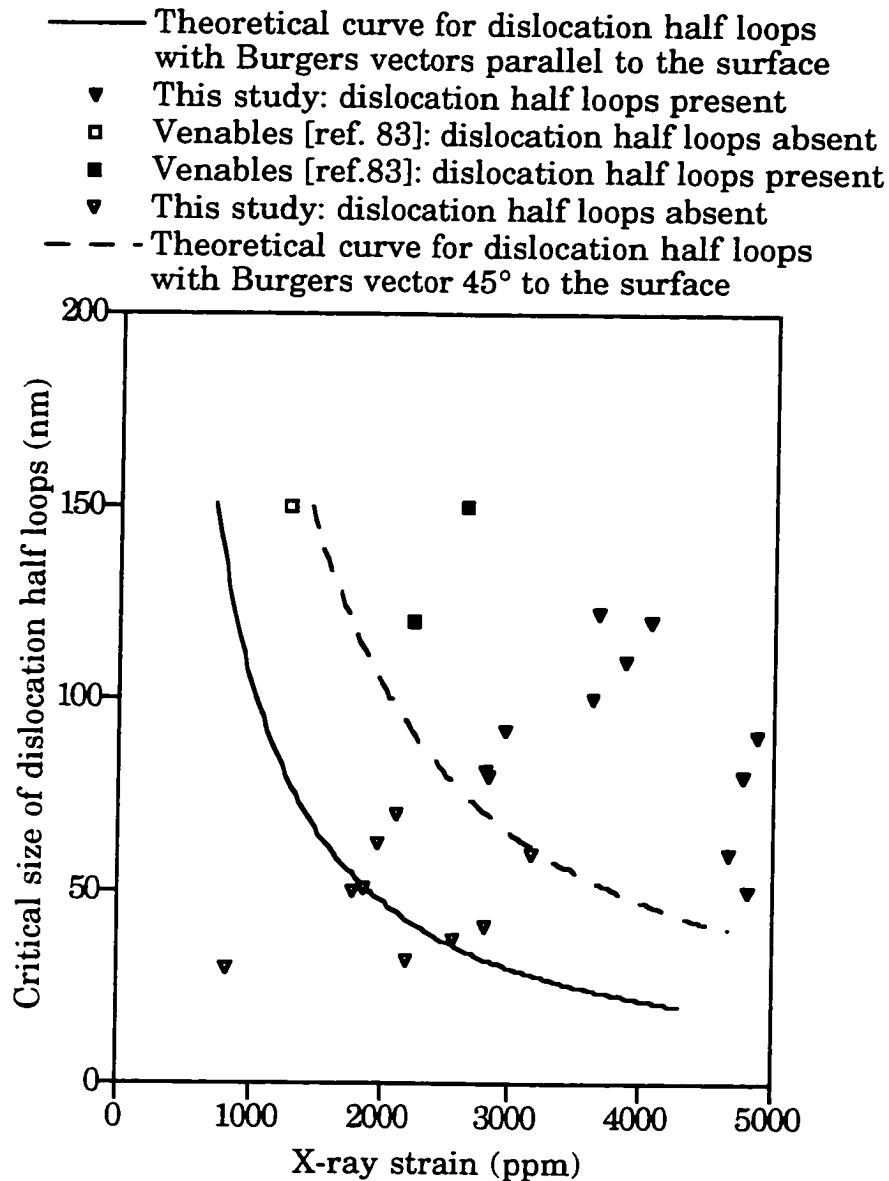


Figure 3.35. Theoretical (from equation 3.1) and experimental values of the critical radius of dislocation half loops as a function of near surface strain. The data from Venables [83] include only half loops at an angle to the surface.

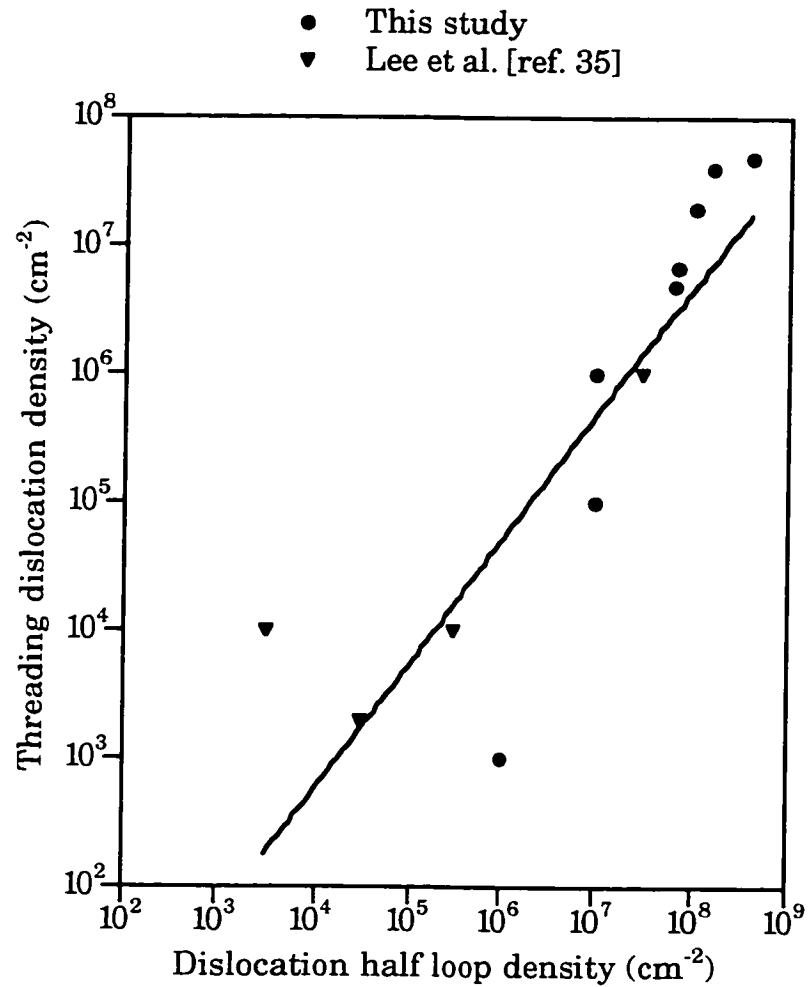


Figure 3.36. Threading dislocation density after annealing as a function of the dislocation half loop density in the as-implanted state. Only the half loops with Burgers vector parallel to the surface are plotted from this study and literature.

dose, irrespective of implant energy. Substrate temperature variation during implantation at a dose of $0.4 \times 10^{18} \text{ cm}^{-2}$, did not affect the buried oxide microstructure significantly. Therefore, it can be deduced that substrate temperature variation possibly does not affect the buried oxide microstructure for substoichiometric doses.

From the analysis of the as-implanted structures it was apparent that doses at which striations were present in the as-implanted state within the buried oxide, resulted in a high density of silicon islands. SIMS results on the other hand, proved that there were no large scale variations in oxygen concentrations in the as-implanted state. To understand the correlation between the striated structure in the as-implanted state and the formation of Si islands in the annealed state requires a more intensive study of the precipitation process in the as-implanted state, which is the objective of the next chapter.

CHAPTER 4

PRECIPITATION PROCESSES IN ION BEAM SYNTHESIS

The synthesis of the buried oxide involves a series of physical stages. The ion implantation of oxygen into silicon causes a supersaturation of oxygen in the matrix. This supersaturation provides the driving force for nucleation of precipitates. When the nucleation process saturates, precipitate growth and, eventually, impingement of precipitates occur. During post implantation annealing, which is performed at a very high temperature, Ostwald ripening is the dominant mechanism. In this stage, the surface tension of the Si/SiO₂ interface provides the driving force for oxygen redistribution. The Si/SiO₂ interface contributes significantly to the free energy of the system, thus dissolution of smaller precipitates and growth of large precipitates diminishes the free energy of the system. The coalescence of large precipitates creates a buried oxide.

Although the thermodynamic driving forces behind these microstructural evolution processes are identical to those in conventional (i.e., not ion implanted) phase transformations, the fact that the solute is introduced by ion implantation may have important consequences for the kinetics of the processes. During the nucleation and growth stages, new solute is constantly being introduced by the continued implantation. Thus, the kinetics of the phase transformation may be controlled by this external factor (the source or production term) rather than strictly by conventional diffusion or interface controlled processes. In addition, the implantation process may lead to an inhomogeneous distribution of precipitate sizes,

number densities and of solute concentration. These inhomogeneities may have important consequences during post-implantation annealing.

The coarsening behavior of homogeneous precipitate distributions is essentially independent of the initial state, i.e., the long time annealing behavior follows well known scaling laws. In contrast, the coarsening behavior of inhomogeneous precipitate distributions depends very sensitively on the initial state. Since SIMOX contains an inhomogeneous precipitate distribution after implantation, it is critical to understand and model the as-implanted precipitate microstructure. There are no models at all of the precipitate distribution in the as-implanted state. Moreover, there are not even any measurements of the as-implanted precipitate distributions. As a result of this lack of experimental and theoretical data, it has proven extremely difficult to understand the overall characteristics of the buried oxide. This poor understanding is especially apparent for the sub-stoichiometric doses, where, as discussed in Chapter 3, the buried oxide may have a large variety of configurations. These configurations include a discontinuous layered structure at a dose of $0.2 \times 10^{18} \text{ cm}^{-2}$, an entirely continuous buried oxide at a dose of $\sim 0.4 \times 10^{18} \text{ cm}^{-2}$, and buried oxides with large numbers of undesirable Si inclusions at higher sub-stoichiometric doses.

Thus, the objective behind this part of the study was to analyze and model the precipitation process in the as-implanted state, since this stage may control the subsequent development of the buried oxide during post-implantation annealing. An in-depth analysis of the precipitation process during ion implantation for substoichiometric implant doses has been performed. High-resolution cross-sectional TEM images have been used to obtain the precipitate size distributions and number densities as a function

of depth of substoichiometric dose implants of $0.2 \times 10^{18} \text{ cm}^{-2}$, $0.4 \times 10^{18} \text{ cm}^{-2}$ and $0.6 \times 10^{18} \text{ cm}^{-2}$ at an energy of 175 keV, a substrate temperature of 590°C and with a beam current density of 3.0 mA/cm^2 . SIMS analysis provided the total oxygen concentration as a function of depth for these same samples. In conjunction with simple theoretical models, this data has provided for the first time a more comprehensive view of the nucleation, growth and impingement of precipitates during the ion beam synthesis of SIMOX.

Experimental Details

Perhaps one of the main reasons for the lack of experimental measurements in the literature of the precipitate distribution in the as-implanted state is the extreme difficulty in performing such a study. Since the second phase (i.e., SiO_2) is not crystalline, dark field analysis is not feasible. The analysis is further complicated by the extremely small size of the precipitates in the as-implanted state.

The approach taken in the present study has been to image cross-sectional samples in a high-resolution TEM at high magnifications ($\sim 300 \text{ kx}$). The silicon matrix yields a lattice image under these conditions, thus enabling a distinction to be made between the non-crystalline precipitates and the crystalline matrix. To image the entire precipitate distribution required a montage of ~ 15 to 20 high resolution images for each sample. The precipitate sizes were then measured from $8'' \times 10''$ enlargements of each image.

To obtain a precipitate number density requires knowledge of the thickness of the thin foil sample. Conventional convergent beam electron diffraction techniques for measuring the foil thickness are not useful for the ultra-thin foils necessary for lattice imaging. Thus, the foil thickness

was estimated from the many-beam thickness fringes (Pendollosung fringes) produced by the multi-beam imaging conditions. An example of these fringes is shown in Figure 4.1. These fringes are the many-beam analog of two-beam thickness fringes, i.e., they arise from beating effects of the Bloch waves excited in the crystal. For Si $\langle 110 \rangle$ many-beam conditions at 200 keV, the fringe periodicity is ~ 27 nm [90]. The number density measurements were all taken at the first visible fringe, which corresponds to a thickness of ~ 13.5 nm.

The size of the precipitates is reported as the mean equivalent radius, R . For non-spherical precipitates, this parameter was obtained from a consideration of equivalent areas. Given the mean size, R , and the number density, N , the volume fraction, V_f , was estimated as

$$V_f = \frac{4}{3} \pi N R^3 \quad (4.1)$$

The total concentration of oxygen contained in the precipitates was then estimated from

$$C_{ox} = C_p V_f \quad (4.2)$$

where $C_p = 4.56 \times 10^{22} \text{ cm}^{-3}$ is the oxygen atom density of stoichiometric, thermally grown, SiO_2 . Note that this analysis does not account for possible non-stoichiometric precipitation. SIMS analysis provided the total oxygen concentration in each sample as a function depth for comparison to the TEM data.

Results

A cross sectional view of the as-implanted structure for the dose of $0.2 \times 10^{18} \text{ cm}^{-2}$ dose is shown in the Figure 4.2a. High resolution images of

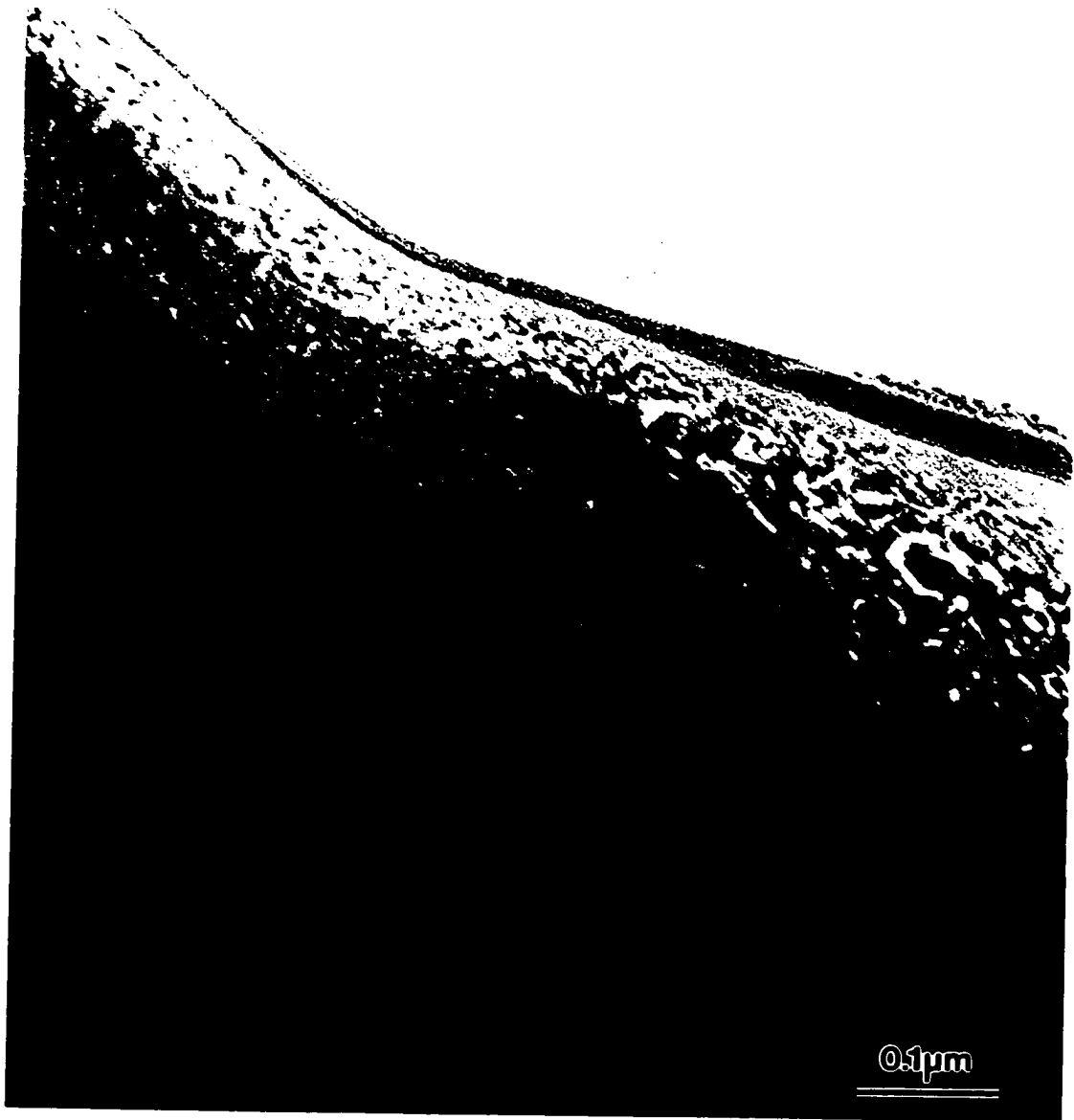


Figure 4.1. HRTEM micrograph taken at the $\langle 011 \rangle$ zone axis showing many-beam thickness fringes at the edge of a sample.

the precipitates in regions marked B, C, D, and E shown in Figure 4.2a are shown in Figure 4.2b, 4.2c, 4.2d and 4.2e. These images show that the precipitates are spherical or oblate spheroidal in shape. Precipitates appear at a depth of 200 nm and their size increases until a depth of 375 nm from the surface. Beyond this depth the size of the precipitates decreases.

The overall as-implanted structure observed at a dose of $0.4 \times 10^{18} \text{ cm}^{-2}$ is shown in Figure 4.3a. The variations in the precipitates size and shape with depths marked as B, C, D, and E, in Figure 4.3a, are shown in Figure 4.3b, 4.3c, 4.3d, and 4.3e. The precipitate sizes show a similar variation as in the $0.2 \times 10^{18} \text{ cm}^{-2}$ dose; i.e., the mean size increases to a maximum value and then decreases with increase in depth from the surface. In contrast to the uniformity in shape observed in the $0.2 \times 10^{18} \text{ cm}^{-2}$ sample, the shape of the precipitates at $0.4 \times 10^{18} \text{ cm}^{-2}$ is rectangular in nature within a depth of 338 nm and 563 nm (Figure 4.3c). The precipitates in all the other regions are spherical or oblate spheroidal.

The entire cross sectional structure of the $0.6 \times 10^{18} \text{ cm}^{-2}$ dose is shown in Figure 4.4a with the depths denoted by B, C, D, and E. A distinct difference at this dose is the presence of striations within a depth of 380 nm and 520 nm from the surface. The corresponding variation of precipitate shapes with depth is shown in Figure 4.4b, 4.4c, 4.4d, and 4.4e. The prominent difference in the shape of precipitates is apparent from Figure 4.4d. The general trend for the precipitate size to reach a maximum value at a certain depth below the surface and decrease afterwards is still observed at this dose. However, extremely large slabs of SiO_2 are present along with small rectangular precipitates within a depth of 335 nm and 446 nm from the surface.

(a)

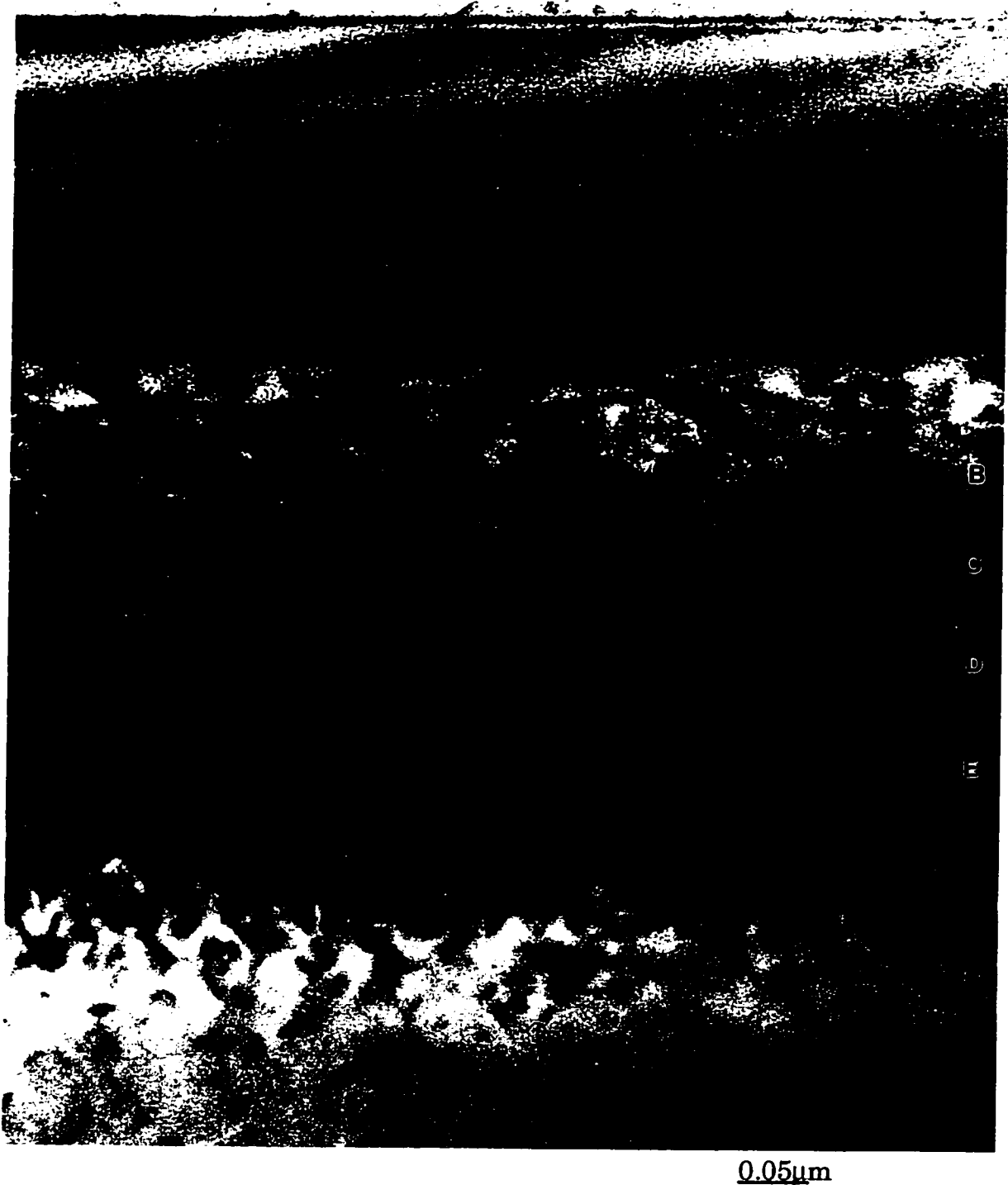
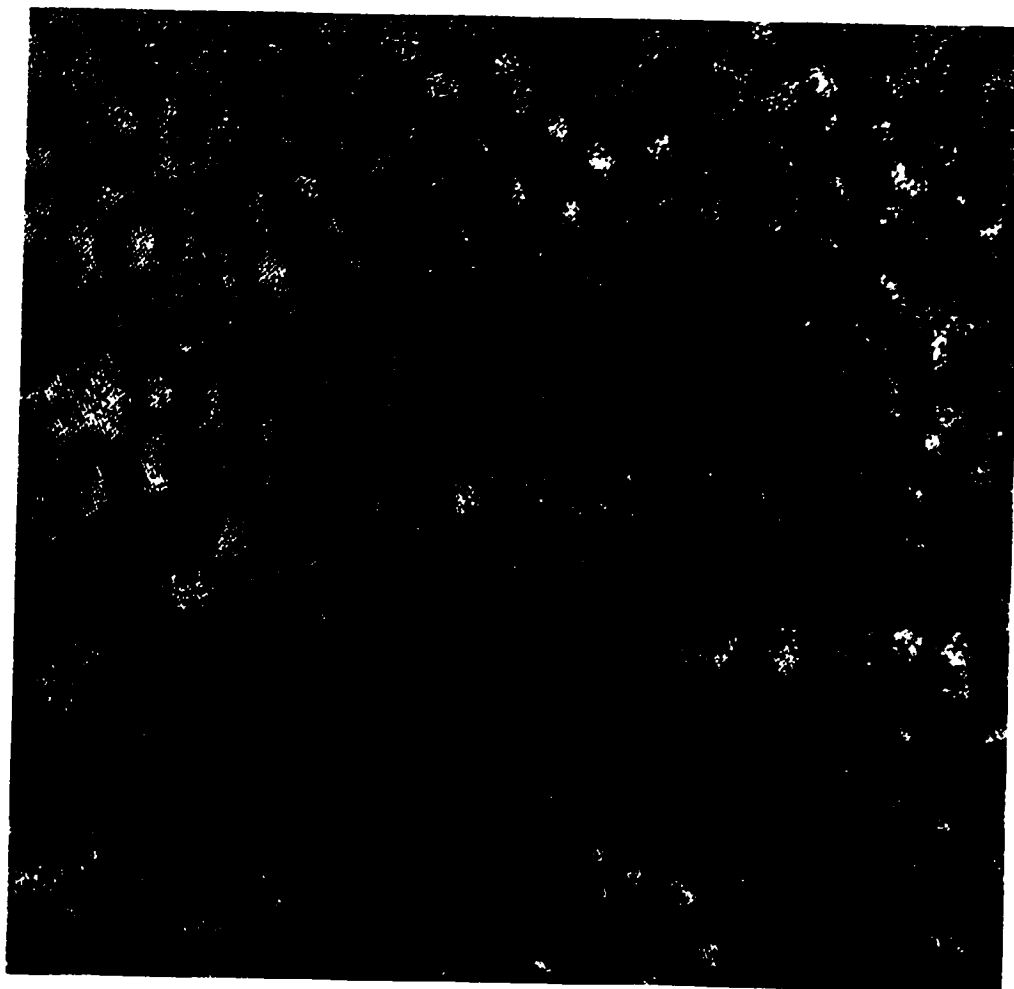


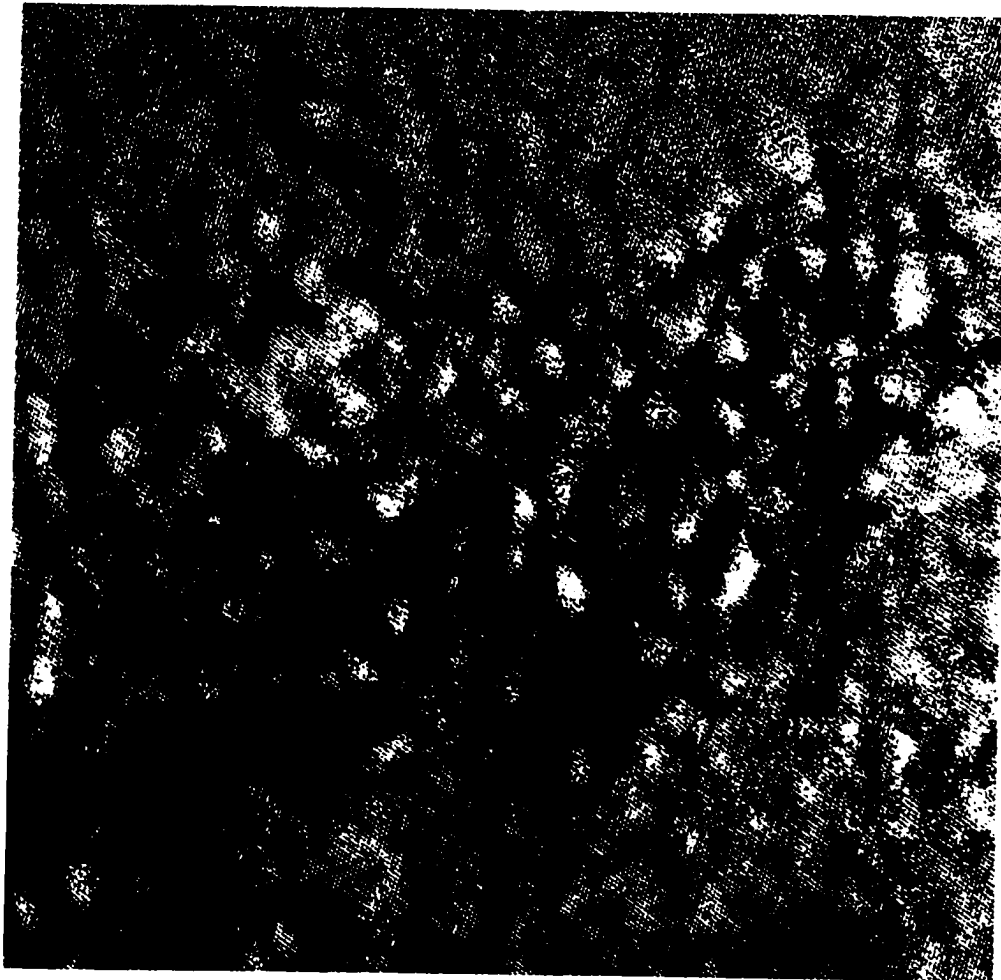
Figure 4.2. Cross-sectional HRTEM micrographs of SiO₂ precipitates at locations marked in (a) for sample in as-implanted condition after implantation at 175 keV to a dose of $0.2 \times 10^{18} \text{ cm}^{-2}$.
a) overall view;

(b)

10 nmFigure 4.2. -- continued

b) precipitates at location B;

(c)

10 nmFigure 4.2. -- continued

c) precipitates at location C;

(d)

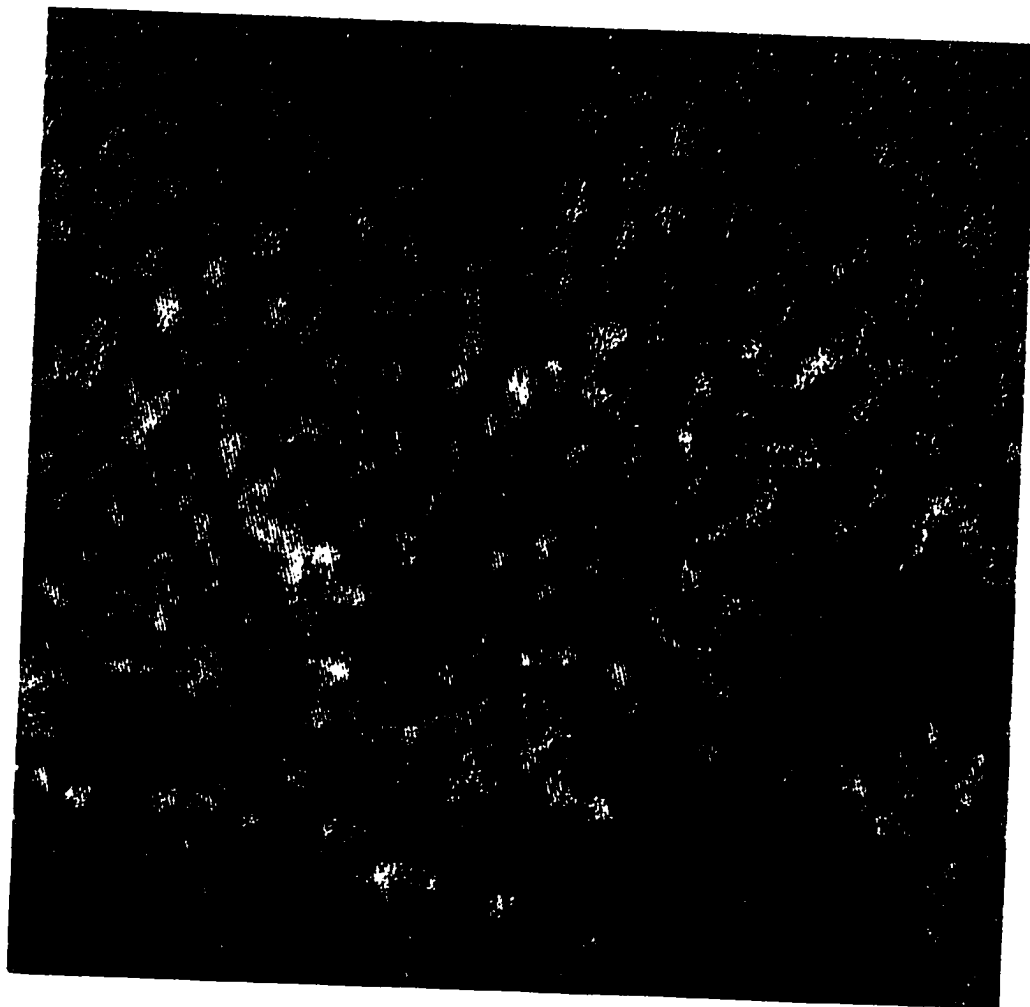
10 nm

Figure 4.2. -- continued
d) precipitates at location D;

(e)

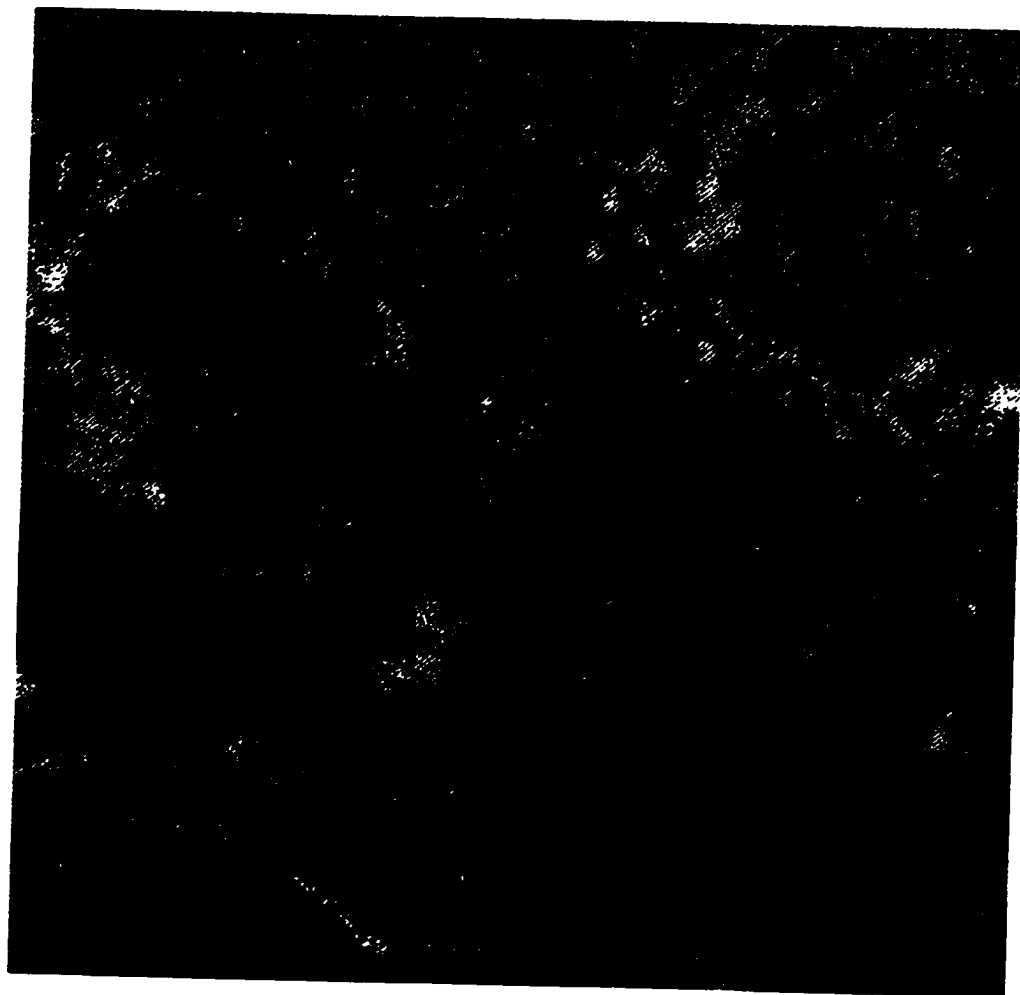
10 nm

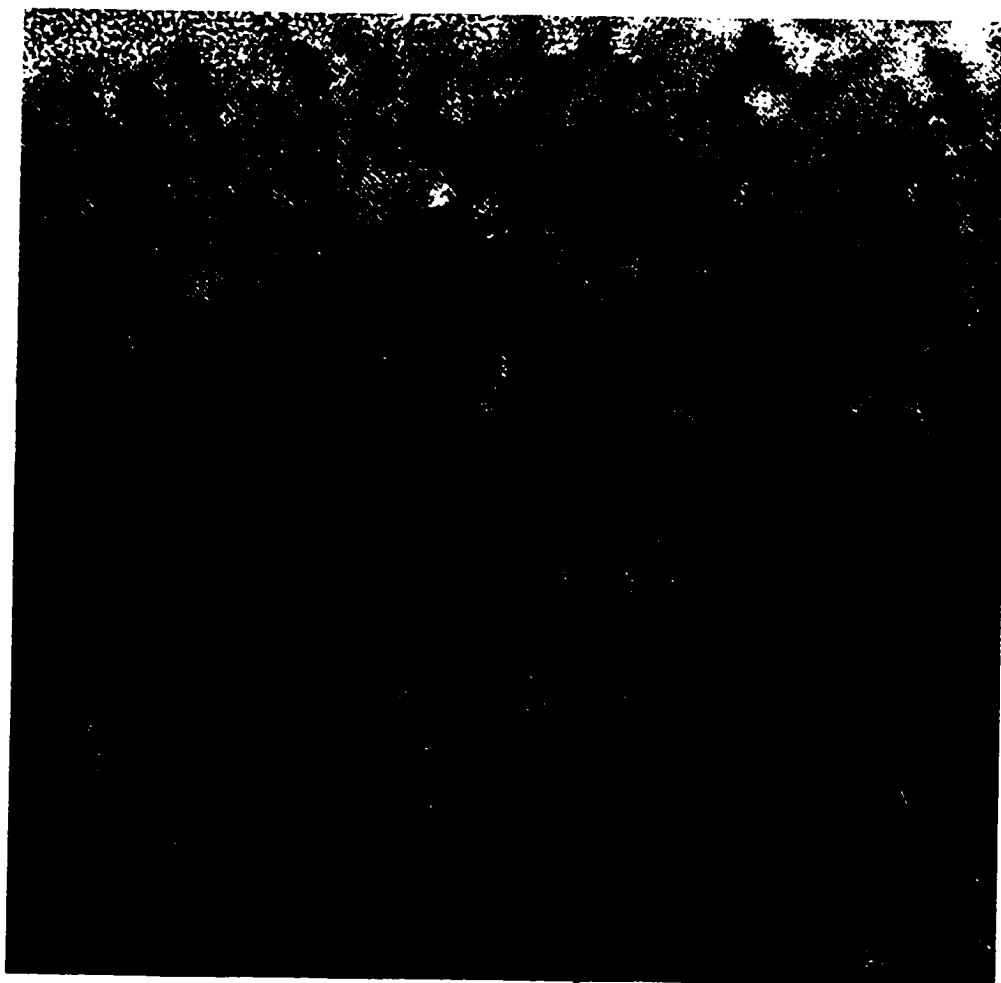
Figure 4.2. -- continued
e) precipitates at location E;

(a)

0.05 μ m

Figure 4.3. Cross-sectional HRTEM micrographs of SiO₂ precipitates at locations marked in (a) for sample in as-implanted condition after implantation at 175 keV to a dose of $0.4 \times 10^{18} \text{ cm}^{-2}$.
a) overall view;

(b)

10 nmFigure 4.3. -- continued

b) precipitates at location B;

(c)

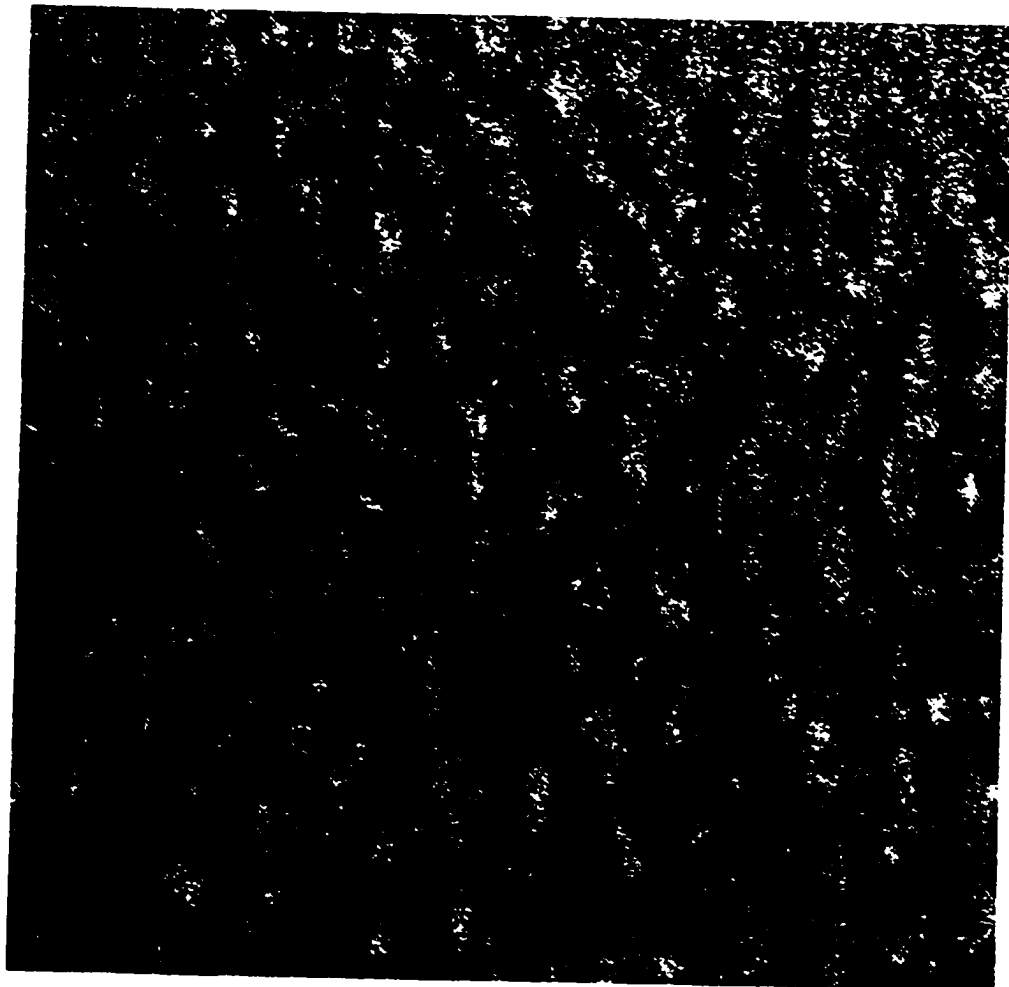
10 nm

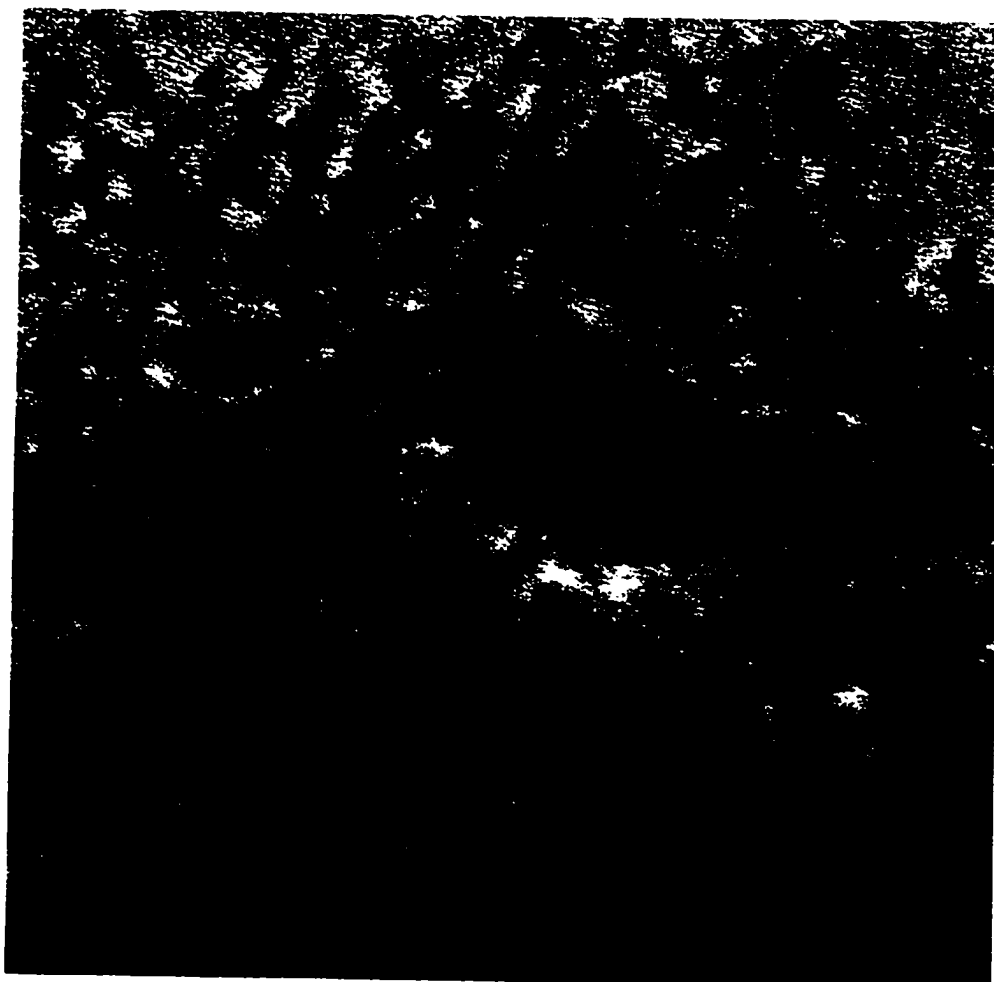
Figure 4.3. -- continued
c) precipitates at location C;

(d)

10 nm

Figure 4.3. -- continued
d) precipitates at location D;

(e)

10 nmFigure 4.3. -- continued

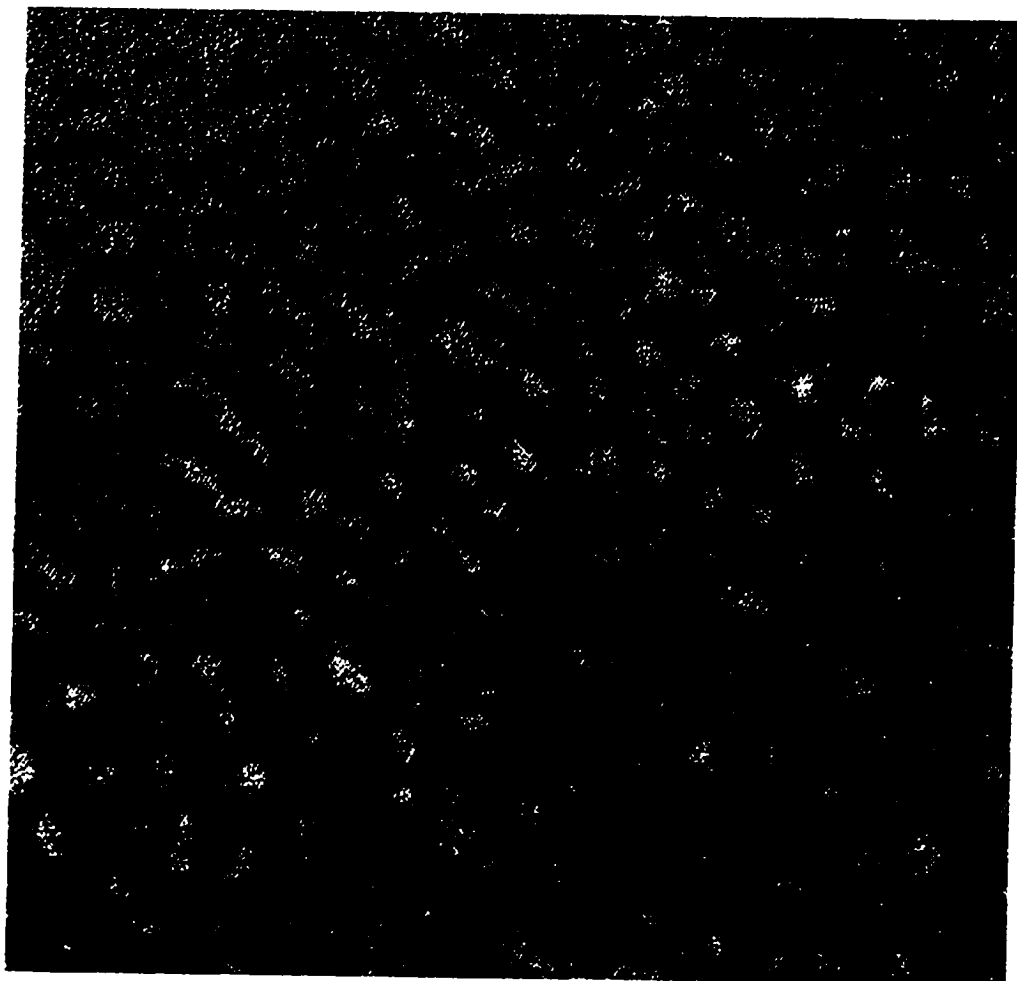
e) precipitates at location E;

(a)



Figure 4.4. Cross-sectional HRTEM micrographs of SiO₂ precipitates at locations marked in (a) for sample in as-implanted condition after implantation at 175 keV to a dose of $0.6 \times 10^{18} \text{ cm}^{-2}$.
a) overall view;

(b)

10 nmFigure 4.4. -- continued

b) precipitates at location B;

(c)

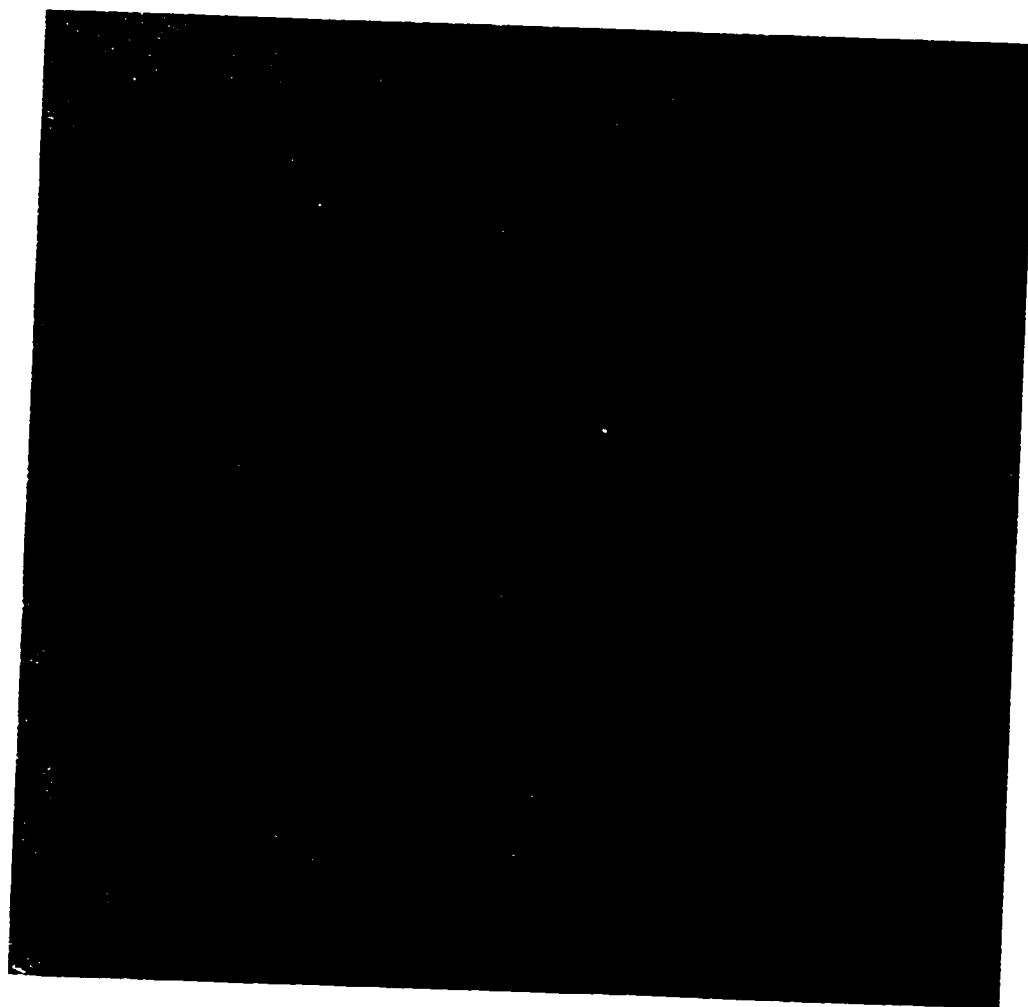
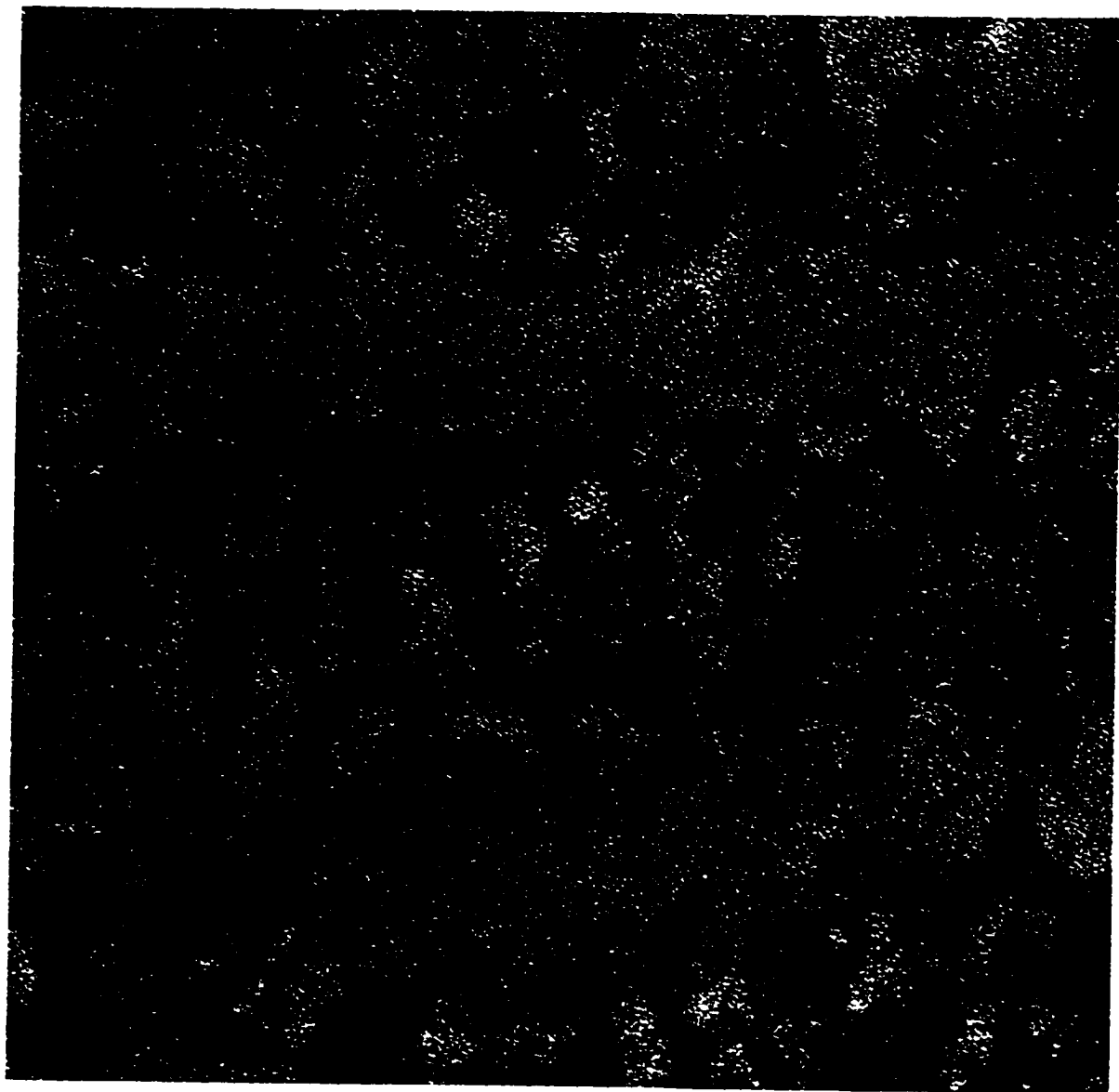
10 nm

Figure 4.4. -- continued
c) precipitates at location C;

(d)

10 nmFigure 4.4. -- continued

d) precipitates at location D;

(e)

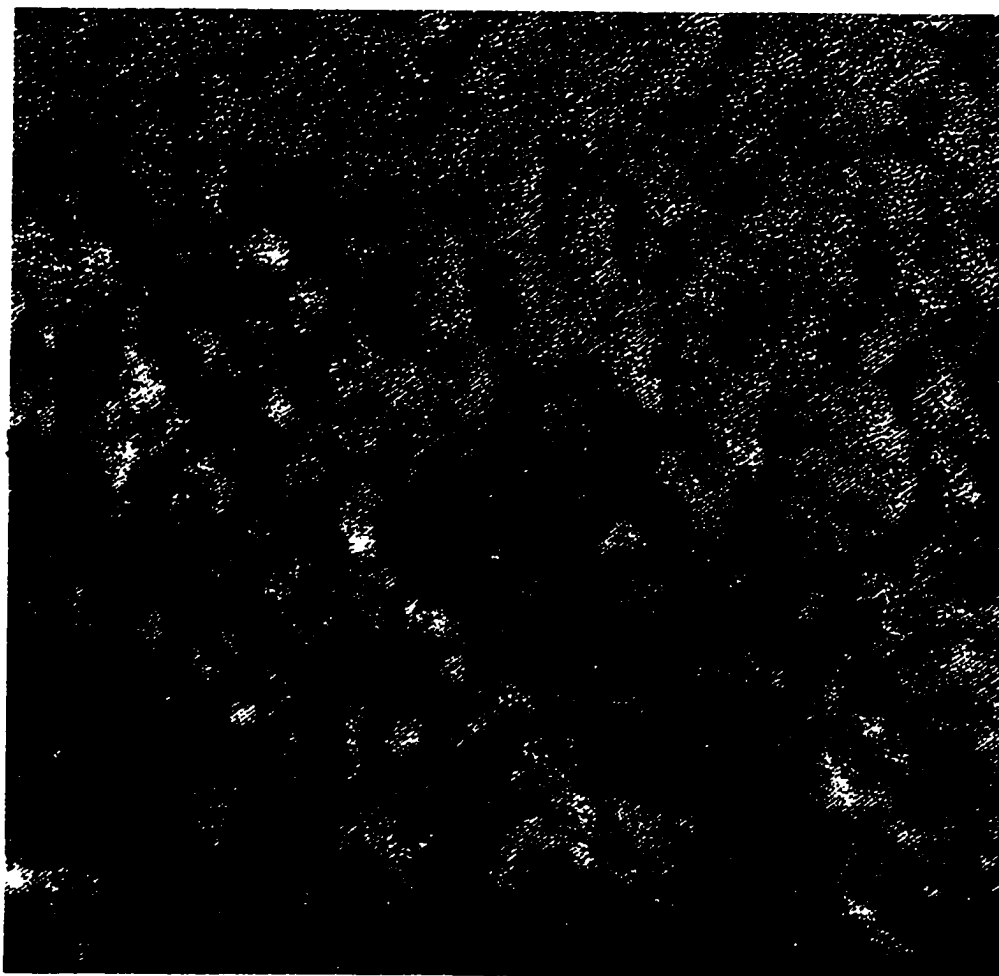
10 nm

Figure 4.4. -- continued
e) precipitates at location E;

A quantitative analysis of the radius of the precipitates with depth for the three doses is shown in Figure 4.5. From the graph, it is evident that at the dose of $0.2 \times 10^{18} \text{ cm}^{-2}$ the precipitates have a maximum size ranging between 2.7 nm and 2.3 nm within a depth of 375 nm and 475 nm. There is an explosive increase in the maximum size of the precipitates at the higher doses of $0.4 \times 10^{18} \text{ cm}^{-2}$ and $0.6 \times 10^{18} \text{ cm}^{-2}$. The maximum diameter of the precipitates estimated for the $0.4 \times 10^{18} \text{ cm}^{-2}$ dose is about 4.8 nm occurring at a depth of 425 nm from the surface. For the highest dose, the maximum size ranges from 5.1 to 5.4 nm at a depth of 350 to 450 nm. The maximum precipitate sizes in each case correspond approximately to the location of the peak ion concentration ($\sim 440 \text{ nm}$) found by SIMS analysis, and predicted by TRIM '95 simulations.

It should be noted that the error bars in Figure 4.5 represent the measurement errors only. The actual variation in precipitates size at each depth was much larger than the measurement error. Figure 4.6 shows the standard deviation of the mean radius at each depth. Figure 4.7 illustrates this variation in precipitate size more clearly with a plot of the largest precipitate dimension measured at each depth, for all three of the doses. It is readily apparent that the size distribution in the $0.6 \times 10^{18} \text{ cm}^{-2}$ dose is grossly inhomogeneous compared to that at the lower doses.

The precipitate number density as a function of depth was evaluated from the montage of HRTEM images, and these results are shown in Figure 4.8 for the three doses. The highest number densities for all of the doses occur near the surface. This region corresponds to the location of large stacking faults which serve as heterogeneous nucleation sites for the precipitates [29]. Thus, the higher number density probably reflects this heterogeneous nucleation process. A striking result for the lowest dose, is

that the number density is nearly constant at $\sim 3 \times 10^{18} \text{ cm}^{-3}$ throughout the remainder of the structure, even though the precipitate size varies substantially. In contrast, the number densities for the higher doses show a substantial reduction at the center of the distribution corresponding to the maximum precipitate size.

These results on precipitate size and number density were used to estimate the volume fraction of SiO_2 as a function of depth, as shown in Figure 4.9. It is apparent that the portion of the matrix occupied by precipitates increases with increase in dose. Further, the maximum fraction of the matrix occupied by precipitates at a dose of $0.2 \times 10^{18} \text{ cm}^{-2}$ is about 0.21 (21%). For the doses of $0.4 \times 10^{18} \text{ cm}^{-2}$ and $0.6 \times 10^{18} \text{ cm}^{-2}$ the precipitates occupied a maximum fraction of .3 and .38 respectively, of the matrix. An important observation was that these maxima occurred at depths lying between 375 nm and 450 nm from the surface, which is in the vicinity of the projected range (440 nm).

The oxygen concentration for these 3 doses as a function of depth was found from SIMS and the results were compared with TEM data shown in Figure 4.10. The values obtained for the concentration of oxygen from the TEM and SIMS results indicate that essentially all of the oxygen is captured by the precipitates.

In summary, it is apparent from the experimental results that the radius of the precipitates varies with the implanted profile, i.e., in proportion with the local oxygen concentration. Further, with the increase in dose, a severe inhomogeneity in precipitate shape and size develops, i.e. above a dose of $0.4 \times 10^{18} \text{ cm}^{-2}$. In addition, the number density of precipitates especially, at the lowest dose, is relatively a constant. This result implies that the process of nucleation has saturated and an increase

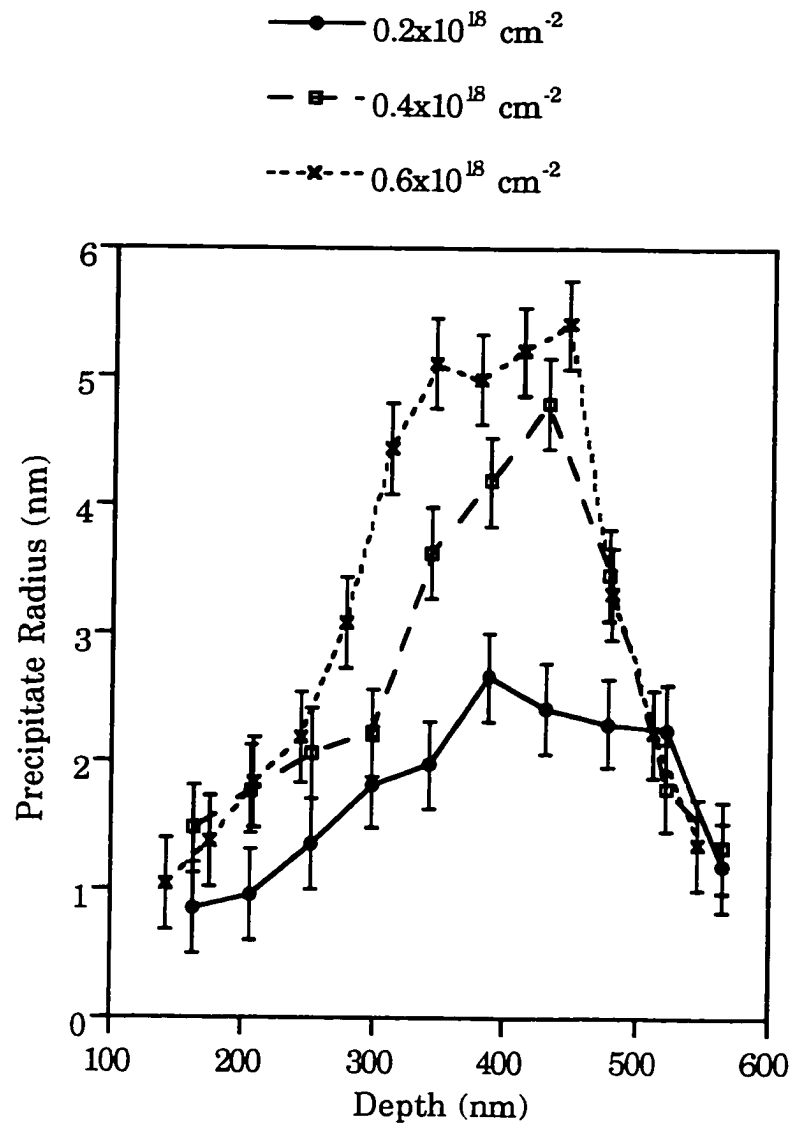


Figure 4.5. Mean precipitate radius, as measured from HRTEM micrographs, as a function of depth for samples in as-implanted condition after implantation at 175 keV for various doses.

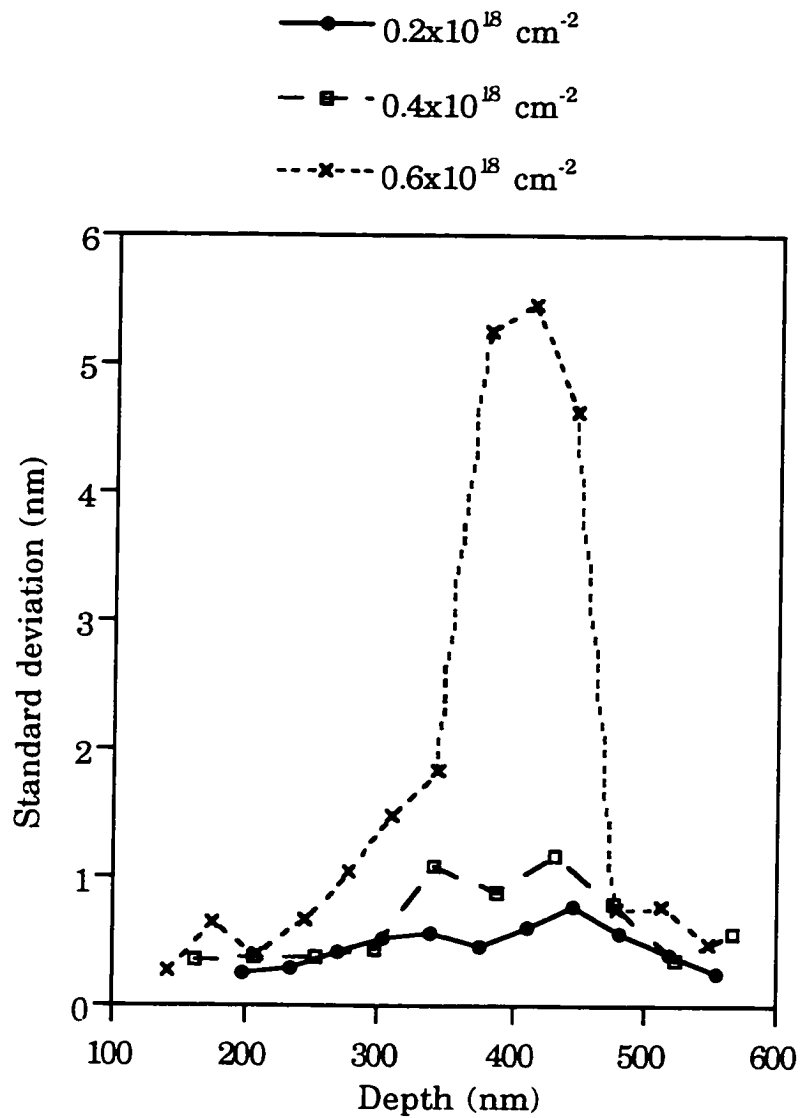


Figure 4.6. Standard deviation of mean precipitate radius, as measured from HRTEM micrographs, as a function of depth for samples in as-implanted condition after implantation at 175 keV for various doses.

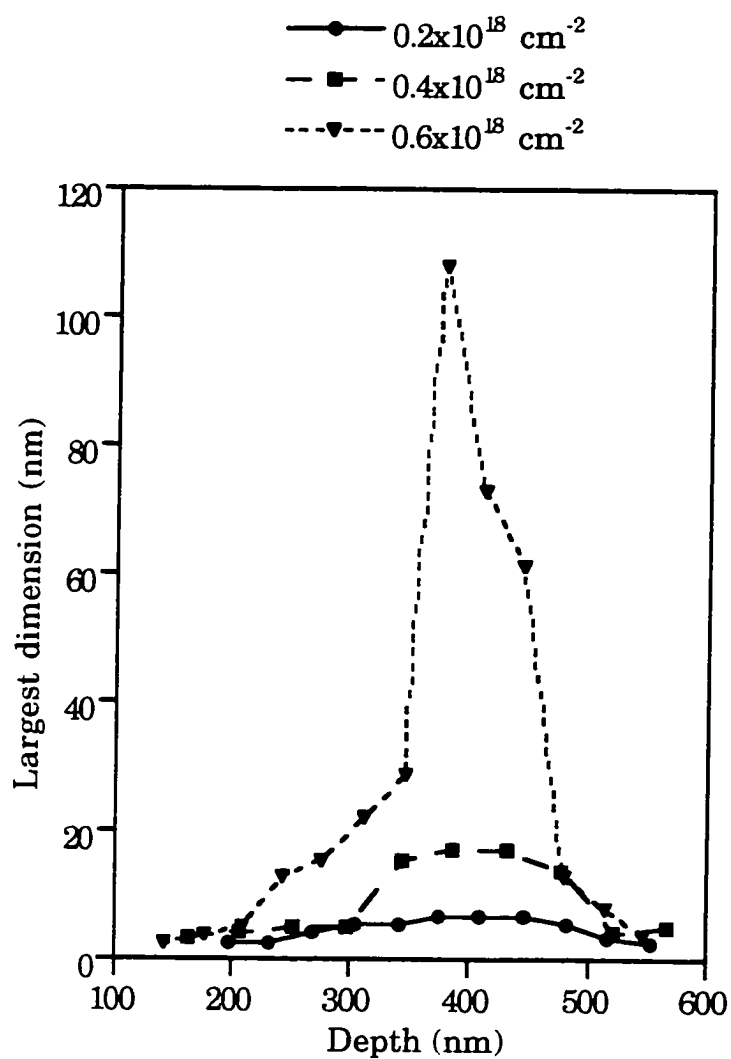


Figure 4.7. Largest precipitate dimension measured from HRTEM micrographs, as a function of depth for samples in as-implanted condition after implantation at 175 keV for various doses.

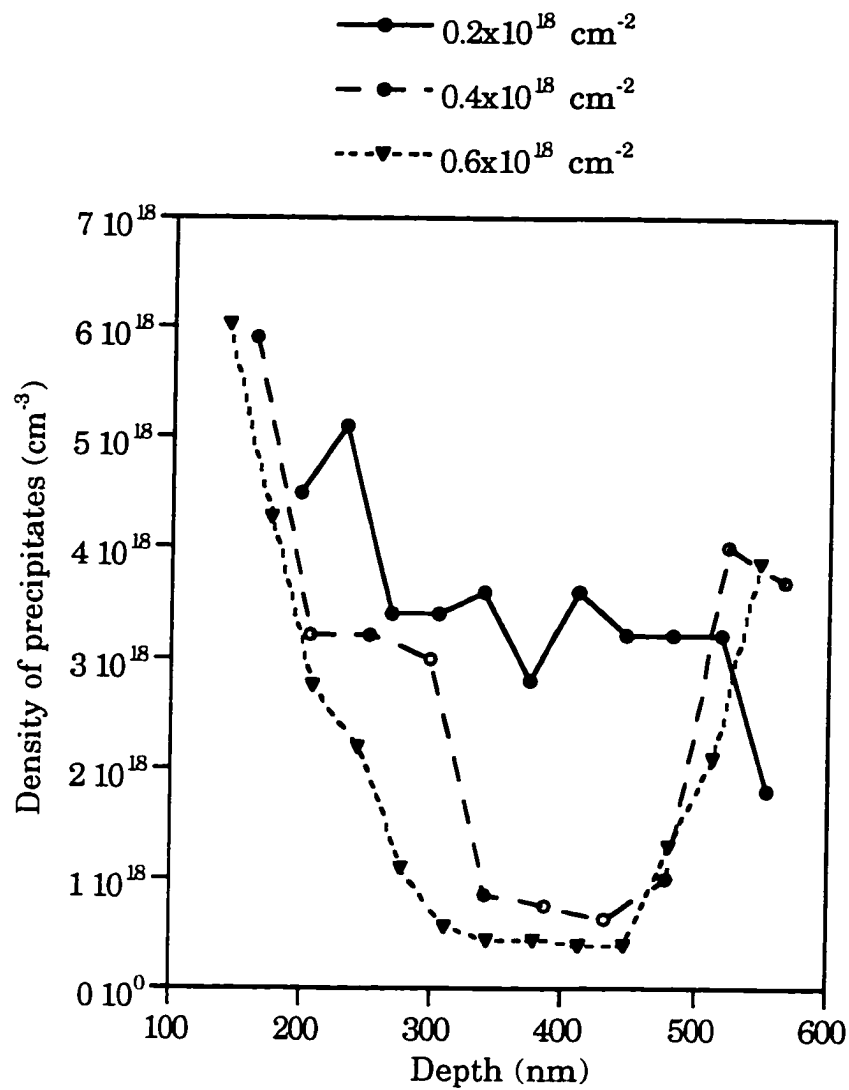


Figure 4.8. Precipitate number density as a function of depth for samples in as-implanted condition after implantation at 175 keV for various doses.

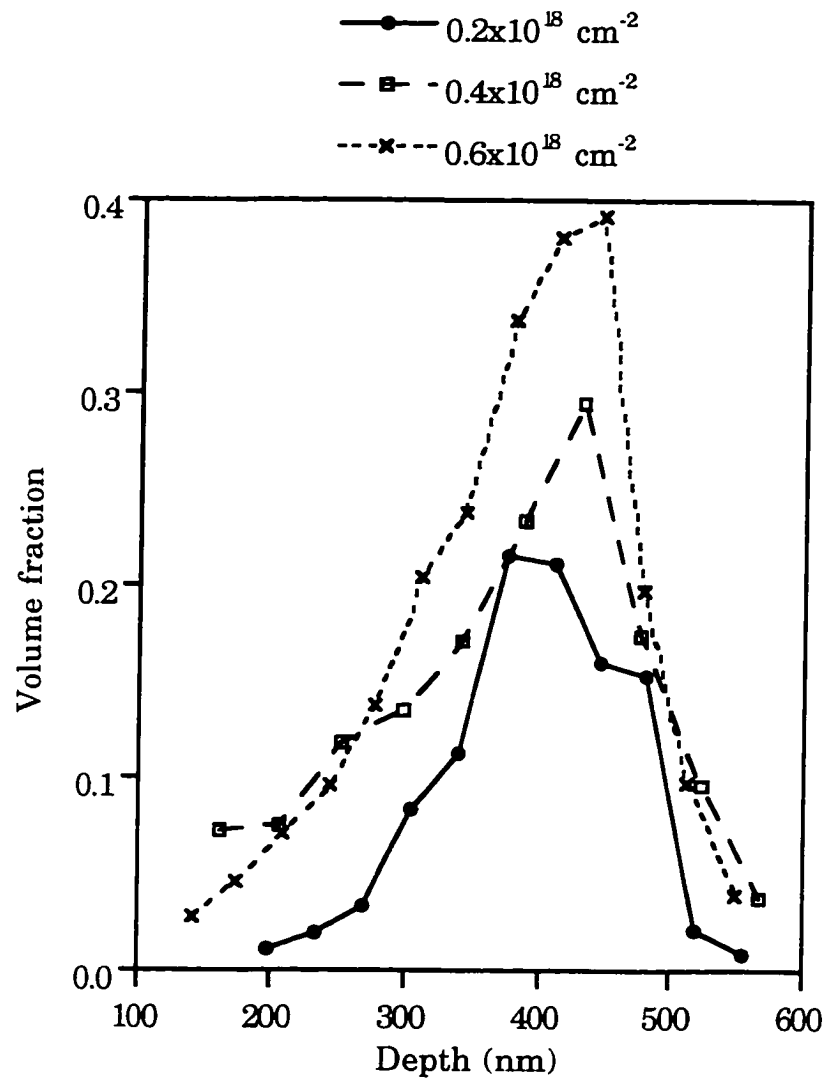


Figure 4.9. Precipitate volume fraction as a function of depth for samples in as-implanted condition after implantation at 175 keV for various doses.

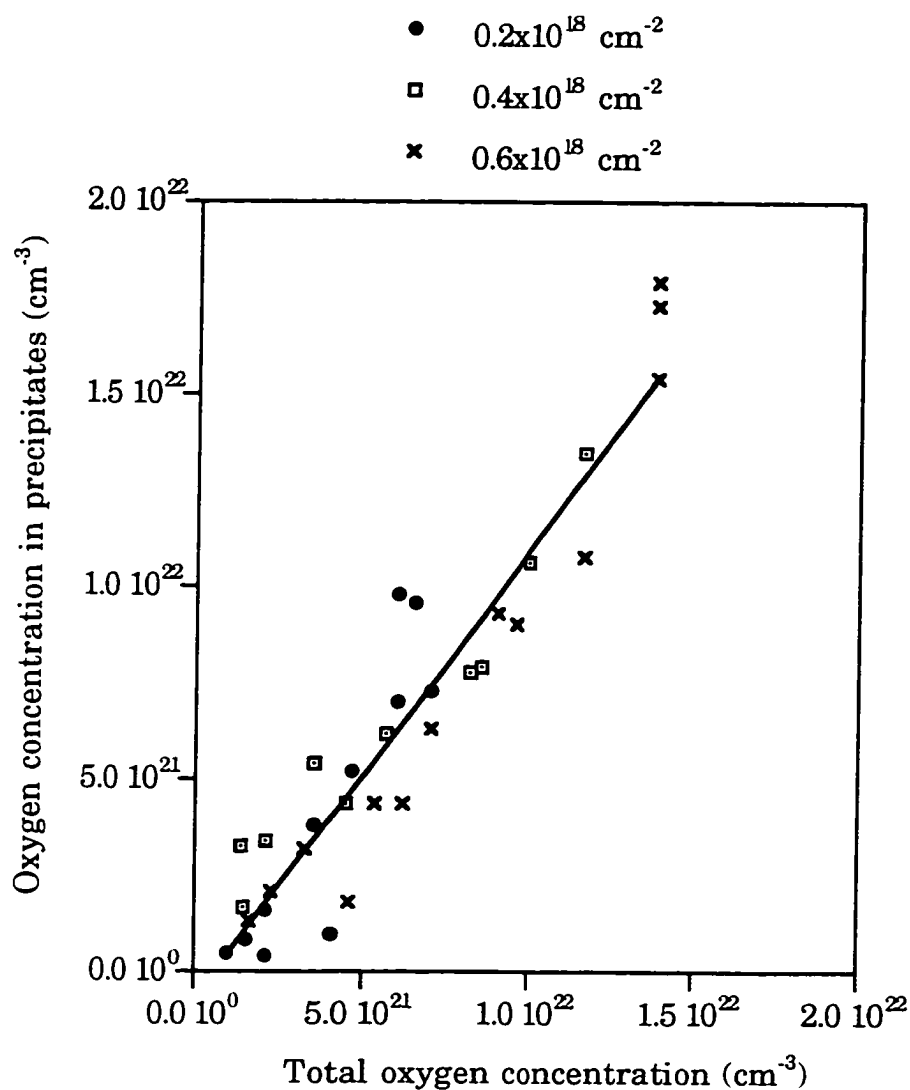


Figure 4.10. Oxygen concentration in precipitates (derived from quantitative analysis of precipitates from HRTEM) as a function of total oxygen concentration (derived from SIMS depth profiles) for samples in as-implanted condition after implantation at 175 keV for various doses.

in dose should contribute only to the growth of existing precipitates, which is exactly the phenomenon observed at the higher doses. Finally, within measurement error, the TEM and SIMS comparison established that essentially all the implanted oxygen was trapped by precipitates.

Models And Discussion

High dose ion implantation used to synthesize a compound within a material is an extremely complex process. Under the non equilibrium conditions of ion implantation process the precipitation mechanism may be complicated by defects produced and the large variety of complexes formed by the implanted species. Moreover, unlike conventional phase transformations, continuous solute introduction by ion implantation may play a crucial role in determining the kinetics of the process. In order to understand the basic physical mechanisms it is necessary to make a few assumptions to simplify the complexity of these systems. In the following sections, simple models, applicable to ion beam synthesized systems, for nucleation, growth and impingement, and coarsening are presented.

Nucleation

It is assumed that only single impurity species, i.e., oxygen, is allowed to migrate. From classical nucleation theory [91, 92] it is known that the critical radius, r_c , for homogenous nucleation is given by

$$r_c = \frac{2\gamma V_p}{kT \ln(C_{ox}/C_{ox}^*)} \quad (4.3)$$

where γ is the interfacial energy (410 ergs/cm²), V_p is the molecular volume of the precipitating species (0.038 nm³), k is Boltzman's constant, T is the temperature (863K), C_{ox}^* is the equilibrium solubility (1.2x10¹⁴ cm⁻³) and C_{ox} is the solute concentration (7x10²¹ cm⁻³). This calculation gives a value of $r_c = 0.13$ nm.

Hence, from this calculation it is apparent that the critical nucleus for the formation of a precipitate is vanishingly small. It should be noted that a heterogeneous nucleation mechanism would only decrease the critical radius further. Thus a single SiO_2 molecule is itself a stable nucleus. Hence it is reasonable to assume a case of triatomic nucleation, whereby the association of one Si atom and two oxygen atoms creates a stable precipitate nucleus. Since silicon is the matrix species this model reduces to the diatomic case i.e. the association of two oxygen atoms. Such situations have been treated in an approximate way in the literature [93, 94].

Adopting the method suggested by Trinkaus and Mantl [93] and Trinkaus [94], the rate of change of single impurity atoms (i.e. impurity concentration in solution in the matrix) dC_s/dt , and of the precipitate nuclei of number density C can be written by the coupled equations as

$$\frac{dC_s}{dt} = D\Delta C_s + P(z) + K[C_p] - 2\pi r_0 D C_s^2 - 4\pi r D C_s C \quad (4.4)$$

$$\frac{dC}{dt} = \pi r_0 D C_s^2 \quad (4.5)$$

In equation (4.4), $D\Delta C_s$ stands for the long-range impurity diffusion, where D is the diffusion coefficient, Δ the Laplacian and C_s the impurity concentration in the matrix. $P(z)$ represents the rate at which the impurity is implanted into the matrix which is a function of the depth/spatial distance z . The third term $K[C_p]$ denotes the rate at which impurities could be liberated into the matrix due to incoming ions. This is a function of the concentration of impurities within the precipitates, and the number of precipitates, C , which is a function of the depth/spatial distance z . The last two terms represent the rate at which the matrix loses impurities during the creation of a nucleus and the rate at which the matrix loses impurities

to the growth of existing precipitates, respectively. Here r_0 denotes the reaction radius of two impurities, while r denotes the radius of an existing precipitate. It should be noted that for this model, we assume that the precipitates are all spherical in shape. Equation(4.5) denotes the rate of nucleation, dC/dt , which is half the rate at which the solute is depleted from the matrix.

An analytical solution of these equations is difficult without some further simplifications. $D\Delta C_s$ in equation (4.4) represents long-range diffusion, which can be neglected since the mean diffusional range of the mobile oxygen within the ensemble of existing precipitates is very small compared to the straggle. Hence, the diffusional broadening of the implanted profile can be neglected. $K[C_p]$ can also be ignored during implantation for cases where the volume fraction is low.

Under steady state nucleation conditions, $dC_s/dt=0$. This steady state nucleation period will cease when the probability of a newly implanted oxygen atom to join a pre-existing nucleus is the same as the probability of the atom to find another oxygen atom and form a new nucleus, i.e. when $C_s=C$. Using these assumptions, equation(4.4) reduces to

$$P(z) = 6\pi r_0 D C^2 \quad (4.6)$$

Following the suggestion of Trinkaus and Mantl [93], the reaction radius has been taken to be of the order of 0.5 nm. The equilibrium diffusivity was taken as $2.2 \times 10^{-16} \text{ cm}^2/\text{s}$ [17]. Assuming that the implanted profile is Gaussian in nature, having a standard deviation σ , the maximum value of $P(z)$ is

$$P_{\max} = \frac{\phi}{\sqrt{2\pi}\sigma} \quad (4.7)$$

where $\dot{\phi}$ is the dose rate. Substituting (4.7) into (4.6), and solving for C yields

$$C = 0.3 \left(\frac{\dot{\phi}}{\sigma r_0 D} \right)^{1/2} \quad (4.8)$$

Hence, an estimate for the number of nuclei at the center of the distribution can be found as $C = 2.2 \times 10^{20} \text{ cm}^{-3}$.

The value of the density of nuclei, C, calculated from this equation is nearly two orders of magnitude greater than the precipitate density found experimentally. This discrepancy could be accounted for by increasing either the reaction radius r_0 , or the diffusivity D, by about four orders of magnitude. Clearly, a reaction radius of 2 μm is unrealistic. However, it is possible that the diffusivity is radiation enhanced. Such effects are clearly demonstrated for dopants in silicon, and have also been observed for oxygen in silicon [92]. An enhancement of $\sim 3800\times$ in the oxygen diffusivity would provide the experimentally observed density of $\sim 3.5 \times 10^{18} \text{ cm}^{-3}$.

Growth and Impingement

From the experimental data, it is apparent that the number of precipitates in the matrix is almost a constant. This implies $dC/dt=0$ and the ensemble is in steady state growth mode. In the growth stage, the production term/rate of implantation is balanced by the absorption term/growth

$$P(z) = 4\pi D C_s C(z) r(z) \quad (4.9)$$

Using flux balance equations [91], we know that

$$\frac{DC_s}{r(z)} = C_p \frac{dr(z)}{dt} \quad (4.10)$$

Combining equations (4.9) and (4.10) and integrating yields

$$r(z) = \left(\frac{3\phi(z)}{4\pi C_p C(z)} \right)^{\frac{1}{3}} \quad (4.11)$$

where $\phi(z)$ is the local oxygen concentration. The implication of this result is simply that all of the incoming oxygen is incorporated in the growth of precipitates, as was observed experimentally (see Figure 4.10).

The model indicates that the local radius of the precipitates should vary as the 1/3rd power of the ratio between the local oxygen concentration in the precipitates to the local number density of precipitates. In Figure 4.11, the experimental data for all three doses have been plotted. The line that best fits all the experimental data points shows a power law dependence of .32, which is in good agreement with the value predicted from the model, i.e. .33. This simple model essentially states that, all the implanted oxygen is incorporated within the precipitates. From the HRTEM images it is evident that besides the growth of precipitates with increasing dose, impingement between precipitates begins to occur for a local oxygen concentration higher than $7 \times 10^{21} \text{cm}^{-2}$, and for precipitate radii exceeding 3 nm, in the vicinity of the projected range.

From the theoretical model it is predicted that r varies as the one third power of the local implanted concentration and hence it is obvious that the precipitates at the peak of the ion distribution will grow much faster than those at the tails of the ion distribution. Growth of precipitates at the peak of the ion profile will be subsequently restricted by the amount of space

available in this region. After this stage, impingement between precipitates will begin to occur. If this impingement is uniform in all directions, it is expected that larger spherical precipitates should evolve. However the experimental results do not show this behavior. The morphology of the rectangular precipitates observed at doses of $0.4 \times 10^{18} \text{ cm}^{-2}$ and $0.6 \times 10^{18} \text{ cm}^{-2}$ indicate that these precipitates have their shorter dimensions parallel to the surface and longer dimensions perpendicular to the surface. This unusual structure may be a result of the stresses exerted by the lattice on the precipitates.

It is known that the volume occupied by SiO_2 is 2.25 times greater than Si. Thus the underlying Si lattice restricts the growth and impingement in the planes parallel to the surface by exerting a biaxial compressive stress on the precipitates. The presence of a biaxial compressive stress has been established in previous studies [94]. Further, there is no such stress acting in the direction perpendicular to the surface. This indicates that impingement and growth in the plane parallel to the surface is restricted and should be much slower than in the direction perpendicular to the surface.

Further increase in dose causes growth and increased impingement between precipitates. Thus at a dose of $0.6 \times 10^{18} \text{ cm}^{-2}$, not only is the mean size of precipitates larger, but also increased impingement between the rectangular precipitates leads to the formation of large slabs of SiO_2 . These large SiO_2 slabs have their longer dimensions parallel to the surface. The shorter dimension of these SiO_2 slabs closely matches with the average size of the longer dimensions of the rectangular precipitates ($\sim 16 \text{ nm}$).

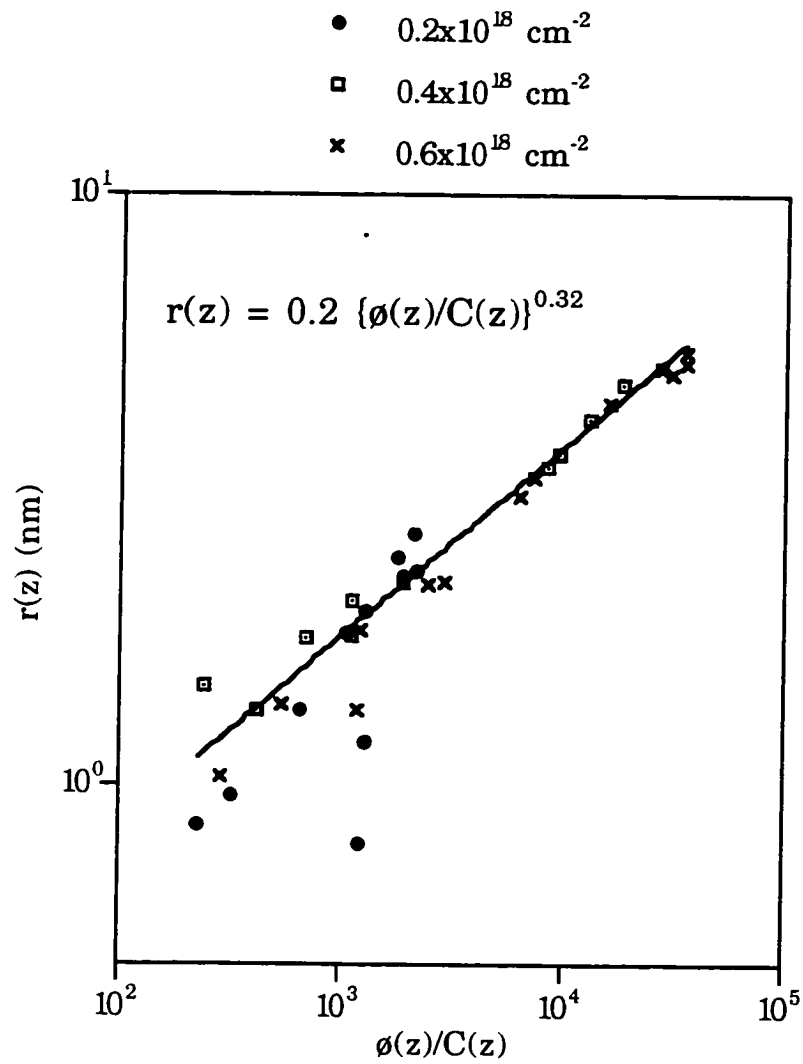


Figure 4.11. Radius of precipitates as a function of the dimensionless parameter $\phi(z)/C(z)$ from equation (4.11). The slope of the best fit is 0.32.

Coarsening

From the experimental results in Chapter 3, it was found that after post implantation annealing, some striking differences in the buried oxide structures were evident as a function of dose, for a particular implant energy. For an implant energy of 175 keV, it was observed that a dose of $0.2 \times 10^{18} \text{ cm}^{-2}$ yielded two spatially separated bands of precipitates, and no continuous buried oxide formed. For the dose of $0.4 \times 10^{18} \text{ cm}^{-2}$, a continuous buried oxide layer with extremely low Si island density was created. At the dose of $0.6 \times 10^{18} \text{ cm}^{-2}$, the continuous buried oxide layer was decorated with large Si islands, thereby degrading its quality. Such behavior has been observed by others [77, 96-102] and some models have been proposed to explain these structures. These models are discussed below.

The most recent model proposed to explain the formation of islands within the buried oxide [77] involves the growth and coalescence of precipitates in the annealed state. Based on intermediate anneals, this study reports that large precipitates form in two spatially separated regions. One region is located at the vicinity of the oxygen range at 300 - 400 nm from the surface and the other at a depth of 150 - 200 nm from the surface, at the tips of the multiply faulted defects. Larger precipitates occur at the lower region where the buried oxide eventually forms. With increase in dose they claim that the vertical separation between the two layers decreases.

Based on these features they claim that at the low dose of $0.225 \times 10^{18} \text{ cm}^{-2}$ the horizontal and vertical separation between precipitates precludes their coalescence into a continuous buried oxide. At a dose of $0.445 \times 10^{18} \text{ cm}^{-2}$ 'thin tubular precipitates' form in the upper region which are horizontally separated and cannot form a continuous layer, but grow

vertically and join the lower layer of larger precipitates without entrapping silicon. At a higher dose, the horizontal separation between precipitates decrease in the upper region. These precipitates coalesce to form a layer and the vertical growth of this layer into the lower layer of precipitates entraps silicon and gives rise to islands.

There are several limitation which make this model unrealistic. Since the precipitate distribution in the as-implanted state was not analyzed the initial conditions governing Ostwald ripening were ignored. Only one intermediate anneal was performed to model the evolution of the buried oxide. This limits the true time dependent precipitation evolution process to be analyzed. Ostwald ripening, which controls the precipitate dissolution and growth processes during annealing, demands that smaller precipitates which are located at the wings of the implant distribution dissolve. However, the model by Bagchi et al. [77] describes a process contrary to this, and emphasizes the growth of smaller precipitates to form layers at the wings of the implanted profile. The tubular precipitate structure, which this study reports at an intermediate annealing time and temperature, is possibly a direct consequence of the dissolution of smaller precipitates and growth of larger ones. Hence, this model fails to illustrate the true mechanism behind Si island formation and their dependence on dose.

On the other hand, an attempt to explain the banding of SiO₂ buried oxide layers based on the self structuring of precipitates during Ostwald ripening has been done for extremely low doses using experimental data and computer simulations [96 - 100]. This model assumes an ensemble of equally sized precipitates embedded within the matrix and removed from the surface. Conceiving this scenario as an inhomogeneous distribution, self organization results due to a concentration gradient which exists

initially between the precipitate layer and the surface. This gradient causes dissolution of the outermost precipitates in the layer. These outer precipitates screen the inner precipitates from the influence of the surface. The dissolution of the outer precipitates increases the solute concentration locally. Thus, a concentration gradient is established between the outer region and the inner precipitates. Since the innermost precipitates have a constant radius, material diffuses into the layer due to the concentration gradient. The dissolution and growth process continues and, with time, sublayers are created. A 'structure wavelength' , λ , is defined by the authors to determine the distance between the sublayers. This structure wavelength is related to the screening length, κ , by

$$\lambda = \pi \kappa \quad (4.12)$$

with κ defined as

$$\kappa^{-2} = 4\pi N R_0 \quad (4.13)$$

where N is the number density of the precipitates and R_0 is the initial radius of the precipitates. These relationships imply that the distance between the sublayers decreases with the increase in volume fraction (increasing N and/or R_0) and any inhomogeneity with depth in the radius of precipitates.

This is an excellent model for doses at or lower than $0.2 \times 10^{18} \text{ cm}^{-2}$ where the banding has been observed by others [77] and in this study. However, as the authors of the above study indicate, their results may be unrealistic since the initial as-implanted structure was not considered, and all precipitates were assumed to have the same initial radius. Further,

they also emphasize that if the sizes of precipitates at the center of the implant are extremely large no such structuring will occur [96].

These shortcomings have been proved to be true in this study. Indeed, the as-implanted precipitate distribution, which controls the post implantation anneal distribution, has a plethora of precipitates with different sizes and shapes. Moreover, there is a distinctive shape and enormous size difference between precipitates at the center of the profile from those located at the tails of the implanted profile. These differences are most pronounced for doses of $0.4 \times 10^{18} \text{ cm}^{-2}$ and higher. These inhomogeneities must have a profound effect on the Ostwald ripening process.

Model for Silicon Island Formation

Ostwald ripening is the dominant mechanism which dictates the growth and coalescence of precipitates during annealing. Larger precipitates grow at the expense of smaller ones and the driving force behind this process is the reduction in free energy of the system. When a pre-implanted structure is annealed at a high temperature, all precipitates below a critical radius are unstable and will dissolve. Theoretically, the equilibrium solubility at the precipitate interface depends on the radius of the precipitate, as given by the Gibbs-Thompson equation

$$C(r) = C_{\infty} \exp\left(\frac{2\gamma V}{rkT}\right) \quad (4.14)$$

where $C(r)$ is the concentration in equilibrium with a precipitate of radius r , C_{∞} is the equilibrium concentration of the impurity at the annealing temperature, γ is the interfacial energy, V is the atomic volume, T the anneal temperature and k the Boltzman's constant.

In an ensemble of say, 'i' precipitates, the mean concentration field created due to precipitates of different radii can be estimated by

$$\bar{C} = C_{\infty} \sum_i \exp\left(\frac{2\gamma V}{rkT}\right) \quad (4.15)$$

The value of the critical radius can be calculated by substituting \bar{C} into the Gibbs-Thompson equation and solving for r . The critical radius was calculated for each dose based on the ensemble of precipitate radii found experimentally. The graph in Figure 4.12 shows that the critical radius increases with increase in dose, from a value of 1.4 nm for a dose of $0.2 \times 10^{18} \text{ cm}^{-2}$ to a value of 2.8 nm for a dose of $0.6 \times 10^{18} \text{ cm}^{-2}$. During the initial annealing stage, the precipitates with radii below the critical value dissolve and transfer their mass to those with radii greater than r_c . This dissolution and growth process alters the mean field value of \bar{C} . Consequently, at a later instant of time the changed value of \bar{C} dictates another critical radius value, which will obviously be larger than the initial value of the critical radius. Hence, dissolution and growth takes place continuously, leading to the coarsening of the microstructure. This process makes \bar{C} and r_c strongly dependent on time.

Since the smaller precipitates are located predominantly at the tails of the impurity distribution, these dissolve initially, thereby transferring their mass to the larger precipitates situated closer to the location where the final buried oxide forms. This dissolution process due to the change in the mean field dictated by the precipitates controls the growth of the continuous buried oxide even for substoichiometric doses.

In Chapter 3, it was shown that after annealing the buried oxide was continuous for a dose of $0.4 \times 10^{18} \text{ cm}^{-2}$. Si islands appeared for doses

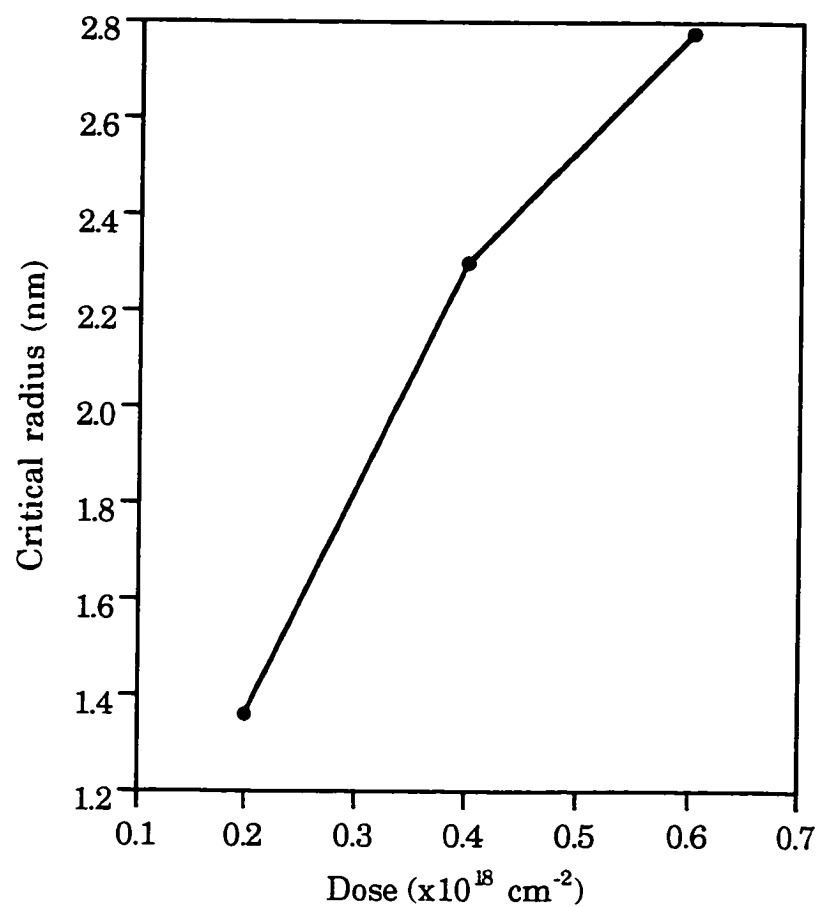


Figure 4.12. Critical radius for coarsening of precipitates at the initial stages of annealing, as a function of dose.

between $0.5 \times 10^{18} \text{ cm}^{-2}$ and $1.0 \times 10^{18} \text{ cm}^{-2}$ for the 175 keV implant. On the basis of the analysis presented here, the presence of islands within the buried oxide may be understood as a consequence of the inhomogeneous precipitate size distribution at the vicinity of the projected range in the as-implanted state. At $0.4 \times 10^{18} \text{ cm}^{-2}$ it is apparent from the HRTEM image in Figure 4.3c that all the rectangular precipitates are approximately the same size. Moreover, they are significantly larger than the spherical precipitates at the tails of the distribution. This implies that the spherical precipitates would be unstable with respect to the rectangular precipitates upon annealing. Moreover, since the rectangular precipitates are approximately of homogeneous size they will grow and coalesce to form a uniform buried oxide layer.

Upon increasing the dose to $0.6 \times 10^{18} \text{ cm}^{-2}$, impingement between precipitates is further intensified. The rectangular precipitates impinge in some regions and form large slabs of SiO_2 in the as-implanted state. The average length of the longest dimension of the SiO_2 is 80 nm, which is 400% greater than the longest dimension of the rectangular precipitates. It is immediately obvious that all other precipitates present at this dose will be unstable with respect to these SiO_2 slabs. The HRTEM image in Figure 4.4c shows that the SiO_2 slabs are surrounded by smaller rectangular precipitates. However, since these SiO_2 slabs are discontinuous at this dose, during coarsening, large volumes of unoxidized Si can get entrapped giving rise to Si islands within the buried oxide. Once unoxidized silicon is entrapped within the SiO_2 layer it is incapable of escaping due to the low diffusivity of silicon in silicon dioxide [17].

Based upon this analysis, it is apparent that as the dose increases more SiO_2 slabs will be formed due to the impingement of rectangular

precipitates. Thus, they will occur with higher density and become more continuous, which was observed for the doses of $0.8 \times 10^{18} \text{ cm}^{-2}$ and $1.0 \times 10^{18} \text{ cm}^{-2}$ in Chapter 3. This clearly explains the reason behind the occurrence of smaller but higher density of Si islands observed at the higher doses. Si islands occupy 42% of the buried oxide at a dose of $0.5 \times 10^{18} \text{ cm}^{-2}$ while they occupy only 13% of the buried oxide at the dose of $1.2 \times 10^{18} \text{ cm}^{-2}$. At the dose of $1.2 \times 10^{18} \text{ cm}^{-2}$, which is above the stoichiometric dose for buried oxide at 175 keV, a continuous buried oxide exists in the as-implanted state. Remnants of SiO_2 slabs are observed near the top and bottom of the interfaces. This is precisely the location at which islands are observed after annealing. Thus islands form as a result of inhomogeneous precipitation in the as-implanted state.

Conclusions

From this analysis it has been established that the initial precipitate distribution in the as-implanted state is critical in determining the final quality of the buried oxide. Extreme inhomogeneities in precipitate sizes, present at the vicinity of the projected range, in the as-implanted state can lead subsequently to Si islands within the buried oxide, after annealing. A simple model has been suggested which could be used to control implantation conditions to improve the quality of the buried oxide.

Nucleation, growth and impingement and subsequently, coarsening are the dominant physical processes which govern the final quality of the buried oxide. These processes have been found to be dependent on implantation conditions. This also shows the uniqueness of ion beam synthesis in comparison to other cases of phase transformations.

During nucleation, the number of nuclei have been shown to be dependent on the dose rate, temperature (due to dependence on diffusivity) and the energy (due to dependence on the straggle).

During growth, the experimental and theoretical analysis suggests that the radii of the precipitates is dependent on the local concentration of oxygen and the local concentration of the precipitates. Impingement between precipitates is a direct consequence of growth and should be avoided in order to obtain island-free buried oxides.

Coalescence is purely controlled by Ostwald ripening and hence is strongly dependent on temperature and time. However, the ultimate structure of the buried oxide cannot be controlled at this stage. The final structure of the buried oxide is absolutely determined by the precipitate distribution in the as-implanted state.

Based on the model, which is supported by the experimental results in this study, some suggestions for modification of implantation conditions can be made to yield device quality buried oxides. To avoid banding of precipitates at the dose of $0.2 \times 10^{18} \text{ cm}^{-2}$, the energy of the implant needs to be lowered. This would reduce the straggle, resulting in a tighter implant profile. Since at this dose, the precipitates are all spherical, with no significant inhomogeneities in size or shape, a continuous buried oxide could result. For the dose of $0.6 \times 10^{18} \text{ cm}^{-2}$ it was seen that severe inhomogeneities in precipitate sizes at the projected range in the as-implanted state, possibly led to silicon inclusions within the buried oxide after annealing. Thus, for the dose of $0.6 \times 10^{18} \text{ cm}^{-2}$ the energy, temperature or dose rate could be modified to obtain a finer distribution of precipitates, which would yield a silicon island free buried oxide.

In this simple model, only the dominant implantation effect, i.e. the continuous introduction of impurities (the production term) has been considered. The model could be further improved by introducing the effects due to other physical processes which occur during ion implantation. If the precipitate sizes become appreciable during implantation, bombardment by incoming ions may result in impurity ions reentering solution from the precipitates. In addition, ions may be directly implanted into precipitates. The effect of long range diffusion was not considered but in cases where straggle is comparable to the mean diffusion range of impurities, this term may need to be included. These effects were neglected to obtain an analytical solution since such solutions are not possible when these terms are considered. Therefore, computationally intensive methods will be necessary. From the experimental viewpoint, it is necessary to analyze doses lower than $0.2 \times 10^{18} \text{ cm}^{-2}$ to obtain a better understanding of the nucleation, and early growth stages of the precipitates.

CHAPTER 5 SUMMARY AND CONCLUSIONS

Ion beam synthesis of SIMOX (separation by implantation of oxygen), uses a high energy and high dose of oxygen to create an insulating buried oxide layer underneath a single crystalline silicon overlayer. This process mainly consists of two steps. In the first step, oxygen is implanted into a single crystalline silicon wafer, which is kept at an elevated temperature to prevent amorphization of the silicon overlayer. The second step is annealing at extremely high temperatures ($\sim 1300^{\circ}\text{C}$). This post implantation anneal is primarily done to obtain a continuous buried oxide layer, and to reduce the damage created in the silicon overlayer during irradiation. The final quality of the SIMOX structure is dictated by the silicon overlayer and the buried oxide structures. However, it has been observed that, after post implantation annealing, threading dislocations in the silicon overlayer and silicon islands within the buried oxide may form, both of which degrade the quality of the SIMOX structure. Hence, the main objective of this study was to develop an understanding of the effects of the implantation conditions, and to determine the underlying physical mechanisms, governing the evolution of the microstructure in SIMOX.

The implantation conditions (implant energy, implant dose, substrate temperature, and beam current) determine the microstructural changes in SIMOX. It is critical to develop an understanding of the individual effects of these parameters on the microstructure. Using independent implantation parameter control, it was found from this study, that the implantation

parameters were interlinked and affected the evolution of the microstructure in a variable manner. It is obvious, that this interdependence makes controlling this system extremely complex. Hence, an attempt was made to clearly define the parameters which were most critical to obtain device quality SIMOX.

The independent effects of the processing conditions on threading dislocation density and buried oxide structure (which are response variables) were determined in this study. The single most important variable was the implant dose. For a given set of implant conditions, there are only certain dose ranges, or windows, in which high quality SIMOX can be fabricated. To illustrate the influence of other implant parameters on these dose windows, the schematic diagrams shown in Figure 5.1 have been developed. In this figure, the response variables (threading dislocation density and Si island fraction in the buried oxide) have been represented as a function of dose. The arrows are meant to show how the dose windows would respond to decreasing the indicated parameters. From the experimental results obtained in this present study, it was apparent that the microstructural behavior at substoichiometric doses was very different from stoichiometric ones.

Figure 5.1a shows that there exists a window at intermediate doses in which the threading dislocation density in the silicon overlayer is low. For very low substoichiometric doses, increases in energy might lead to a bilayered distribution of precipitates, instead of a continuous buried oxide. In such cases, it has been established from this study, that these precipitates pin defects and consequently increase the final threading dislocation density in the silicon overlayer enormously. Moreover, this banded precipitate structure precludes the formation of a continuous buried

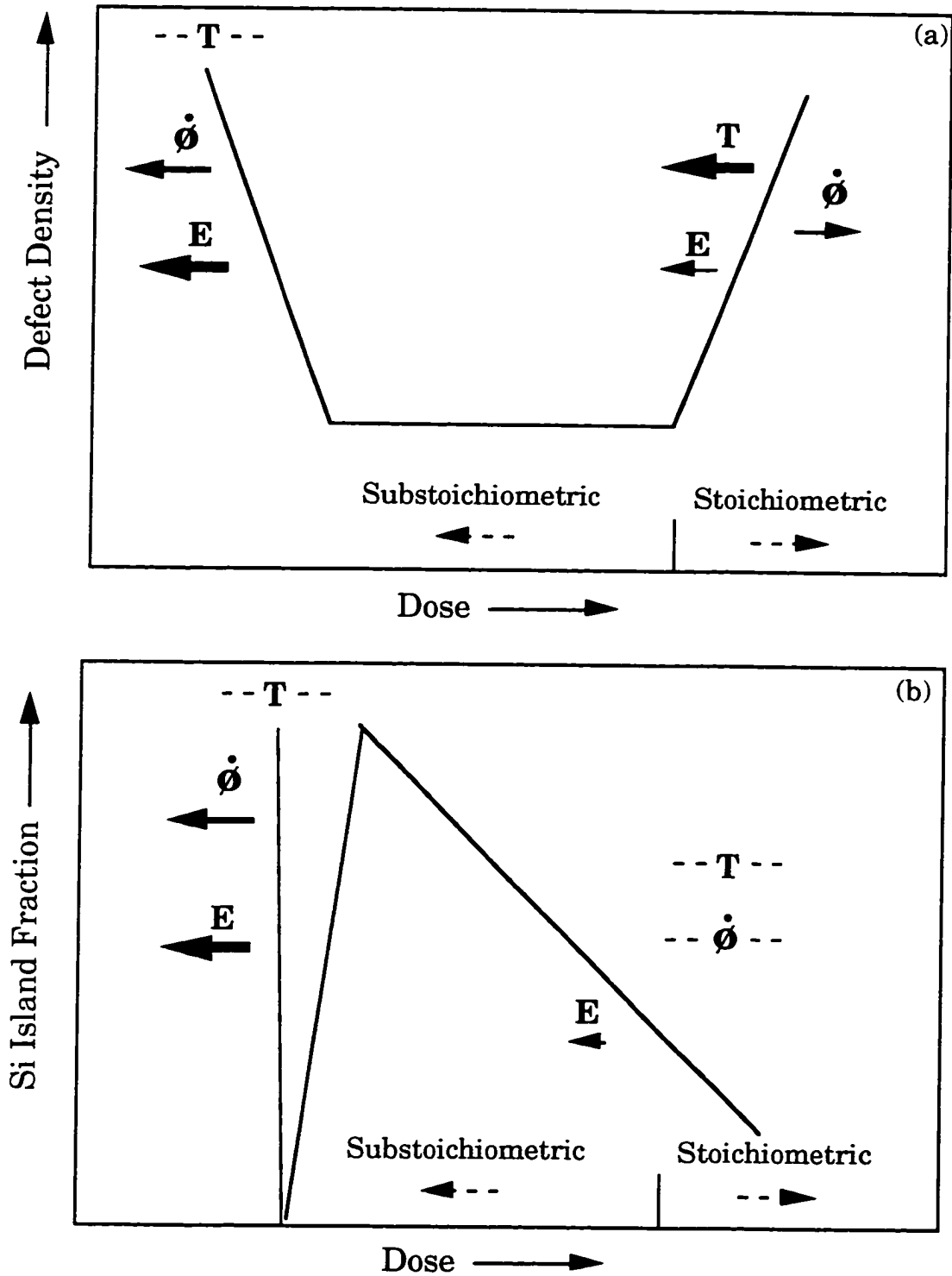


Figure 5.1. Schematic representation of the effect of implantation parameters (E =energy, T =substrate temperature, ϕ =dose rate) on microstructural evolution. The arrows indicate the effect of decreasing the indicated parameters.
 a) silicon overlayer quality; b) buried oxide quality

oxide and fails to meet the necessary criterion for device grade SIMOX. However, a decrease in energy would increase the dose window allowed for device quality SIMOX. It was established from this study that, provided a continuous buried oxide is formed, the threading dislocation densities are not strongly affected by changes in implant energy. It was also found that substrate temperature did not play a vital role in determining the final threading dislocation densities. Based on the results and models discussed in Chapter 4, the beam current has a potentially large effect on threading dislocation density, primarily because of its influence on the formation of a bilayered precipitate structure

For stoichiometric doses, increase in energy has been found from this study and previously [85], to decrease the threading dislocation density. Hence, increased energies will broaden the dose window for device quality silicon overlayer in stoichiometric cases. Substrate temperature was found to play a crucial role in determining the final threading dislocation density in the silicon overlayer. Low substrate temperatures (less than $\sim 600^{\circ}\text{C}$) resulted in a dramatic increase in defect densities in the silicon overlayer. Thus, for stoichiometric dose implants it is necessary to maintain elevated substrate temperatures ($\sim 600^{\circ}\text{C}$) during implantation. Increase in the instantaneous beam current was found from this present study, to increase the final threading dislocation density. This implied use of lower beam currents would prove beneficial to improve the quality of the silicon overlayer. However, it must be noted that use of low beam currents increases the total implantation time, and especially at stoichiometric doses, this might not prove economical.

Coupling the above effects of implantation conditions on threading dislocation density, to the response of the buried oxide microstructure.

significantly restricts the choice of implantation parameters. Silicon islands within the buried oxide, deteriorate the quality of the buried oxide. The response of the silicon islands to changes in implantation conditions is represented schematically in Figure 5.1b. The experimental results from this study showed that the behavior of the silicon islands to changes in implantation conditions at substoichiometric doses was very different from those at stoichiometric doses.

For very low substoichiometric doses, it was found that the formation of a continuous buried oxide was interdependent on the dose and energy. At these very low doses, depending on the implant energy, spatially separated banding of precipitates precludes the formation of the buried oxide. These precipitates pin dislocations and contribute immensely to high defect densities in the silicon overlayer. Since for device grade SIMOX both of these effects are deleterious, increased energy at substoichiometric doses is detrimental. Decrease in energy would have the opposite effect and thereby widen the dose window. For substoichiometric cases where a continuous buried oxide is formed the fraction of the buried oxide occupied by silicon islands is not significantly affected by changes in energy. Moreover, from the experimental results of this study, the substrate temperature also does not seem to affect the silicon island formation appreciably. Extensive evaluation and modeling of the precipitation mechanism for substoichiometric doses was performed in this study. These studies showed that the time averaged dose rate controlled the as-implanted precipitate distribution significantly. In brief, the results indicated that, an overly coarse precipitate distribution leads to the formation of silicon islands. The number density of precipitates was found to be directly proportional to the time averaged local dose rate. Hence, for doses which do yield a continuous

buried oxide, but are decorated with silicon islands, a higher dose rate is recommended. This is also economical, since the time necessary for implantation is reduced.

For stoichiometric doses, where a continuous buried oxide is formed in the as-implanted state, the implantation parameter variation is much more flexible. It is known that silicon islands at the lower buried oxide/silicon substrate interface do not deteriorate the quality of the buried oxide significantly. Consequently, the changes in energy, substrate temperature and beam current for such structures are not constrained.

The other objective of this study was to develop an understanding of the mechanisms underlying the evolution of the response variables (i.e. threading dislocations and silicon islands).

Speculations exist in the literature about the correlation between near surface strain and the nucleation and growth of dislocation half loops in the as-implanted state. From the experimental analysis, it was found that the density of dislocation half loops did not consistently vary with the near surface strain, i.e., there does not exist a unique critical strain value for half loop formation. Instead, theoretical calculations based on strain energy considerations showed that half loop formation depends on both the thickness of the strain layer as well as the magnitude of the strain. The experimental results agreed remarkably well with these calculations for half loops on habit planes at an angle to the surface. However, the calculated activation energy required for the homogeneous nucleation of dislocation half loops at the silicon surface was unrealistically large. Hence, it was concluded that homogeneous nucleation of dislocation half loops due to the near surface strain induced by cavities is not possible. Nucleation of dislocation half loops at the surface is probably due to

heterogeneous nucleation. These heterogeneous nucleation processes apparently occur to unequal extents for the two types of loop habit planes. As a result, nucleation of half loops perpendicular to the surface is a more difficult, but still operative process.

It was also established that threading dislocations for stoichiometric doses were a result of dislocation half loops in the as-implanted state. However, only dislocation half loops on planes perpendicular to the silicon surface evolved into threading dislocations. A quantitative correlation based on data from this study and the literature indicated that only about 1% of these dislocation half loops developed into threading dislocations.

Dislocation half loops were not observed for substoichiometric doses. The dominant defects in the as-implanted state were stacking faults, which were spatially separated from the surface. When a bilayered distribution of precipitates occurred instead of a continuous buried oxide, these precipitates pinned the defects and resulted in a high density of threading dislocations. To develop an understanding of such banding of precipitates and the formation of silicon islands within the buried oxide, extensive studies were performed to determine the as-implanted precipitate distribution.

The most important result from the study of the as-implanted precipitate distribution was that, for the first time, it was possible to understand the mechanism behind buried oxide growth and silicon island formation. In particular, it was concluded that the as-implanted precipitate size and number density distributions control subsequent formation of the buried oxide during annealing. The as-implanted precipitate distribution showed significant variations with respect to implant dose. With increase in implant dose, there was an explosive

increase in the precipitate sizes in the vicinity of the projected range, while the increase in size for precipitates at the tails of the oxygen profile was more gradual. From HRTEM images and SIMS analysis, it was apparent that when the local oxygen concentration exceeded $7 \times 10^{21} \text{ cm}^{-3}$ impingement between precipitates was initiated. This impingement process was responsible for severe inhomogeneities in the precipitate size distribution in the vicinity of the projected range.

A simple model was developed based on these observations to predict the microstructural evolution, and the manner in which it is influenced by implantation conditions. It was found that banding was possibly a result of widely separated precipitates present in the as-implanted state, which was possibly a consequence of the energy of implant. On the other hand, the formation of silicon islands within the buried oxide, was a consequence of the coarsening of inhomogeneous precipitates present at the vicinity of the projected range.

Thus, from this study it was possible to achieve a better understanding of the physical mechanisms governing microstructural evolution in SIMOX as a function of implantation parameters. Based on this understanding, a roadmap for manipulating these implantation parameters to obtain an improved SIMOX structure has been developed.

REFERENCES

1. K. Izumi, M. Doken and H. Ariyoshi, *Electron. Lett.* **14**, 593 (1978).
2. J. S. Williams and J. M. Poate, in *Ion Implantation and Beam Processing*, edited by J.S. Williams and J.M. Poate (Academic Press, New York, 1984) p. 1.
3. J. F. Ziegler, in *Ion Implantation Science and Technology*, edited by J. F. Ziegler (Academic Press, New York, 1988) p. 3.
4. J. M. Poate and J. S. Williams, in *Ion Implantation and Beam Processing*, edited by J. S. Williams and J. M. Poate (Academic Press, New York, 1984) p. 14.
5. J. P. Colinge, in *SOI Technology*, edited by J. P. Colinge (Kluwer Press, Boston, 1991) p. 45.
6. H. W. Lam, A. F. Tasch and R. J. Pinizotto, in *VLSI Electronics: Microstructure Science*, **4**, edited by N. G. Einspruch (Academic Press, New York, 1982) p. 1.
7. B. Y. Tsaur, *Mater. Res. Soc. Symp. Proc.* **53**, 365 (1986).
8. J. C. Sturm, *Mater. Res. Soc. Symp. Proc.* **107**, 295 (1988).
9. P. L. F. Hemment, *Mater. Res. Soc. Symp. Proc.* **53**, 207 (1986).
10. B. O. Colbesen and H. P. Strunk, in *VLSI Electronics: Microstructure Science*, **12**, edited by N. G. Einspruch and H. R. Huff (Academic Press, New York, 1985) p. 144.
11. K. V. Ravi, *Imperfections and Impurities in Semiconductor Silicon* (Wiley-Interscience, New York, (1981).
12. J. E. Lawrence and H. R. Huff, in *VLSI Electronics: Microstructure Science*, **5**, edited by N. G. Einspruch and H. R. Huff (Academic Press, New York, 1982) p. 51.
13. M. K. El-Ghor, S. J. Pennycook, F. Namavar and N. H. Karam, *Appl. Phys. Lett.* **57**, 156 (1990).

14. D. Hill, P. Fraundorf and G. Fraundorf, J. Appl. Phys. **63**, 4933 (1988).
15. D. G. Beanland, in Ion Implantation and Beam Processing, edited by J. S. Williams and J. M. Poate (Academic Press, New York, 1984) p. 263.
16. Y. Takano and M. Maki, in Semiconductor Silicon 1973, edited by H. R. Huff and R. B. Burgess (Electrochem. Soc., Pennington, N.J., 1973) p. 469.
17. J. C. Mikkelsen, Jr., Mater. Res. Soc. Proc. **59**, 19 (1986).
18. L. C. Kimerling and J. R. Patel, in VLSI Electronics: Microstructure Science, edited by N. G. Einspruch and H. R. Huff (Academic Press, New York, 1985) p. 223.
19. A. Bourret, Mater. Res. Soc. Symp. Proc. **59**, 223 (1986).
20. S. M. Hu, Appl. Phys. Lett. **36**, 561 (1980).
21. S. M. Hu, Mater. Res. Soc. Symp. Proc. **59**, 249 (1986).
22. A. Bourret, J. Thibault-Desseaux and D. N. Seidman, J. Appl. Phys. **55**, 825 (1984).
23. J. Stoemenos, A. Garcia, B. Aspar, and J. Margail, J. Electrochem. Soc. **142**, 4 (1995).
24. S. M. Hu, J. Appl. Phys. **45**, 1567 (1974).
25. K. Car, P. J. Kelly, A. Oshiyama, and S. T. Pantelides, Phys. Rev. Lett. **52**, 1814 (1984).
26. W. P. Maszara, J. Appl. Phys. **64**, 123 (1988).
27. D. Venables and K. S. Jones, Nuc. Inst. and Methods **B74**, 65 (1993).
28. O. W. Holland, D. S. Zhou, and D. K. Thomas, Appl. Phys. Lett. **63**, 896 (1993).
29. S. Visitserngtrakul, C. O. Jung, B. F. Cordts, P. Roitman and S. J. Krause, Mat. Res. Soc. Symp. Proc. **183**, 135 (1990).
30. O. W. Holland, T.P. Sjoreen, D. Fathy, and J. Narayan, Appl. Phys. Lett. **45**, 1081 (1984).
31. S. Nakashima and K. Izumi, J. Mater. Res. **5**, 1918 (1990).
32. S. Nakashima and K. Izumi, J. Mater. Res. **8**, 523 (1993).

33. O. W. Holland, L. Xie, B. Nielsen and D. S. Zhou, *J. Elec. Mat.* **25**, 1, (1996).
34. M. K. El-Ghor, S. J. Pennycook, T. P. Sjoreen, C. W. White and J. Narayan, *Mater. Res. Soc. Symp. Proc.* **107**, 79 (1988).
35. J. D. Lee, J. C. Park, D. Venables, S. J. Krause, and P. Roitman, *Mater. Res. Soc. Symp. Proc.* **316**, 753 (1994).
36. J. Stoemenos, K. J. Reeson, A. K. Robinson and P. L. F. Hemment, *J. Appl. Phys.* **69**, 793 (1991).
37. S. Bagchi, J. D. Lee, S. J. Krause and P. Roitman, *Electrochem. Soc. Proc.* **96**, 74 (1996).
38. A. De Veirman, J. Van Landuyt, J. Vanhellemont, H. Maes and K. Yallup, *Vacuum* **42**, 367 (1991).
39. S. S. Gill and I. H. Wilson, *Mat. Res. Soc. Symp. Proc.* **56**, 275 (1988).
40. H. H. Hosack, J. Hollingsworth, M. K. El-Ghor and K. A. Joyner, *Mat. Res. Soc. Symp. Proc.* **235**, 159 (1992).
41. R. Weber, R. Yankov, R. Muller, W. Skorupa, S. Reiss and K.-H. Heinig, *Mat. Res. Soc. Symp. Proc.* **316**, 729 (1994).
42. S. Nakashima and K. Izumi, *J. Mater. Res.* **8**, 523, (1993).
43. C. Jassaud, J. Margail, J. Stoemenos and M. Bruel, *Mat. Res. Soc. Symp. Proc.* **100**, 17 (1988).
44. A. Yoshino, K. Kasama, M. Sakamoto, *Nuc. Inst. and Methods*, **B39**, 203 (1989).
45. A. H. Van Ommen, H. J. Ligthart, J. Politiek and M. P. A. Vieggers, *Mat. Res. Soc. Symp. Proc.* **93**, 119 (1987).
46. S. Bagchi, J. D. Lee, S. J. Krause and P. Roitman, *Proc. 1995 IEEE Intl. SOI Conf.* 118 (1995).
47. V. V. Afanas'ev, G. A. Brown, H. L. Hughes, S. T. Liu and A.G. Revesz, *J. Electrochem. Soc.* **143**, 695 (1996).
48. S. D. Littlewood and J. A. Kilner, *J. Appl. Phys.* **63**, 2173 (1988).
49. Y. Li, J. A. Kilner, R. J. Chater, A. Nejim, P. L. F. Hemment and T. J. Tate, *J. Appl. Phys.* **74**, 82 (1993).

50. O. W. Holland, C. W. White, M. K. El-Ghor and J. D. Budai, *J. Appl. Phys.* **68**, 2081 (1990).
51. Y. Li, J. A. Kilner, P. L. F. Hemment, A. K. Robinson, J. P. Zhang, K. J. Reeson, C. D. Marsh, and G. R. Brooker, *Appl. Phys. Lett.* **59**, 3130 (1991).
52. S. S. Gill, Ph.D. Dissertation, Univ. Of Surrey, U. K. (1980).
53. S. S. Gill and I. H. Wilson, *Thin Solid Films* **55**, 435 (1978).
54. Y. Li, J. A. Kilner, A. K. Robinson, P. L. F. Hemment, and C. D. Marsh, *J. Appl. Phys.* **70**, 3605 (1991).
55. P. L. F. Hemment, K. J. Reeson, J. A. Kilner, R. J. Chater, C. D. Marsh, G. R. Booker, C. K. Celler, and J. Stoemenos, *Vacuum* **36**, 877 (1986).
56. M. E. Twigg, L. P. Allen, B. J. Mrstik and L. T. Ardis, *Proc. 1993 IEEE Intl. SOI Conf.* 50 (1993).
57. M. J. Anc, B. F. Cordts, L. P. Allen, W. A. Krull and M. A. Guerra, *Proc. 1993 IEEE Intl. SOI Conf.* 46, (1993).
58. M. J. Anc and W. A. Krull, *Proc. 1994 IEEE Intl. SOI Conf.* 79 (1994).
59. J. Narayan and K. Jagannadham, *J. Appl. Phys.* **62**, 1694 (1987).
60. A. E. White, K. T. Short, J. L. Batstone, D. C. Jacobson, J. M. Poate and K. W. West, *Appl. Phys. Lett.* **50**, 19 (1987).
61. A. E. White, K. T. Short, L. N. Pfeiffer, K. W. West and J. L. Batstone, *Mater. Res. Soc. Symp. Proc.* **74**, 585 (1987).
62. C. G. Tuppen, M. R. Taylor, P. L. F. Hemment and R. P. Arrowsmith, *Appl. Phys. Lett.* **45**, 57 (1984).
63. C. G. Tuppen, M. R. Taylor, P. L. F. Hemment and R. P. Arrowsmith, *Thin Solid Films* **131**, 233 (1985).
64. J. Stoemenos and J. Margail, *Thin Solid Films* **135**, 115 (1986).
65. S. J. Krause, C. O. Jung, S. R. Wilson, R. P. Lorigan and M.E. Burnham, *Mater. Res. Soc. Symp. Proc.* **53**, 257 (1986).
66. S. Visitserngtrakul, C. O. Jung, T. S. Ravi, B. F. Cordts, D. E. Burke and S. J. Krause, *Inst. Phys. Conf. Ser. No.* **100**, 557 (1989).
67. S. J. Krause, C. O. Jung, T. S. Ravi, S. R. Wilson and D. E. Burke, *Mater. Res. Soc. Symp. Proc.* **107**, 93 (1988).

68. P. L. F. Hemment, E. A. Maydell-Ondrusz, J. E. Castle, R. Paynter, M. C. Wilson, R. G. Booker, J. A. Kilner and R. P. Arrowsmith, *Thin Solid Films* **128**, 125 (1985).
69. S. Maillet, R. Stuck, J. J. Grob, A. Golanski, R. Pantel and A. Perio, *Nuc. Instr. and Methods* **B19/20**, 294 (1987).
70. J. Vanhellemont and C. Claeys, *J. Appl. Phys.* **62**, 3960 (1987).
71. M. K. El-Ghor, S. J. Pennycook, T. P. Sjoreen and J. Narayan, *Mater. Res. Soc. Symp. Proc.* **74**, 591 (1987).
72. S. Visitserngtrakul, B. F. Cordts and S. J. Krause, *Mater. Res. Soc. Symp. Proc.* **157**, 161 (1990).
73. S. Visitserngtrakul, S. J. Krause and B. F. Cordts, *J. Appl. Phys.* **69**, 1784 (1991).
74. S. R. Wilson and D. Fathy, *J. Electron. Mater.* **13**, 127 (1984).
75. D. Fathy, O. L. Krivanek, R. W. Carpenter, and S. R. Wilson, *Inst. Phys. Conf. Ser. No.* **67**, 479 (1983).
76. M. Bruel, J. Margail, J. Stoemenos, P. Martin and C. Jassaud, *Vacuum*, **35**, 589 (1985).
77. S. Bagchi, S. J. Krause, and P. Roitman, *Proc. 1997 IEEE Intl. SOI Conf.*, 36 (1997).
78. J. W. Edington, *Practical Electron Microscopy in Materials Science* (Van Nostrand Reinhold, New York, 1976).
79. M. Ruhle and M. Wilkens, *Crystal Lattice Defects* **6**, 129 (1975).
80. J. W. M. Dumond, *Phys. Rev.* **52**, 872 (1937).
81. W. J. Bartels, *J. Vac. Sci. and Technol.* **B1**, 338 (1983).
82. W. J. Bartels, U. S. Patent No. 4567605 (1986).
83. D. Venables, Ph.D. Dissertation, Univ. of Florida (1992).
84. D. S. Zhou, O. W. Holland, and J. D. Budai, *Appl. Phys. Lett.* **63**, 3580 (1993).
85. R. Datta, L. P. Allen, R. P. Dolan, K. S. Jones and M. Farley, *Mat. Sci. and Eng.* **B46**, 8 (1997).
86. J. W. Matthews and A. E. Blackslee, *J. Crystal Growth* **27**, 118 (1974).

87. J. W. Matthews, J. Vac. Sci. and Technol. **12**, 126 (1975).
88. J. P. Hirth and J. Lothe, Theory of Dislocations (Krieger Publishing Co., Malabar, FL, 1982).
89. R. People and J. C. Bean, Appl. Phys. Lett. **47**, 322 (1985).
90. D. M. Maher and B. Zhang, J. Vac. Sci. and Technol. **B12**, 347 (1994).
91. D. A. Porter and K. E. Easterling, Phase Transformations in Metals and Alloys (Van Nostrand Reinhold, London, 1981).
92. A. Borghesi, B. Pivac, A. Sassella, and S. Stella, J. Appl. Phys. **77**, 4169 (1995).
93. H. Trinkaus and S. Mantl, Nuc. Inst. and Methods **B80/81**, 862 (1993).
94. H. Trinkaus, Radiation Effects **101**, 91 (1986).
95. D. Venables, K. S. Jones, F. Namavar, and J. M. Manke, Mater. Res. Soc. Symp. Proc. **235**, 103 (1992).
96. S. Reiss and K. -H Heinig, Nuc. Inst. and Methods **B112**, 223 (1996).
97. S. Reiss, K. -H. Heinig, R. Weber, and W. Skorupa, Mat. Res. Soc. Symp. Proc. **316**, 819 (1994).
98. S. Reiss and K. -H. Heinig, Nuc. Inst. and Methods **B84**, 229 (1994).
99. S. Reiss, R. Weber, K. -H Heinig, and W. Skorupa, Nuc. Inst. and Methods **B89**, 337 (1994).
100. S. Reiss and K. -H. Heinig, Nuc. Inst. and Methods **B102**, 256 (1995).
101. H. U. Jager, Nuc. Inst. and Methods **B65**, 67 (1992).
102. R. Weber, R. Yankov, R. Muler, W. Skorupa, S. Reiss, and K. -H. Heinig, Mat. Res. Soc. Symp. Proc. **316**, 729 (1994).

BIOGRAPHICAL SKETCH

Ranju Datta was born on December 12th, 1969, in Calcutta, India. The author received her Bachelor of Science degree in physics from Jadavpur University (India) in August 1991. She pursued her studies in physics at the same university and obtained her Master of Science degree in 1993. In August of 1993, she came to the United States, as a graduate student in the Department of Materials Science and Engineering, at the University of Florida, specializing in electronic materials. She started her doctoral studies under the supervision of Dr. Kevin S. Jones, in January 1994 and will complete her requirements for the Ph.D. in December 1997.

I certify that I have read this study and that in my opinion it conforms to acceptable standards of scholarly presentation and is fully adequate, in scope and quality, as a dissertation for the degree of Doctor of Philosophy.



Kevin S. Jones, Chairman
Professor of Materials Science
and Engineering

I certify that I have read this study and that in my opinion it conforms to acceptable standards of scholarly presentation and is fully adequate, in scope and quality, as a dissertation for the degree of Doctor of Philosophy.



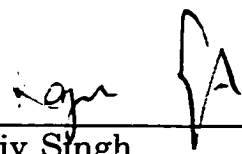
Cammy Abernathy
Professor of Materials Science
and Engineering

I certify that I have read this study and that in my opinion it conforms to acceptable standards of scholarly presentation and is fully adequate, in scope and quality, as a dissertation for the degree of Doctor of Philosophy.



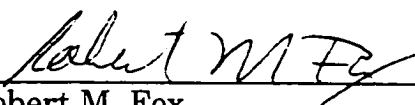
Stephen S. Pearton
Professor of Materials Science
and Engineering

I certify that I have read this study and that in my opinion it conforms to acceptable standards of scholarly presentation and is fully adequate, in scope and quality, as a dissertation for the degree of Doctor of Philosophy.



Rajiv Singh
Professor of Materials Science
and Engineering

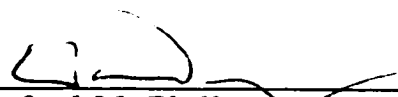
I certify that I have read this study and that in my opinion it conforms to acceptable standards of scholarly presentation and is fully adequate, in scope and quality, as a dissertation for the degree of Doctor of Philosophy.

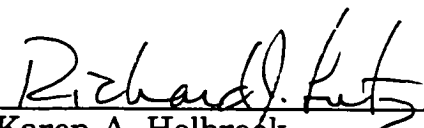


Robert M. Fox
Associate Professor of Electrical
and Computer Engineering

This dissertation was submitted to the Graduate Faculty of the College of Engineering and to the Graduate School and was accepted as a partial fulfillment of the requirements for the degree of Doctor of Philosophy.

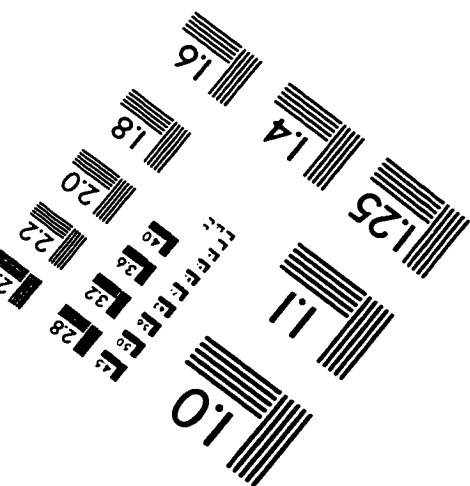
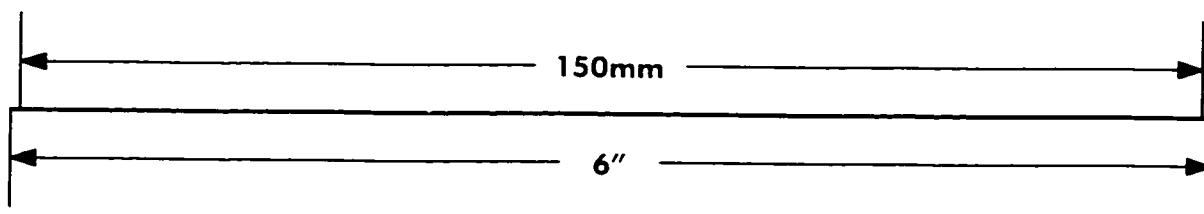
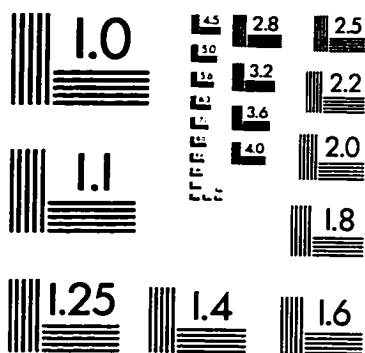
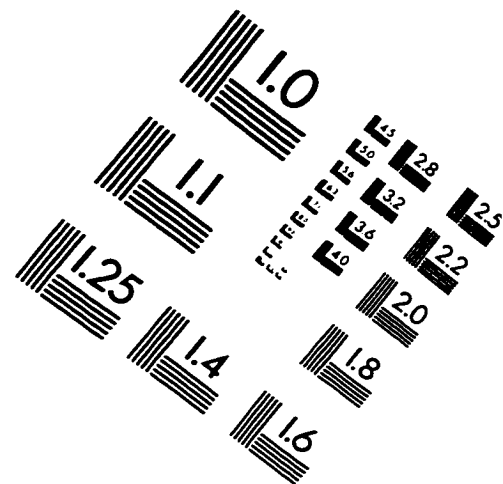
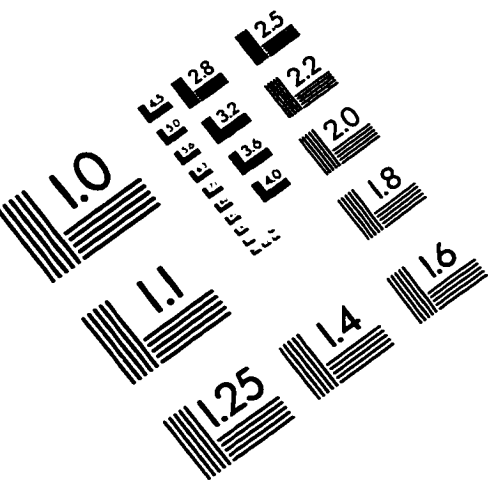
May 1998



Winfred M. Phillips
Dean, College of Engineering

Karen A. Holbrook
Dean, Graduate School

IMAGE EVALUATION TEST TARGET (QA-3)



APPLIED IMAGE, Inc
1653 East Main Street
Rochester, NY 14609 USA
Phone: 716/482-0300
Fax: 716/288-5989

© 1993, Applied Image, Inc., All Rights Reserved

